SEISMIC-RESISTING SELF-CENTERING STRUCTURES WITH SUPERELASTIC SHAPE MEMORY ALLOY DAMPING DEVICES

QIU CANXING

Ph.D

The Hong Kong Polytechnic University

2016

THE HONG KONG POLYTECHNIC UNIVERSITY

Department of Civil and Environmental Engineering

Seismic-resisting Self-centering Structures with Superelastic Shape Memory Alloy Damping Devices

Qiu Canxing

A thesis submitted in partial fulfillment of the requirements for the degree of Doctor of Philosophy

October 2015

CERTIFICATE OF ORIGINALITY

I hereby declare that this thesis is my own work and that, to the best of my knowledge and belief, it reproduces no material previously published or written, nor material that has been accepted for the award of any other degree or diploma, except where due acknowledgement has been made in the text.

________________________ (Signed)

Qiu Canxing (Name of student)

To my family

Abstract

The pursuit of post-earthquake resilience challenges the design of seismic-resisting structures in earthquake prone regions. The objectives of minimizing repair cost and downtime after earthquakes have motivated the development of high-performance self-centering (SC) structures that are associated with minimal post-earthquake permanent deformation. This thesis systematically investigates an emerging type of seismic-resisting SC structures that take advantage of superelastic shape memory alloys (SMAs). Although previous studies have revealed the prospects of such innovative SMA-based SC structures, the relevant research is still in its infant stage, with many questions with regard to seismic performance, practical implementation, and design methodology remaining unanswered. This thesis aims to fill in the existing knowledge gaps through a combination of numerical and experimental studies. Seismic performance of two novel structures, namely, steel braced frames with SMA-based damping braces (SMADB) and highway bridges with SMA-based isolators, is particularly investigated in this thesis and the corresponding design methodology is developed.

The major outcomes of this thesis are summarized as follows:

(1) Two types of superelastic SMA wires, namely, the monocrystalline Cu-Al-Be and Ni-Ti wires, are cyclically characterized and their major mechanical properties relevant to seismic applications are systematically discussed. Particularly, monocrystalline Cu-Al-Be is identified as an emerging and promising SMA material for seismic applications, because of its substantial superelastic strain and superior low-temperature behavior. Subsequently, SMA wire- and spring-based dampers are also experimentally characterized.

(2) Seismic performance of steel frames with SMADB and highway bridges with SMA-based isolators at different seismicity levels is numerically evaluated via

incremental dynamic analysis (IDA). The potential high-mode contribution in multi-story steel frames with SMADB is particularly highlighted and the corresponding mitigation measure is discussed.

(3) The superior seismic performance of steel braced frames with SMADB, such as limited damage and residual deformation, and the ability to sustain several significant earthquakes without repair and replacement, is successfully validated by a series of shaking table test on a 1/4-scale frame model with SMADB.

(4) An *ad hoc* performance-based seismic design (PBSD) method is developed for steel braced frames with SMADB, and the designed structures can effectively meet the prescribed seismic performance objectives.

The presented work and corresponding new findings in this thesis offers more in-depth understanding of SC structures with SMA-based damping devices, and the demonstrated superior performance, together with the developed design methodology, will facilitate the practical implementation of SMA-based seismic-resisting structures in future. Although this thesis is focused on two particular forms of structures with SMA-based damping devices, its outcome will also shed light on the seismic assessment and design of other types of seismic-resisting SC structures.

Publications

Journal Papers:

Zhu, S., and Qiu, C.X., (2014), "Incremental dynamic analysis of highway bridges with novel shape memory alloy isolators", *Advances in Structural Engineering*, 17(3): 429–438.

Qiu, C.X., and Zhu, S., (2014), "Characterization of cyclic properties of superelastic monocrystalline Cu–Al–Be SMA wires for seismic applications", *Construction and Building Materials*, 72: 219–230.

Qiu, C.X., and Zhu, S., (2016), "High-mode effects on seismic performance of a multi-story self-centering-braced steel frame", *Journal of Constructional Steel Research*, 119: 133-143.

Qiu, C.X., and Zhu, S., (2015), "Shaking table test and numerical study of self-centering steel frame with SMA-based damping braces", *Earthquake Engineering and Structural Dynamics*, (under review).

Qiu, C.X., and Zhu, S., (2015), "Performance-based seismic design of self-centering steel frames with SMA-based damping braces", *Engineering Structures*, (under review).

Conference Papers:

Zhu, S., and Qiu, C.X., (2012), "Incremental dynamic analysis of self-centering seismic resisting structures: SDOF", *Proceedings of International Conference on Earthquake Engineering Research Challenges in the 21st Century*, 18–21, May, Harbin, China.

Qiu, C.X., and Zhu, S., (2012), "Incremental dynamic response of highway bridges with self-centering isolators", *Proceedings of the 1st International Conference on Performance-based and Life-cycle Structural Engineering*, 5–7, December, Hong Kong, China.

Qiu, C.X., and Zhu, S., (2014), "Investigations on monocrystalline Cu-Al-Be SMA wires in seismic vibration controls", *Proceedings of the 6th World Conference on Structural Control and Monitoring*, 15–17, July, Barcelona, Spain.

Qiu, C.X., and Zhu, S., (2015), "Performance-based seismic design of self-centering steel frames with SMA-based damping braces", *Proceedings of the 6th Cross-strait Workshop on Structural Monitoring and Vibration Control in Civil Engineering*, 13–16, August, Xiamen, China. (Best Student Paper Award)

Acknowledgements

I would like to express my sincere gratitude to my chief supervisor, Dr. Songye Zhu. I am grateful that he provided me the opportunity to pursue a PhD degree. I always felt it very challenging when he placed high expectations on me and was motivated to achieve them. I am indebted to him for his valuable guidance, particularly when I was in the tough times. I really appreciate him for his vision, supervision, and patience on my work.

I would also like to thank my co-supervisor, Prof. You-lin Xu, for giving me academic guidance and encouragement.

I am grateful to Messrs. T.T. Wai, Y.H. Yiu, W.K. Ho and W.F. Tam for their very professional and useful suggestions and assistances in my laboratory experiments. Gratitude also goes to former FYP students.

I would also like to thank my fellows Dr. Xiao-hua Zhang, Dr. Wen-ai Shen, Dr. Wen-yu He, Dr. Bin Wang, Dr. Qian Geng, Mr. Zhi-lu Lai, Mr. Xiang Shi, Mr. Jin-yang Li, Mr. Quan Liu, Dr. Zhi-wei Chen, Dr. Bing Wang, Dr. Yue Zheng, Dr. Qing Zhu, Mr. Jing-hua Lin, Mr. Chao-dong Zhang, Mr. Jian-fu Lin, Miss. Yi-xin Peng, Mr. Rong-pang Hu, for their discussions and constructive comments.

Lastly, I wish to acknowledge all my family members and friends for their love and support.

Contents

CERTIFICATE OF ORIGINALITY i
Abstract v
Publications vii
Journal Papers: vii
Conference Papers: vii
Acknowledgements ix
Contents xi
Chapter 1 Introduction 1
1.1 Background and Motivation 1
1.2 Literature Review 3
1.2.1 PT-based SC Structures 3
1.2.2 Shape Memory Alloys 5
1.2.2.1 Fundamentals of SMAs 5
1.2.2.2 Mechanical Properties of SMA 7
1.2.2.3 Constitutive Models of SMA 12
1.2.3 SMA-based Devices 14
1.2.3.1 SMA-based Dampers 14
1.2.3.2 SMA-based Isolators 15
1.2.3.3 SMA-based Braces 16
1.2.3.4 SMA-based Connections 18
1.2.3.5 SMA-based Springs 18
1.3 Performance-based Seismic Design 19
1.3.1 Capacity Spectrum Design (CSD) 20
1.3.2 Direct Displacement-based Design (DDBD) 20
1.3.3 Performance-based Plastic Design (PBPD) 21
1.4 Remarks 22
1.5 Research Objectives 22
1.6 Thesis Outline 23

Chapter 2 Superelastic SMA Wires 35
2.1 Introduction........ 35
2.2 Investigated Cyclic Properties 35
2.3 Experimental Setup and Method 36
2.4 Testing Results and Discussions 38
2.4.1 Hysteretic Characteristics 38
2.4.2 Training Effect 40
2.4.3 Strain Amplitude Effect 42
2.4.4 Internal Hysteretic Loops 45
2.4.5 Loading Frequency Effect 46
2.4.6 Temperature Effect 47
2.4.7 Fatigue 50
2.5 Summary 50
Chapter 3 SMA-based Dampers 67
3.1 Introduction 67
3.2 SMA-Wire Damper 67
3.2.1 SMA Wire 67
3.2.2 Configuration 68
3.2.3 Cyclic Properties 69
3.3 SMA-Spring Damper 70
3.3.1 Fabrication of SMA Springs 70
3.3.2 Plain-end Spring 71
3.3.3 Closed-end Spring 73
3.3.4 Quench Method Effect 74
3.3.5 Loading Frequency Effect 74
3.3.6 Pre-loading Effect 75
3.3.7 Geometric Effect 76
3.3.7.1 Spring Index 76
3.3.7.2 Number of Active Coils 77
3.3.8 Wire Types Effect 77

3.4 Discussions on Two Types of SMA-based Dampers 78
3.5 Summary 78
Chapter 4 Highway Bridges with SMA-based Isolators 89
4.1 Introduction 89
4.2 Constitutive Model for Superelastic SMA 89
4.3 Highway Bridge with SMA-based Isolators 90
4.5 IDA 93
4.6 Analysis Results 94
4.7 Summary 98
Chapter 5 Steel Braced Frame with SMADB: Numerical Study 105
5.1 Introduction 105
5.2 Constitutive Models of SMADB 105
5.3 Multi-Story Steel Frame 106
5.4 Pushover Analysis of Multi-story Frames 108
5.5 IDA of SDOF Systems 109
5.6 IDA of Multi-Story Frames 111
5.7 High-Mode Effect in Multi-Story Frame 114
5.8 Effect of Improving α and β 116
5.9 Summary 118
Chapter 6 Shaking Table Test and Numerical Study of SMADBF 129
6.1 Introduction 129
6.2 Design of the Tested Frame 130
6.2.1 Prototype Frame 130
6.2.2 Scaled Tested Frame 131
6.3 Preparation of the Tested Frame 131
6.4 Experimental Setup and Program 133
6.4.1 Testing Apparatus and Sensor System 133
6.4.2 Ground Motions and Testing Program 134
6.5 Numerical Simulation Model 135
6.6 Experimental and Numerical Results 136

6.6.1 Dynamic Characteristics 137
6.6.2 Displacement Response 137
6.6.3 Base Shear 138
6.6.4 IDA Curves 139
6.6.5 Truss Mechanism 140
6.6.6 Behavior of SMADB 141
6.7 Summary 142
Chapter 7 Performance-based Seismic Design Method 155
7.1 Introduction 155
7.2 SMADB 156
7.3 SC SDOF System 157
7.3.1 μ-R-T Relationship 157
7.3.2 Modified Energy Equivalent Condition 158
7.4 PBSD Approach for SMADBF 160
7.4.1 Performance-based Plastic Design Method 160
7.4.2 Lateral Force Pattern 163
7.4.3 Design of SMADBs 164
7.4.4 Design of Frame Members 165
7.4.5 Step-by-step Design Procedure 166
7.5 Design Example of SMADBF 167
7.5.1 Building Model 167
7.5.2 Seismic Performance Targets 167
7.5.3 Seismic Performance Assessment 170
7.6 Summary 174
Chapter 8 Conclusions 185
8.1 Summary 185
8.2 Conclusions 186
8.3 Future work 188
References 191

List of Figures

Figure 1.1 FS hysteresis of SC structural systems 26

Figure 1.2 Typical behavior of the superelastic Ni-Ti SMA wires 26

Figure 1.3 Typical SC rocking systems: (a) rocking bridge pier (Marriott et al. 2009) and (b) rocking structural frame (Eatherton et al. 2014a) 27

Figure 1.4 Comparison between MRF connections: (a) welded connection and (b) SC MRF connection (Ricles et al. 2001) 27

Figure 1.5 Concept of SC braces (Christopoulos et al. 2008) 27

Figure 1.6 Fundamentals of Ni-Ti SMA: (a) stress-temperature diagram; (b) shape memory effect and (c) superelastic effect. (Patoor et al. 2006) 28

Figure 1.7 Typical tensile loading test of superelastic Ni-Ti SMA wires (DesRoches et al. 2004) 28

Figure 1.8 Training effect on superelastic polycrystalline Cu-Al-Be wires (Zhang et al. 2008) 29

Figure 1.9 Deformation amplitude effect on superelastic Ni-Ti SMAs (DesRoches et al. 2004) 29

Figure 1.10 Stress-strain curves of superelastic Ni-Ti wires for 1st and 10th cycles under different loading rates (Zhu and Zhang 2013) 29

Figure 1.11 Superelastic Ni-Ti SMAs: (a) stress strain relationship at different temperatures; and (b) phase transformation stress as a function of temperature (Dolce and Cardone 2001) 30

Figure 1.12 Stress distribution of solid SMA bar under torsion; Regions I, II, and 30

Figure 1.13 Mechanical response of s superelastic SMA tube under (a) tension and (b) compression (Reedlunn et al. 2014) 30

Figure 1.14 A versatile SMA-based damper (Zhang and Zhu 2007b) 31

Figure 1.15 SMA-based isolators for elevated highway bridge (Wilde et al. 2000) 31

Figure 1.16 A large-scale SMA-based brace (Dolce et al. 2001) 31

Figure 1.17 SMA-based connection in RC frame (Youssef et al. 2008) 32
Figure 1.18 SMA-based spring (Speicher et al. 2009) 32
Figure 1.19 Fundamental of CSD (Freeman et al. 1975) 32
Figure 1.20 Fundamental of DDBD (Priestley et al. 1993) 33
Figure 1.21 Fundamental of PBPD (Leelataviwat et al. 1999) 33
Figure 1.22 Framework of the thesis 34
Figure 2.1 Typical stress-strain relationships of superelastic SMA wires 55
Figure 2.2 Experimental Setup 55
Figure 2.3 Cyclic loading protocol with loading frequency = 0.025 Hz 56
Figure 2.4 Representative superelastic behavior of monocrystalline Cu-Al-Be wire (Lot B), polycrystalline Cu-Al-Be wire and Ni-Ti wire at room temperature 56
Figure 2.5 Training effect of Ni-Ti wires at a loading frequency of 1.0 Hz 57
Figure 2.6 Training effect of monocrystalline Cu-Al-Be wires (Lot B) at a loading frequency of 1.0 Hz 58
Figure 2.7 Testing results of Ni-Ti wires under cyclic tensile loadings with a loading frequency of 1.0 Hz 59
Figure 2.8 Testing results of monocrystalline Cu-Al-Be wires under cyclic tensile loadings with a loading frequency of 0.025 Hz (Red: small-strain cycles; Blue: large-strain cycles) 59
Figure 2.9 Variations of cyclic properties of monocrystalline Cu-Al-Be with loading strain amplitude 59
Figure 2.10 Internal hysteretic loops with partial unloading/reloading of monocrystalline Cu-Al-Be (Lot B) 60
Figure 2.11 Stress-strain relationships of Ni-Ti wires at different loading frequencies . 61
Figure 2.12 Stress-strain relationships of monocrystalline Cu-Al-Be wires (Lot B) at different loading frequencies 61
Figure 2.13 Loading frequency effect on cyclic properties of monocrystalline Cu-Al-Be and Ni-Ti wires 62
Figure 2.14 Stress-strain cycles of Ni-Ti wires at different ambient temperatures 63
Figure 2.15 Stress-strain cycles of monocrystalline Cu-Al-Be wires at different ambient

temperatures......63
Figure 2.16 Temperature effect on cyclic properties of Ni-Ti wires under 4% strain amplitude......64
Figure 2.17 Temperature effect on cyclic properties of monocrystalline Cu-Al-Be wires (Lot B) under 19% strain amplitude......65
Figure 2.18 Large-strain fatigue of three SMA wires......66
Figure 3.1 Stress-strain relationship of superelastic Ni-Ti wire (loading frequency = 2.0 Hz, 10 consecutive cycles)......81
Figure 3.2 SMA-wire damper: (a) configuration of SMA-wire damper, (b) deformation under tension and compression, and (c) idealized FS hysteresis......81
Figure 3.3 Some configuration details of the SMA-wire dampers: (a) moving steel rod and (b) U-connector......81
Figure 3.4 SMADB: (a) schematic view, (b) dimensions (unit: mm), and (c) photo of the tested brace......82
Figure 3.5 Cyclic behavior of SMA-wire dampers at a loading frequency of 2.0 Hz......82
Figure 3.6 Geometric dimensions of a typical spring......83
Figure 3.7 Procedures of making SMA-spring dampers......83
Figure 3.8 Experimental setup and tested specimen......83
Figure 3.9 A representative cyclic loading protocol (loading frequency = 0.025 Hz)......84
Figure 3.10 Cyclic behavior of plain-end spring (S1)......84
Figure 3.11 Loading amplitude effect on (a) equivalent damping ratio and (b) residual displacement (S1)......84
Figure 3.12 Tension-compression behavior of closed-end spring (S6)......85
Figure 3.13 Geometric nonlinear of the closed-end springs (S6)......85
Figure 3.14 Loading amplitude effect on (a) equivalent damping ratio and (b) residual displacement (S6)......85
Figure 3.15 Cyclic behavior by different cooling method, S6 (water quench) vs. S7 (air quench)......86
Figure 3.16 Cyclic behaviors at different loading frequencies (S6)......86
Figure 3.17 Effect of pretension on (a) cyclic behavior and (b) equivalent damping ratio

(S6)..86
Figure 3.18 Effect of spring index on cyclic behavior, S1 (C = 8) vs. S3 (C = 16)........87
Figure 3.19 Effect of number of active coils on cyclic behavior, S1 (N = 6) vs. S2 (N = 2) 87
Figure 3.20 Effect of wire types on cyclic behavior, S4 (solid) vs. S5 (hollow)............87
Figure 4.1 Constitutive model of SMAs...100
Figure 4.2 Simplified model of a highway bridge with SMA isolators........................101
Figure 4.3 The median response spectrum of ground motion set and seismic design spectra at three hazard levels 101
Figure 4.4 Illustration of numerical model in DRAIN2DX..102
Figure 4.5 Displacement demand of the highway bridge with SMA isolators 103
Figure 4.6 Comparison of seismic IDA curves between the equivalent SDOF system and the full-scale model of the highway bridge with SMA isolators.....................103
Figure 4.7 Seismic hysteresis and displacement response under seismic record LA01 with different scaling factors 104
Figure 5.1 Simplified constitutive model of SMADBs and BRB................................121
Figure 5.2 Modeling of the prototype frame in OpenSees...121
Figure 5.3 Elastic response spectra of the selected ground motion records 122
Figure 5.4 Nonlinear pushover analysis of the frames (SMADBF-I and BRBF) subjected to the first-mode lateral force pattern 122
Figure 5.5 Nonlinear pushover analysis of the frames (SMADBF-I and BRBF) subjected to the second-mode lateral force pattern...122
Figure 5.6 Cyclic pushover curves of the SMADBF-I and BRBF 123
Figure 5.7 Definition of strength reduction factor, R 123
Figure 5.8 Effect of α and β on seismic deformation demand of SDOF systems with various natural periods...124
Figure 5.9 IDA curves of SMADBF-I under varying seismic intensity levels............124
Figure 5.10 IDA curves of SMADBFs and BRBF in comparison with the corresponding SDOF predictions...125
Figure 5.11 Relationship between θ_{max} and θ_{roof}..125

Figure 5.12 Height-wise distribution of peak inter-story drift ratio in SMADBF-I at the DBE level 125
Figure 5.13 Geometric mean of peak inter-story drift ratio at FE, DBE and MCE levels 126
Figure 5.14 Geometric mean of transient inertia forces over the building height at the moments when θ_6 and θ_1 reach their peak values 126
Figure 5.15 Time history response of interstory drift ratio, subjected to ground motion record LA20×1.2 126
Figure 5.16 Results of the first-mode pushover analysis of all structural systems.......127
Figure 5.17 IDA curves of various structural systems that indicate the effect of increasing α and β in SMADBFs 127
Figure 5.18 Geometric-mean θ_{peak} over building height at the DBE and MCE levels, exhibiting effect of increasing α or β on mitigating higher modes effect 127
Figure 5.19 Geometric mean of maximum residual inter-story drift ratio in IDA 128
Figure 5.20 Geometric mean of σ_{story} in IDA..128
Figure 5.21 Standard deviation of $\theta_{\max}$ under different seismic records in IDA 128
Figure 6.1 Perspective and plan views of the prototype frame 146
Figure 6.2 The schematic of the tested SMADBF model: (a) elevation view (dimension unit: mm) and (b) close-up view of brace-frame and frame-mass connections.....146
Figure 6.3 The tested frame on the shaking table: (a) global view of the model, (b) pinned connection between the frame and mass system, (c) beam-to-column connection, (d) ball-bearing of the out-of-plane constraint frame, and (e) pinned joint at the column base 147
Figure 6.4 Sensor setup in the shake table test: (a) strain gauge, (b) LVDT, and (c) accelerometer 147
Figure 6.5 Time histories of selected input ground motion records: 148
Figure 6.6 Elastic response spectrum of the selected ground motion records (5% damping ratio): (a) spectral acceleration and (b) spectral displacement................148
Figure 6.7 Numerical model of the SMADBF in OpenSees (unit: mm) 149
Figure 6.8 Modeling of the cyclic behavior of SMADB 149

Figure 6.9 Time histories of the roof displacement, subjected to ground motion records (a) LA17 and (b) NF09 at different seismic intensities 150
Figure 6.10 Maximum interstory drift ratio along the building height at different ground motion intensities: (a) LA17 and (b) NF09 151
Figure 6.11 Time histories of the base shear, subjected to ground motion records (a) LA17 and (b) NF09 at different seismic intensities 152
Figure 6.12 IDA curves: (a) roof drift ratio, (b) 1st-story brace displacement, (c) roof acceleration, and (d) base shear 153
Figure 6.13 Force diagram of the framing system at the moment when the base shear reaches its maximum, taking the case of LA17 × 1.0 as an example. (Numerical results are enclosed in brackets; unit: kN for force and kN·m for moment.) 154
Figure 6.14 Pre- and post-earthquake performance of the 2nd story SMA-based damper 154
Figure 7.1 Inelastic SC SDOF systems with FS hysteresis 177
Figure 7.2 μ-R-T relationships of SC SDOF (Dots: numerical simulation; Lines: fitting curves) 177
Figure 7.3 Energy equivalence concept in PBSD method 178
Figure 7.4 Relationship between design base shear and properties of SMADBF 178
Figure 7.5 Different lateral force patterns (T = 1.2 s) 178
Figure 7.6 Design flow chart of SMADBF 179
Figure 7.7 Prototype 6-story frame building with SMADB: (a) plan layout; (b) brace-to-frame and beam-to-column connections; (c) elevation view 180
Figure 7.8 Performance targets at three discrete seismic hazard levels 180
Figure 7.9 Seismic performance of Structure S1 at three hazard levels 181
Figure 7.10 Seismic performances of the four designed frames with various hysteretic parameters of SMADBs 182
Figure 7.11 Peak floor acceleration along the building height at three seismic hazard levels 183
Figure 7.12 Residual inter-story drift ratio along the building height at three seismic hazard levels 183

Figure 7.13 The most critical P-M interactions at the column bases at three seismic hazard levels..184
Figure 7.14 Stress-strain of the outermost fiber at column base section of Structural S1 under ground motion LA18...184

List of Tables

Table 2.1 Comparison of material properties of three superelastic SMAs at room temperature........54
Table 3.1 Cyclic properties of SMA-wire dampers........80
Table 3.2 Parameters of SMA-spring dampers........80
Table 5.1 Parameters of BRB and SMADBs........120
Table 6.1 Seismic design parameters of SMADBF prototype........144
Table 6.2 Similitude laws used for the reduced model........144
Table 6.3 Ground motions in the shake table tests........145
Table 6.4 Shake table test sequence........145
Table 7.1 Building design information........176

List of Abbreviations

BRB	buckling-restrained brace
BRBF	buckling-restrained braced frame
CSD	capacity spectrum design
DBE	design basis earthquake
DDBD	direct displacement-based design
EP	elasto-plastic
FOE	frequently occurring earthquake
FS	flag-shape
IDA	incremental dynamic analysis
MCE	maximum considered earthquake
MDOF	multi-degree-of-freedom
MRF	moment-resisting frame
PBEE	performance-based earthquake engineering
PBSD	performance-based seismic design
PT	posttension
SC	self-centering
SDOF	single-degree-of-freedom
SE	superelastic effect
SMA	shape memory alloy
SMADB	shape memory alloy based damping brace
SMADBF	shape memory alloy based damping braced frame
SME	shape memory effect

Chapter 1 Introduction

1.1 Background and Motivation

The current seismic provisions in building codes have primarily focused on limiting peak displacement and acceleration demands to prevent structural collapse and preserve life safety. However, such a collapse prevention target may not effectively control post-earthquake repair cost. For example, following the 1995 Kobe earthquake, Otani (1997) noted that although some buildings survived the earthquake without collapse, the cost of repairing many locations of inelastic action was technically challenging and generally expensive. As a result, damaged structures are often demolished, which are in turn translated into large economic losses and long downtime until facilities are rebuilt. Therefore, increasing interests have been given to a seismic design strategy that involves the use of fuse-like damping devices, particularly after the 1994 Northridge and 1995 Kobe earthquakes. These devices were invented to protect primary structural members against potential severe damage by dissipating seismic energy. The research community has developed various types of damping devices over the past decades, including but not limited to metallic yield dampers (Kelly et al. 1972; Whittaker et al. 1991; Tsai and Tsai 1995), friction dampers (Pall and Marsh 1982; Filiatrault and Cherry 1987), viscoelastic dampers (Shen and Soong 1995), viscous fluid dampers (Constantinou and Symans 1993), and buckling-restrained braces (BRB) (Wada and Nakashima 2004).

The substantial repair cost of buildings is typically owing to both structural and nonstructural damage. The nonstructural elements, accessories, and equipment in the structures may also probably be damaged due to excessive seismic response of structures. In fact, some sophisticated equipment in buildings is often even more costly than the structures. Apart from economic losses, the service interruptions of critical facilities (e.g., hospitals, emergency management centers, and fire and police stations) may lead to additional serious losses to the society. In light of this situation, Poland and Hom (1997) emphasized the need to include business interruption costs in post-earthquake repair cost. In particular, Kawashima et al. (1998) accentuated the need to consider residual deformation in defining damage control performance level. A recent investigation suggested that a residual interstory drift ratio of 0.5% in Japan makes rebuilding a new structure more favorable than retrofitting or repairing the damaged structure (McCormick et al. 2008). The above studies imply that limiting residual post-earthquake deformation is as important as controlling peak demands during earthquakes. Therefore, an ideal structural system should successfully withstand the collapse risk during earthquakes and effectively limit the residual deformation after earthquakes, which has been recognized as an additional seismic index required by the modern framework of performance-based earthquake engineering (PBEE). The motivation of conceiving these structural systems has led to the increasing interest in self-centering (SC) structural systems shown in Figure 1.1. For comparison, a typical elasto-plastic (EP) structure is also included in the figure. Upon loading, the SC structure can yield at a large force level in a manner similar to that of the EP structure. When the applied force is removed, the EP structure clearly shows a noticeable residual deformation, whereas the SC structure recovers to its original position. The different loading/unloading paths form a flag-shape (FS) hysteretic loop and dissipate energy.

In recent years, shape memory alloys (SMAs) emerge as a potential candidate for developing innovative SC structures (DesRoches and Smith 2004; Ozbulut et al. 2011). SMAs are a special kind of metallic alloy, which recovers deformation upon heating (shape memory effect, SME) or unloading (superelastic effect, SE) (Duerig et al. 1990; Shaw and Kyriakides 1995). Superelastic SMAs possess stable SC and damping properties without residual deformation when they experience cyclic loading loops. Figure 1.2 shows the typical cyclic behavior of superelastic Ni-Ti SMA wires. The cyclic behavior of superelastic SMAs forms an FS hysteresis, which is unique from conventional materials and is of particular interest from the viewpoint of earthquake engineering. Superelastic SMAs also have a good corrosion resistance and a high low-cycle fatigue life (DesRoches et al. 2004). These appealing properties make superelastic SMAs favored by the community in making SC structures.

Although past research has suggested the prospect of using SMAs in civil engineering structures, the viability of SMA-based seismic-resisting SC structures is yet to be established. This thesis addresses several critical concerns and problems regarding the application of SMAs as the kernel component of seismic-resisting SC structures.

1.2 Literature Review

This section reviews previous research works relevant to the current study. First, post-tension (PT)-based SC structures, which produce FS behavior similar to that of SMA-based SC structures, are introduced; Second, as the critical component of the SC structures in this thesis work, SMAs are discussed with regard to their fundamental behavior and mechanical properties. Third, SMA-based devices of various forms for different applications are presented. Finally, selected performance-based seismic design (PBSD) methods that are related to the design method developed in the current study are introduced.

1.2.1 PT-based SC Structures

PT steel tendons are popularly utilized in SC structures to provide the SC force, in which conventional energy dissipation devices are often used to offer damping capacity (Priestley and Macrase 1996; Priestley et al. 1999; Ricles et al. 2001; Christopoulos et al. 2002b; Garlock et al. 2005; Christopoulos et al. 2008; Marriott et al. 2009; Clayton et al. 2011; Erochko et al. 2013; Eatherton et al. 2014). The PT-based SC structures can generally be grouped into the following major categories according to their structural forms: SC rocking system, SC moment-resisting frame (MRF), and SC-braced frame.

SC rocking systems allow the structures to form a rocking mechanism by permitting gap opening between the structure and the foundation under seismic loading. Upon loading, concentrated deformation occurs at the gap location. PT steel tendons close the gap and bring the system back to the original position. Energy dissipating devices are activated to mitigate seismic demands as the gap opens and closes. Housner (1963) was the first to notice the advantage of rocking behavior in assisting structures to resist earthquakes. A precast seismic structural system research program was then conducted for 10 years by Priestley et al. (1999) to extend the utilization of precast concrete structure in seismic zones. This program paved the way for the development of another rocking systems. Figure 1.3(a) shows the configuration of a rocking bridge pier (Marriott et al. 2009). The rocking bridge piers applied unbonded PT tendons to provide SC force and used low-cost mild steel dissipaters as the damping source. Quasi-static and pseudo-dynamic loading tests were performed, and minor physical damage was observed in the specimens, which exhibited stable energy dissipation and SC properties. Figure 1.3(b) presents a deformed rocking structural frame (Eatherton et al. 2014a). This framing system also exploited vertical PT strands to provide SC force and applied steel energy dissipating fuses to control seismic demands. The main frame remained essentially elastic and damage-free by concentrating the deformation in steel strands and dampers.

SC MRFs are constructed by post-tensioning beams-to-column connections using high-strength strands. Energy dissipating elements are added and activated as the strands elongate. Figure 1.4 shows a typical SC MRF connection along with a conventional welded connection. Ricles et al. (2001) proposed an innovative post-tensioned connection, in which PT strands ran through the frame width parallel with beams and were anchored at column flanges. The bolted angles connecting the beams and columns were intended to dissipate energy. The test results showed that such SC connections demonstrated good energy dissipation capacity and experienced no residual deformation after a couple of inelastic cycles. Garlock et al. (2003, 2005, and 2007) continued to explore this kind of SC MRF experimentally and theoretically, and proposed a design procedure. In addition to steel angles, energy dissipating elements can also be friction damped connections at the outside of beam flanges (Rojas et al. 2005), beam bottom flange friction device (Wolski et al. 2009), or friction channel at the beam web (Lin et al. 2013). All these connections can avoid any yielding in steel beam and column members if the friction force is properly controlled.

The SC braces that combine PT elements and energy dissipating components have an outlook similar to that of conventional braces. Christopoulos et al. (2008) first explained the mechanics of this new brace as depicted in Figure 1.5. This full-scale SC braces exhibited a damage-free behavior and a stable energy dissipation capacity upon large axial deformation. Christopoulos et al. (2008) then concluded that SC braces can be a viable alternative to conventional braces because of their attractive SC property and flexibility to be scaled to a desired strength level. Tremblay et al. (2008) numerically studied the seismic response of frame buildings of various story numbers with SC braces. The comparison with similar BRB frames (BRBF) showed that SC-braced frames can achieve better seismic performance than BRBF. The SC brace configurtion was later revised to double the ductility using a novel telescoping configuration known as the T-SCED (Erochko et al. 2012). Erochko et al. (2013) conducted shaking table tests on SC braces within a scaled steel frame model. The result showed that the SC braces successfully withstood consecutive strong earthquakes without damage, and that the structure exhibited excellent SC response with no residual deformation.

1.2.2 Shape Memory Alloys

This sub-section describes the fundamental behavior of SMAs and reviews their mechanical properties under different types of loading.

1.2.2.1 Fundamentals of SMAs

This part provides a brief introduction of SMAs. SMAs demonstrate two different temperature-dependent features, namely, SME and SE (Duerig et al. 1990; Shaw and Kyriakides 1995). The stress–strain relationship varies to a certain degree among various types of SMA. For conciseness, only Ni-Ti SMAs, which are currently the most popular SMA in earthquake engineering, are introduced in this study to address the fundamentals and mechanical behavior of SMAs. However, the SMAs that have significantly different properties from Ni-Ti SMAs (e.g., monocrystalline Cu-Al-Be SMAs) are particularly addressed in Chapter 2, and their characteristics are discussed therein.

Figure 1.6(a) shows the uniaxial thermomechanical response of Ni-Ti SMAs through the stress–temperature diagram (Patoor et al. 2006). This SMA can exist in either austenite (A) or martensite (M) or the mixture of these two phases. Martensite can further be divided into twinned (M_t) and detwinned (M_{dt}). Three regions exist in which the material can be in a pure phase along with the transformation lines. When the material deforms into a transformation surface, it undergoes phase transformation ($A \leftrightarrow M$) or detwinning ($M_t \leftrightarrow M_{dt}$). M_s denotes the critical temperature for initiating the stress-induced martensite phase transformation at zero stress level. M_f depicts the critical temperature at zero stress level for the completion of $A \rightarrow M$ (forward) phase transformation. The start and end of the $M \rightarrow A$ (reverse) phase transformation at zero stress level are denoted by A_s and A_f, respectively. Two loading processes, shown as $1 \rightarrow 2 \rightarrow 3 \rightarrow 4 \rightarrow 1$ and $a \rightarrow b \rightarrow c \rightarrow d \rightarrow e \rightarrow a$, are marked to demonstrate the behavior of SME and SE, respectively.

SME is a property of SMAs undergoing thermoelastic martensitic transformation. This property is exhibited when the SMA is deformed and unloaded at the martensitic phase (i.e., at a temperature below M_f). When heated above A_f, the SMA regains its original shape by transforming back into the austenitic phase. The phase transformation path is schematically plotted in a stress–strain–temperature space illustrated in Figure 1.6(b). At temperature below M_f, the material is loaded ($1 \rightarrow 2$), thereby resulting in stress-induced detwinning and inelastic strains. Upon unloading ($2 \rightarrow 3$), the material remains in the detwinned state, and the inelastic strains are not recovered. The SMA is then heated above A_f ($3 \rightarrow 4$). In this case, the SMAs return to the austenite phase, and the inelastic strains are recovered. Finally, upon cooling of the austenite phase ($4 \rightarrow 1$), the material transforms into twinned martensite without inducing any deformation.

Figure 1.6(c) demonstrates the SE behavior associated with stress-induced phase transformation and strain recovery upon unloading at temperatures above A_f. A typical thermomechanical loading path $a \rightarrow b \rightarrow c \rightarrow d \rightarrow e \rightarrow a$ begins at zero stress level. The parent phase (A) undergoes thermoelastic loading ($a \rightarrow b$) up to a critical stress level called the $A \rightarrow M$ transformation stress (σ^{M_s}). At this stress level, the material undergoes a stress-induced phase transformation ($b \rightarrow c$) from austenite into detwinned martensite, during which large inelastic strains develop. The transformation is completed when the stress reaches σ^{M_f}. The subsequent unloading ($c \rightarrow d$) does not produce further phase transformation. When the point (d) is reached, the reverse transformation begins ($M \rightarrow A$), leading to the recovery of the inelastic strains. The material fully transforms into austenite at (e), and the final segment of the loading path ($e \rightarrow a$) is characterized by the recovery of elastic strains. As a result, zero macroscopic strains are obtained upon completion of the path. The transformation results in a hysteresis, which represents the dissipated energy in the cycle.

The superelastic SMAs draw considerable attention in seismic applications because of their large superelastic strain and good damping capability. Therefore, this thesis focuses only on seismic applications of superelastic SMAs. Hence, SMA refers to superelastic SMA in the following sections of the paper unless otherwise noted.

1.2.2.2 Mechanical Properties of SMA

SMAs significantly differ from one another in terms of their mechanical properties. Such difference may be due to different alloy compositions, crystal structures, heat treatments, or fabrication processes (Otsuka and Wayman 1999). A small change in the chemical composition of the alloy considerably affects its mechanical properties (Birman 1997). The processing method also influences the mechanical properties of SMAs (Otsuka and Wayman 1998). Understanding the mechanical properties of SMAs can provide clear guidance on how SMA-based dampers of different forms can be produced. The mechanical properties of SMAs are comprehensively reviewed, in the order of tension, torsion, and bending.

Tension is the most widely used behavior in SMA-based damping devices. Figure 1.7 shows a representative result of a tensile loading test on Ni-Ti SMA wires (DesRoches et al. 2004). SMAs exhibit a linear elastic behavior until phase transformation occurs at approximately 1% strain upon loading. The phase transformation then generates a stable plateau with low stiffness until approximately 6% strain. With the removal of load, reverse transformation is activated at a low stress level, and the wire recovers the deformation shape. The different phase transformation paths generate a damping capacity for SMAs. The hysteretic loops are featured by FS. Tensile behavior is generally influenced by several factors, including training, deformation amplitude, loading rate, and ambient temperature. This section further introduces the tension of SMAs by discussing the effects of these factors.

Training effect occurs when the SMA mechanical properties degrade upon repeated cyclic loadings as shown in Figure 1.7 and Figure 1.8. During this process, residual strain is slightly accumulated in SMAs in the initial several loops, but it becomes stable as the loading continues. This result is attributed to the microstructural slips during martensitic transformation (Xie et al. 1998; DesRoches et al. 2004; Zhang et al. 2008). These slips decrease the forward transformation stress, thereby inhibiting the occurrence of martensitic transformation in the succeeding loading loops. Nevertheless, with a proper cold working, annealing process, and preloading treatment, this effect can be significantly eliminated, and SMAs can display a stable mechanical performance (Miyazaki et al. 1986; Hedba and White 1994).

Deformation amplitude effect implies that the cyclic properties of SMAs depend on deformation amplitude. Figure 1.9 selectively plots the forward transformation stress and equivalent viscous damping as a function of maximum cyclic strain for SMAs of different sizes (DesRoches et al. 2004). Phase transformation stress remains stable and is less affected by the deformation amplitude. The stiffness of austenite and martensite shows the same trend. However, the equivalent damping ratio is significantly affected by the deformation amplitude because of the variations of energy dissipation and secant stiffness. Damping capacity increases rapidly at a moderate strain and levels off at a large strain.

Loading rate effect refers to the changes in cyclic properties induced by loading rate variations. This effect is caused by the heat generated at different loading rates. Figure 1.10 plots a representative study on the loading rate effect (Zhu and Zhang 2013). The increase of loading frequency will shift up the phase transformation plateau, but the effect becomes minimal when the loading frequency is above 1 Hz. Previous studies on loading rate effect have presented conflicting conclusions. For example, Tobushi et al. (1998) observed that a high loading rate leads to a high energy dissipation capacity. By contrast, Wolons et al. (1998) determined that a huge amount of energy is dissipated when loading rate decreases. Nonetheless, recent studies tend to agree that damping capacity decreases with the increase of loading rate (Dolce and Cardone 2001a; DesRoches et al. 2004). The test results of this line of research showed that the cyclic properties of SMAs are stable within the earthquake loading frequency ranging from 1 Hz to 4 Hz.

Temperature effect signifies that the mechanical properties of SMAs depend on ambient temperature. An increase in temperature generally increases the phase transformation stress linearly, which is governed by the Clausius–Clapeyron thermodynamic equation (Dolce and Cardone 2001b; DesRoches et al. 2004). Considering that phase deformation is a thermomechanical process, SMAs are sensitive to temperature change to different extents. For example, Figure 1.11(a) shows the stress strain curves of Ni-Ti wires at temperature ranging from 40 °C to −10 °C with a step of 10 °C (Dolce and Cardone 2001b). The wires lose SC ability when the temperature is below 0 °C. Figure 1.11(b) identifies and summarizes the critical phase transformation stress points. This figure particularly shows that the stress points clearly exhibit a linear trend. Zhang et al. (2008) found that Ni-Ti wires lose superelasticity at 0 °C, whereas Cu-Al-Be wires remain superelasticity down to −40 °C. The use of SMAs is challenged by their sensitivity to temperature. As such, this issue should be properly considered in designing novel SMA structures.

Among various mechanical properties, the tension of SMAs is preferred because the material is subjected to uniform deformation and is thus fully utilized. In addition, SMA wires and bars are produced in different dimensions, offering high flexibility to meet different strength demands. Therefore, tensile behavior is commonly utilized in SMA-based damping devices.

Although tension receives the most scholarly attention, researchers also tried to explore the other mechanical properties of SMAs. Figure 1.12 illustrates the stress distribution along the sectional area for SMA bars under torsion. A strong nonlinear relationship is observed between the stress and the radius (Mirzaeifar et al. 2010). Only a part of the material generates phase transformation, and stress state becomes complicated under the torsion load.

Dolce and Cardone (2001a) conducted a notable study to explore the potential seismic applications of torsional behavior of SMAs. These researchers identified that the sensitivity of mechanical properties of SMA bars subjected to torsion depends on crystalline type. Martensite SMA bars are practically insensitive to loading frequency, whereas the secant stiffness and equivalent damping of austenite SMA bars are 12% reduced when the loading frequency is increased from 0.1 Hz to 1.0 Hz. Austenite SMA bars also show other interesting behavior. An apparent residual deformation is observed after the loading stress is removed because only a part of martensite is reverted into austenite. The equivalent damping ratio is less than 10%, which is significantly lower than that of many conventional seismic damping devices. Fatigue life is over 220 cycles at the peak tangential strain of 11%.

Other authors conducted experimental and numerical studies on torsion. Chung et al.

(2006) numerically analyzed the circular SMA rods under tension–torsion combined loadings. These researchers found that the central region of SMA rod remains elastic, whereas its outer layer undergoes a martensite transformation. Residual stress and unrecovered deformation are observed after unloading. Predki et al. (2006) compared the torsion behavior of hollow and solid Ni-Ti SMA shafts. Fatigue life is comparable between different shafts. No significant differences are observed in terms of the martensite phase transformation stress. The authors suggested that a stable cyclic behavior can be obtained through a pre-cycling treatment. Mirzaeifar et al. (2010) provided the exact closed-form solutions for SMA circular bars under pure torsion. The exact solution was validated through finite element analysis. Using this model, the researchers also evaluated the effect of temperature and material properties on the torsion behavior. The work of Mirzaeifar et al. (2010) can be exploited to analyze SMA helical springs.

Dolce et al. (2001a) concluded that torsional devices depend on an additional mechanism to transfer displacement into rotation, and they require reliable end clamps to provide considerable strength. In light of this observation, torsional devices face several challenges in their practical implementations. The corresponding issues also motivate researchers to determine an effective means to utilize the torsion of SMAs.

Apart from the tension and torsion, the bending of SMAs also receives increasing scholarly attention. Substantial research has looked into the flexural property of SMAs from the material or mechanical viewpoint. Nonetheless, only a few studies have been focused on seismic applications. The bending behavior of SMAs is fairly complicated because of the asymmetric behavior in tension and compression as shown in Figure 1.13 (Reedlunn et al. 2014). The transformation plateau in compression is shorter and higher than that in tension. Thus, the asymmetry of tension/compression behavior causes the neutral plane to deviate from the centroid of the cross-section area when subjected to bending moment.

Gillet et al. (1998) tested the bending behavior of Cu-Al-Be beams and provided good theoretical predictions. The test results showed that the load–displacement cycles is always narrow regardless of the loading methods used. Auricchio and Sacco (2001) studied the bending behavior of SMA wires and proposed a thermomechanical model, which can consider the loading frequency effect. Liew et al. (2002) conducted three- and four-point bending experiments on Ni-Ti beams with a rectangular cross section of 2.9 mm width and 0.95 mm depth. The tests showed no residual deformation after loading/unloading loops. The three-point bending test notably produced an extremely narrow hysteresis, while the four-point bending test produced a wider width because of its improved martensite transformation. Hashemi and Khadem (2006) looked into the bending behavior of Ni-Ti beam under free vibration and obtained a narrow moment-curvature hysteresis. Mirzaeifar et al. (2013) presented a closed-form solution for the bending behavior of SMA beams. The analytical predictions matched the experimental data of Ni-Ti beams reasonably well. The authors expected that the predictions will be improved by considering the thermomechanical coupling effect. Reedlunn et al. (2014) studied the bending behavior of Ni-Ti SMA tubes and obtained a good damping capacity.

1.2.2.3 Constitutive Models of SMA

The development of constitutive models of SMAs has received extensive attention for decades because of the complicated stress–strain relationship. The mechanical behavior of SMAs can be modeled from either a phenomenological or a micromechanical approach (Brocca et al. 2002). Phenomenological models are generally preferred over the micromechanical ones in seismic analyses because of their simpler expression and higher computation efficiency. The following phenomenological models are of particular interest to the earthquake engineering community: (i) the thermomechanical model, (ii) the Graesser–Cozzarelli model (1992) and its modified versions, and (iii) the piecewise-linear FS model. These models are introduced in the succeeding text.

The thermomechanical model can be traced back to the work of Tanaka (1986), in which thermodynamic theory was used to model phase transformation. However, the model cannot be applied easily in the engineering field, and the required thermomechanical parameters cannot be easily measured. Liang and Rogers (1990) and Brinson (1993) later improved the Tanaka model by overcoming the aforementioned limitations. The updated models only use common engineering variables and can accurately present the mechanical behavior of SMAs. Thus, they are widely accepted by the engineering community. The model introduced by Brinson was further modified by Prahlad and Chopra (2003) by considering the strain-rate effect. Zhu and Zhang (2007) recently amended the model considering the strong dependence of SMA on the earthquake loading frequency of interest. This model accurately captures the strain-rate effect of SMAs and is therefore an attractive tool for designing and analyzing SMA-based damping devices.

As the earliest user-friendly model for SMAs, the Graesser–Cozzarelli model (1992) is a phenomenological model that describes the macroscopic behavior of SMA material. This model is based on the hysteresis model proposed by Ozdemir (1976). The superelastic behavior of SMAs is achieved by adding a stress term, which is only activated at the onset of unloading with an effect of increasing backstress. Although this model is rate independent, it well describes the dynamic behavior of SMAs when the strain-rate effect is minimal. The Graesser–Cozzarelli model was later extended by Wilde et al. (2000) to account for the hardening behavior of SMAs after the martensite phase transformation is completed. Zhang and Zhu (2007) further modified the model presented by Wilde et al. by enhancing the stability of its numerical simulation and by increasing its computation efficiency.

The piecewise-linear FS model has been widely used to model SMAs in seismic analyses (Andrawes and DesRoches 2007a; Li et al. 2008; Sharabash and Andrawes 2009; Dezfuli and Alam 2014). A typical FS model that describes the stress–strain relationship of superelastic SMAs can be fully defined by the elastic modulus of austenite, elastic modulus of martensite, phase transformation slope, forward and backward phase transformation stresses, and transformation finish strain. The FS model can capture the key features of the superelastic hysteresis of SMAs. Moreover, the simple FS model can offer comparable predictions to those from more sophisticated models in seismic analyses of single-degree-of-freedom (SDOF) and multi-degree-of-freedom (MDOF) systems (Zhu and Zhang 2013).

1.2.3 SMA-based Devices

Many SMA-based devices make use of SMA wires or bars because of the superiority of tension. The damping devices that use bending or torsion properties emerge recently as possible alternatives, but they need further investigations. The seismic applications of SMAs have been intensively reviewed in recent years (DesRoches and Smith 2004; Wilson and Wesolowsky 2005; Song et al. 2006; Dong et al. 2010; Ozbulut et al. 2011). In addition, the research community has devoted considerable effort in developing SMA-based devices. This section discusses the latest development in SMA-based devices in five categories, namely, dampers, isolators, braces, connections, and springs.

1.2.3.1 SMA-based Dampers

A large-scale experimental investigation was conducted at the Laboratory of Structures of the University of Basilicata under the Brite-Euram MANSIDE (Memory Alloys for New Seismic Isolation and Energy Dissipation Devices) project to explore the seismic applications of SMAs (Nicoletti et al. 1997). The first known practice of SMA-based dampers for seismic retrofitting is the rehabilitation of the San Giorgio Church, Trignano, Italy (Indirli et al. 2001). Another representative practical application of SMAs to protect structures is the installation of SMA-based seismic dampers to enhance the seismic safety of the Basilica of St. Francis in Assisi, Italy, which was seriously damaged by an earthquake (Abbott 2001).

Various types of SMA-based damper have been invented in the past decades (DesRoches and Delemont 2002; Faravelli and Casciati 2003; Andrawes and DesRoches 2005; Zhu and Zhang 2007b; Andrawes and DesRoches 2007a; Johnson et al. 2008; Li et al. 2008; Van de Lindt and Potts 2008; Casciati and Faravelli 2009; Zhang et al. 2009; Padgett et al. 2010; Shrestha et al. 2013; Araki et al. 2014; Parulekar et al. 2014; Branco et al. 2014). Most of these dampers are versatile to be reformed and scaled into a desired configuration for practical applications.

Andrawes and DesRoches (2005) compared SMA and steel cables to mitigate the unseating risk for several bridges. These researchers determined that SMA cables are superior over the steel ones in controlling the maximum hinge opening owing to their excellent elastic strain limit. Andrawes and DesRoches (2007a) further concluded that SMA restrainer is better than other retrofit devices in limiting joint displacement. Zhang and Zhu (2007) invented an SMA damper whose properties can easily be tuned to the desired values (Figure 1.14). A numerical study showed that installing this damper effectively reduces the peak and residual deformation demand for a multi-story frame building. Van de Lindt and Potts (2008) invented an SMA-based damper for a wood shear wall. Full-scale tests indicated that this damper significantly reduces seismic deformation and protects the wood shear wall. Li et al. (2008) constructed two types of SMA-based tension dampers. Both of these dampers are mounted at the first floor, thereby significantly reducing its displacement. Casciati et al. (2008) successfully mitigated cable vibration by employing SMA wires. Shrestha et al. (2013) clarified that SMA bars are superior over conventional steel bars in protecting historical masonry constructions.

1.2.3.2 SMA-based Isolators

SMA-based isolators are the isolation systems that use SMAs to provide lateral restoring force. Compared with conventional isolators, SMA-based isolators are better because they can control both the peak and residual isolator deformation (Wilde et al. 2000; Cardone et al. 2006; Dolce et al. 2007b; Casciati et al. 2007, Casciati et al. 2009; Liu et al. 2011; Attanasi and Auricchio 2011; Ozbulut and Hurlebaus 2011; Ozbulut and Hurlebaus 2012; Dezfuli and Alam 2013). Several studies have investigated the use of SMAs in bridges isolators, but the associated research in building structures is still limited. Only a few studies have been performed in recent years (Gur and Mishra 2013; Gur et al. 2014; Ozbulut and Silwal 2014; Shinozuka et al. 2015). One possible challenge is to optimize the seismic capacity of the isolator and the superstructure performance simultaneously.

Wilde et al. (2000) proposed a concept of smart isolation system for bridges. This concept combines a laminated rubber bearing with an SMA device as depicted in Figure 1.15. SMAs can offer damping through martensitic transformation at moderate earthquake and can provide additional force through hardening at large earthquake. Dolce et al. (2007b) developed SMA-based isolators for both buildings and bridges. These isolators are composed of pre-stressed austenite wires and martensite wires, which provide SC and damping capacity, respectively. The researchers consequently determined that the buildings with SMA-based isolators outperformed those with fix-based ones, and produced higher acceleration demand than those with rubber isolators. This result indicates the urgent need to optimally design SMA-based isolators for buildings. Ozbulut and Hurlebaus (2011) studied the performance of highway bridges with SMA-friction isolators against near-field earthquakes and then compared the SMA isolator with other isolators in case of bridges (2012). Both of these studies highlight the superiority of SMAs as the kernel component of an isolator. A few works have looked into the seismic performance of SMA-based isolators in building structures. For example, Gur et al. (2014) combined SMA with lead rubber bearing (LRB) to form a new isolation system for multi-story frames. The near-fault seismic analyses indicated that multi-story frames can attain improved performance by adding SMA. Shinozuka et al. (2015) conducted stochastic analysis on SMA-LRB for multi-story buildings to achieve the dual-objective optimization of reducing isolator displacement and capping the superstructure demands. The robustness of the optimal design is reasonably verified.

1.2.3.3 SMA-based Braces

Many studies have combined SMAs with the other components to achieve a bracing form (Dolce et al. 2000; Saadat et al. 2001; Dolce et al. 2005; Auricchio et al. 2006;

Lafortune et al. 2007; Zhu and Zhang 2007b; Walter et al. 2010; Asgarian and Moradi 2011; Ghassemieh and Kargarmoakhar 2013; Moradi et al. 2014). Figure 1.16 illustrates a large-scale SMA-based brace (Dolce et al. 2001). In a braced frame, the SMA-based braces always play the key role in dissipating energy and concentrating deformation, while protecting the other parts of the structural system.

Most studies have evaluated the seismic performance of SMA-based braces through numerical simulations. For example, McCormick et al. (2007) analyzed the seismic performance of braced steel frame with SMA braces or conventional steel braces under two suites of ground motions. The results showed that SMA braces are better than conventional steel braces in controlling both peak and residual deformations. Zhu and Zhang (2007b) replaced BRBs with identical SMA-based braces in multi-story steel frames. The frames installed with different braces achieve a comparable peak seismic performance. In addition, given their excellent SC capacity, SMA-based frames can nearly eliminate residual deformation. Similar to SMA-based isolators, SMA-based braces are yet to be more widely investigated through experiments. For example, Dolce et al. (2000) conducted a well-known experimental study on SMA-based braces funded by the MANSIDE project (Nicoletti et al. 1997). Large-scale specimens were made with martensite and austenite wires. The simple configuration made it easy to change the ratio of different types of alloys and allowed the brace to exhibit a versatile behavior. The test results indicated that SMA-based braces are suitable for seismic applications. This project also performed the shaking table tests of SMA-braced reinforce concrete frame (Dolce et al. 2005). The tests validated the reliability and reusability of SMA braces upon consecutive earthquakes. The success of the MANSIDE project has inspired other scholars to further investigate SMA-based braces. For example, Zhu and Zhang (2008) developed a novel SMA-based brace, whose energy dissipation was enhanced through friction. The cyclic behavior of the braces was obtained on an MTS machine. The mechanical properties of the braces are quite repeatable without strength degradation.

1.2.3.4 SMA-based Connections

Considering their large ductility capacity and minimal residual deformation, SMA bars and bolts have been implemented in various kinds of connection (Youssef et al. 2008; Alam et al. 2008; Alam et al. 2009; DesRoches et al. 2010; Ellingwood et al. 2010; Speicher et al. 2011; Muntasir and Alam 2012; Fang et al. 2014; Yam et al. 2015). In these innovative connections, SMAs usually replace conventional materials at the critical locations to provide strength and concentrate deformation. Figure 1.17 shows an example of an SMA-based connection.

To enhance the deformation capacity of conventional reinforced concrete frame connections, Youssef et al. (2008) conducted an experimental study on SMA-based beam-column joints, in which the SMA rebar was coupled with steel rebar at the potential plastic hinge location in RC connections. The SMA-based connection left an extremely small residual displacement and remained functional after cyclic loadings. In addition, the use of SMA relocated the plastic hinge away from the column and assured the strong-column weak-beam mechanism. Alam et al. (2008) presented an associated analytical prediction of the connection. A good agreement was observed between the analytical and experimental results. SMA-based connections have also been used in steel beam-to-column connections. Fang et al. (2014) recently conducted full-scale tests on SMA-based steel connections, in which four large-sized SMA bolts were installed along the extended end plate upon the column face. The connections exhibited excellent SC ability and moderate damping capability. Deformation was concentrated in the SMA bolts, and the column and beam remained elastic. Yam et al. (2015) conducted intensive numerical studies on this connection and proposed a practical design methodology.

1.2.3.5 SMA-based Springs

SMA-based springs have also been widely studied experimentally (Wu 1990; Morgan and Broadley 2004; Schmidt and Lammering 2004; Jee et al. 2008; Speicher et al. 2009; Attanasi et al. 2011; Savi et al. 2015) and analytically (Tobushi and Tanaka 1991; Toi et al. 2004; Mirzaeifar et al. 2011; Rao and Srinivasa 2013). The main advantage of using

SMA-based springs is that they increase deformation capacity while shortening the length of dampers in comparison with straight SMA wires.

Various SMA-based springs have been studied recently. For example, Speicher et al. (2009) produced large-sized Ni-Ti springs made of solid and hollow Ni-Ti bars (Figure 1.18). A repeatable SC behavior can be experimentally obtained from both specimens. The hollow spring has a more stable damping over the loading range than the solid spring. However, the potential seismic applications of SMA-based springs are yet to be extensively investigated. Attanasi and Auricchio (2011) reported the SC ability and damping capability of a small-scale SMA spring and simulated the experimental results with finite element method. Through numerical approach, these researchers modeled high-strength SMA springs and proposed a possible form of isolation using SMA springs. SMA springs were also applied to suppress dynamic vibrations. Liu et al. (2007) constructed three conical springs and installed them to mitigate the vibration of stay cables. A satisfactory control effect was achieved. Attanasi and Auricchio (2011) proposed a new seismic isolation system, which incorporates several SMA-based springs. The analytical results indicated that the innovative isolator can sustain large deformation without damage, can dissipate energy, and can recover the deformed shape after seismic events. Huang et al. (2014) deployed SMA-based springs to build an innovative base isolation. The SMA-based spring is considered superior over a conventional steel spring in controlling the seismic response of superstructures.

1.3 Performance-based Seismic Design

A simple yet effective seismic design method is required to implement SMA-based seismic-resisting structures. Considering this need, the existing seismic design methods are reviewed. Seismic design methods can be either force- or displacement-based. Some studies (Uang 1991; Priestley 1995) have suggested that force-based design procedure is flawed with a few noticeable drawbacks, including its (i) inability to capture the redistribution of force demand when the structure yields, (ii) difficulty in considering the influence of high modes, and (iii) the need for iteration to meet the prescribed performance target. As long as the structure yields, a large displacement demand is triggered even if the force level is still relatively constant. This condition implies that force is not as direct measurement as displacement. Therefore, the displacement-based design procedure is probably more rational and effective than the force-based design. Three popular seismic design methods are addressed in the following sections.

1.3.1 Capacity Spectrum Design (CSD)

CSD was originally introduced by Freeman et al. (1975) and Freeman (1978). Figure 1.19 shows the fundamentals of this method, in which the structural capacity and the seismic demand are plotted on the same graph. Structural capacity refers to the force–displacement relationship from pushover curve, and seismic demand is the acceleration–displacement response of a damped SDOF structure. This method aims to determine the matching point of capacity and demand within an allowable tolerance. ATC-40 (1996) and FEMA-274 (1997) adopted this concept using an equivalent linear system to predict the response of an inelastic nonlinear system. The equivalent linear system has a stiffness equal to the secant stiffness, and a viscous damping equal to the hysteretic energy dissipated in a loading/unloading cycle.

However, Chopra and Goel (1999, 2000) stated that an equivalent linear system produces unacceptable unconservative predictions of deformation, particularly if the systems are subjected to near-fault earthquake ground motions. Therefore, these researchers revised CSD using the constant-ductility design spectrum and presented numerical examples to validate the improvement. Lin and Chang (2003) modified the approach by accurately estimating the equivalent damping ratio. Casarotti and Pinho (2007) adopted the adaptive pushover method (Reinhorn 1997) and developed the adaptive capacity spectrum method. Satisfactory predictions were achieved in numerical case studies on an ensemble of bridges.

1.3.2 Direct Displacement-based Design (DDBD)

First introduced by Priestley (1993), DDBD designs a structure based on deformation demand. The underlying motivation in this approach is to design a structure that can reach a prescribed deformation target at a specified ground motion intensity level. Priestley et al. (2007) published a book that provides detailed design examples of various structural systems.

Figure 1.20 shows the fundamentals of DDBD. A key issue associated with the implementation of this method is the determination of the equivalent damping ratio for inelastic systems (Priestley 2000; Priestley 2003; Priestley et al. 2007). Using additional damping to consider the inelastic behavior lacks a strict theory; hence, intensive numerical studies have been conducted to establish the relationship between ductility demand and equivalent damping ratio; calibrations are also constructed for various hysteretic shapes, ground motion characteristics, and structural periods (Priestley and Grant 2005; Dwairi and Kowalsky 2006). A satisfactory seismic performance can be reasonably achieved with the proper estimation of equivalent damping. Some successful application cases are selected from recent studies. For example, DDBD has been applied to precast walls (Pennucci et al. 2009), concrete bridges with single-column piers (Kappos et al. 2012), steel-braced RC frames (Malekpour et al. 2013), industrial rack clad buildings (Rafiqul and Alam 2013), and flexible earth retaining structures in coarse-grained soils (Cecconi et al. 2014).

1.3.3 Performance-based Plastic Design (PBPD)

The performance-based plastic design procedure was first proposed by Leelataviwat et al. (1999). Figure 1.21 shows the fundamentals of this method. The design idea was originated from the energy equivalence concept (Housner 1956), and the design procedure was developed through an investigation on the EP structural system. This method assumes that the total energy absorbed by an MDOF system is approximately equal to the elastic and plastic energy absorbed by an identical SDOF system.

PBPD has been successfully applied to the seismic design of concentrically braced frame (Chao and Goel 2006a), eccentrically braced frame (Chao and Goel 2006b), truss moment frame (Goel and Chao 2008), buckling-restrained-braced frame (Sahoo and Chao 2010), and buckling-restrained knee-braced truss moment frame (Yang et al. 2014). Lee et al. (2004) determined that input seismic energy is a function of natural period and ductility demand of structures, and they consequently introduced a modification factor for input energy. The energy dissipation capacity is later considered dependent on the hysteretic shapes of structures. Sahoo and Chao (2010) proposed a corresponding energy reduction factor.

1.4 Remarks

In the context of recently proposed PBEE, high-performance seismic-resisting structures are required to control both the peak and residual deformation. These dual objectives can be achieved by providing sufficient energy dissipating and SC capabilities. The energy dissipating and SC capabilities usually rely on plasticity and elastic restoring force, respectively. Therefore, they are typically realized using two separate materials or systems. However, SMAs offer a simple implementation solution to this problem through their superelasticity that involves energy dissipation and an elastic restoring force simultaneously. For this reason, superelastic SMAs have received increasing research attention over the past two decades. However, the seismic applications of SMAs is still in its infancy, and many critical problems and challenges are yet to be addressed before these advanced materials can be widely accepted by civil engineers.

1.5 Research Objectives

The community has gained an appreciative insight into the performance of SMAs in seismic applications. However, the further practical implementation of SMAs in earthquake engineering faces quite a few challenges. The superiority in using SMAs, including the reduction of peak seismic demand and the elimination of residual deformation, should be validated numerically and experimentally. A simple yet effective seismic design method for SMA-based structures is also needed. This study aims to fill the existing knowledge gap by achieving the following objectives:

1) To evaluate the mechanical properties of various types of SMAs and identify those with ideal mechanical properties, such as remaining superelasticity and excellent ductility in an extremely cold environment. The potential applications of these SMAs in earthquake engineering will be discussed.
2) To examine the performance of highway bridges with SMA-based isolators at different seismicity levels. A rigorous assessment will be conducted through incremental dynamic analysis (IDA).
3) To understand the seismic behavior of SMA-braced frames with a new focus on high-mode effect. Counterpart BRB frames will be introduced for comparison. Suggestions will be given to improve the seismic performance of SMA-braced frames.
4) To develop new SMA-based dampers for seismic applications. Dampers using different forms of SMAs will be developed.
5) To validate the observations and conclusions obtained from numerical studies. This objective will be achieved by conducting shaking table tests on the scaled model of an SMA-braced braced frame. The ground motion records of different characteristics and intensities will be used in the tests on the frame model.
6) To develop a simple yet effective performance-based design method for SMA-based SC structures. The concept of PBPD method will be extended to the new structural systems.

1.6 Thesis Outline

Systematical investigations, including experimental and numerical studies, on SMA-based SC structures are conducted in this PhD work. Figure 1.22 demonstrates the framework of this thesis, which is organized into eight chapters.

Chapter 1 describes the background and motivation of this work. In particular, this chapter reviews the applications of SMAs in earthquake engineering and the state-of-the-art development of SMA-based SC structures. After a review on the latest development in this field, the research objectives and scope are presented. This chapter lays a foundation for the remaining chapters.

Chapter 2 presents the material testing results of Ni-Ti (also known as Nitinol) wires and monocrystalline Cu-Al-Be wires. The cyclic properties of these wires are systematically compared with respect to hysteresis characteristics, training effect, strain amplitude effect, loading frequency effect, temperature effect, etc. The potential of different SMA wires in seismic applications are discussed.

Chapter 3 introduces two damping devices based on Ni-Ti SMA wires: one uses Ni-Ti wires, whereas the other is in the spring form. The wire-based damper directly utilizes the tensile property of SMA wires, whereas the spring damper exploits the torsion property of SMA wires. The pros and cons of these two forms are discussed.

Chapter 4 conducts IDA for a highway bridge with SMA-based SC isolators. The IDA curves clearly indicate that the seismic behavior of the bridge varies from a linearly elastic stage into a fully plastic stage. The seismic performance of the SMA-based isolator is assessed.

Chapter 5 discusses the high-mode effect on SMA-based (or other PT-based) SC structures. A prototype BRBF is selected for comparison, and an equivalent SC braced frame is obtained by replacing the BRBs with the SMA-based damping braces. Through pushover and nonlinear time history analyses, the high-mode effect on SC structures is recognized. Finally, two approaches for controlling the high-mode effect on SC structures are proposed.

Chapter 6 studies the seismic behavior of SMA-based braced frame by conducting shaking table tests. During the tests, ground motion records are scaled and input to the reduced-scale frame model. The ground motion intensity is scaled to cover a wide range of seismic hazard levels. This shaking table test aims to validate the observations from prior numerical studies. The corresponding numerical simulations of the scaled model are performed in OpenSees (2013). Good agreement is observed in the comparison between the testing data and numerical results.

Chapter 7 proposes a seismic design procedure for SMA-based SC structures within the PBEE framework. The proposed method originates from the performance-based plastic design method, and revisions and improvements are made to consider the features of SC structures. An SMA-based braced frame is selected to demonstrate the design methodology. Although the proposed method is used to design the SMA-based SC structures, it can be extended to other types of SC structure.

Chapter 8 summarizes the conclusions of this thesis, particularly elaborating the findings and contributions to the seismic applications of SMAs. Future work in this active research field is suggested at the end of this chapter.

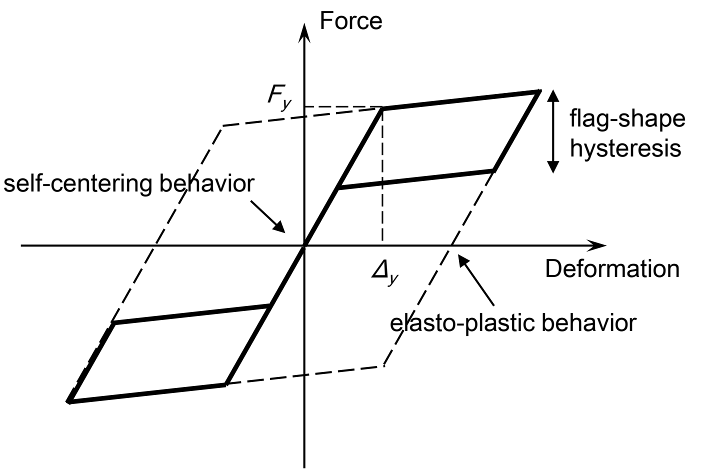

Figure 1.1 FS hysteresis of SC structural systems

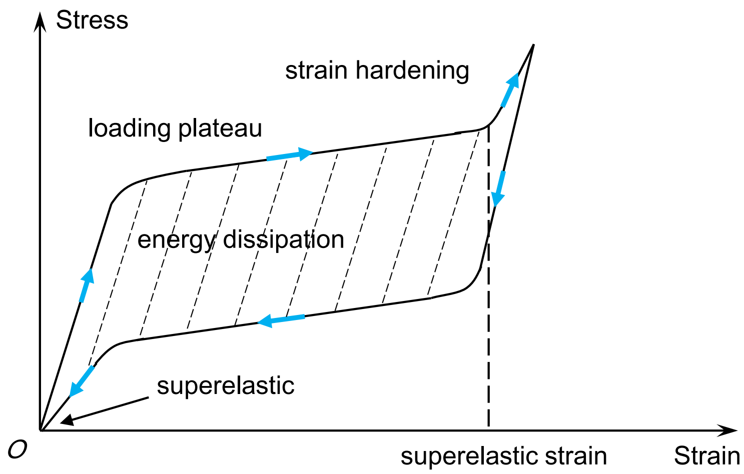

Figure 1.2 Typical behavior of the superelastic Ni-Ti SMA wires

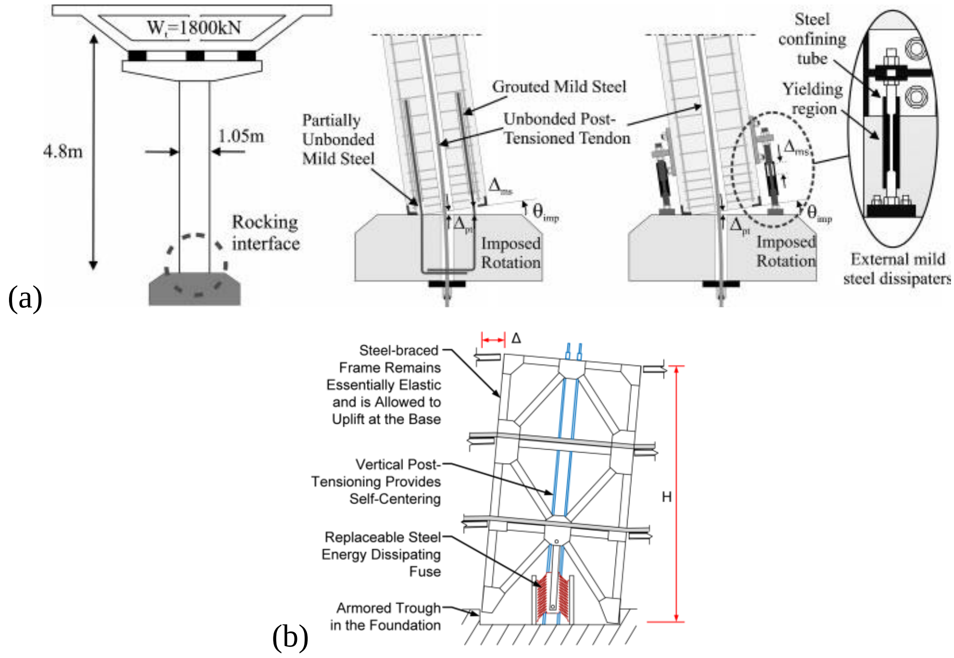

Figure 1.3 Typical SC rocking systems: (a) rocking bridge pier (Marriott et al. 2009) and (b) rocking structural frame (Eatherton et al. 2014a)

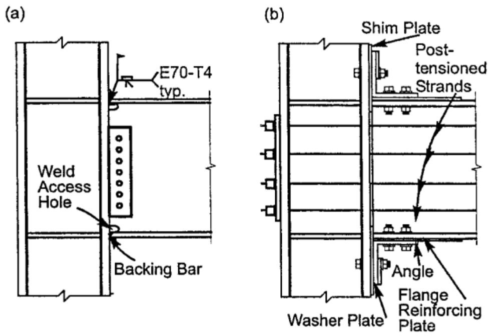

Figure 1.4 Comparison between MRF connections: (a) welded connection and (b) SC MRF connection (Ricles et al. 2001)

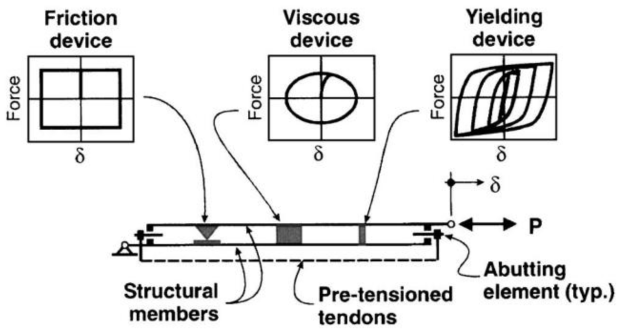

Figure 1.5 Concept of SC braces (Christopoulos et al. 2008)

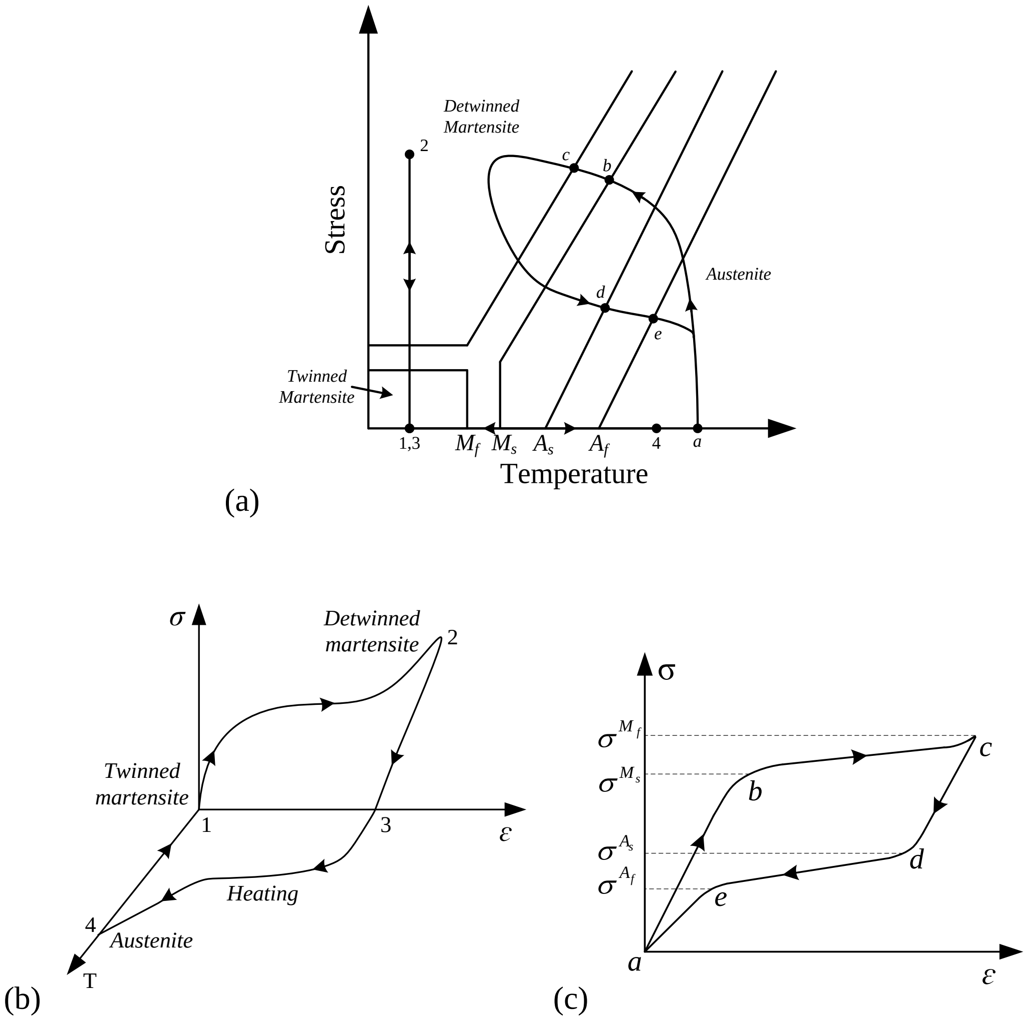

Figure 1.6 Fundamentals of Ni-Ti SMA: (a) stress-temperature diagram; (b) shape memory effect and (c) superelastic effect. (Patoor et al. 2006)

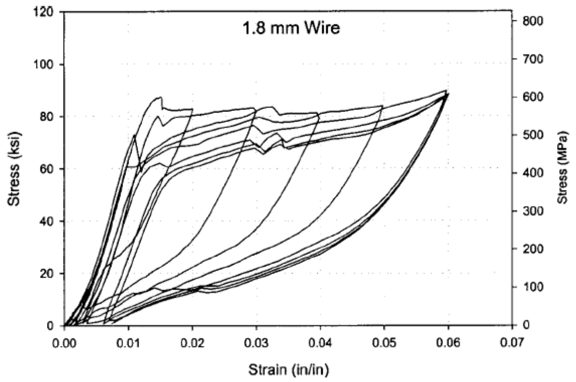

Figure 1.7 Typical tensile loading test of superelastic Ni-Ti SMA wires (DesRoches et al. 2004)

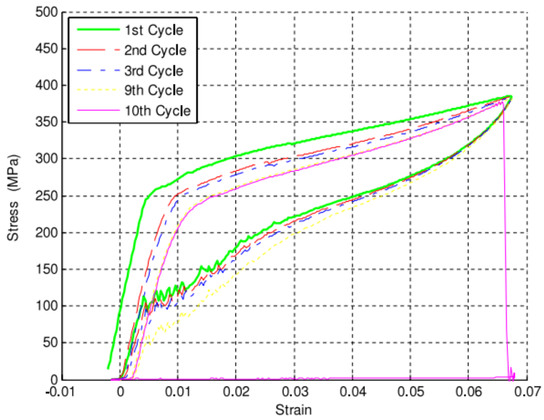

Figure 1.8 Training effect on superelastic polycrystalline Cu-Al-Be wires (Zhang et al. 2008)

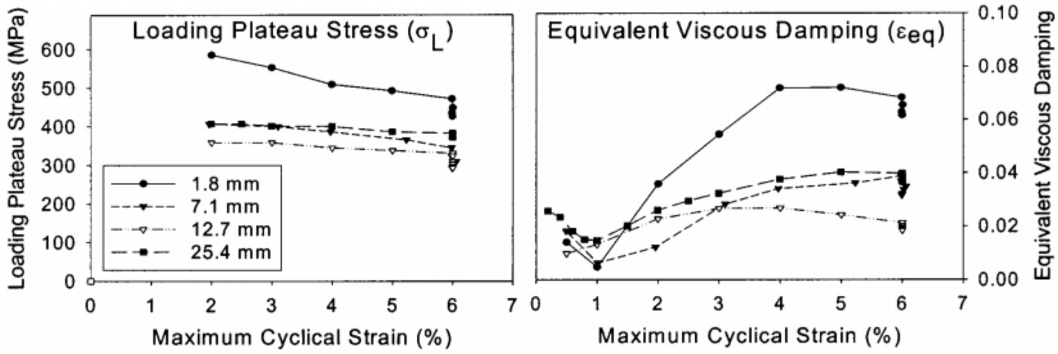

Figure 1.9 Deformation amplitude effect on superelastic Ni-Ti SMAs (DesRoches et al. 2004)

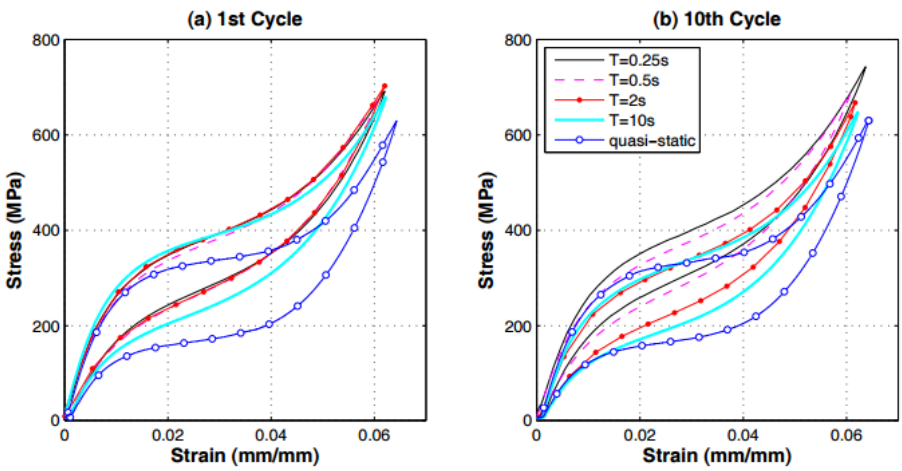

Figure 1.10 Stress-strain curves of superelastic Ni-Ti wires for 1st and 10th cycles under different loading rates (Zhu and Zhang 2013)

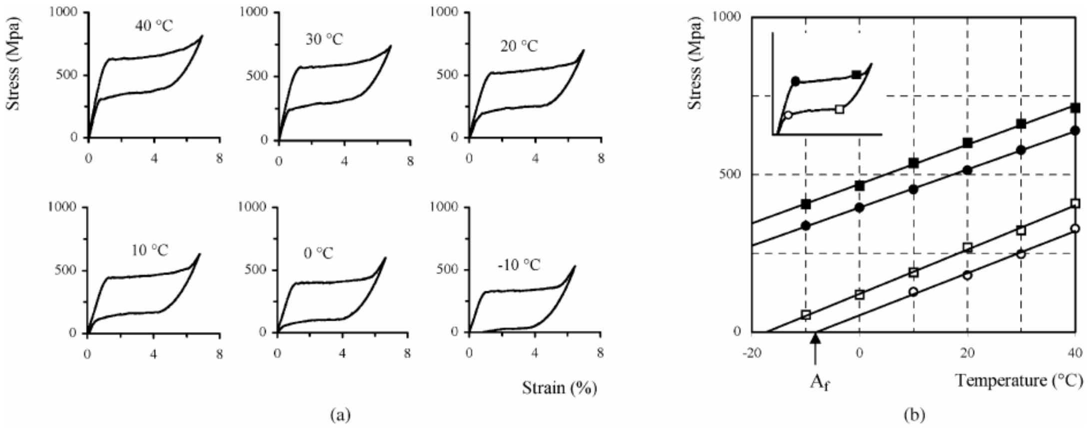

Figure 1.11 Superelastic Ni-Ti SMAs: (a) stress strain relationship at different temperatures; and (b) phase transformation stress as a function of temperature (Dolce and Cardone 2001)

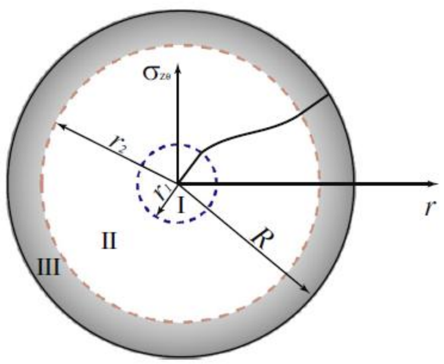

Figure 1.12 Stress distribution of solid SMA bar under torsion; Regions I, II, and III are the austenite, transition and the martensite, respectively (Mirzaeifar et al. 2010)

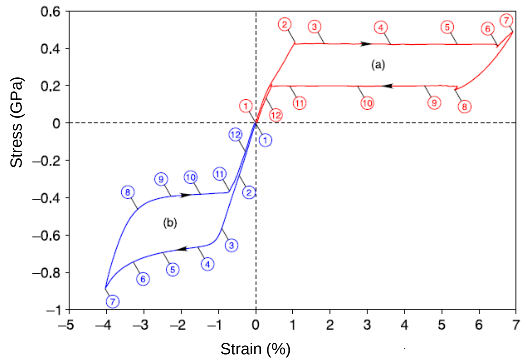

Figure 1.13 Mechanical response of s superelastic SMA tube under (a) tension and (b) compression (Reedlunn et al. 2014)

Figure 1.14 A versatile SMA-based damper (Zhang and Zhu 2007b)

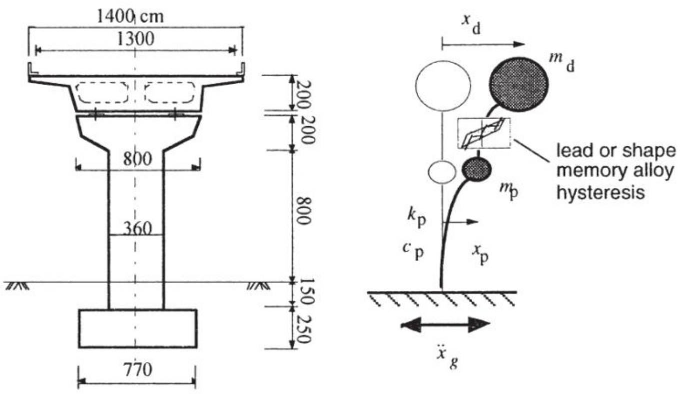

Figure 1.15 SMA-based isolators for elevated highway bridge (Wilde et al. 2000)

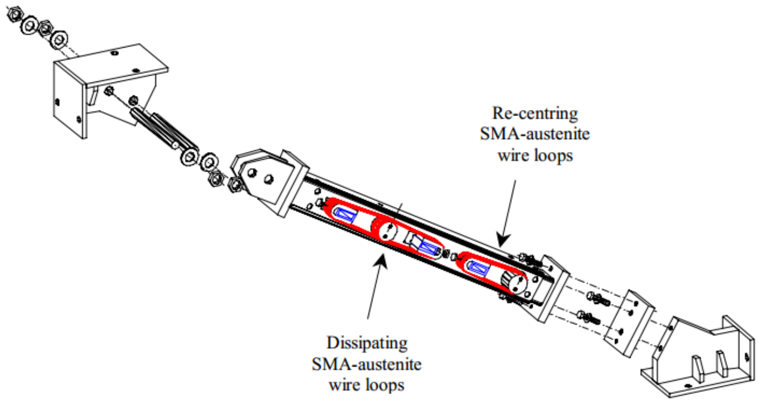

Figure 1.16 A large-scale SMA-based brace (Dolce et al. 2001)

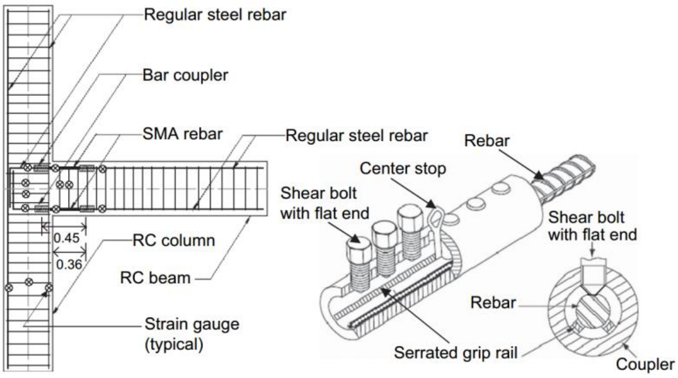

Figure 1.17 SMA-based connection in RC frame (Youssef et al. 2008)

Figure 1.18 SMA-based spring (Speicher et al. 2009)

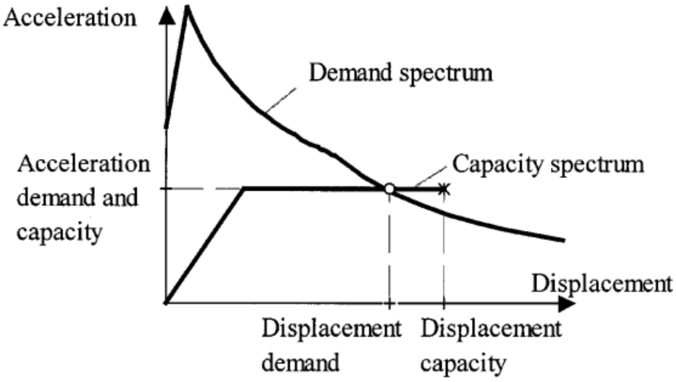

Figure 1.19 Fundamental of CSD (Freeman et al. 1975)

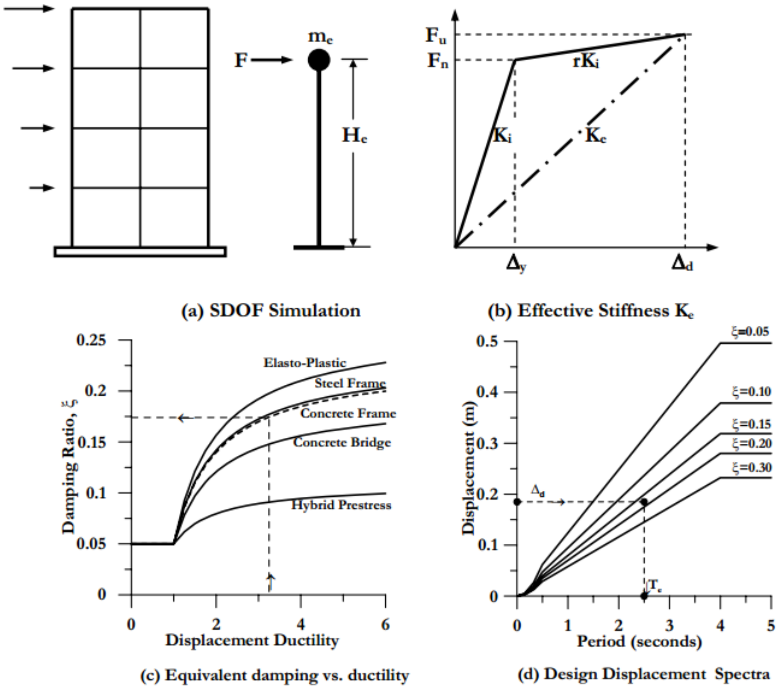

Figure 1.20 Fundamental of DDBD (Priestley et al. 1993)

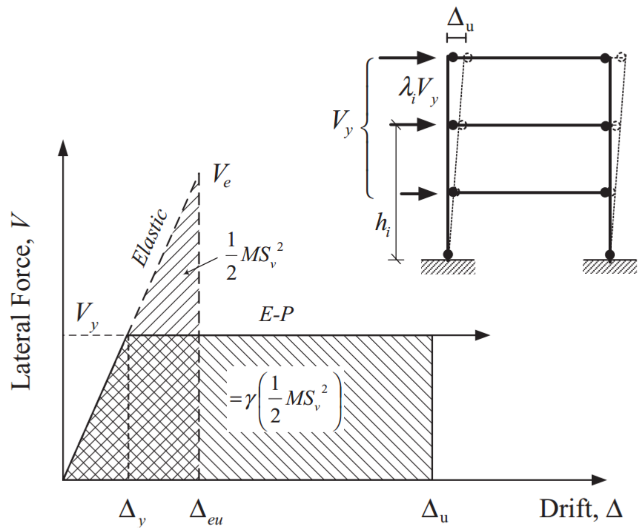

Figure 1.21 Fundamental of performance-based plastic design (Leelataviwat et al. 1999)

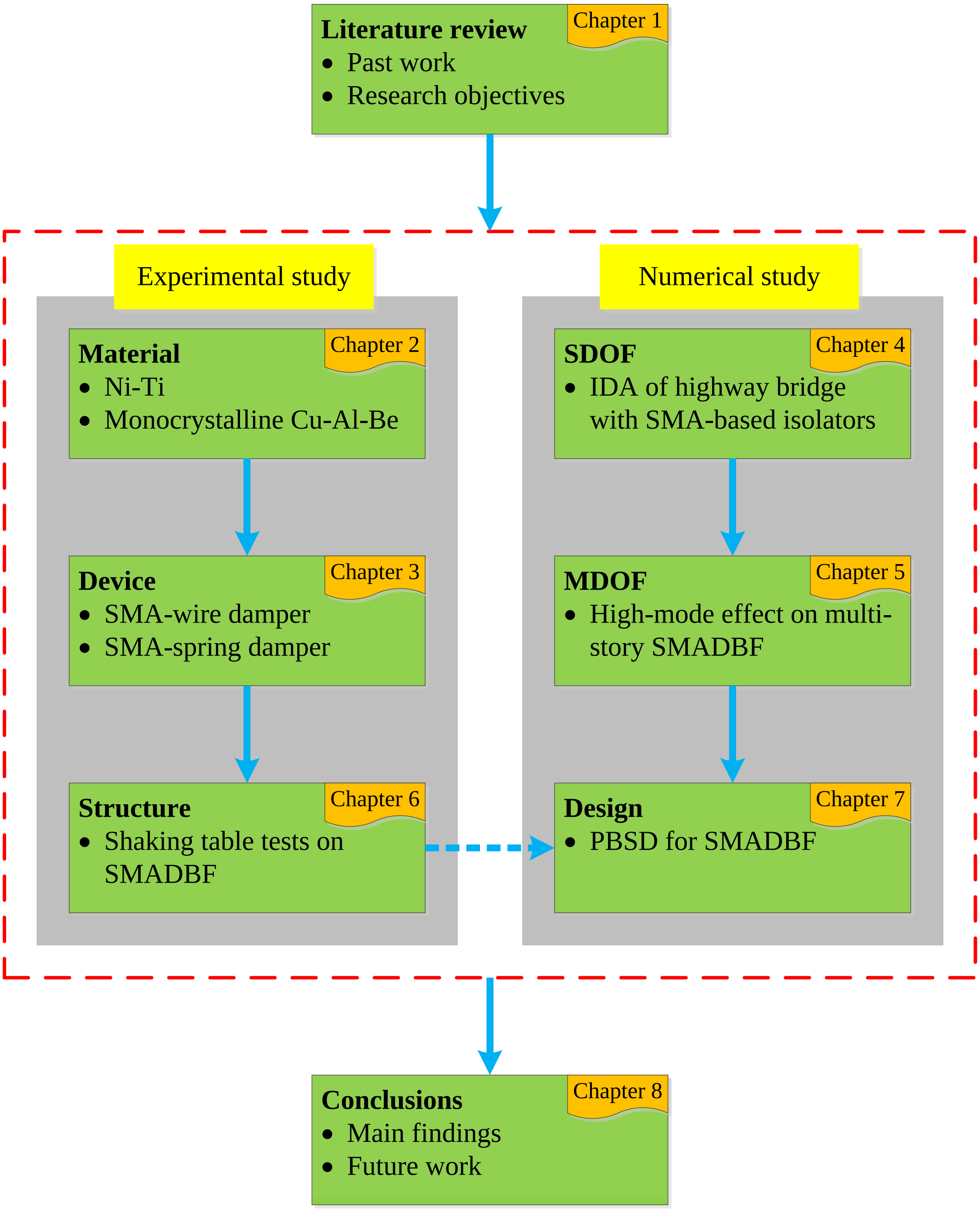

Figure 1.22 Framework of the thesis

Chapter 2 Superelastic SMA Wires

2.1 Introduction

This chapter experimentally studies the cyclic properties of three SMA wires, including Ni-Ti, polycrystalline and monocrystalline Cu-Al-Be wires. The first is the most commonly used SMA material, while the second and third are emerging Cu-based SMA materials. In past decades, the Ni-Ti SMAs have received the most attention from the community, and are deemed as the most appropriate SMA for seismic applications (DesRoches and Smith 2004). On the other hand, although monocrystalline copper-based SMAs have shown unique features from other SMAs, very limited research has been conducted to characterize their hysteretic properties relevant to potential seismic applications. The material properties of fully monocrystalline copper-based SMAs relevant to seismic applications have never been systematically reported. To this end, this chapter presents seismic application-oriented characterization of both Ni-Ti and monocrystalline Cu-Al-Be wires through cyclic loading tests. Research aspects of interest include basic hysteretic characteristics, “training” effect, loading amplitude effect, internal hysteretic loops, loading frequency effect, temperature effect, and fatigue life.

2.2 Investigated Cyclic Properties

Figure 2.1(a) shows a typical FS hysteresis that is frequently used to describe the superelastic behavior of Ni-Ti SMA when $T > A_f$; whereas Figure 2.1(b) shows a representative hysteresis of monocrystalline Cu-Al-Be SMA when $T > T_c$, where T is the environmental temperature, A_f is the austenite finish temperature of SMAs, and T_c is the critical temperature of monocrystalline Cu-Al-Be. The following material properties that are of common interest in seismic applications are investigated and discussed through the experimental program in this chapter:

E_i – the initial modulus of elasticity when SMA is in an austenite state;

α – the ratio of phase transformation stiffness to the initial stiffness, which is analogous to post-yield stiffness ratio of steel material in seismic applications;

σ_L – the forward transformation stress in the loading path, which is analogous to yield stress of steel material in seismic applications. Notably, two distinct forward transformation stresses $\sigma_{L,1}$ and $\sigma_{L,2}$ can be observed in Figure 2.1(b);

σ_{UL} – the reverse transformation stress in the unloading path. Again, two distinct reverse transformation stresses $\sigma_{UL,1}$ and $\sigma_{UL,2}$ can be observed in Figure 2.1(b);

ε_{f} – the ultimate strain of SMAs at the moment of fracture;

$\varepsilon_{\mathrm{se}}$ – the maximum recoverable strain that is upper bound of superelasticity;

ε_{R} – the residual strain after fully unloading;

e_{dis} – the dissipated strain energy density that is equal to the total area enclosed by the stress-strain loop in one cycle divided by the material volume;

ζ_{eq} – the equivalent damping ratio calculated by $\zeta_{\mathrm{eq}}=E_D/(4\pi\times E_S)$, where E_D is dissipated energy, and E_S is strain energy;

The above fundamental properties are essential factors in determining seismic behavior of SMA-based damping devices installed in civil structures. For example, the “post-yield” stiffness and energy dissipation of FS hysteresis play important roles in controlling seismic peak displacement of SC structural systems (Christopoulos et al. 2002a); the maximum recoverable strain and residual strain determine the SC capability after earthquakes. In addition to these properties, the effects of strain amplitude, loading frequency and temperature on the superelastic behavior, and large-strain fatigue life, are experimentally studied as well.

2.3 Experimental Setup and Method

The superelastic Ni-Ti wires with a diameter of 0.58 mm were provided by Johnson Matthey Inc. The chemical composition in terms of weight is Ni=55.94% and Ti=54.06%. According to the manufacturer, the austenite finish temperature A_f of the Ni-Ti wires is around 0 °C. The testing results of polycrystalline Cu-Al-Be were reported by Zhang et al. (2008), in which two batches of polycrystalline Cu-Al-Be wires with different heat treatment were tested under room and cold temperatures. Zhang et al. (2008) found that although the polycrystalline Cu-Al-Be wires could maintain superelasticity down to -85 °C, their superelastic strain was very limited. The tested superelastic monocrystalline Cu-Al-Be wires were obtained from NIMESIS Technology Inc. The chemical composition in terms of weight is close to Cu≈87% Al=12.0%, and Be=0.45-0.68%. According to the manufacturer, the austenite finish temperature A_f of the wires is around -91 °C. The monocrystalline Cu-Al-Be wires have a diameter of 1.9 mm. The wire specimens were taken from two different parent lots, namely Lot A and Lot B. The stress-strain relationships obtained in the cyclic tests show slight difference between the specimens from these two lots, whereas those from the same lot show quite consistent results. The difference may be due to the differences of many factors, such as the composition, crystal structure, heat treatment and fabrication procedure in production process. The results of both lots are reported in this paper. The cyclic tensile tests of wire specimens were conducted on an MTS universal testing machine. Both wire ends were griped by two rigid steel plates fastened by four bolts (as shown in Figure 2.2(a)). The gage length of the Ni-Ti wire specimens is 288 mm, while the gage length of the monocrystalline Cu-Al-Be wire specimens ranges from 162 mm to 170 mm.

The SMA wire specimens were cyclically tested at different loading frequencies, namely 0.025, 0.5 and 1.0 Hz. The first loading frequency is regarded as quasi-static testing in which dynamic effect is minimal, whereas the second and third frequencies represent dynamic loading rates within the typical frequency range of interest in earthquake engineering. The cyclic tensile tests were conducted using the displacement control method. Figure 2.3 shows a representative quasi-static testing protocol in which the strain amplitude keeps increasing with increments of 2% until the wire fractures or exhibits noticeable residual deformation.

The wire specimens were cyclically tested at different temperatures, namely 20 °C (room temperature), 10 °C, 0 °C, -10 °C, -20 °C, -30 °C and -40 °C. To investigate the superelastic hysteresis of SMA wires at a low temperature, a temperature-controlled testing chamber was employed to maintain the target temperature. Figure 2.2(b) shows the schematic diagram of the homemade temperature chamber that consists of liquid nitrogen tank, solenoid valve, a T-type thermocouple, a temperature process controller and a solid state relay. The testing temperature was monitored by the thermocouple inside the temperature chamber. The homemade temperature chamber can maintain a cold temperature as low as -100 °C with limited temperature ripples (less than ±3 °C).

2.4 Testing Results and Discussions

2.4.1 Hysteretic Characteristics

Figure 2.4 shows the representative stress-strain relationships of three concerned SMA wires obtained in cyclic tensile tests. Although all three SMAs exhibit apparent superelasticity, difference in the hysteretic loops can be clearly observed in Figure 2.4. The superelastic Ni-Ti wire exhibits a single plateau in loading and unloading paths. Upon loading beyond a critical stress level, austenitic to martensite phase transformation is activated and results in the stress plateau. With the removal of loading, the martensite becomes unstable, transforming back to austenite along a lower stress plateau. The superelastic monocrystalline Cu-Al-Be wire exhibits two distinct plateaus in loading and unloading paths, which are not observed in the hysteresis of Ni-Ti and polycrystalline Cu-Al-Be wires. This is induced by the unique two-stage stress-induced phase transformation of monocrystalline Cu-Al-Be SMAs (Hautcoeur et al. 1995). In the loading path, the first stress plateau is induced by the transformation from β austenite phase to β' martensite phase, whereas the second is induced by the successive transformation from β' martensite phase to α' martensite phase. In the unloading path, the reverse phase transformation happens: the first unloading path corresponds to $\beta'\rightarrow\beta$ transformation, whereas the second corresponds to $\alpha'\rightarrow\beta'\rightarrow\beta$ transformation. Therefore, the loading and unloading stresses $\sigma_{L,1}$, $\sigma_{L,2}$, $\sigma_{UL,1}$, and $\sigma_{UL,2}$ in Figure 2.1(b) are also referred to as $\sigma_{\beta\rightarrow\beta'}$, $\sigma_{\beta'\rightarrow\alpha'}$, $\sigma_{\beta'\rightarrow\beta}$, and $\sigma_{\alpha'\rightarrow\beta'\rightarrow\beta}$ (e.g. Otsuka et al. 1979). Figure 2.4 shows representative two-stage superelasticity of monocrystalline Cu-Al-Be when

$T>T_c$, where T_c is the critical temperature above which the $\alpha' \rightarrow \beta'$ and $\beta' \rightarrow \beta$ reverse transformations take place simultaneously (Hautcoeur et al. 1995). The shapes of superelastic stress-strain cycle of SMAs are typically temperature dependent. The two successive phase transformation stages offer monocrystalline Cu-Al-Be substantial superelastic strain. Additionally, the higher stress plateau at large strain can benefit deformation control under large seismic intensity levels.

Table 2.1 shows the comparison of the concerned material parameters identified from Figure 2.4. The peak strains in Figure 2.4 are equal to 8%, 19% and 3%, respectively, for Ni-Ti, monocrystalline Cu-Al-Be and polycrystalline Cu-Al-Be wires, and are close to the maximum superelastic strain amplitudes beyond which the deformation may not be fully recovered and noticeable residual strain may exist. The maximum recoverable strain of monocrystalline Cu-Al-Be wires is over twice of that of Ni-Ti wires. It is seen that the elastic strain amplitude of these SMA wires is significantly higher than that of steel material in seismic applications. Therefore, as long as the SMA wires are properly designed in SC seismic resistant structures, they could maintain SC capability, dissipate seismic energy and minimize structural permanent deformation even after extremely strong earthquakes.

The fracture strains were also evaluated through monotonically tensile tests and summarized in Table 2.1. An examination of the monocrystalline Cu-Al-Be specimen revealed that the fracture occurred at one clamped end, where initial crack caused by the clamp can be visualized. Thus, the fracture was probably induced by the initial defect, and the true ultimate deformation of monocrystalline Cu-Al-Be wires may be underestimated. Compared with polycrystalline Cu-Al-Be, the considerably higher fracture strain of Ni-Ti and monocrystalline Cu-Al-Be implies much greater usable ductility or greater safety margin in seismic design.

Table 2.1 also compares the transformation stress, initial modulus of elasticity, dissipated energy density and equivalent viscous damping ratio that are computed based on Figure 2.4. The Ni-Ti wires show relatively high strength capacity and good damping density. The monocrystalline Cu-Al-Be wires are associated with much greater energy dissipation capability but lower stiffness and transformation stress than the other two SMAs. It should be noted that high damping density and deformation capacity is often favorable in seismic metallic yield dampers (Tsai and Tsai 1995).

Notably, among three types of SMAs, polycrystalline Cu-Al-Be wires exhibit inferior superelasticity in terms of energy dissipation and allowable ductility, which may significantly limit its effectiveness when used in seismic energy dissipating devices.

2.4.2 Training Effect

"Training" effect usually refers to the variation of transformation stress and the accumulation of residual deformation in SMAs. The variation of transformation stress and residual deformation is often more obvious in the initial tens of cycles. To obtain stabilized stress-strain cycles, a cyclic pre-loading (referred to as "training" process) is often conducted before the formal use of SMAs. Different levels of training effects were observed in Ni-Ti and copper-based SMA wires in the past. For example, Zhang et al. (2008) observed the training effect in polycrystalline Cu-Al-Be wires; whereas Araki et al. (2011) concluded that Cu-Al-Mn rods have no training effect, as no obvious variation of transformation stress and residual deformation were observed in cyclic tests. The difference may be due to different alloy composition, crystal structure, heat treatment or fabrication process.

To evaluate the training effect of the Ni-Ti wire, cyclic tests with a loading frequency of 1.0 Hz and constant strain amplitude of 8% were conducted for 20 cycles. The 8% strain is close to the maximum recoverable strain of Ni-Ti wires. Figure 2.5(a) shows the consecutive 20 testing cycles. It is seen the global hysteresis shape almost keeps constant during the repeated loading cycles. Within the training cycles, both the forward and reverse transformation plateau tends to shift down. This trend mainly occurs in the first 10 cycles. After the 10th cycle, both the residual strain and energy dissipation become very stable. The instable hysteresis of SMAs in the initial cycles is caused by localized slip, and the low levels of localized slip assist the forward transformation (Miyazaki et al. 1986; DesRoches et al. 2004).

The direct comparison of the stress-strain cycles of Ni-Ti wire before and after the training process demonstrates the following “training” treatment effects: 1) the forward/reverse transformation stress plateaus tend to shift down but the hysteretic shape almost keeps constant, 2) slight accumulation of residual strain, and 3) moderate decrease of energy dissipation capacity. Figure 2.5(b) and (c) show the accumulation of residual strain and variation of equivalent damping ratio, respectively, within the training process. Both become stabilized quickly in the first 10 cycles. The maximum residual strain is about 0.6%, and the equivalent damping ratio decreases by 13% after the training process. Although the training effects are insignificant, an initial training process (pre-loading treatment) with tens of cycles is still recommended, if repeatable superelastic stress-strain cycles are desirable in seismic applications.

To evaluate the training effect of the concerned monocrystalline Cu-Al-Be, cyclic tests with a loading frequency of 1.0 Hz and constant strain amplitude of 19% were conducted for 40 cycles. The 19% strain, close to the maximum recoverable strain of monocrystalline Cu-Al-Be wires, is enough to induce the two-stage phase transformation and cover the typical strain amplitudes in seismic applications. Slightly different training effect may be observed if different strain amplitude is used. Figure 2.6(a) only shows the first to 20th cycles because the stress–strain cycles stabilized after the 20th strain cycle. The most significant variation occurs in the initial 13 cycles. In the first cycle, two plateaus can be observed in both the loading and unloading paths. Within the training cycles, the first forward transformation plateau tends to shift up, and the first reverse transformation plateau tends to shift down; whereas the second loading and unloading plateaus vary very slightly. In the 13th cycle, only one transformation plateau can be observed in the loading and unloading paths. From the 13th to 20th cycles, only very slight changes in energy dissipation and residual strain accumulation occur. After the 20th cycle, both the energy dissipation and residual strain become very stable. The instable hysteresis of SMAs in the initial cycles may be caused by two potential actions, namely, localized slip and dynamic self-heating phenomenon. The low levels of localized slip assist the forward transformation, while the self-heating effect accumulates in the specimen, thus causing the transformation stress to increase. However, the comparison in Section 2.4.5 reveals that the dynamic self-heating effect is insignificant in monocrystalline Cu-Al-Be wires. Thus, the training effect shown in Figure 2.6 is mainly due to the localized slip in this study.

The direct comparison of the stress-strain cycles of monocrystalline Cu-Al-Be wire before and after the training process demonstrates the following "training" treatment effects: 1) two forward/reverse transformation stress plateaus merge into one and the hysteretic loops become wider, 2) slight accumulation of residual strain, and 3) moderate increase of energy dissipation capacity as a consequence of transformation stress variation. Figure 2.6(b) and (c) show the accumulation of residual strain and variation of equivalent damping ratio, respectively, within the training process. Both become stabilized quickly in the first twenty cycles, which is not conflicted with that shown in Figure 2.6(a), since the observed variation of the cyclic shape after the 13th cycle has become very slight. The maximum residual strain is about 0.9%, and the equivalent damping ratio increases by 30% after the training process. Again, although the training effects are insignificant, an initial training process (pre-loading treatment) with tens of cycles is still recommended, if repeatable superelastic stress-strain cycles are desirable in seismic applications.

2.4.3 Strain Amplitude Effect

The strain amplitude effect on Ni-Ti is examined by applying dynamic cyclic loading at a frequency of 1.0 Hz. Figure 2.7 shows the stress-strain cycles of Ni-Ti wire specimens. The cyclic behavior of Ni-Ti wires varies as the loading strain amplitude increases. Similar amplitude-dependent behavior in other tests was observed (DesRoches et al. 2004). The major observations on the amplitude effect shown in Figure 2.7 are summarized as:

1) The cyclic behavior is a FS superelastic hysteresis with single forward and reverse transformation plateaus.
2) Beyond 6% strain, the Ni-Ti wires begin to experience strain hardening.
3) The maximum superelastic strain of the wires is around 8%.
4) The equivalent damping ratio varies as a function of loading amplitude (as shown in Figure 2.9(b)). When the strain amplitude is below 2%, the equivalent damping ratio is less than 4.0%; as the cycle is between 3% and 7%, the equivalent damping ratio tends to level off and is about 4.5%. At the largest strain amplitude, the equivalent damping ratio drops slightly due to the strain hardening behavior.
5) The forward and reverse transformation stresses are nearly unaffected by the strain amplitude.

The strain amplitude effect on monocrystalline Cu-Al-Be is examined by applying quasi-static cyclic loading, where the corresponding loading protocol is shown in Figure 2.3. Figure 2.8 shows the stress-strain cycles of monocrystalline Cu-Al-Be wire specimens taken from Lots A and B, in which the small- and large-strain cycles are distinguished by red and blue curves, respectively. The cyclic behavior of monocrystalline Cu-Al-Be SMA wires varies as the loading strain amplitude increases. Similar amplitude-dependent behavior in other copper-based SMAs was explained by Sakamoto et al. (1985). The major observations on the amplitude effect shown in Figure 2.8 are summarized as:

1) In small-strain cycles (typically when the peak strain is below 11%), a FS superelastic hysteresis with single forward ($\beta \rightarrow \beta'$) and reverse ($\beta' \rightarrow \beta$) transformation plateaus is similar to that of Ni-Ti wires.
2) When the peak strain is beyond 22%, the hysteresis shows two separate transformation plateaus (successive $\beta \rightarrow \beta'$ and $\beta' \rightarrow \alpha'$ forward transformations) in the loading path, but only one unloading plateau because of a continuous $\alpha' \rightarrow \beta' \rightarrow \beta$ reverse transformation.

3) When the peak strain is within the range of 11-22%, both loading and unloading paths exhibit two separate transformation plateaus. The two loading plateaus still correspond to the $\beta \rightarrow \beta'$ and $\beta' \rightarrow \alpha'$ forward transformations, but the latter is incomplete. As a result, the wires are in a $\beta'+\alpha'$ state. Upon unloading, the existing β' martensite is first transformed back to β phase, and subsequently, the continuous $\alpha' \rightarrow \beta' \rightarrow \beta$ reverse transformation takes place (Sakamoto et al. 1985).
4) Apparent difference in cyclic behavior can be observed between the two wire specimens. For example, the wire specimen from Lot A shows very close $\sigma_{L,1}$ and $\sigma_{L,2}$, which implies that $\beta \rightarrow \beta' \rightarrow \alpha'$ transformation takes place almost continuously; whereas the specimen B shows two distinct forward transformation stages. The difference may be due to different alloy composition, heat treatment or both.
5) The maximum superelastic strain of the wires is around 23%, with the corresponding accumulated residual strain measured to be only 0.3%. This maximum recoverable strain is considerably higher than those of Ni-Ti and polycrystalline SMAs.

Such two-stage loading and unloading paths and the corresponding phase transformation are illustrated in Figure 2.1(b). However, the two-stage loading and unloading paths may become indistinct after training process, as discussed in Section 2.4.2. Figure 2.9 shows the variation of transformation stress and equivalent damping ratio with the loading strain amplitude for the two wire specimens. Several other major observations from the testing results are summarized and discussed as follows:

6) The equivalent damping ratio of monocrystalline Cu-Al-Be wires varies remarkably as a function of loading amplitude (as shown in Figure 2.9(b)). When the strain amplitude is between 5% and 13%, the average equivalent damping ratio is approximately 2.5%; in the cycles with 19% strain amplitude, the equivalent damping ratio is about 8.8% and 5.2% for the wire Specimens A

and B, respectively. Although monocrystalline Cu-Al-Be wires have smaller equivalent damping ratio than Ni-Ti wires at small strain, the value can develop to a level comparable to (or even higher than) that of Ni-Ti wires when the strain amplitude of monocrystalline Cu-Al-Be wires exceeds 15%. The larger recoverable strain and greater energy dissipation at large strain amplitudes will benefit seismic response control under intensive earthquakes.

7) Figure 2.9(a) shows the variations of forward and reverse transformation stresses $\sigma_{L,1}$ and $\sigma_{UL,1}$ with the strain amplitude, where the forward and reverse transformation stresses are defined as the turning points of the first loading and unloading plateaus. Both the forward and reverse transformation stresses vary slightly between 160 and 175 MPa.
8) The initial elastic modulus values of Specimens A and B are approximately 17 and 12 GPa, respectively.

2.4.4 Internal Hysteretic Loops

As an emerging SMA material in seismic applications, the monocrystalline Cu-Al-Be wires are exclusively subjected to an additional analysis concerning the internal hysteretic loops. To examine internal hysteretic loops of monocrystalline Cu-Al-Be wires, three cyclic tests with partial unloading were conducted. The loading protocols are plotted with the internal stress-strain loops with the partial unloading/reloading, as shown in Figure 2.10. A simple internal loop is observed in Figure 2.10(a) when unloaded from a relatively small peak strain; however, Figure 2.10(b) and (c) show much more complex internal loops when unloaded from a peak strain of 19%. The energy dissipation, forward and reverse transformation stress, and occurrence of strain hardening vary in the internal hysteretic loops. For example, the forward transformation stress shifts downwards in the internal loops in Figure 2.10(b). Sepulveda et al. (2008) attributed this “stress degradation” to training or fatigue effects. However, similar internal loops can still be observed after sufficient training cycles. Figure 2.6 also indicates that the training effect tends to increase the forward transformation stress and expand the hysteretic loops. These facts imply that the internal loops cannot be explained by training or fatigue effects. The internal loop is essentially associated with thermo-mechanical mechanism. With partial unloading, the martensitic phase cannot be fully recovered to austenitic phase. The energy requirements for both forward and reverse transformations are a function of the residual martensite ratio. Bo and Lagoudas (1999) discussed the internal loops in details from a material point of view.

Notably, complex internal loops of monocrystalline Cu-Al-Be wires have not been paid enough attention to in previous studies. Considering the impact of transformation stress and energy dissipation in seismic response control, the development of a phenomenological model that can accurately capture the internal hysteretic behavior of monocrystalline Cu-Al-Be SMAs will be challenging yet necessary.

2.4.5 Loading Frequency Effect

The loading frequency effect on the superelastic behavior of SMA wires is an important issue that has to be addressed in seismic applications. Ni-Ti SMA wires were reported to be sensitive to loading frequency (Zhu and Zhang 2007a), whereas Cu-Al-Mn SMAs exhibit less sensitivity in loading frequency testing (Araki et al. 2011). The loading frequency effect on monocrystalline Cu-Al-Be SMA wires has never been reported. Thus, cyclic tests of Ni-Ti and monocrystalline Cu-Al-Be wires were conducted at three loading frequencies, namely 0.025, 0.5 and 1.0 Hz, where the first represents a quasi-static test, and the second and third represent dynamic frequencies in the frequency range of common interest in seismic applications.

Figure 2.11 shows the loading frequency testing results of Ni-Ti wires. It is seen that the superelastic stress strain relationships at dynamic loading differ from the quasi-static testing results significantly. But highly overlap is found between different dynamic testing results, which implies the cyclic behavior of Ni-Ti wires is stable within the frequency of interest in earthquake engineering. The dynamic loading slightly affects the forward transformation plateau, but significantly shifts up the reverse phase transformation plateau.

Figure 2.12 presents the stress-strain cycles of monocrystalline Cu-Al-Be wires at various loading frequencies, where Figure 2.12(a) and (b) represent small- and large-strain cycles respectively. The stress-strain cycles at two dynamic loading frequencies nearly overlap with each other, exhibiting stable cyclic properties in the dynamic frequency range of interest. Compared with the quasi-static test results, the dynamic loading frequency causes transformation stress to shift upwards slightly.

Correspondingly, Figure 2.13 shows the comparison of the transformation stresses and equivalent damping ratios at different loading frequencies. For monocrystalline Cu-Al-Be wires, the forward and reverse transformation stress was slightly increased at a degree of 5% to 10% under dynamic loading, and the equivalent damping ratio is changed by 2% (19% strain cycle) or 24% (11% strain cycle). Ni-Ti wires shows more evident property changes in Figure 2.13. With the application of dynamic loading, the forward and reverse transformation stress and equivalent damping ratio of Ni-Ti wires are changed by 9%, 157% and 52%, respectively, in comparison with the quasi-static testing. In general, the loading frequency effect on the monocrystalline Cu-Al-Be wires is comparable between small and large strain cycles, and is much smaller in comparison with that of the Ni-Ti wires. However, as aforementioned, the Ni-Ti wires show stable cyclic behavior within the frequency of interest in earthquake engineering.

The loading frequency effect is essentially a consequence of thermal effect induced by self-heating. The transformation stress increases with specimen temperature. A higher loading frequency induces more heat accumulation, further resulting in the requirement for larger transformation stress. As presented in Section 2.4.6, the monocrystalline Cu-Al-Be wires are much less sensitive to ambient temperature variation than Ni-Ti wires. It explains the slight loading frequency effect of the former in this sub-section.

2.4.6 Temperature Effect

The phase transformation of SMAs can be induced either by stress or temperature change. The cyclic properties of SMAs are dependent on ambient temperature because of coupled thermo-mechanical behavior. To investigate the cyclic properties of SMA wires under cold temperature, five consecutive tests were conducted on Ni-Ti wires with a loading frequency of 1.0 Hz; while for monocrystalline Cu-Al-Be wires, six consecutive tests at regularly decreasing ambient temperature were conducted with a loading frequency of 0.025 Hz.

Figure 2.14 collects the results of Ni-Ti wires corresponding to the 4% strain cycles at various temperatures ranging from -5 °C to 20 °C at an increment of 5 °C. It is seen Ni-Ti wires partially lose superelasticity at temperature below 0 °C, which presents a practical problem preventing the outdoor use of superelastic Ni-Ti SMA in the area with cold winter. But the indoor use of this SMA is viable, since the indoor temperature is seldom below 0 °C.

Figure 2.15 assembles all 11% and 19% strain cycles of monocrystalline Cu-Al-Be wires at various temperatures ranging from -40 °C to 20 °C at an increment of 10 °C. Notably, the monocrystalline Cu-Al-Be specimens maintain its superelasticity even at temperatures down to -40 °C. The transformation temperature A_f of the tested monocrystalline Cu-Al-Be wires is down to -91 °C. The $\beta \rightarrow \beta'$ and $\beta' \rightarrow \beta$ transformations shift downwards with the decreasing temperature, with their slope being unaffected by decreasing temperature. The $\beta' \rightarrow \alpha'$ and $\alpha' \rightarrow \beta' \rightarrow \beta$ transformations are nearly unaffected by the ambient temperature. Therefore, the monocrystalline Cu-Al-Be is more favored than Ni-Ti in the outdoor environment.

Figure 2.16 plots the cyclic properties as a function of temperature for Ni-Ti wires, including σ_L, σ_{UL}, E_i, α, E_D and ζ_eq. For example, Figure 2.16(a) and (b) show the transformation stresses σ_L and σ_{UL} decrease with decreasing ambient temperature. The slopes of σ_L and σ_{UL} curves are estimated to be 7.92 and 9.40 MPa/°C, respectively. As shown in Figure 2.16(c)–(d), initial stiffness varies moderately at around 45 GPa with changing ambient temperature; the transformation stiffness ratio is also slightly affected by temperature. Figure 2.16(e) indicates that decreasing ambient temperature has a negligible effect on energy dissipation capacity. Figure 2.16(f) shows equivalent damping ratio decreases as temperature increases, which is due to the higher strength of Ni-Ti wire at higher temperature.

Figure 2.17 plots the cyclic properties as a function of temperature for monocrystalline Cu-Al-Be wires, including $\sigma_{L,1}$, $\sigma_{UL,1}$, $\sigma_{L,2}$, $\sigma_{UL,2}$, E_{i}, α, E_D and ζ_{eq}. For example, Figure 2.17(a) and (b) show the transformation stresses $\sigma_{L,1}$ and $\sigma_{UL,1}$ decrease with decreasing ambient temperature. The results of polycrystalline Cu-Al-Be and Ni-Ti wires are also presented for comparison. The slopes of $\sigma_{L,1}$ (or σ_L) and $\sigma_{UL,1}$ (or σ_{UL}) curves are estimated to be 1.46 and 1.44 MPa/°C, respectively, for monocrystalline Cu-Al-Be; 2.03 and 1.92 MPa/°C, respectively, for polycrystalline Cu-Al-Be. Among three types of SMAs, the monocrystalline Cu-Al-Be is the least sensitive to ambient temperature variation in terms of phase transformation stresses. The results of $\sigma_{L,2}$ and $\sigma_{UL,2}$ curves are plotted in Figure 2.17(c)–(d) as well for monocrystalline Cu-Al-Be, in which the slopes are estimated to be -0.46 and 0.54 MPa/°C, respectively, showing minimal temperature sensitivity.

As shown in Figure 2.17(e)–(f), initial stiffness varies moderately at around 10 GPa with changing ambient temperature; the transformation stiffness ratio becomes slightly higher at colder temperatures. Figure 2.17(g)–(h) indicates that decreasing ambient temperature has a negligible effect on energy dissipation capacity and equivalent damping ratio.

Therefore, superelastic monocrystalline Cu-Al-Be SMAs may be more preferred than the other two SMAs in cold environment without significant degradation of cyclic properties. However, the overall temperature effect on the Ni-Ti and superelastic monocrystalline Cu-Al-Be is still not negligible, and the variation of transformation stress needs to be properly considered in the design stage. For example, a higher transformation stress may transmit a greater force to adjacent structural members, while a smaller transformation stress may lead to greater displacement response and ductility demand. Therefore, the seismic performance of structures equipped with SMA-based damping devices need be comprehensively evaluated in consideration of the likely temperature range.

2.4.7 Fatigue

Figure 2.18 presents the fatigue testing results of three SMA wires with different peak strain levels. Both Ni-Ti and monocrystalline Cu-Al-Be SMAs exhibit excellent fatigue life at 2% and 8% strain cycles, approximately ranging from 2000 cycles to 4000 cycles. Since the later has significantly high superelastic strain, and thus was also tested with peak strains of 11% and 19%. As shown in Figure 2.18, the monocrystalline Cu-Al-Be wires can sustain over 1700 and 35 cycles at 11% and 19% strain cycles, respectively.

Considering the duration and number of cycles of structural seismic vibrations, the excellent fatigue performance enables Ni-Ti and monocrystalline Cu-Al-Be SMAs to sustain several severe earthquakes without the need for replacement. Thus, they are a promising type of superelastic SMAs with SC and reusable features for seismic applications.

Polycrystalline Cu-Al-Be wires exhibit very low fatigue life, implying that it may not be suitable for seismic applications. Furthermore, the number of fatigue cycles is in general less than 10,000 in Figure 2.18. Thus, none of these three types of SMAs are suitable for damping devices used for wind-induced response mitigation, although such a use was proposed by some researchers.

2.5 Summary

In this study, the cyclic properties of three SMA wires were experimentally investigated to explore their application potential in seismic response mitigation devices. The wire specimens were cyclically tested under different conditions, and hysteretic characteristics relevant to seismic applications were systematically characterized, including basic hysteretic features, training effect, loading amplitude effect, loading frequency effect, temperature effect, and fatigue. The following major conclusions are drawn for Ni-Ti and monocrystalline Cu-Al-Be wires:

- When subjected to large cyclic strain, the Ni-Ti wires show a single phase transformation plateau; while the monocrystalline Cu-Al-Be wires show two distinct phase transformation plateaus in stress-strain cycles. The Ni-Ti wires exhibit a superelastic strain up to 8%. The two loading stress plateaus of monocrystalline Cu-Al-Be wires correspond to $A \rightarrow M$ and $M \rightarrow M$ forward transformations, respectively. Accordingly, the monocrystalline Cu-Al-Be wires exhibit a substantial superelastic strain up to 19%. It implies that when used in seismic resistant structures, both Ni-Ti and monocrystalline Cu-Al-Be SMAs can maintain SC capability and minimize structural residual deformation even after severe earthquakes.

- Initial training of Ni-Ti and monocrystalline Cu-Al-Be wires, typically consisting of tens of pre-loading cycles, are necessary to obtain stabilized stress-strain cycles and residual deformation. In general, the training process slightly decreases the energy dissipation for Ni-Ti wires, but increases the energy dissipation, and makes two transformation plateaus indistinct after training process for monocrystalline Cu-Al-Be wires.

- The hysteretic shapes and equivalent damping ratios of Ni-Ti and monocrystalline Cu-Al-Be wires show noticeable dependence on strain amplitude. Particularly, when the monocrystalline Cu-Al-Be wire specimens are partially unloaded, the stress-strain relationships show complex internal loops with apparent amplitude dependence. Similar hysteretic behavior has not been observed in Ni-Ti SMAs, and thus some new constitutive models for monocrystalline Cu-Al-Be SMAs need to be developed to accurately capture such complex amplitude-dependent hysteresis.

- The comparison between the quasi-static and dynamic testing results indicates that monocrystalline Cu-Al-Be wires are generally less sensitive to loading frequency than Ni-Ti wires in terms of hysteretic shape, transformation stress and energy dissipation. The Ni-Ti wires show quite stable cyclic behavior upon dynamic loadings with frequency of interest in earthquake engineering.

- Ambient temperature has a different degree of effect on the cyclic property of SMA wires. In general, the monocrystalline Cu-Al-Be is less sensitive to temperature than Ni-Ti. The Ni-Ti wires could maintain superelasticity at a temperature above 0 °C, and the monocrystalline Cu-Al-Be wires maintain superelasticity at extremely cold temperatures below -40 °C.

- The Ni-Ti and monocrystalline Cu-Al-Be wires show comparable fatigue performance. In addition, the monocrystalline Cu-Al-Be wires can sustain 2000–4000 cycles at cyclic strain less than 11%, and sustain over 35 cycles at 19% strain cycles. The excellent fatigue performance will enable Ni-Ti and monocrystalline Cu-Al-Be SMAs to sustain several severe earthquakes and aftershocks without the need for replacement.

- Although polycrystalline Cu-Al-Be SMAs also show stable superelasticity at very low temperature, their limitations in superelastic strain, energy dissipation and fatigue life may prevent their practical use in seismic applications.

In summary, the Ni-Ti and monocrystalline Cu-Al-Be SMAs show excellent performance in the concerned seismic aspects. The monocrystalline Cu-Al-Be SMAs seems to be a more promising alternative to conventionally Ni-Ti SMAs in cold-temperature outdoor environment, even though the present unit price of monocrystalline Cu-Al-Be SMAs is higher than that of Ni-Ti SMAs.

As a relatively new type of SMA materials, many important aspects of monocrystalline Cu-Al-Be SMA requires more future study before their practical applications. For example, a sophisticated phenomenological model needs to be developed to facilitate seismic analysis and design, and their corrosion resistance needs to be evaluated.

In the following chapters, major focus will be paid on the SMA-based braces, which are expected to be installed in the braced frames in an indoor environment. So both Ni-Ti and monocrystalline Cu-Al-Be SMA wires could maintain superelasticity in such a condition. In terms of the mechanical properties, it has been shown that either Ni-Ti or monocrystalline Cu-Al-Be has excellent superelastic strain and good damping capability. Although the monocrystalline Cu-Al-Be SMA exhibits higher superelasticity than Ni-Ti, its hysteresis shape is so complicated that it seems impossible to accurately model the cyclic behavior within the existing finite element software. However, the community has developed accurate constitutive models for Ni-Ti SMAs in several popular softwares, such as OpenSees, ANSYS, and SeismoStruct. This makes an intensive study on Ni-Ti based SC structures possible. Due to the above two reasons, this study decides to use Ni-Ti SMA throughout the rest of the work.

Table 2.1 Comparison of material properties of three superelastic SMAs at room temperature

Characteristics	Unit	Ni-Ti	Monocrystalline Cu-Al-Be	Polycrystalline Cu-Al-Be [a]
E_i	GPa	38.3	17	33.8
α	-	0.0	0.03	0.09
σ_L (or $\sigma_{L,1}$)	MPa	500	170	232
σ_{UL} (or $\sigma_{UL,1}$)	MPa	351	167	270
e_{dis}	J/mm^3	0.012	0.017	5.5×10^{-4}
ζ_{eq}	-	3.4%	5.2%	1.0%
ε_{se}	-	8%	19%	4%
ε_f [b]	-	15%	25%	6%

(a) The testing results of polycrystalline Cu-Al-Be wires were reported in Ref. (Zhang et al. 2008).
(b) The fracture strain was measured through monotonically tensile tests.

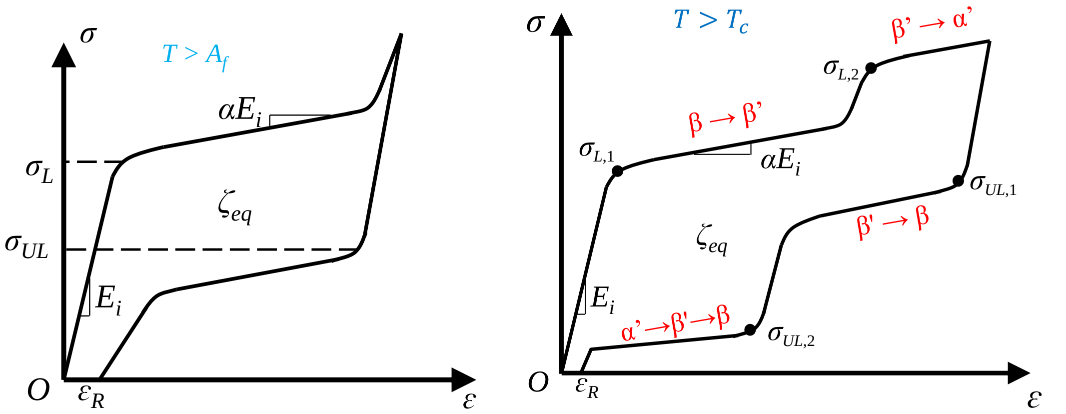

(a) Ni-Ti (b) Monocrystalline Cu-Al-Be

Figure 2.1 Typical stress-strain relationships of superelastic SMA wires

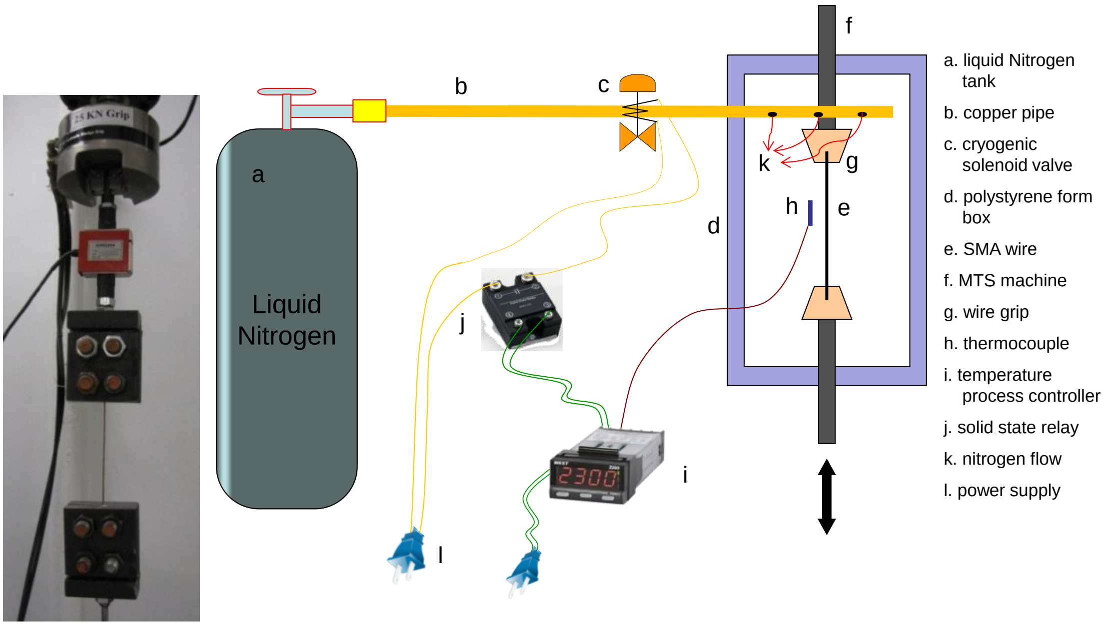

(a) The tested wire (b) Schematic of the homemade temperature chamber

Figure 2.2 Experimental Setup

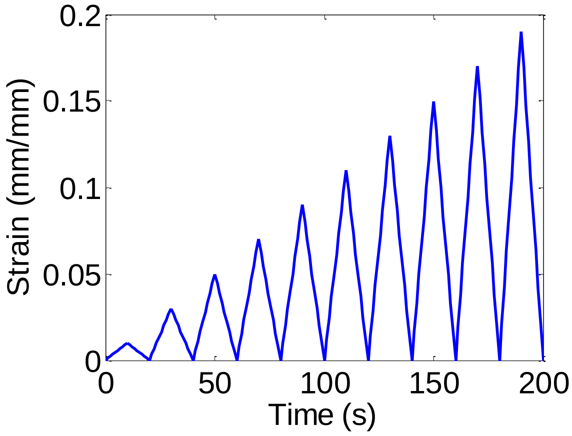

Figure 2.3 Cyclic loading protocol with loading frequency = 0.025 Hz

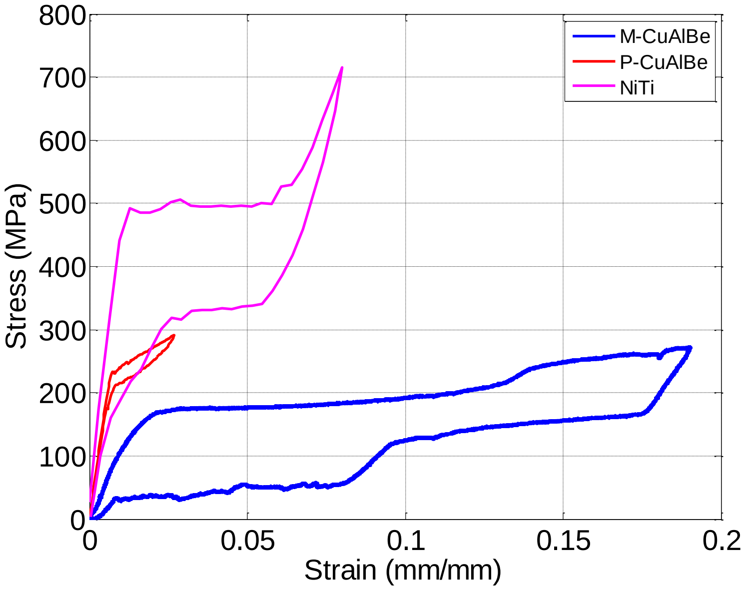

Figure 2.4 Representative superelastic behavior of monocrystalline Cu-Al-Be wire (Lot B), polycrystalline Cu-Al-Be wire and Ni-Ti wire at room temperature

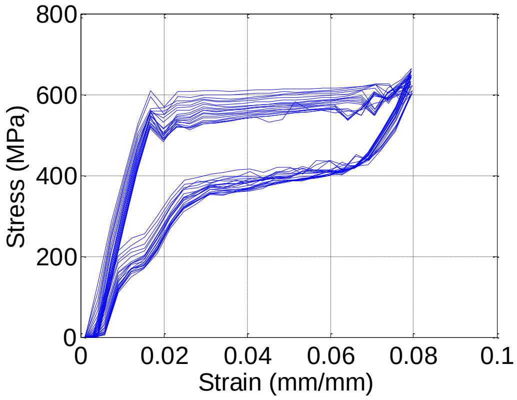

(a) Stress-strain relationship, 20 cycles

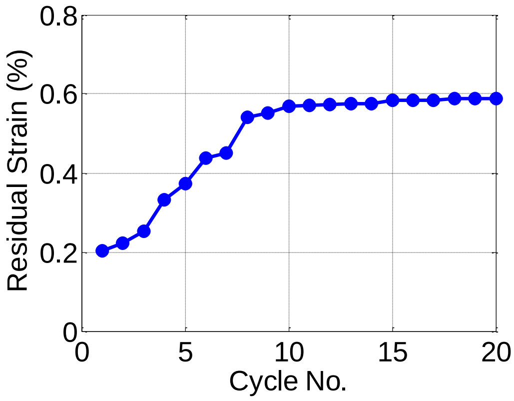

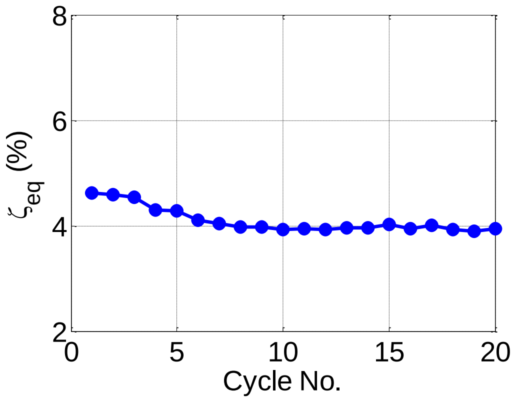

(b) Accumulation of residual strain (c) Equivalent damping ratio

Figure 2.5 Training effect of Ni-Ti wires at a loading frequency of 1.0 Hz

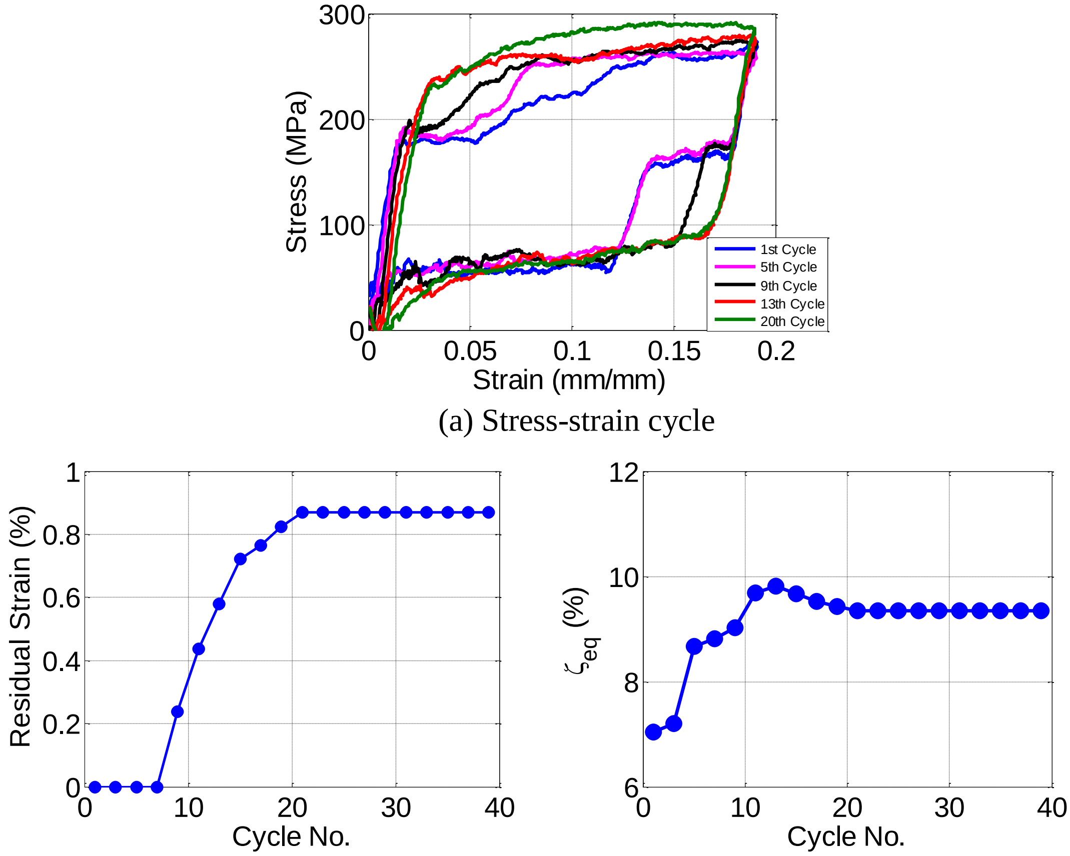

(a) Stress-strain cycle

(b) Accumulation of residual strain

(c) Equivalent damping ratio

Figure 2.6 Training effect of monocrystalline Cu-Al-Be wires (Lot B) at a loading frequency of 1.0 Hz

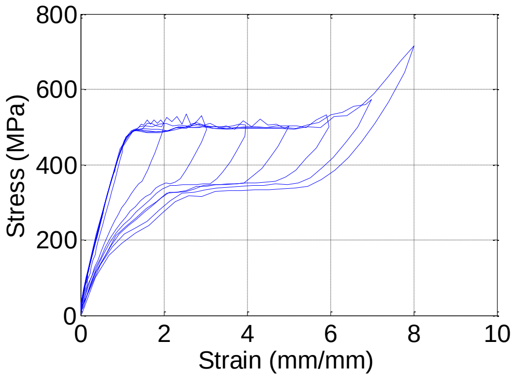

Figure 2.7 Testing results of Ni-Ti wires under cyclic tensile loadings with a loading frequency of 1.0 Hz

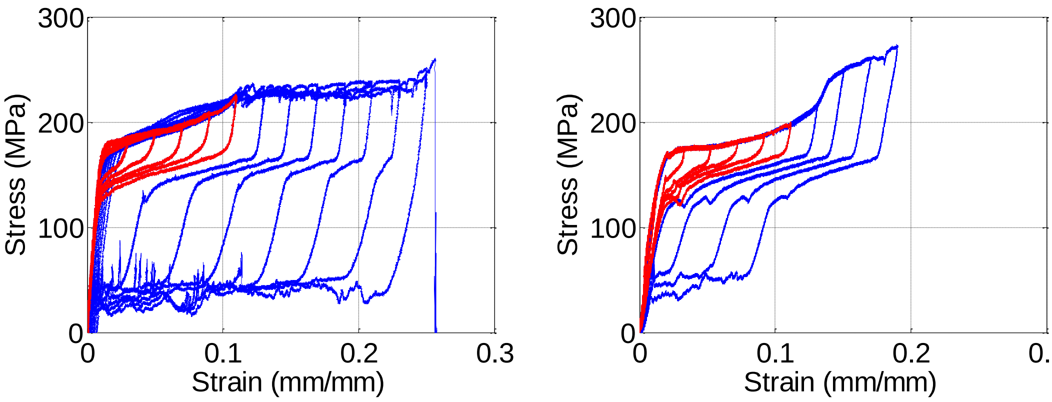

(a) Lot A (b) Lot B

Figure 2.8 Testing results of monocrystalline Cu-Al-Be wires under cyclic tensile loadings with a loading frequency of 0.025 Hz (Red: small-strain cycles; Blue: large-strain cycles)

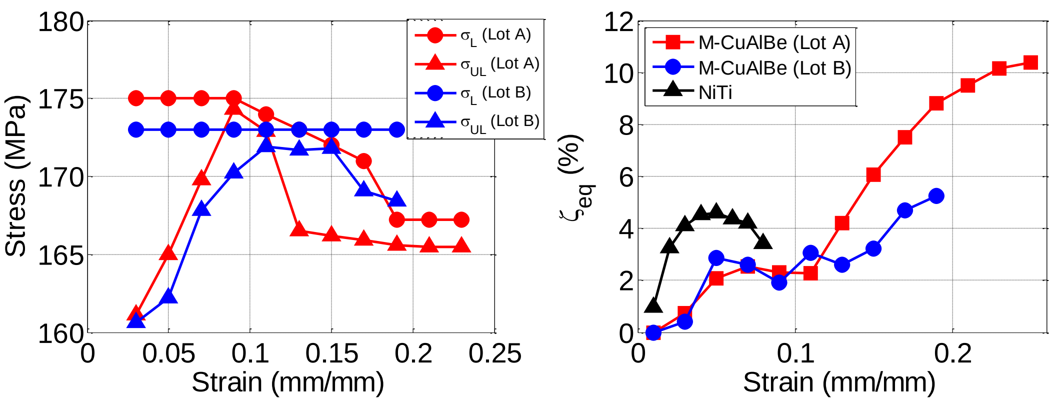

(a) Transformation stress (b) Equivalent damping ratio

Figure 2.9 Variations of cyclic properties of monocrystalline Cu-Al-Be with loading strain amplitude

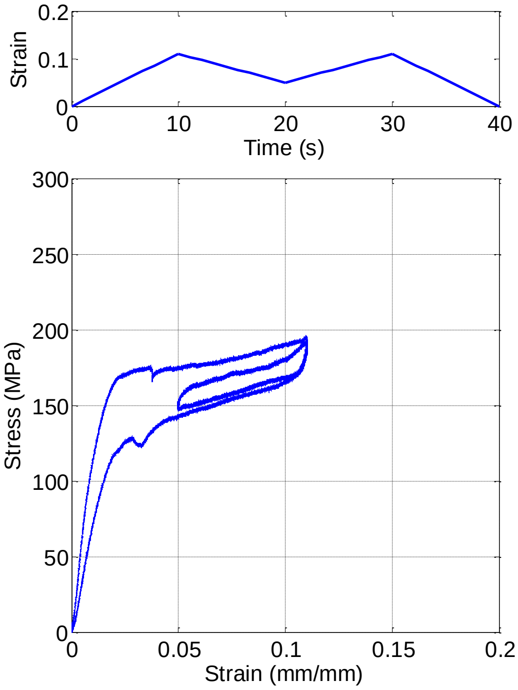

(a)

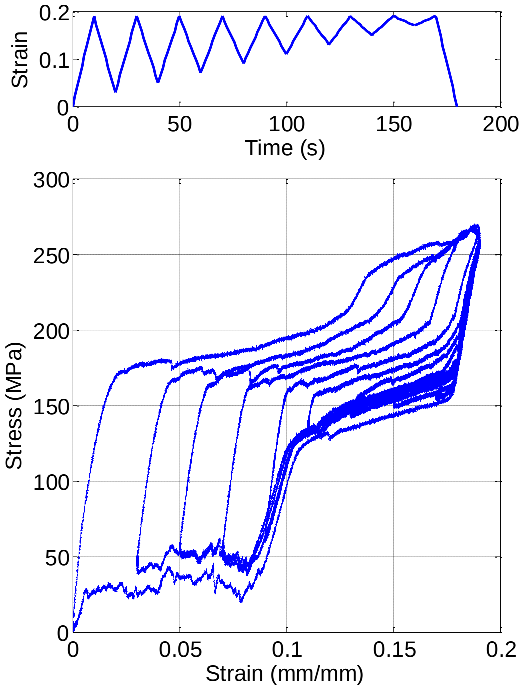

(b)

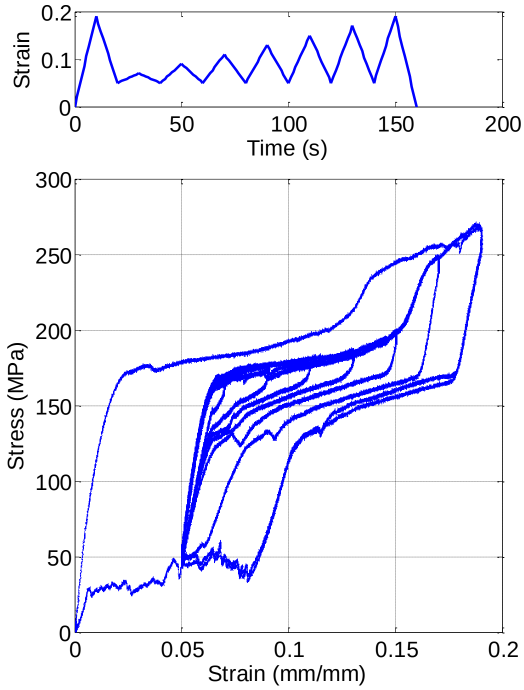

(c)

Figure 2.10 Internal hysteretic loops with partial unloading/reloading of monocrystalline Cu-Al-Be (Lot B)

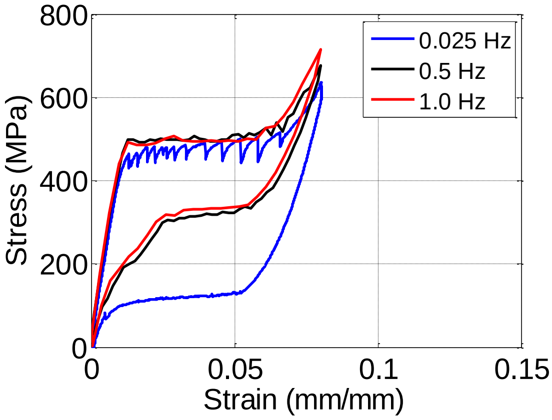

Figure 2.11 Stress-strain relationships of Ni-Ti wires at different loading frequencies

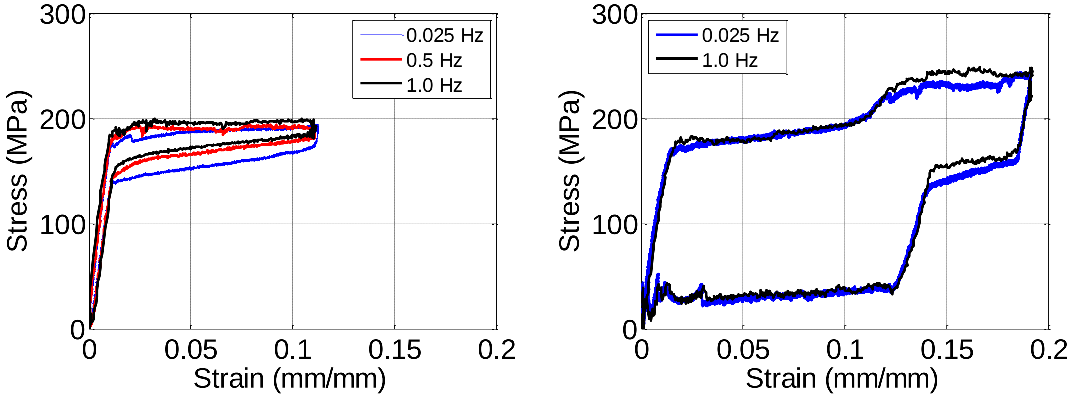

(a) Small-strain cycle (b) Large-strain cycle

Figure 2.12 Stress-strain relationships of monocrystalline Cu-Al-Be wires (Lot B) at different loading frequencies

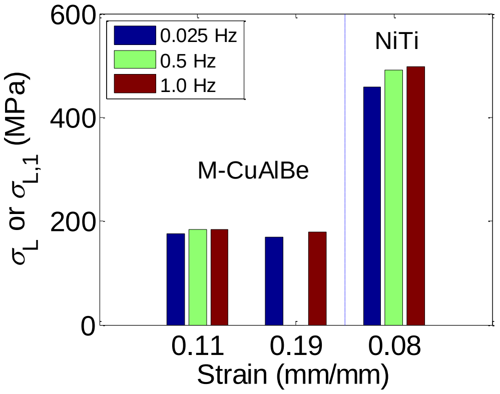

(a) Forward transformation stress

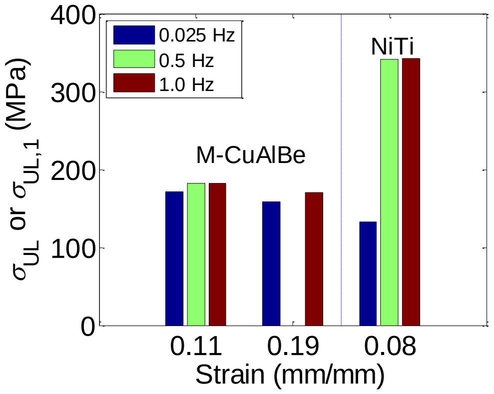

(b) Reverse transformation stress

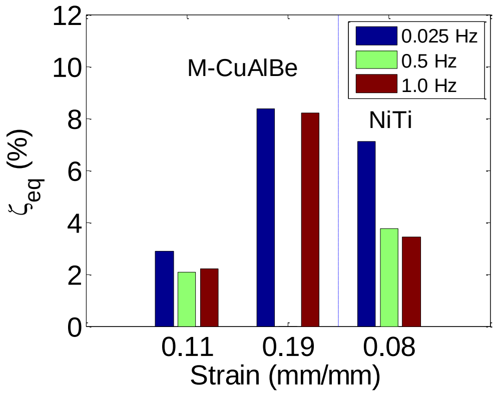

(c) Equivalent damping ratio

Figure 2.13 Loading frequency effect on cyclic properties of monocrystalline Cu-Al-Be and Ni-Ti wires

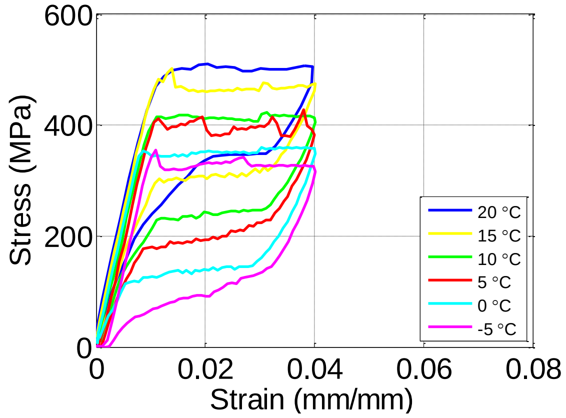

Figure 2.14 Stress-strain cycles of Ni-Ti wires at different ambient temperatures

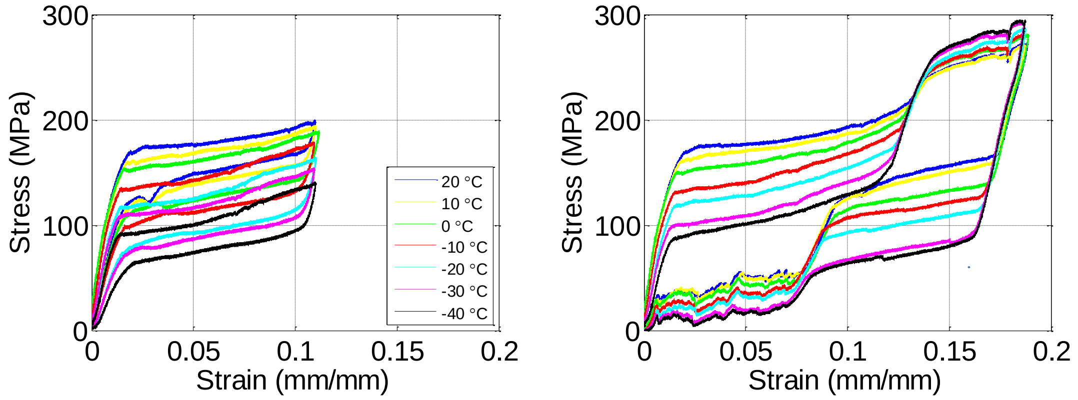

(a) Small-strain cycle

(b) Large-strain cycle

Figure 2.15 Stress-strain cycles of monocrystalline Cu-Al-Be wires at different ambient temperatures

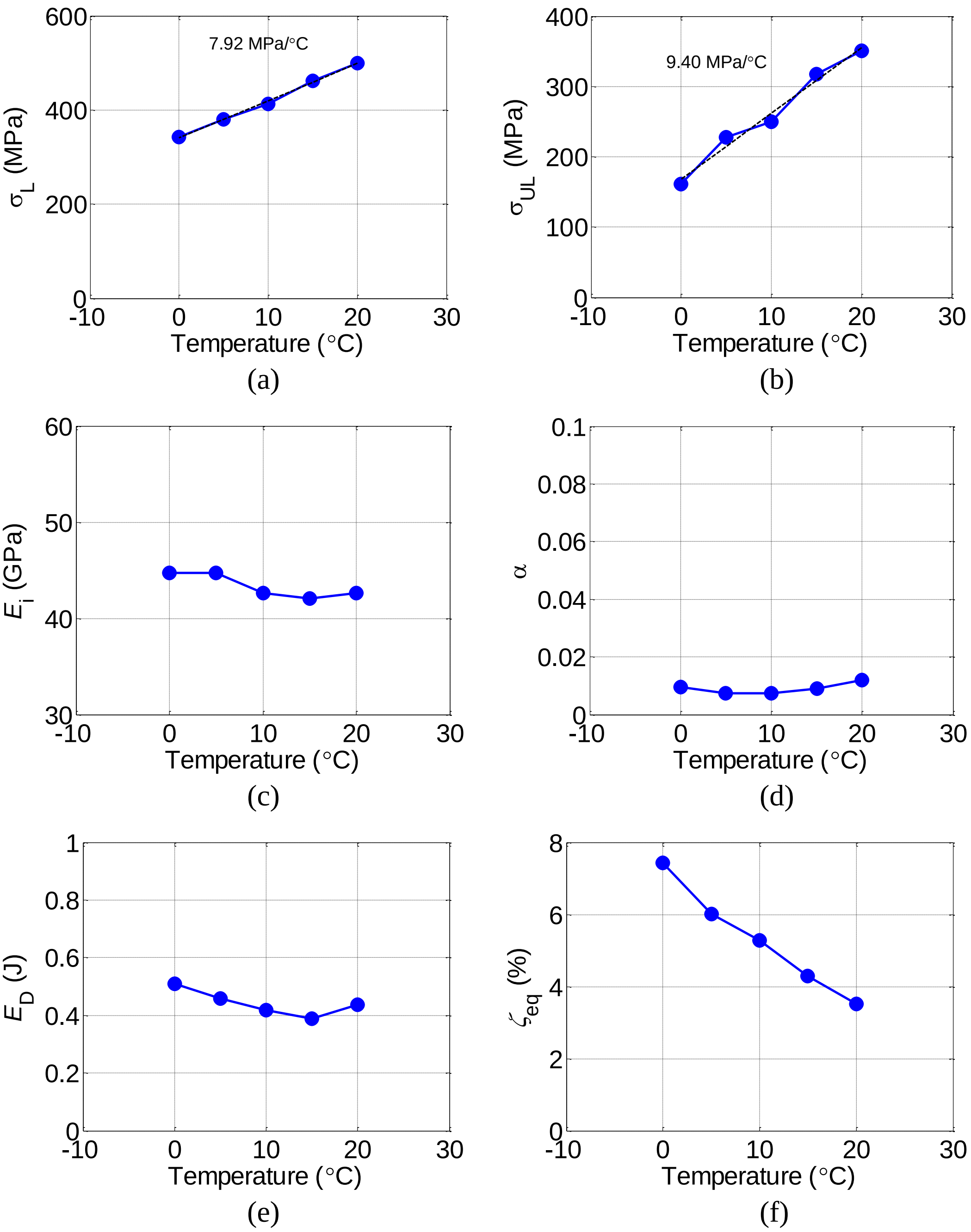

Figure 2.16 Temperature effect on cyclic properties of Ni-Ti wires under 4% strain amplitude

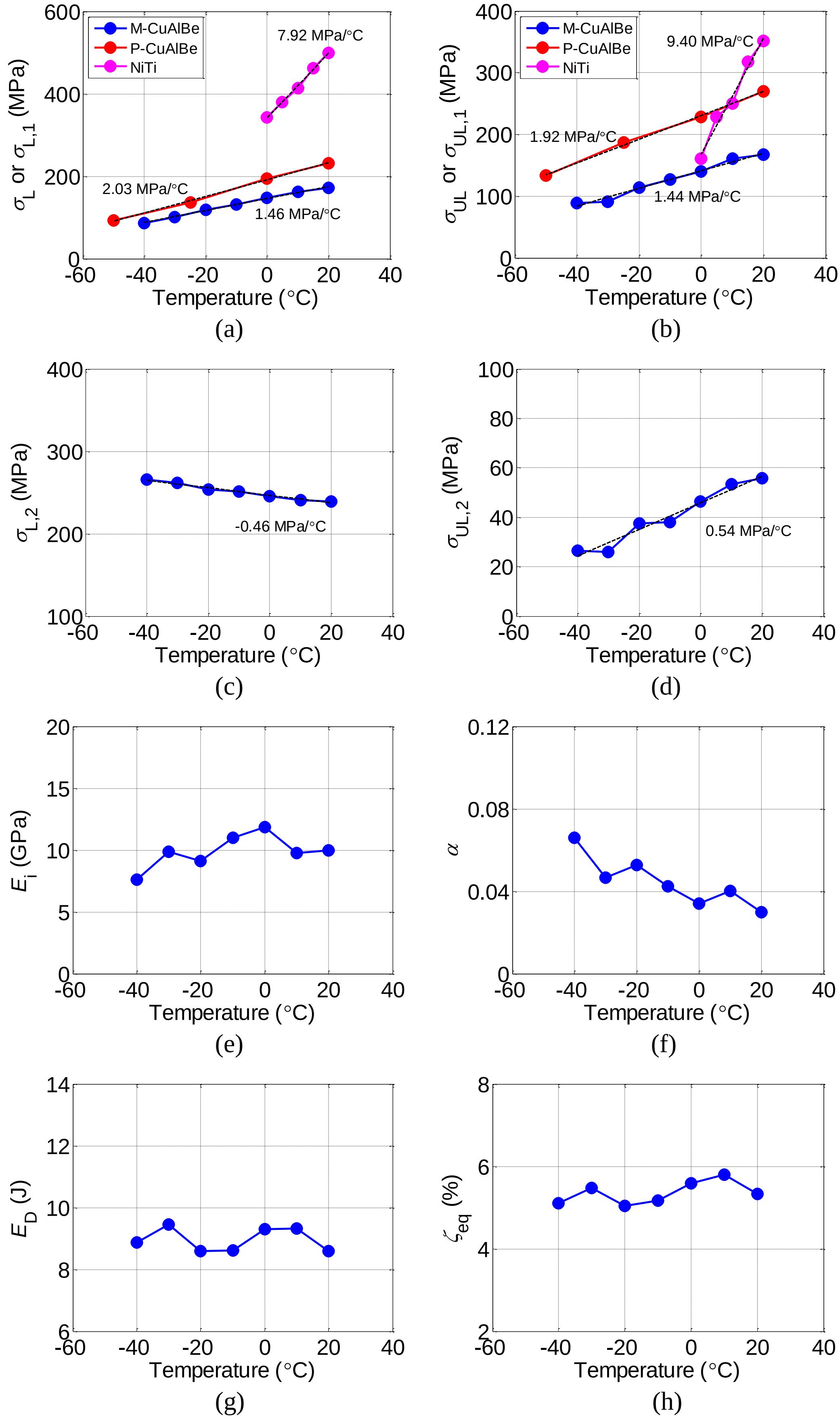

Figure 2.17 Temperature effect on cyclic properties of monocrystalline Cu-Al-Be wires (Lot B) under 19% strain amplitude

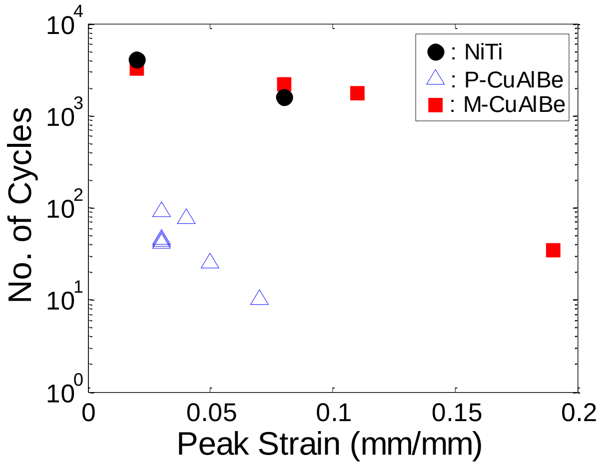

Figure 2.18 Large-strain fatigue of three SMA wires

Chapter 3 SMA-based Dampers

3.1 Introduction

This chapter presents the experimental study on two types of SMA-based dampers made of Ni-Ti SMA. The first type is an SMA-wire that utilizes the tension of SMA wires, whereas the other is essentially an SMA-spring damper that uses the torsion behavior. The mechanisms and fabrication procedures of these dampers are introduced in detail, and the mechanical behavior is characterized through cyclic loading tests. The testing results are discussed and compared, focusing on the potential applications of these dampers in earthquake engineering. This chapter finally selects a damper that will be used in the succeeding chapters.

3.2 SMA-Wire Damper

This subsection presents a study on SMA-wire dampers. These dampers will be extended to SMADBs to be installed in a braced steel frame in the subsequent chapter. The mechanical properties of the dampers are intended for a 1/4-scale SMADBF model, which is thoroughly explained in Chapter 6. This part focuses on the fabrication and testing of SMA-wire dampers.

3.2.1 SMA Wire

Superelastic Ni-Ti wires recover deformation up to 6%–8% of the strain and can dissipate energy through hysteresis under cyclic loading. This material also has a relatively stable temperature performance and outstanding fatigue property. Given these advances, Ni-Ti wires are selected as the core component of the SMA-wire damper. The adopted Ni-Ti wires are acquired from Xi’an Siwei Metal Materials Development Co., Ltd. The weight percentage of titanium in this SMA alloy is 55.8%. The phase transformation temperature ranges from 0 °C to 5 °C. Thus, the wire exhibits a superelastic behavior at room temperature.

Wires, instead of bars, are employed in this study because of two reasons. First, although the direct use of large SMA bars can provide the expected behavior, the machining and fabrication of the connections between the SMA bars and the adjacent members is challenging. Second, SMA bars exhibit asymmetrical tensile and compressive behavior, whereas SMA wires or cables serve as tension-only members that avoid such asymmetry. Considering their easier machinability and better superelasticity than bars, wires are adopted in the dampers described in this thesis. The wire diameter is set as 1.0 mm. Prior to being used in the dampers, the Ni-Ti wires are preloaded for 20 cycles at 1.0 Hz to eliminate the training effect discussed in Chapter 2. Figure 3.1 plots the stress–strain cycles of the “trained” Ni-Ti wires at a loading frequency of 2.0 Hz for 10 consecutive cycles. The Ni-Ti wires show a superelastic strain up to 6% without residual deformation. Stable and repeatable FS hysteresis is observed without strength or stiffness degradation. The loading frequency effect discussed in Chapter 2 illustrates that the cyclic behavior of the Ni-Ti wires is fairly stable over the interested frequency range in earthquake engineering. Therefore, the selected Ni-Ti wires are suitable for SMA-wire dampers.

3.2.2 Configuration

Figure 3.2 shows the configuration of an SMA-wire damper, which consists of two sliding steel blocks, two steel rods, and two groups of Ni-Ti wires. The Ni-Ti wires serve as the kernel component of the damper. As illustrated in Figure 3.2(a), two steel rods that run through the slots elongate the Ni-Ti wires and transfer the resisting force between the wires and the steel blocks. Figure 3.2(b) shows the mechanism of the SMA-wire damper. The Ni-Ti wires are always in tension whether the damper is subjected to either tension or compression. Such a mechanism enables the sufficient use of the Ni-Ti wires. Figure 3.2(c) plots the idealized FS hysteretic behavior of the damper that is similar to that of other types of SC devices. The steel rods are designed to be sufficiently strong to prevent excessive bending deformation. Figure 3.3 illustrates a few fabrication details of the SMA-wire damper, including the addition of some cushion material to the contact surfaces between different parts to mitigate the impact effect, which may prematurely fracture the Ni-Ti wires, and the use of U-connector to effectively anchor the wire ends.

The proposed SMA-wire dampers can be installed at various locations in a structure for different purposes. In this research, the dampers are extended into bracing elements called SMADBs. Figure 3.4 shows the configuration, dimensions, and photo of the SMADB, which is composed of a central SMA-wire damper and two extension parts. The middle damper is welded to two steel square tubes to be extended to the desired length of the brace. The final length of the SMADB is 1360 mm. The braces can be bolted to the main structure through the holes on the gusset plates. The steel square tubes have a cross section of 50 mm × 50 mm × 3 mm, where 3 mm is the wall thickness. The extension parts are designed to remain elastic such that inelastic deformation is concentrated in the middle segment.

3.2.3 Cyclic Properties

Two SMA-wire dampers are cyclically tested on an MTS universal testing machine. Figure 3.5 shows the cyclic behavior of these dampers at a loading frequency of 2.0 Hz, and Table 3.1 summarizes their cyclic properties. The force–displacement relationships of the tested dampers show a typical FS and repeatable hysteresis. However, a low initial stiffness is also observed. This stiffness is caused by the initial slackness of the wrapped wire loops (approximately 2 mm to 3 mm) and the backlash of the fabricated dampers. Normal elastic stiffness rapidly gains afterwards until the phase transition plateau of the SMA wires. The cyclic behavior of SMADBs with the extended length is essentially identical to that of SMA-wire dampers.

Compared with other types of braces reported in the literature (e.g., BRB (Fahnestock et al. 2007) or post-tensioned SC energy-dissipative brace (Erochko et al. 2014)), the SMADBs in this study have a relatively smaller strength. The primary reason behind this condition is the limited capacity of the testing facilities in the laboratory. Ni-Ti wires with a diameter of 1.0 mm are used in this study. The capacity of SMADBs in practical applications can be conveniently increased by using SMA wires with large diameter. Therefore, SMADBs are considered scalable and can achieve a force level similar to that of conventional braces or damping devices.

3.3 SMA-Spring Damper

Previous studies have shown the promise of SMA springs in vibration controls. However, the cyclic properties of these springs relevant to seismic applications are yet to be systematically investigated. In view of this deficiency, this section presents a seismic application-oriented characterization of SMA springs through cyclic loading tests. Figure 3.6 shows the notation of typical geometric dimensions of a spring. Four geometric parameters are usually considered in the design of a helical spring, namely, wire diameter d, spring diameter D, pitch angle θ, and the number of active coils N that is equal to the ratio of free length to coil distance (i.e., L/Δ). Spring index is defined as $C = D/d$.

SMA springs with different end types are experimentally characterized and compared through cyclic tests. In particular, parametric studies are conducted to evaluate the influence of the spring geometric parameters (e.g., spring index and the number of active coils). The effects of different wire types, loading frequencies, quench methods, and pre-loading are evaluated as well.

3.3.1 Fabrication of SMA Springs

This section presents the design and fabrication procedure of SMA springs. The springs are divided into two groups according to the types of their ends (i.e., plain and closed end). A spring with plain ends has a non-interrupted helicoid, and its ends are the same as if a long spring has been cut into sections. Contrarily, a spring with closed ends is obtained by deforming the ends to a zero-degree helix angle. A variety of spring specimens are fabricated for parametric studies.

Heating treatment affects the mechanical properties of SMA springs. Wu (2001) performed heating treatment at 500 °C. Morgan and Broadley (2004) tried various heating temperatures and recommended that the proper temperature ranges from 450 °C to 550 °C. Jee et al. (2008) heated their research specimens up to 550 °C for 30 min. Savi et al. (2015) recently confirmed that heating treatment at 500 °C for 30 min is the best means to produce an ideal SMA-based superelastic spring after a series of trials. To determine an optimal heating method, the present study adopts three temperatures: 300 °C, 400 °C, and 500 °C, and three heating treatment durations: 5, 10, and 30 min. After the trials, the heating treatment at 500 °C for 30 min is considered the best choice. Water or air quench of the spring specimens is conducted after heating. In sum, the SMA springs are fabricated in the following steps: 1) mechanical conformation of the springs, 2) heating treatment at 500 °C in a furnace for 30 min, 3) air or water quench over a sufficient time. Figure 3.7 clearly demonstrates these procedures.

A total of seven spring specimens are produced, and their parameters are listed in Table 3.2. As noted in the preceding paragraph, the springs are divided into two groups according to their end types. The springs with plain ends are buckled during compression tests due to eccentric load; hence, they are referred to as tension springs. By contrast, the springs with closed ends show a stable tension and compression behavior and are therefore denoted as tension-compression springs. Specimen 1 (denoted as S1 hereafter for brevity) is generated to study the behavior of plain-end springs, whereas S6 is used to examine the behavior of closed-end springs. S2 and S3 are compared with S1 to observe the effect of the number of active coils (N) and spring index (C), respectively. S4 and S5 are made of solid bars and hollow tubes, respectively. These specimens are compared with each other to reveal the change induced by using different wire types. S7 is subjected to air quench and is compared with S6 to identify the difference induced in using various quench methods.

3.3.2 Plain-end Spring

In this part, S1 demonstrates the typical cyclic loading behavior of SMA-based springs.

The cyclic loading tests of the spring specimens are conducted on an MTS universal testing machine at room temperature. Both specimen ends are clamped by two steel shims bolted to rigid fixtures as shown in Figure 3.8. The cyclic tensile tests are conducted using the displacement control method. Figure 3.9 shows a representative quasi-static testing protocol, in which the displacement amplitude continuously increases with an increment of 20 mm until either the specimen exhibits a noticeable residual deformation or the displacement amplitude exceeds the loading limit of the MTS machine. The loading procedure is stopped at 140 mm, which is the upper limit of the loading machine.

Figure 3.10 shows the representative force–displacement relationship of S1 obtained in cyclic tensile tests. As previously mentioned, the maximum displacement amplitude is 140 mm. The cyclic behavior of SMA-springs shows a typical FS hysteresis. The "yielding" behavior occurs at the point in which the tangent stiffness starts to decrease. This definition implies that the "yielding" displacement occurs almost constantly at 32.1 mm. The "yielding" strength and spring stiffness are expressed as F_y = 63.3 N and k_i = 1.97 N/mm, respectively. The strength and stiffness of springs are significantly lower than those of wires. The "post-yield" stiffness ratio, α, and the energy dissipation parameter, β, are approximately estimated as 0.29 and 0.5, respectively. Contrary to conventional elastic springs, the SMA springs show a highly nonlinear behavior. The deformation of SMA springs is essentially a summation of elastic deformation and martensite transformation-induced deformation (Liang and Rogers 1997). Stable and repeatable hysteresis loops without obvious training effect are observed. Training effect is usually exhibited by Ni-Ti wires at the initial several loading cycles as discussed in Chapter 2, whereas the elimination of this effect in springs may be attributed to the heating treatment (Ozbulut et al. 2007; Zhang et al. 2008).

Figure 3.11 plots the equivalent damping ratio and residual displacement as functions of loading amplitude. The dissipated energy only considers the area in the first quadrant for the plain-end springs because these springs buckle upon compression. Damping is relatively small within the range of 1% to 3%. Damping increases with loading amplitude because of the development of martensite fraction. The complete martensite phase transformation causes the accumulation of residual displacement with the loading amplitude. At the 140 mm loading loop, only 6 mm residual displacement is detected. This observation implies that the SMA springs have an excellent SC capacity.

3.3.3 Closed-end Spring

The closed-end spring (i.e., S6) is made of 4 mm wire/bar and has a pitch angle of 26°, which is significantly larger than that of ordinary springs. The geometric nonlinear effects can noticeably change the behavior of springs with a large pitch angle when subjected to large displacements (Shigley 1989). The free height of S6 is 52 mm, and the corresponding maximum compression stroke is 40 mm. Figure 3.12 plots the cyclic behavior of S6 as a function of loading amplitude. To protect the load cell, contact between spring coils should be avoided. Therefore, the compression testing is stopped at −40 mm, and the tension displacement amplitude is stopped at 40 mm. Further tension of the closed-end spring shows a behavior similar to that of the plain-end spring. As observed, the spring successfully carries compression without an instability problem. In addition, the spring shows a stable FS hysteresis upon tension and compression within the limited cyclic loading stroke, which has never been obtained in prior studies. S6 is appealing in various applications because of its stable bi-directional behavior.

Upon tension, F_y, k_i, α, and β are approximately estimated as 134.6 N, 6.52 N/mm, 0.42, and 0.35, respectively, but they are 110.4 N, 7.89 N/mm, 0.06, and 0.45 upon compression. The asymmetrical tension–compression behavior of the closed-end springs is notable. In fact, similar behavior is observed in a pre-compressed SMA spring (Speicher et al. 2009). This behavior may be due to the varying pitch angle. During the cyclic loading test, the pitch angle is decreased upon compression, but is increased upon tension. Figure 3.13 illustrates a schematic view of this behavior. The variations in pitch angle generate a noticeable effect on spring behavior, particularly when subjected to large deformation (Shigley 1989). Ordinary elastic springs are either designed for compression or tension application. However, the current tension-compression springs can sustain bi-directional forces. The unique bi-directional behavior is a superiority of SMA springs over ordinary springs, but their asymmetric performance should be given due attention.

Figure 3.14 shows equivalent damping ratio and residual displacement as a function of loading displacement amplitude. The equivalent damping ratio is calculated for both compression and tension behavior. At the 40 mm loading cycle, ζ_{eq} is approximately 1.2% and 2.3% upon tension and compression, respectively. The total ζ_{eq} is up to 3.5%, which is relatively larger than that of plain-end springs because closed-end springs also dissipate energy upon compression. The residual displacement is unnoticeable within the available loading range because the martensite phase transformation is incomplete.

3.3.4 Quench Method Effect

The heated spring specimens can be cooled down either through water or air quench. Various cooling methods may lead to different mechanical behavior. For example, Savi (2015) determined that air quench produces SME for SMA springs. To clarify the effect of quenching, this subsection analyzes the effect of different quench methods on the cyclic properties of SMA springs. S6 and S7 with the same configurations are cooled down in water and air, respectively.

Figure 3.15 presents the cyclic behavior of identical SMA springs that have undergone different quench procedures. The findings show that air and water quench both produce excellent superelastic capability for SMA spring, which exhibits nearly overlapping cyclic loops to the specimen quenched in water. Therefore, water and quench methods do not significantly influence the mechanical behavior of SMA springs, but the former is more efficient than the latter.

3.3.5 Loading Frequency Effect

The loading frequency effect on the superelastic behavior of SMA-based dampers is an important issue that should be addressed in seismic applications. Nonetheless, this topic is yet to be discussed thoroughly. Thus, cyclic tests are conducted on SMA springs at three loading frequencies (i.e., 0.025, 0.5, and 1.0 Hz). The first frequency represents a quasi-static test, and the latter two represent dynamic frequencies within the frequency range of common interest in seismic applications.

Figure 3.16 compares the force–displacement cyclic loops of S6 at different loading frequencies, in which only the compressive behavior is considered. The force–displacement cycles nearly overlap with the quasi-static test results in both small and large displacement loops. A minimal increase of strength is observed under the dynamic loading frequencies. Compared with the loading frequency effect study on SMA wires in Chapter 2, the SMA springs in this part are significantly less sensitive to loading frequency variations.

3.3.6 Pre-loading Effect

Figure 3.14 depicts that energy dissipation increases with loading displacement amplitude. Considering this finding, a cyclic test is performed on a pre-loaded specimen. Pre-loading is considered an effective means to enhance damping for SC devices (Zhang and Zhu 2007a). To be consistent with the previous test, S6 is selected. Before the formal test, the specimen is pre-compressed to −25 mm. At this pre-compressed level, the external force produces a relatively high amount of martensite transformation in the wire. The considered cyclic loading range is from ±2 mm to ±10 mm at an increment of 2 mm, relative to the pre-compression level. Pre-compression can activate the phase transformation at a relatively low displacement level and can avoid completing this transformation at the upper limit of loading range.

Figure 3.17(a) shows the cyclic behavior of the pre-compressed spring and Figure 3.17(b) plots the equivalent damping ratio as a function of loading displacement. Given that the hysteresis is asymmetric, strain energy is calculated with the following equation:

$$E_s = \frac{1}{2}\left(E_s^+ + E_s^-\right) \tag{3.1}$$

where E_s^+ and E_s^- are the strain energy corresponding to the maximum and minimum loading displacement, respectively.

Figure 3.17(b) shows that the equivalent damping ratio increases with loading amplitude, and it can reach up to 15% at the maximum loading amplitude. Therefore, the damping capacity of SMA springs can be significantly improved by properly using pre-loading. In an actual SMA-spring damper, pre-loading (either pre-tension or pre-compression) can be easily achieved by connecting two pre-loaded springs in a series. One application example was made by Dolce et al. (2000).

3.3.7 Geometric Effect

This section aims to investigate the effect of geometric parameters on the cyclic behavior of SMA springs. The considered geometric parameters include the spring index and the number of active coils.

3.3.7.1 Spring Index

Spring index, *C*, refers to the ratio of spring diameter to wire diameter. S1 and S3 have identical parameters, except for their *C* that is 8 and 16, respectively. Figure 3.18 plots the cyclic loading loops for the selected specimens. This figure particularly indicates that a large spring diameter leads to a low "yielding" force, large "yielding" displacement, and small stiffness. Increasing the spring diameter directly increases the shear stress in SMA wire, thereby facilitating the martensite phase transformation. Accordingly, "yielding" occurs at a lower force level for S3 than S1. The large "yielding" displacement for S3 can be explained by the force–displacement relationship, which was derived by Liang and Rogers (1997). This relationship is expressed as:

$$y_e = \frac{8NC^3}{Gd}F \tag{3.2}$$

where y_e is the "yielding" displacement, and G is the shear modulus of SMA wire. Eq.(3.2) clearly indicates that increasing C will produce a large "yielding" displacement.

3.3.7.2 Number of Active Coils

Apart from spring index, the number of active coils, N, is also an important index affecting the mechanical behavior of springs. A comparison is made between springs with different N. To this end, S1 (N = 6.0) and S2 (N = 2.0) are also compared as shown in Figure 3.19. As observed, an increase in N leads to a large "yielding" displacement, but it does not affect the "yielding" force (Shigley 1989). The "yielding" property can also be explained by Eq. (3.2). The small "yielding" displacement of S2 implies that the martensite phase transformation is completed sooner, compared with S1.

3.3.8 Wire Types Effect

The effect of wire types on the cyclic properties of SMA springs is evaluated by comparing S4 and S5. S4 is made of 4 mm-diameter solid wire, whereas S5 is made of hollow tubes whose outer and inner diameters are equal to 4 and 2 mm, respectively. Figure 3.20 presents the comparison of the hysteretic behavior of these specimens. The stiffness and "yielding" force of a hollow spring are a fraction of a solid spring according to elastic spring theory (Shigley 1989), although the difference in current test is not visibly detected.

The phase transformation shows noticeable variations between different specimens. For the solid spring, the 80-mm loading cycle produces an equivalent damping ratio ζ_{eq} = 1.67%, and the "post-yield" stiffness ratio is α = 0.4. These properties are 20% lower and 33% higher than those of hollow springs. Further comparisons show that the hollow spring has a higher damping than the solid spring. From the viewpoint of seismic applications, hollow springs may be preferred because of their comparable strength, higher damping ratio, and significantly smaller material amount than those of solid springs. This observation is consistent with the conclusion presented by Schmidt and

Lammering (2004). The testing results indicate that the cyclic behavior of SMA springs can be adjusted by changing the wall thickness of SMA tubes to meet the desired behavior.

3.4 Discussions on Two Types of SMA-based Dampers

The majority of the existing SMA-based dampers are made of SMA wires, and numerous researchers have developed various wire-based damping devices. Several representative configurations of these devices were proposed by Dolce et al. (2000), Zhang and Zhu (2007), and Padgett et al. (2010). Previous studies have shown the advantages of using SMA wires (e.g., excellent machinability, reliable axial behavior, and can be fully utilized). This study also determines that SMA-wire dampers can offer large strength capacity and are convenient to be scaled to the desired performance.

The advantages of adopting SMA-spring dampers are also noted. These dampers can be used as a stand-alone damping device, and they have extraordinary deformation capacity by transforming axial stress into shear stress. The cyclic properties of SMA-spring dampers depend on a large number of parameters. Accordingly, designers are provided with the flexibility to select suitable spring configurations to meet the practical requirements. However, compared with SMA-wire dampers, the currently made SMA-spring dampers have significantly lower strength capacity.

3.5 Summary

This chapter investigates two types of SMA-based dampers (i.e., SMA-wire and SMA-spring dampers) through a series of cyclic loading tests. Both of these dampers are made of SMA wires, bars, or tubes. The fabrication process and loading test results of these dampers are presented and discussed.

The SMA-spring dampers show a stable and repeatable FS hysteresis. In particular, this study fabricates and analyzes a tension-compression bi-directional SMA spring, which has never been explored in previous research. Parametric studies are conducted based on the tests of various SMA-spring dampers. The main observations in the comparative analysis are summarized as follows:

1) Air quench and water quench both produce excellent FS hysteresis for SMA-spring dampers, and the corresponding difference in cyclic properties is negligible;
2) Different loading frequencies insignificantly affect the behavior of SMA-spring dampers;
3) Spring index significantly affects SMA springs. A large spring index reduces the "yielding" force and increases the "yielding" displacement, but the number of active coils only affects the spring stiffness;
4) Pre-loading can enhance the energy dissipation of SMA-spring dampers;
5) SMA springs made of hollow tubes produce lower strength but larger damping than those made of solid wires.

SMA-spring dampers can be used as a stand-alone device or can be installed in another damper configuration. In practice, SMA-spring dampers can be flexibly designed by adjusting their parameters. In addition, by properly combining the preloaded and un-preloaded springs, the desired SC behavior with enhanced energy dissipation can be obtained. The research of SMA-spring dampers in seismic engineering is still in its infancy. As such, further research should look into the seismic applications of SMA-spring dampers.

The tensile behavior of SMA wires in SMA-wire dampers plays the key role in providing SC force and damping capacity. The reliable and stable cyclic properties of these dampers are obtained with negligible strength degradation or residual deformation. In this study, SMA-wire dampers are further extended to SMADBs given their desired strength capacity and good scalability. The braces are installed in a reduced scale braced frame and are tested under real earthquake ground motions in Chapter 6.

Table 3.1 Cyclic properties of SMA-wire dampers

Mechanical properties	SMA-wire damper 1	SMA-wire damper 2
Yield strength (kN)	11.89	8.95
Initial stiffness (kN/m)	2530	1630

Table 3.2 Parameters of SMA-spring dampers

End type	Specimen No.	Parameters					
		D_{outer} (mm)	d (mm)	C	N	Δ (mm)	L (mm)
Plain-end	1	16	2	8	6	8	62
	2	16	2	8	2	18	42
	3	32	2	16	6	8	62
	4	40	4	10	2	20	52
	5[a]	40	4	10	2	20	52
Closed-end	6	40	4	10	1	40	52
	7[b]	40	4	10	1	40	52

a: circular hollow section, thickness is 1 mm;
b: air quench;

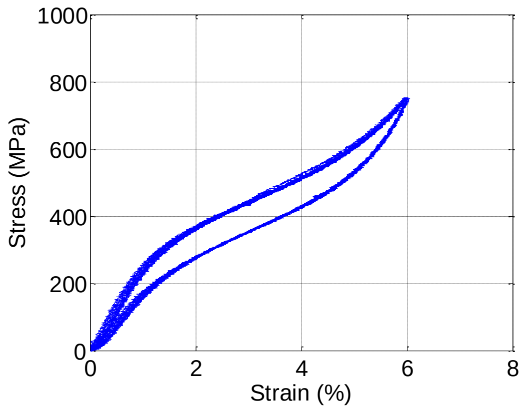

Figure 3.1 Stress-strain relationship of superelastic Ni-Ti wire (loading frequency = 2.0 Hz, 10 consecutive cycles)

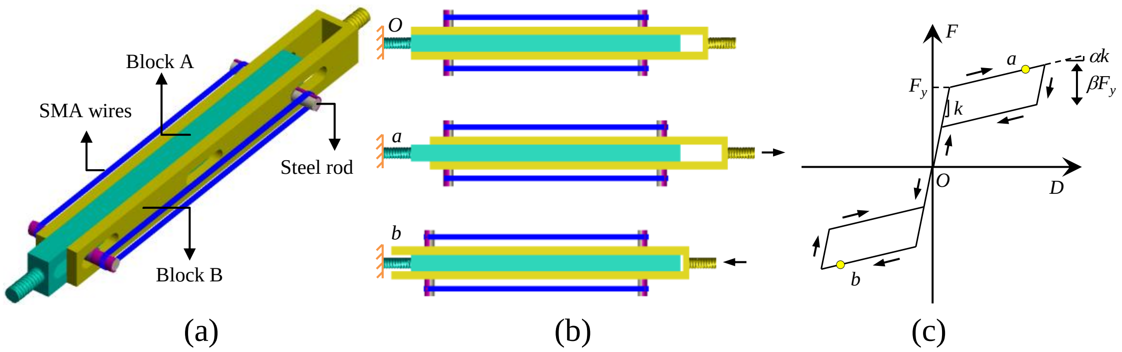

Figure 3.2 SMA-wire damper: (a) configuration of SMA-wire damper, (b) deformation under tension and compression, and (c) idealized FS hysteresis

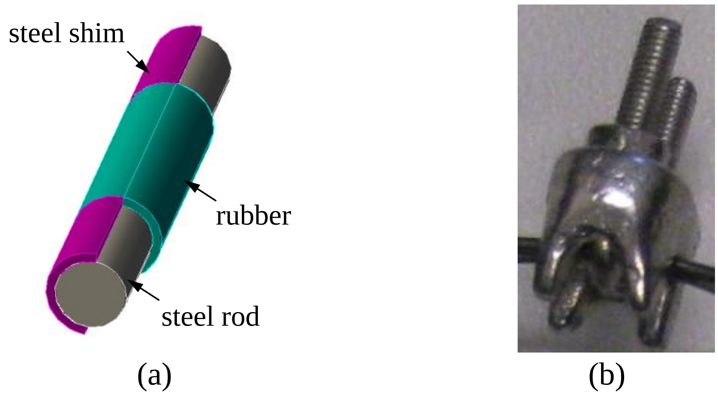

Figure 3.3 Some configuration details of the SMA-wire dampers: (a) moving steel rod and (b) U-connector

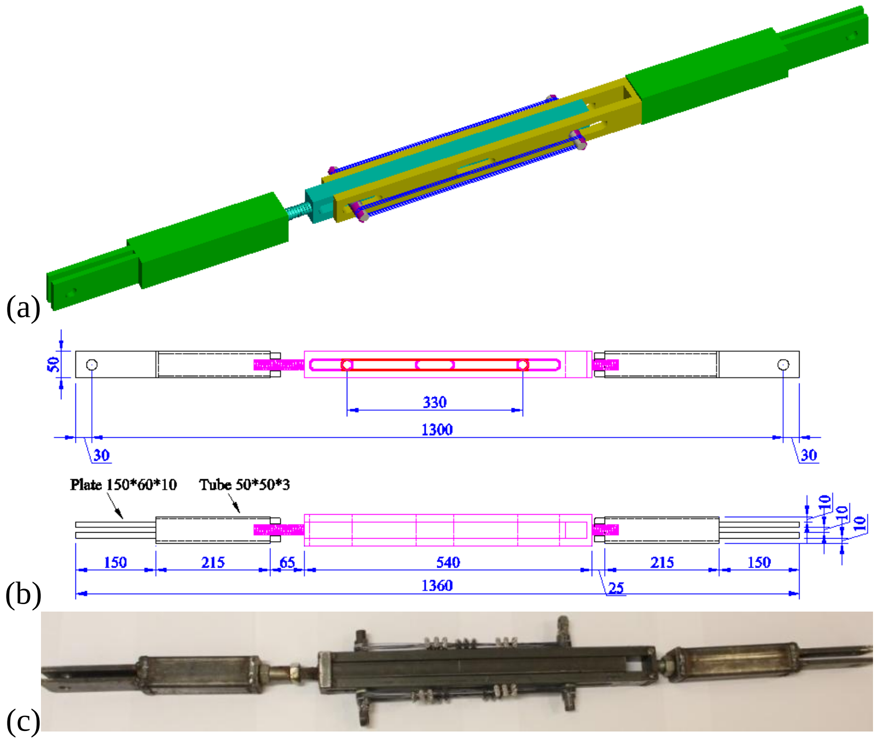

Figure 3.4 SMADB: (a) schematic view, (b) dimensions (unit: mm), and (c) photo of the tested brace

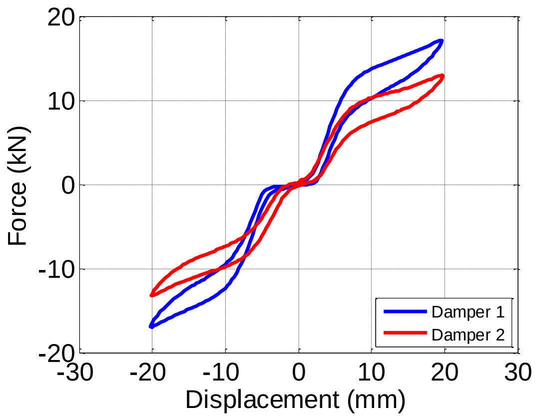

Figure 3.5 Cyclic behavior of SMA-wire dampers at a loading frequency of 2.0 Hz

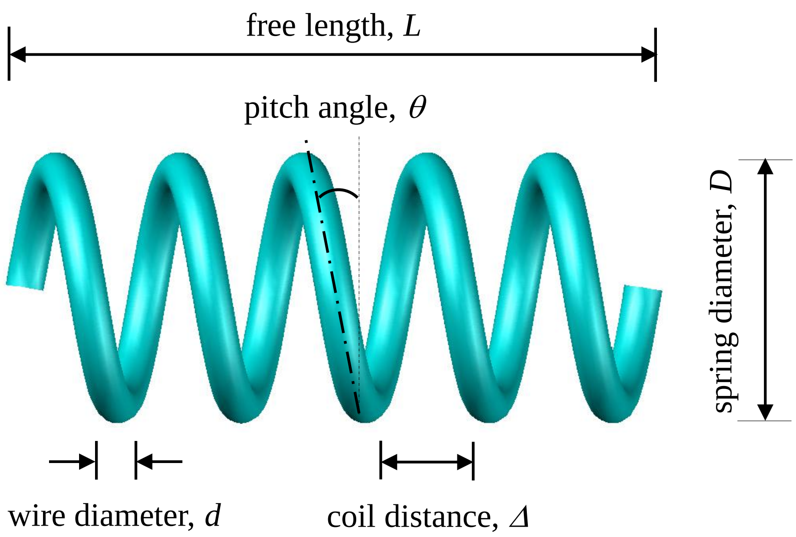

Figure 3.6 Geometric dimensions of a typical spring

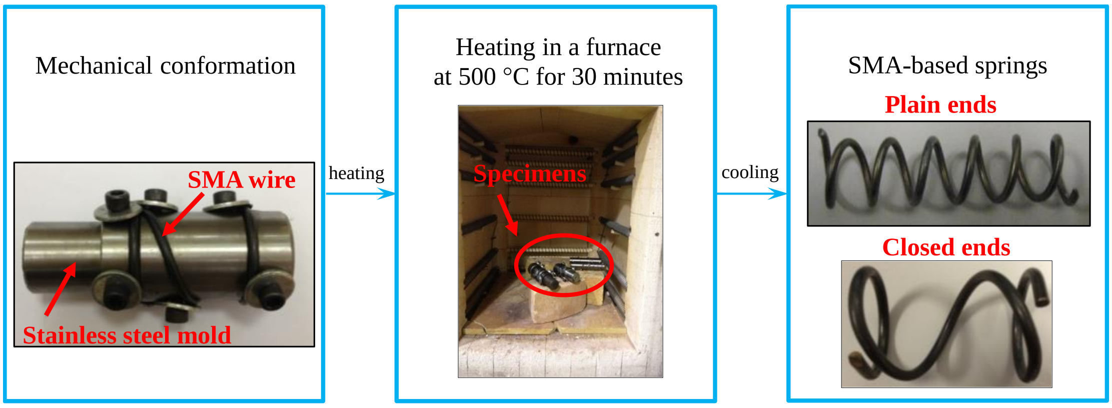

Figure 3.7 Procedures of making SMA-spring dampers


Figure 3.8 Experimental setup and tested specimen

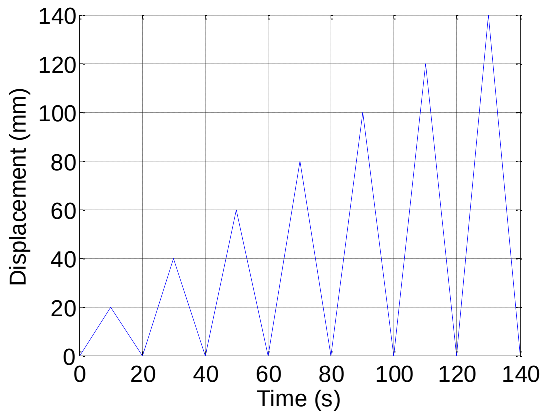

Figure 3.9 A representative cyclic loading protocol (loading frequency = 0.025 Hz)

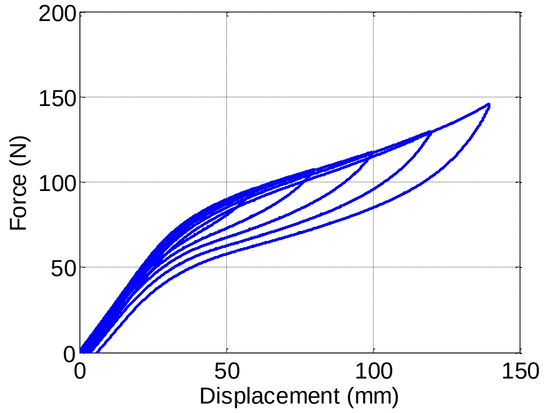

Figure 3.10 Cyclic behavior of plain-end spring (S1)

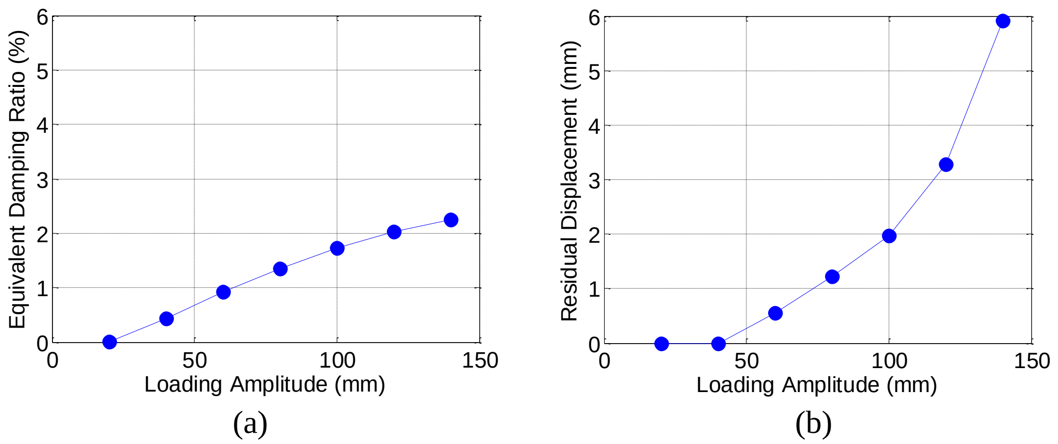

Figure 3.11 Loading amplitude effect on (a) equivalent damping ratio and (b) residual displacement (S1)

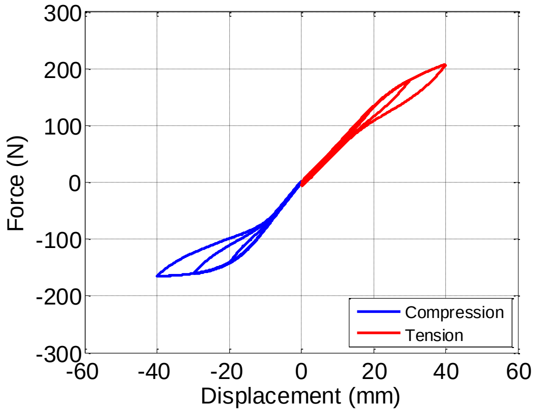

Figure 3.12 Tension-compression behavior of closed-end spring (S6)

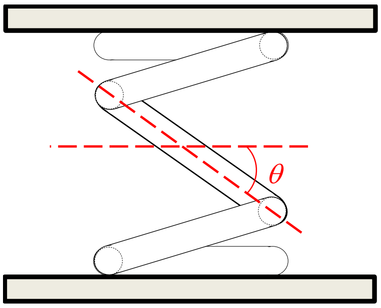

Figure 3.13 Geometric nonlinear of the closed-end springs (S6)

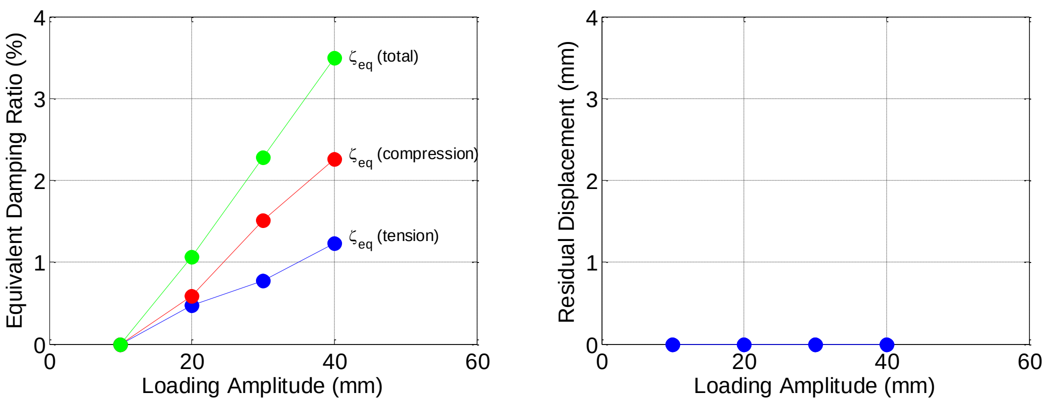

(a) (b)

Figure 3.14 Loading amplitude effect on (a) equivalent damping ratio and (b) residual displacement (S6)

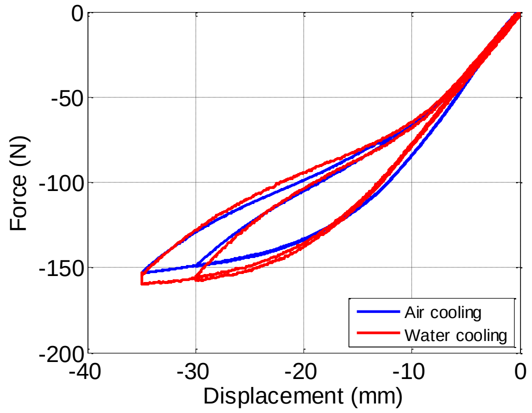

Figure 3.15 Cyclic behavior by different cooling method, S6 (water quench) vs. S7 (air quench)

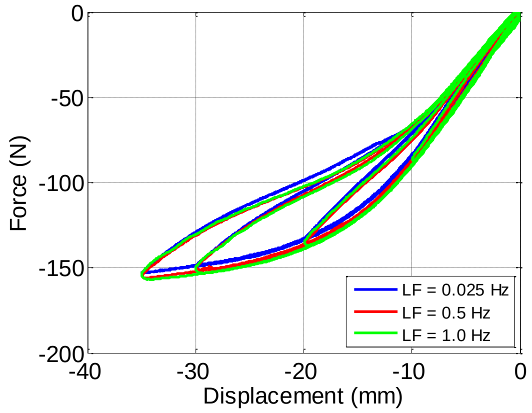

Figure 3.16 Cyclic behavior at different loading frequencies (S6)

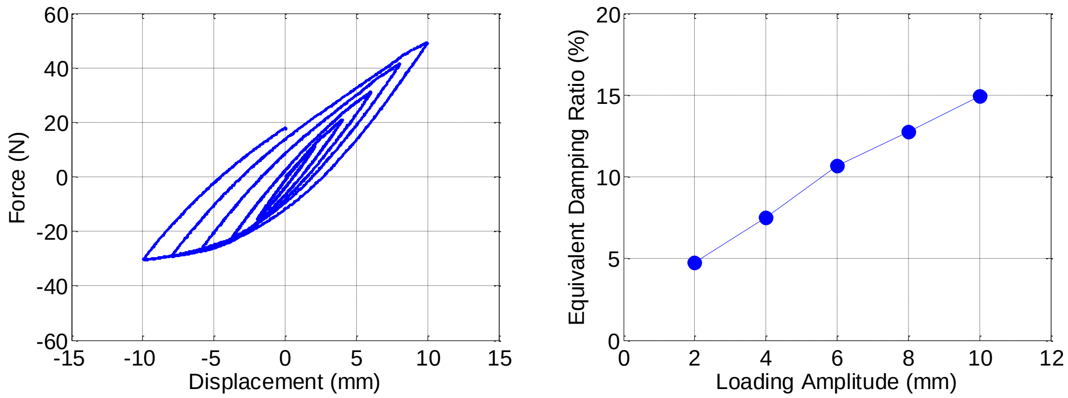

(a) (b)

Figure 3.17 Effect of pretension on (a) cyclic behavior and (b) equivalent damping ratio (S6)

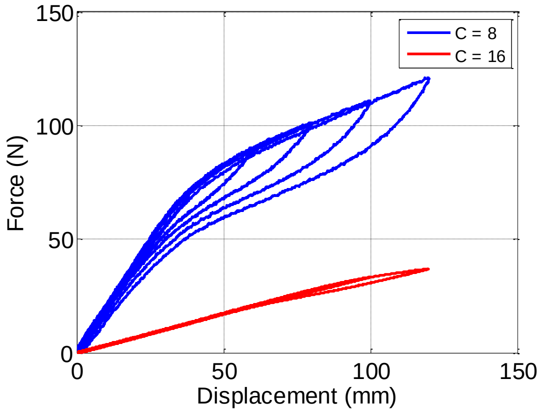

Figure 3.18 Effect of spring index on cyclic behavior, S1 (C = 8) vs. S3 (C = 16)

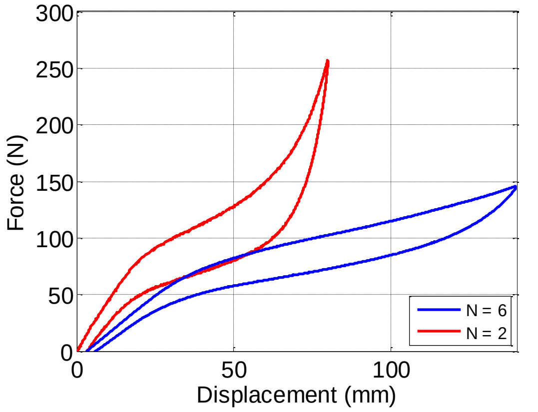

Figure 3.19 Effect of number of active coils on cyclic behavior, S1 (N = 6) vs. S2 (N = 2)

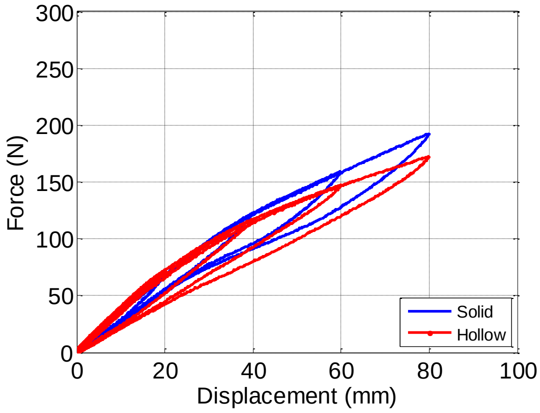

Figure 3.20 Effect of wire types on cyclic behavior, S4 (solid) vs. S5 (hollow)

Chapter 4 Highway Bridges with SMA-based Isolators

4.1 Introduction

This chapter presents numerical modeling and investigation of high-performance highway bridges with superelastic SMA-based SC isolators under different seismic intensities. The SMA-based isolators and highway bridges are designed according to an *ad hoc* DDBD approach. The superior seismic performance of prototype four-span RC highway bridges is successfully validated through a series of IDA. Parenthetically, the current design approach is essentially based on the nonlinear response spectra of SDOF systems. Later, a PBSD approach that applicable to MDOF systems, such as a multi-story braced frame, will be developed in Chapter 7, after a numerical study on multi-story SMADBFs in Chapter 5.

4.2 Constitutive Model for Superelastic SMA

The key component in the SC isolators is made of Ni-Ti wires. An accurate constitutive model is necessary in numerical simulations to simulate the stress-strain relationship of superelastic SMA materials. Zhang and Zhu (2007a) presented a modified version of a constitutive model previously proposed by Wilde et al. (2000). The modified Wilde model for superelastic SMA wires is more stable in numerical simulation and reduces the computation effort, which can be expressed as follows:

$$\dot{\sigma} = \begin{cases} E \cdot \left[\dot{\varepsilon} - \dot{\varepsilon} \cdot \left(\dfrac{\sigma - \beta}{Y} \right)^n \right] \cdot u_1(\varepsilon) + E_m \cdot \dot{\varepsilon} \cdot u_2(\varepsilon) + \left(E_y \dfrac{\varepsilon_m - \varepsilon}{\varepsilon_m - \varepsilon_1} + E_m \dfrac{\varepsilon - \varepsilon_1}{\varepsilon_m - \varepsilon_1} \right) \cdot \dot{\varepsilon} \cdot u_3(\varepsilon) & \dot{\varepsilon} > 0 \\ E \cdot \left[\dot{\varepsilon} + \dot{\varepsilon} \cdot H(\varepsilon_{in}) \cdot \mathrm{sgn}(\sigma - \beta) \left(\dfrac{|\sigma - \beta|}{Y} \right)^n \right] & \dot{\varepsilon} < 0 \end{cases}$$

(4.1a)

$$\beta = \begin{cases} \alpha \cdot E \cdot \varepsilon_{in} & \dot{\varepsilon} > 0 \\ \alpha \cdot E \cdot [\varepsilon_{in} + f_T \cdot g(a \cdot \varepsilon_{in} + b)] & \dot{\varepsilon} < 0 \end{cases} \tag{4.1b}$$

$$g(x) = 1 - e^{-x^2} \tag{4.1c}$$

$$u_1(\varepsilon) = 1 - u_2(\varepsilon) - u_3(\varepsilon) \tag{4.1d}$$

$$u_2(\varepsilon)=\begin{cases}1 & \text{if } \dot{\varepsilon}>0 \text{ and } \varepsilon \geq \varepsilon_m \\ 0 & \text{otherwise}\end{cases} \tag{4.1e}$$

$$u_3(\varepsilon)=\begin{cases}1 & \text{if } \dot{\varepsilon}>0 \text{ and } \varepsilon_1 < \varepsilon < \varepsilon_m \\ 0 & \text{otherwise}\end{cases} \tag{4.1f}$$

where sgn(·) and $H(\cdot)$ are the signum and Heaviside functions, respectively; σ refers to one-dimensional tensile stress that is set to be zero if $\varepsilon \leq 0$, as the SMA cables are assumed to be tension-only materials; $\dot{\varepsilon}>0$ and $\dot{\varepsilon}<0$ represent the loading and unloading processes, respectively; ε is the one-dimensional strain; $\varepsilon_{in}=\varepsilon-\sigma/E$ is the inelastic strain. The key parameters characterizing the stress-strain relationship include the initial modulus of elasticity E, the "post-yield" stiffness ratio $\alpha=E_y/(E-E_y)$, where E_y is the "post-yield" stiffness, the martensitic modulus of elasticity E_m, the loading "yield" stress Y, a one-dimensional backstress β, the unloading path control parameters f_T, a, and b, constant n controlling the transition sharpness during loading and unloading histories, and the strain ε_m, where the austenite to martensite transition completed. α, E, and n may take different values for the loading and unloading paths if different stiffness or sharpness of transition is required. Readers may refer to Zhang and Zhu (2007) for a more detailed derivation and explanation of this constitutive model.

Figure 4.1 shows the comparison between the stress-strain curves of Ni-Ti wires predicted by the modified Wilde model and those obtained from a cyclic test at a loading frequency of 2 Hz. Given the properly tuned model parameters, good agreement can be achieved between the model prediction and the experimental data. Although the modified Wilde model was originally proposed for superelastic SMA, this model can also be used to describe the FS hysteresis of other SC devices. In this chapter, the model is calibrated to Ni-Ti wires, which are the most commonly used SMA materials. Compared with EP behavior, SC behavior involves less energy dissipation but shows zero residual deformation after completely unloading.

4.3 Highway Bridge with SMA-based Isolators

Figure 4.2 shows the elevation of a highway bridge, in which the bridge deck and pier are isolated by SMA isolators. Each isolator consists of an elastomeric bearing and SMA cables, in which the former mainly provides vertical support to the deck, and the latter provides lateral stiffness. They constitute an isolation system with SC and energy dissipation capability.

In this study, a prototype highway bridge with SMA-based isolators is designed using a DDBD approach. The DDBD approach has been developed and recognized as a more rational design method than the conventionally adopted force-based method (Priestley, 1997; Kowalsky, 2002). Liu *et al*. (2011) proposed an *ad hoc* DDBD procedure for highway bridges with SMA isolators. Using this method, a highway bridge, including the cross-sectional area and length of SMA cables and the cross section of RC piers, can be designed based on the target pier displacement, isolator displacement, and isolator ductility. The DDBD approach utilizes nonlinear response spectra to predict dynamic response under design basis earthquake (DBE) levels, where the nonlinear response spectra were obtained from an equivalent SDOF system with a FS SC hysteresis in consideration of different hysteretic parameters. It is worth noting the limitation of this *ad hoc* DDBD approach, that is, it only takes into account one single modal contribution in the structural dynamic response.

Figure 4.2(b) expresses a typical segment of a highway bridge as a Generalized Maxwell model, where m_d and m_p are the masses of deck and pier, respectively; u_d and u_p are the relative displacements of deck and pier, respectively; k_p and c_p are the lateral stiffness and damping coefficients of pier, respectively; k_{SMA} represents the nonlinear stiffness of SMA isolators. Bridge piers typically have a relatively smaller mass than bridge deck; thus, the two-DOF system can be further simplified into an SDOF model, as shown in Figure 4.2(c). The equivalent stiffness k_{eq} and the post-yield stiffness ratio α_{eq} of the equivalent SDOF can be computed as follows:

$$k_{eq} = \frac{k_s k_p}{k_s + k_p} \tag{4.2a}$$

$$\alpha_{eq} = \frac{\alpha k_s k_p}{(\alpha k_s + k_p)k_{eq}} = \frac{\alpha(1 + k_s / k_p)}{(\alpha k_s / k_p + 1)} \tag{4.2b}$$

where k_s and α are the elastic stiffness and the post-yield stiffness ratio of SMA isolators. Based on the equivalent SDOF model, the DDBD approach developed by Liu et al. (2011) is based on the following assumptions: (1) the dynamic performance of isolated bridge is dominated by the first mode; (2) piers can be well protected by SMA isolators, so that the seismic behavior of piers is nearly linear; (3) the mass of pier m_p is relatively small compared with that of deck m_d and can be ignored.

A four-span prototype highway bridge with SMA isolators is designed using the DDBD approach [as shown in Figure 4.2(a)]. The bridge is supposed to be located in Los Angeles, with the corresponding design spectra shown in Figure 4.3. Under the DBE level, the bridge deck is expected to behave almost elastically. The fundamental period of the bridge is T_0=1.2 s, which corresponds to a spectral acceleration of S_a=0.60 g. The target displacement of the highway bridge is determined as follows: the peak displacement of pier is u_p^m=2.5 cm, and the peak displacement of deck is u_d^m=25 cm. Using the above-described design procedure, the properties of SMAs can be calculated, where the total cross-sectional area is A=8.3 cm^2, and the length is l=2.83 m. The cross-section of piers is 1.8 m×1.1 m, and a total of 18 steel bars with 25 mm diameter are arranged along the width on each side. The strength of the bridge pier is deliberately designed above the “yield” load of SMA isolator. The primary parameters of the designed bridge differ from those reported by Liu et al. (2011).

The numerical model of the RC highway bridge is built through the nonlinear computation program DRAIN2DX (Prakash et al. 1993). The bridge superstructure consists of a box girder supported on RC piers. The concrete box girder is assumed to be very stiff and is modeled as a rigid body with seismic mass. Fiber beam-column element (Element Type 15 in DRAIN2DX) is used to build the RC sections of piers, and this element can properly model the cracking and crushing of concrete and yielding of steel tendons in the RC piers. The layout and number of fibers are shown in Figure 4.4. In particular, a new element type was developed in DRAIN2DX to simulate the hysteresis of SMA-based isolator using the aforementioned modified Wilde model. The parameter values of the modified Wilde model for the SC SMAs are given as follows: E=39000 N/mm^2, Y=390 MPa, α=0.036, f_T=0.434, a=200, and n=3 for loading and 0.5 for unloading. P-Δ effect is considered in the seismic analysis. Rayleigh damping is applied to the model, where the damping ratio of the fundamental mode is equal to 5%. A small time step of 0.0005 s is used during the time history analysis when the structures are subjected to the ground motion records.

4.4 Ground Motions

Somerville et al. (1997) developed a suite of ground motions containing a total of 20 earthquake records. These records are designated as LA01–LA20 and are generated for Los Angeles with a 10% probability of exceedance in 50 years. These records were derived from historical records with earthquake moment magnitudes ranging from 6.0 to 7.3 and a hypocentral distance ranging from 1.2 km to 36 km. In particular, the 20 earthquake records were modified from soil type S_B–S_C to soil type S_D. Figure 4.3 exhibits the 5%-damped elastic response spectra of the 20 considered ground motions. The median response spectrum of these motions satisfactorily matches the DBE spectrum. The response spectra of the 20 records are also scaled to frequently occurring earthquake (FOE) levels and maximum considered earthquake (MCE) levels. This suite of ground motions is used throughout the rest of the thesis as well.

4.5 IDA

In previous studies on SC structures, their seismic performance was often assessed under a few seismic ground motions corresponding to a specific seismic intensity level. For example, Liu et al. (2011) examined the designed bridge under DBEs only. Owing to the large dispersion in the structural responses induced by record-to-record variability, more comprehensive and unbiased studies are needed. Moreover, the strain hardening behavior of SMA isolator at large deformation is unconsidered in the DDBD approach, which may cause the damage of bridge piers under major earthquakes. Therefore, more accurate and comprehensive assessment of the seismic performance of highway bridges with novel SMA isolators under varying seismic intensity levels is necessary in PBEE. IDA of the prototype highway bridge with SMA isolators is performed in this study to determine the seismic demand on bridge components based on a series of scaled seismic records.

The ground motions are scaled to different magnitudes in IDA. The 5%-damped elastic spectral acceleration $S_a\,(T_1, 5\%)$ corresponding to the first mode is selected as a seismic intensity measure (IM). The main seismic responses, including the peak displacements of the bridge pier, deck, and isolator and the residual displacement of the pier, are estimated through the nonlinear dynamic analyses of the prototype highway bridge under varying seismic intensities. The geometric mean value that tends to give a smooth result is used to evaluate the probabilistic characterization of the analysis results

$$\hat{x} = \left[\prod_{i=1}^{n} x_i\right]^{1/n} = \exp\left[\frac{1}{n}\sum_{i=1}^{n} Ln\left(x_i\right)\right] \tag{4.3}$$

where x_i and n represent the single result in each case and the total number of the considered cases, respectively.

4.6 Analysis Results

Figure 4.5 shows a collection of IDA curves under the aforementioned 20 ground motions, including the peak displacements of the deck and the SMA isolator, and the peak and residual displacements at the pier top. The upper limit of the elastic spectral acceleration of the scaled ground motions is $S_a(T_1)$=1.0 g, which covers *IM*s corresponding to FOE, DBE, and MCE levels (as shown in Figure 4.5). The 20 solid-grey curves show IDA results under individual earthquake records, while the dashed-blue curves represent the 16th, 50th, and 84th percentiles, where the 50th percentile is approximated by the geometric mean.

Figure 4.5(a) shows the results of the peak deck displacement that is the sum of the peak isolator displacement in Figure 4.5(b) and the peak pier displacement in Figure 4.5(c). The record-to-record variability can be clearly observed when the bridge response enters into a nonlinear stage and becomes greater with increasing seismic IMs. Figure 4.5(b) shows the relative displacement of the SMA isolator. In addition to IMs corresponding to FOE, DBE, and MCE, Figure 4.5(b) shows the isolator displacement corresponding to the start and finish points of phase transformation as defined in Figure 4.1. Without inducing any damage and permanent deformation in the isolator, the stress-induced phase transformation from austenite to martensite leads to a yield-like plateau in the force-displacement relationship of the SMA isolator. This plateau can effectively protect the bridge pier against severe damage if the pier capacity is properly designed to be above the “yield” load of the isolator. Thus, the transformation start point essentially stands for the start of the nonlinear seismic behavior of the isolator. After the transformation finish point, the superelastic SMA cables exhibit strain hardening, in which the isolator force increases rapidly with further deformation (as shown in Figure 4.1) and may cause damage in the bridge piers. The maximum recoverable deformation refers to a strain of 8% in the SMA cables. Beyond the maximum recoverable deformation, the SMA cables experience permanent plastic deformation and partially lose its SC capability. As a result, the SMA isolators will exhibit residual deformation after earthquakes. The exceedance probability of experiencing plastic deformation for the SMA isolators increases as the ground motion intensifies. Under FOE, the SMA cables keep superelastic in all cases, whereas 40% and 70% of them would experience plastic deformation under DBE and MCE, respectively.

Figure 4.5(c) shows the peak displacement at the top of the bridge pier. The median peak displacements at the pier top are 1.0 cm, 2.2 cm, and 5.3 cm under FOE, DBE, and MCE, respectively. The displacements corresponding to the cracking of concrete and the yield of steel tendons are also plotted. Although the RC pier cracks at the pier base under small seismic intensities, the superelasticity of the SMA isolators prevent the bridge pier from the yielding of steel tendons under FOE and DBE. Under MCE, the SMA cables are prone to exhibit strain hardening behavior, which may increase the lateral forces acting on the bridge piers. In this situation, steel tendons may be yielded, and permanent deformation can be found after earthquakes. In other words, the substantial damage of the RC piers would occur only under extreme earthquakes corresponding to the MCE levels. The current highway bridge is designed based on the DBE spectrum, so that the seismic performance in the cases of MCE would hardly satisfy the design target. It should be noted that the occurrence of substantial structural damage is often allowable under MCE, as long as bridge collapse can be prevented. However, if very limited damage is desirable even under the MCE levels, a more conservative design of the SMA isolators can be performed by simply replacing the seismic design spectrum in the DDBD approach with the MCE spectrum. Consequently, the damage severity under MCE can be considerably reduced. Such a more conservative design requires the use of more SMA material and much greater yield strength of piers, and is not advisable in real applications considering cost-effectiveness.

Figure 4.5(d) shows the residual displacement of the bridge piers. The RC piers exhibit ignorable residual displacement under FOE and DBE, which implies that the bridge piers have nearly linearly elastic behavior. With the increase of seismic intensity, the residual displacement accumulates gradually because of the significant plastic deformation during earthquakes. The median and 84th percentile of the residual displacement at the pier top under MCE are 0.57 cm and 16 cm, respectively. The residual displacement of the SMA isolators is minimal because of the SC capability, given that its peak deformation is less than the recoverable strain limit. The limited damage and residual displacement in the bridge system would considerably reduce the repair cost and downtime after earthquakes, which is favorable especially in seismic prone areas.

In the DDBD procedure, the highway bridge with SMA isolators is simplified as an equivalent SDOF model, in which the behavior of pier is assumed as nearly linear (as shown in Figure 4.2). However, the piers are modeled as nonlinear members in the numerical analyses, as shown in Figure 4.4; therefore, this elasticity assumption is valid only if the damage in the bridge pier is limited. As reflected in Figure 4.5(c–d), the median value of the peak displacement of the pier at the DBE level lies in the design target, and the residual displacement is nearly zero. However, the residual displacement shown in Figure 4.5(d) implies the occurrence of plastic behavior of the bridge piers under strong earthquakes. Thus, the efficacy of the adopted SDOF model is necessary to examine. Figure 4.6 shows the comparison between the equivalent SDOF model and the full-scale bridge model in terms of the median IDA results for the displacements of the deck, pier, and isolator under the 20 ground motions. The SDOF model can satisfactorily predict the seismic behavior of the highway bridge until the design basis hazard level with S_a=0.6 g. The median displacements of the deck, isolator, and pier under the DBE level, which are respectively 22.67 cm, 20.75 cm, and 1.92 cm, are close to the target displacements specified in the DDBD, that is, 22.74 cm, 20.52 cm, and 2.22 cm, respectively. However, the deviation between the two models becomes apparent under high seismic intensity levels when the steel tendons are yielded and the behavior of the piers becomes nonlinear. IDA results generally indicate that the DDBD approach predicts fairly well the target displacement over the entire range of ground motion intensities.

Figure 4.7 shows the base shear-displacement hysteresis for the piers and decks, as well as the corresponding displacement time histories, under the seismic record LA01 with different scaling factors, that is, 0.4, 0.8, and 1.6. These three ground motions can approximately represent FOE, DBE, and MCE levels, respectively. The difference between the deck and pier displacements is equal to the displacement of the SMA isolators. Under FE level, the piers and SMA isolators behave linearly; consequently, the post-earthquake residual displacement is nearly zero. Under the DBE level, the SMA isolators exhibit the superelastic behavior and thus its hysteresis becomes flag-shaped. Given that the capacity of the bridge pier is appropriately designed above that of the isolators, the displacement will mainly concentrate in the isolators after the "yielding" of the SMA cables. Thus, the bridge piers can be protected effectively by the SMA isolator, and its behavior is almost linearly elastic. The residual displacement of the isolators is zero owing to the SC capacity. For the piers and decks, their residual displacements are also zero in this particular example. In some other cases at the DBE level, minor cracks may occur at the bottom of the piers. Under the MCE level of ground motions, the SMA experiences strain hardening after the stress-induced phase transformation. The rapidly increased isolator force causes the yielding of steel tendons, and the SMA isolators and RC piers show nonlinear hysteresis. As a result, the bridge piers experience a certain residual displacement because of the plastic deformation under significant earthquakes. In all cases, the SMA isolators experience almost zero residual displacement after earthquakes. Compared with conventional highway bridges isolated with LRB, the residual displacement of the studied highway bridges is reduced effectively given the superior SC feature of the novel SMA isolators.

4.7 Summary

This chapter investigated a high-performance seismic-resisting highway bridge structure with a novel type of SC isolators employing superelastic SMA. A four-span RC highway bridge with the SMA isolators designed according to a DDBD approach was selected as the prototype model. The bridge FEM was established through the computer program DRAIN2DX. The seismic performance of the highway bridge with the SMA isolators was evaluated through IDA under varying seismic intensities. IDA results indicate that the designed highway bridge can well achieve the target displacement specified in the DDBD approach under the DBE levels. Furthermore, the SC SMA isolators can effectively protect the superstructure of the highway bridge by reducing the damage in the piers and limiting the total residual displacement of the highway bridge, especially under FE and DBE levels. Such high seismic performance will significantly reduce the post-earthquake repair cost and downtime, which makes the proposed SC highway bridge systems very appealing in seismic prone zones.

This chapter uses Ni-Ti SMA wires in the superelastic SC isolators for highway bridges. Considering they are possible to lose superelasticity in cold temperature, the monocrystalline Cu-Al-Be could be a sound replacement of Ni-Ti as aforementioned in

Chapter 2. In such a case, the design and analysis method can still be applied, and similar conclusions will be obtained.

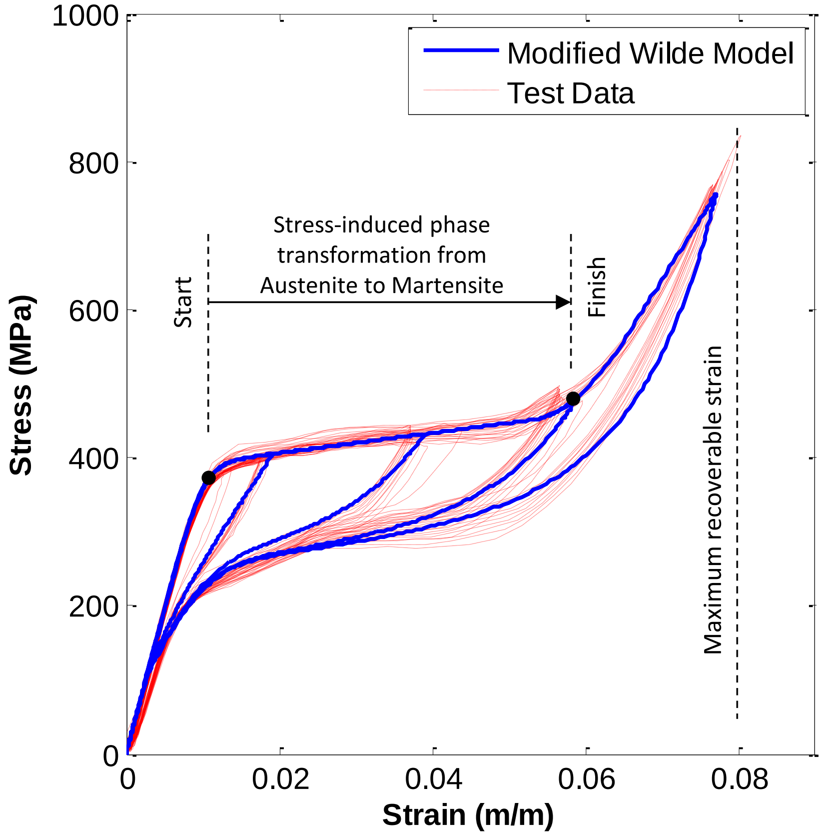

Figure 4.1 Constitutive model of SMAs

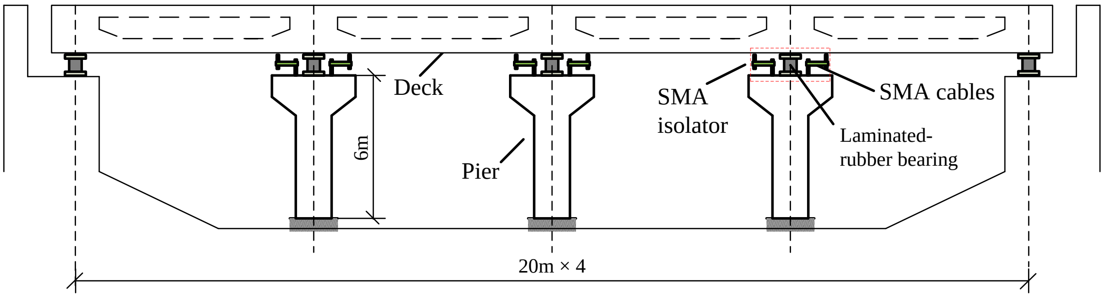

(a) Schematic of a four-span bridge with SMA isolators

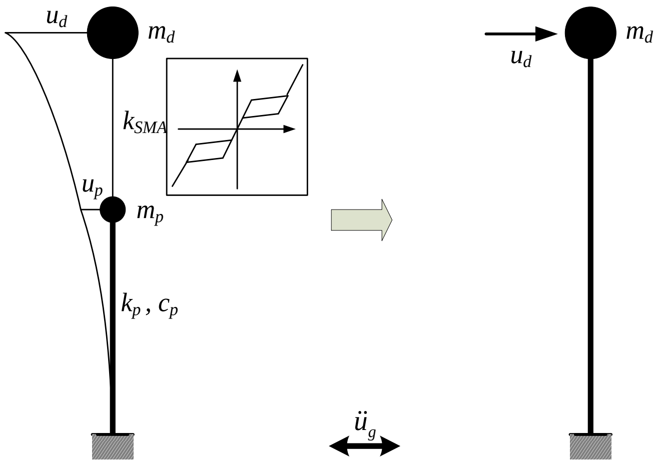

(b) Generalized Maxwell model (c) Equivalent SDOF system

Figure 4.2 Simplified model of a highway bridge with SMA isolators

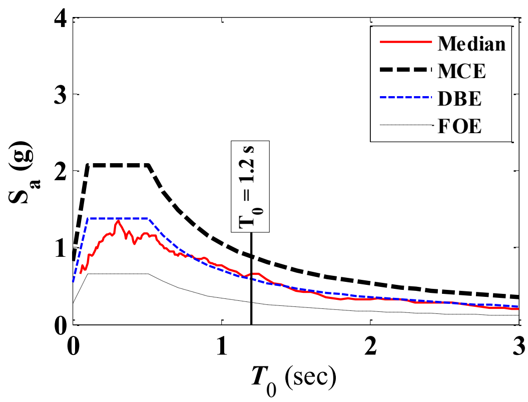

Figure 4.3 The median response spectrum of ground motion set and seismic design spectra at three hazard levels

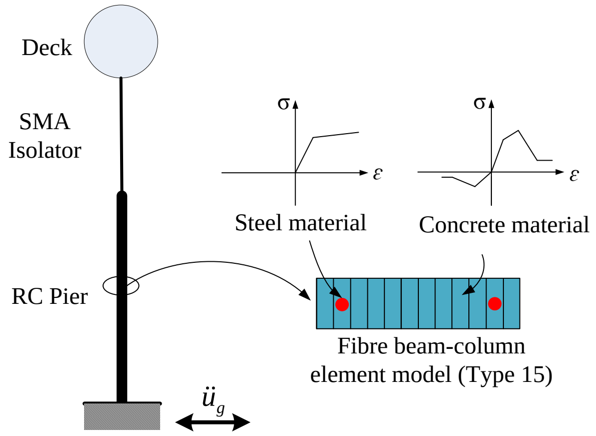

Figure 4.4 Illustration of numerical model in DRAIN2DX

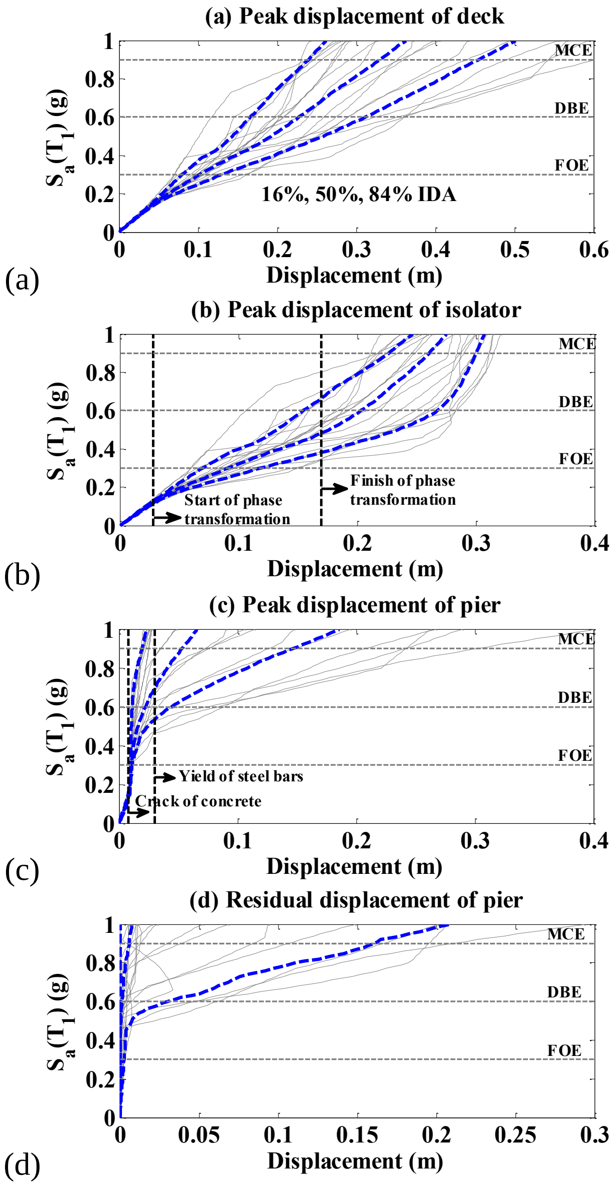

Figure 4.5 Displacement demand of the highway bridge with SMA isolators

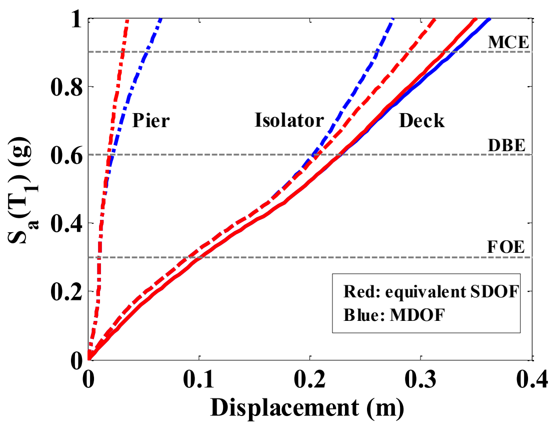

Figure 4.6 Comparison of seismic IDA curves between the equivalent SDOF system and the full-scale model of the highway bridge with SMA isolators

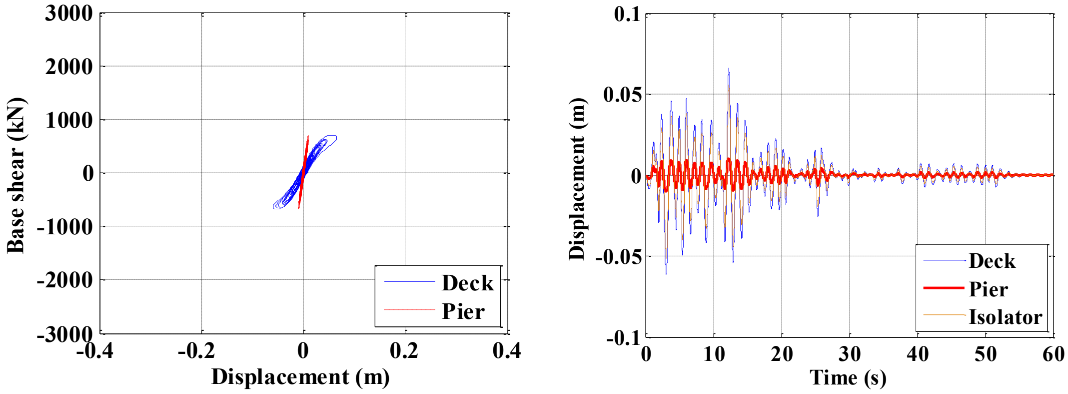

(a) LA01 × 0.4

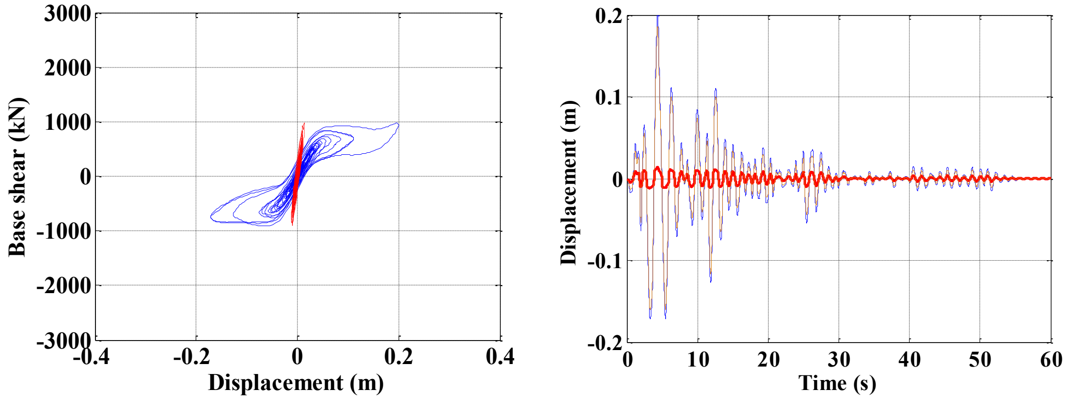

(b) LA01 × 0.8

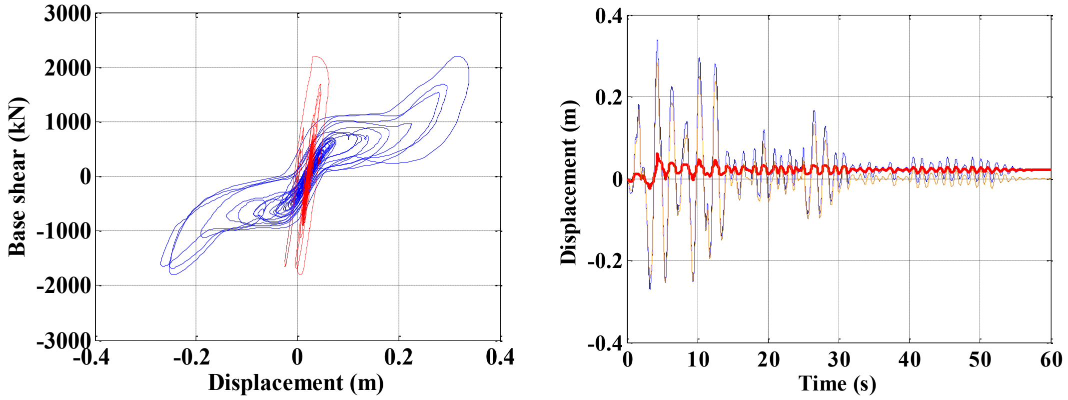

(c) LA01 × 1.6

Figure 4.7 Seismic hysteresis and displacement response under seismic record LA01 with different scaling factors

Chapter 5 Steel Braced Frame with SMADB: Numerical Study

5.1 Introduction

This chapter numerically investigates SMADBF, which is regarded as one type of SC MDOF systems. To achieve a better understanding, the seismic performance of SMADBF is systematically compared with BRBF that has been regarded as a high-performance seismic-resisting braced frame and extensively studied during the past two decades. This chapter conducts SDOF, pushover, and IDA on multi-story steel braced frames with SMADBs or BRBs. The comparison results indicate that SMADBFs are subject to higher deformation demand under strong earthquakes when SMADBFs and BRBFs are designed with the same parameters. This deficiency of SMADBF is mainly caused by reduced energy dissipation and additional high-mode contribution, the latter of which tends to induce the significant concentration of inter-story drift ratios in the top stories of buildings. The effects of increasing energy dissipation or the post-yield stiffness of SMADBs are specifically investigated through a parametric study of six-story frames, as inspired by the SDOF analysis conducted by Christopoulos et al. (2002a). The results indicate that increasing either post-yield stiffness or energy dissipation can effectively reduce the seismic deformation demand on SMADBFs by compensating the aforementioned deficiency. In particular, increasing the post-yield stiffness of SMADBFs can facilitate a seismic performance that is comparable to that of BRBFs in terms of peak deformation control. Meanwhile, all SMADBFs maintain significantly smaller post-earthquake permanent deformations than BRBFs do. Although the current study is focused on the seismic performance of SMADBFs, its conclusions may also shed light on other types of seismic-resisting SC structural systems.

5.2 Constitutive Models of SMADB

This study uses the FS constitutive model to simulate the cyclic behavior of SMADB, as shown in Figure 5.1(a). The different combinations of post-yield stiffness ratio, α, and energy dissipation capacity, β, shown in Table 1 are considered for SMADBs; these combinations are denoted as SMADBF-I, SMADBF-II, and SMADBF-III. SMADBF-I represents a baseline case, and SMADBF-II and SMADBF-III denote the cases with enhanced α and β levels, respectively. The upper bound of β is equalized to 1.0 in order to maintain the SC capability of SMADB. Moreover, significantly high post-yield stiffness may overload connections and the adjacent structural members; thus, the upper bound of α is set at 0.20.

The seismic performance of SMADBs is assessed through a systematic comparison with that of BRBs, which is a promising seismic-resisting bracing element that has been extensively studied in the past two decades. The hysteresis of BRB is described by the bilinear EP model depicted in Figure 5.1(b). The post-yield stiffness ratio of BRB is set to 0.01. BRB and SMADB-I display identical post-yield stiffness ratios. In this comparison, SMADBs are assumed to have the same yield strength and initial stiffness as BRBs do. The comparison aims to reveal the mechanism that results in the difference between these two types of braces.

5.3 Multi-Story Steel Frame

The six-story BRBF designed by Sabelli et al. (2003) according to NEHRP (1997) is adopted in the numerical study with the use of the same parameters of BRBs and frame members. The steel frame, denoted as 6vb2, has a chevron-braced configuration. The bay width is 9.0 m, and the story height is 5.5 m for the first story and 4 m for the other stories. The frame is designed for location in downtown Los Angeles. Additional structural details are provided by Sabelli et al. (2003). Figure 5.2 presents building information, including the beam and column sections, yield strength, and the initial stiffness of the braces at each story. Nonetheless, all of the beam-to-column connections in the original design are modified to hinge connections in the current study because such connections eliminate connection moment and can accommodate heavy rotation demand without damage (Fahnestock et al. 2007). This modification lengthens the fundamental period of the frame slightly.

The SMADBFs in the current chapter are generated by replacing the BRBs in the 6vb2 model with various types of SMADBs. The yield strength F_y and the initial stiffness k_o are equal for the two types of braces in the frame systems. As a result, various frames possess the same elastic dynamic characteristics, including vibration periods and modal shapes. The fundamental period of these steel braced frames is approximately 0.82 s.

All of the steel braced frames are modeled using the computer software OpenSees (2013), as displayed in Figure 5.2. Beams and columns are modeled by force-based beam-column elements. Previous studies (Neuenhofer and Filippou 1997; Scott et al. 2004) have demonstrated the advantages of force-based beam-column elements over displacement-based ones. Columns are continuous and fixed at their bases. The beam-to-column connections in the braced bay are modeled as hinged connections. ASTM A992 steel is assumed for the beam and column elements. A post-yield stiffness ratio of α = 0.003 is considered. It is assumed that the strength and stiffness of steel does not deteriorate due to local buckling or low cycle fatigue.

Each brace is modeled as one element, the cross-sections of which are an assembly of uniaxial fibers at each integration point. Only one braced bay is modelled, and it is subjected to vertical gravity loads and in-plane horizontal seismic ground motions. The torsional response of the structure about a vertical axis is not considered.

The tributary floor mass is idealized as one leaning column (as shown in Figure 5.2). The leaning column is assumed to have the same displacement as the braced bay at each floor level. This column has a large cross-section; however, the leaning columns in the two adjacent stories are connected by a hinge. Consequently, the leaning column does not contribute lateral stiffness or strength to the entire structure. The effective seismic mass for the one-bay braced frame is 1/6 of the total floor mass. This mass is carried by the leaning column. Thus, this column accounts for the P-Δ effect without contributing any strength or stiffness to the braced bay.

The fundamental period of the steel braced frames (i.e., T_1 = 0.82 s) is highlighted in Figure 5.3. Its corresponding spectral accelerations can then be read. The seismic behavior of the steel braced frames concerned is evaluated through IDA. The geometric mean value is used to evaluate the statistical characteristics of the analysis results.

5.4 Pushover Analysis of Multi-story Frames

A pushover analysis is conducted to determine the seismic deformation demand that corresponds to the different modes of SMADBF-I and BRBF. Figure 5.4 shows the results of pushover analyses when the frames are subjected to lateral force with the first-mode pattern. It should be noted that SMADBF-I and BRBF display identical pushover curves because of the aforementioned parameter setting. Figure 5.4(a) presents the normalized base shear demand as a function of roof drift ratio. The yielding points of braces in the different stories are highlighted. The delayed yield point indicates the over-strengthening of the first-story braces in the design. Figure 5.4(b) depicts the relationship between the normalized base shear and the individual story deformations. It illustrates that the first story is stiffer than the upper stories. The story drift ratios in the upper stories are quite uniform in the elastic range. They deviate in the inelastic range but remain similar. Figure 5.5 displays the results of the second-mode pushover analysis. The braces in the different stories yield at significantly different moments; specifically, the sixth-story brace yields considerably earlier than the other stories do. Consequently, the heightwise distribution of the story drift ratios is considerably non-uniform. This occurrence implies that the great contribution of the second mode to the seismic response may enhance the concentration of story deformation in one or two top stories.

Cyclic pushover analyses with lateral force patterns that correspond to the first two modes are also conducted for SMADBF-I and BRBF. Figure 5.6(a) exhibits the base shear vs. roof drift ratio curves for the first-mode cyclic pushover analysis. In the elastic range, the SMADBF-I and BRBF can be regarded as two identical frames; in the inelastic range, the two frames differ significantly in terms of energy dissipation and permanent deformation. The value of the strength factor, which is defined as the ratio of the yielding base shear to the total building weight, is approximately 0.24. The value of the energy dissipation factor β of SMADBF-I is approximately 0.5 and remains similar to that of the braces. The post-yield stiffness ratio is approximately 0.012, which is slightly higher than that of the braces (α = 0.01). This increase is mainly ascribed to the contribution of the fixed column bases. A similar trend is also observed in the pushover analyses of SMADBF-II and SMADBF-III. Figure 5.6(b) shows the results of second-mode cyclic pushover analysis. The inelastic story deformation also concentrates in the upper stories, and the yielding base shear is significantly lower than that in the first-mode results.

5.5 IDA of SDOF Systems

The IDA of SDOF systems that represent SMADBFs and BRBFs is conducted and compared in this section. The hysteresis relationships of the equivalent SDOF systems are determined from the aforementioned first-mode cyclic pushover curves, as depicted in Figure 5.6; the equivalent mass is determined based on the target elastic periods. EP and FS SDOF structures with different strength reduction factors were also compared by Christopoulos et al. (2002a). Nonetheless, the IDA results in the current chapter can demonstrate the variation of performance among various systems with increasing seismic intensity levels more effectively than the previous study did. Figure 5.8 compares the IDA results of the SDOF systems that correspond to BRBF, SMADBF-I, SMADBF-II, and SMADBF-III. Four different natural periods of SDOF systems, namely, 0.2, 0.5, 0.8, and 2.0 s, are considered in this comparison. In the IDA analysis, the ground motions are scaled according to the elastic spectral acceleration $S_a(T_1,5\%)$. This scaling essentially changes the strength reduction factor R for each SDOF system. Thus, the corresponding R value is indicated in each vertical axis as well. The strength reduction faction R is defined as:

$$R = \frac{S_a \times W}{V_y} \tag{5.1}$$

where W is the total building mass; V_y is the yield strength of the equivalent hysteresis; and S_a is the spectral acceleration of the scaled ground motion at the fundamental period of the frames. The definition of R is also depicted in Figure 5.7. The curves plotted in Figure 5.8 are the geometric means of the 20 IDA curves. SMADBF-I and BRB exhibit the identical seismic deformation demand in a linearly elastic range during small earthquakes. Once the seismic behavior enters the inelastic range, the difference between SMADBF-I and BRB is noticeable. SMADBF-I always displays heavier seismic deformation demand than BRBF does. This discrepancy become apparent with increasing seismic intensity levels, because SMADBF-I dissipates significantly less energy than BRBF does although they have the same post-yield stiffness ratio (as shown in Figure 5.6).

Either an increase in post-yield stiffness ratio α (in SMADBF-II) or energy dissipation factor β (in SMADBF-III) can considerably reduce seismic deformation demand and effectively improve the seismic performance of SMADBF to render it comparable to that of BRBF. Increasing α seems more effective in controlling the peak displacement demand for the short initial periods T = 0.2, 0.5, and 0.8 s. Compared with BRBF, SMADBF-I exhibits better performance than BRBF in Figure 5.8(a), and a similar performance level in Figure 5.8(b) and (c). The efficacy of the enhanced α or β tends to decrease with increasing periods. When the initial period is 2.0 s, a high β becomes more effective than a high α; nonetheless, neither can reduce the deformation demand of SMADBF to a level comparable to that of BRBF.

On the basis of the relationship between the MDOF system and the associated equivalent SDOF system, the displacement of the equivalent SDOF system can be used to predict the peak roof displacement of the multi-story frames if we assume that the seismic response is dominated by the fundamental mode. Subsequently, the inter-story drift ratios of the multi-story frame can be estimated on the basis of peak roof displacement and the corresponding pushover analysis results.

The aforementioned conclusion is consistent with the observations made by Christopoulos et al. (2002a). However, an SDOF system considers only a single vibration mode (typically the fundamental mode). It cannot fully identify the complex nonlinear dynamics of an MDOF system with a high potential contribution from high modes excited by ground motions. Therefore, the responses of the MDOF systems remain unclear given that the seismic mechanism of the MDOF system is complicated and that the performance of high modes can be excited by ground motions. Thus, the seismic performance levels of six-story steel braced frames are compared in the following section.

5.6 IDA of Multi-Story Frames

The seismic responses of the aforementioned six-story steel braced frames are simulated under varying seismic intensities through nonlinear time history analysis. Figure 5.9(a) shows a collection of the IDA curves of the peak roof drift ratio $\theta_{\mathrm{peak}}^{\mathrm{roof}}$ under the considered ground motions for SMADBF-I. The peak roof drift ratio is defined as the peak roof displacement during the entire response time history normalized by building height. The 20 solid-grey curves show the IDA results under individual seismic records, whereas the colored curves represent the 16th, 50th, and 84th percentiles. The 50th percentile is approximated by the geometric mean. Figure 5.9(b) shows the IDA curves of the maximum inter-story drift ratio θ_{max} for SMADBF-I. θ_{max} value is considerably greater than that of roof drift ratio $\theta_{\mathrm{peak}}^{\mathrm{roof}}$ because of the non-uniform distribution of the inter-story drift ratios along the building height.

Figure 5.10 compares the geometric means of the IDA curves for SMADBF-I and BRBF in terms of peak roof drift ratio $\theta_{\mathrm{peak}}^{\mathrm{roof}}$ and θ_{max}. The inter-story drift ratio is equal to the relative displacement between two adjacent floors divided by the corresponding story height. θ_{max} is defined as the maximum value of six peak inter-story drift ratios. θ_{max} occurs randomly in different stories when the structures are subjected to various ground motions. $\theta_{\max}$ is more commonly used than $\theta_{\text{peak}}^{\text{roof}}$ as a global damage measure under earthquakes. The performance levels of SMADBF-I and BRBF are identical in the elastic range when subjected to small earthquakes. However, SMADBF-I exhibits significantly heavier deformation demand than BRBF does in the inelastic range. The discrepancy increases with the increase in seismic intensity level S_a. This discrepancy is more significant in the maximum inter-story drift ratio. For instance, the $\theta_{\text{peak}}^{\text{roof}}$ of SMADBF-I is 28% higher than that of BRBF at the DBE level (i.e., S_a = 0.87g), whereas the $\theta_{\max}$ of SMADBF-I is approximately 35% higher. A likely explanation is that $\theta_{\max}$ is more affected by the high-mode response than $\theta_{\text{peak}}^{\text{roof}}$ is.

The predictions based on the aforementioned SDOF system and in consideration of the fundamental vibration mode are shown in Figure 5.10. As indicated in Figure 5.10(a) specifically, SDOF systems predict the peak roof drift ratios effectively for both SMADBF-I and BRBF, thus implying that roof displacement, as a global seismic response, is mainly dominated by the first vibration mode. In Figure 5.10(b), good agreement is found between the BRBF and the corresponding SDOF, whereas evident difference can be observed between SMADBF-I and the SDOF system. This result implies that high-mode contribution affects the maximum inter-story drift ratio of SMADBF-I more significantly than that of BRBF, although this contribution is not evident in the peak roof drift ratio. The high-mode participation leads to much higher deformation demand in SMADBF-I than that in BRBF in the event of severe earthquakes.

Figure 5.11 illustrates the relationship between the θ_{roof} and the $\theta_{\max}$ of SMADBF-I and BRBF. The results of the first-mode pushover analysis and of the dynamic simulations at the FE and DBE levels are represented by the solid line and the dots, respectively. θ_{roof} and $\theta_{\max}$ are equal when the inter-story drift ratios are uniformly distributed along the building height in the elastic range. In the inelastic range, the current frame design makes the inter-story drift ratios non-uniform even under first-mode pushover analysis. This phenomenon is observed in Figure 5.4(b) as well. Nonetheless, the ratio of $\theta_{\max}$ to

θ_{roof} is almost constant in the inelastic range of first-mode pushover analysis. The results of the dynamic simulations of the six-story frames deviate further from the first-mode pushover analysis because of the further amplification of θ_{max} by the high-mode effect. θ_{max} exceeds θ_{roof} more significantly in SMADBF-I than in BRBF.

Figure 5.12 presents the height-wise distribution of the peak inter-story drift ratios extracted from the IDA database at the DBE level (i.e., $S_a = 0.87$ g). Inter-story drift is concentrated in varying stories when subjected to different single ground motions. Nonetheless, the geometric mean curve of the height-wise distribution indicates that the peak inter-story drift ratios θ_{peak} tends to concentrate in top stories more often.

Figure 5.13 compares the height-wise distributions of θ_{peak} in SMADBF-I and BRBF at three different seismic levels (FOE, DBE, and MCE levels). All of the curves represent the geometric means of the 20 individual results. The maximum value of θ_{peak} in Figure 5.13 is not equal to the θ_{max} value presented in Figure 5.10 and Figure 5.11. At the FE level, both SMADBF-I and BRBF are almost elastic. The seismic deformation demands of the two frames are very close, and the inter-story drift ratios are relatively uniform along the building height in both frames. With increasing seismic intensity levels, the seismic behavior of the braced frames becomes inelastic and the uniformity of the height-wise distribution of the inter-story drift ratio decreases. Compared with the BRBF, SMADBF-I exhibits the similar deformation demand in the lower stories, but it displays considerably greater inter-story drift ratios in the upper stories. In general, the discrepancy between the two frames increases with story height. In the top story, the θ_{peak} of BRBF is approximately 1% at the DBE level. The corresponding value for SMADBF-I is approximately 1.6%, which is almost 60% higher than that of BRBF. This discrepancy becomes even more remarkable at the MCE level, in which the θ_{peak} in the top story in SMADBF-I is approximately twice that in BRBF. This finding may be explained by the fact that the response of SMADBF-I is strongly affected by the second-mode contribution that induces the significant concentration of inter-story drift ratios in the top stories, as depicted in Figure 5.5(b).

5.7 High-Mode Effect in Multi-Story Frame

Previous attempts have been made to evaluate the contribution of different vibration modes to the seismic inelastic behavior of the MDOF systems. Two representative examples are the modal pushover analysis (MPA) (Chopra and Geol 2002) and the extended N2 method (Kreslin and Fajfar 2011). On the basis of the assumption that individual vibration modes are weakly coupled in seismic responses, MPA approximates real nonlinear response by synthesizing the contribution of various modes through either square-root-of-sum-of-squares or complete quadratic combination methods. The extended N2 method executes the basic N2 procedure and accounts for high-mode effects by performing an elastic modal analysis. The accuracy of both methods may be limited in the inelastic range when the inelastic behavior modifies the elastic mode shapes or when the inelastic vibration modes are clearly coupled. The observations in the previous section indicate that high-mode contribution is related to inelasticity in the seismic response. Given the significant inelasticity observed in seismic performance, neither method is applied in this study.

To determine the mechanism that induces a more significant concentration of inter-story drift ratios in SMADBF-I than in BRBF, a snapshot of the seismic inertia force on each floor is captured. Figure 5.14 indicates the geometric means of the inertia forces along the building height at two seismic intensity levels. The situation depicted in Figure 5.14(a) occurs when the sixth-story drift ratio θ_6 peaks, and that in Figure 5.14(b) takes place given the peak first-story drift ratio θ_1. Thus, the curves shown in Figure 5.14 do not occur at the same moment. Under small earthquakes (S_a = 0.2 g), SMADBF-I and BRBF are subjected to identical floor inertia forces and are elastic. However, the distribution profiles of the floor inertia forces at the two different moments vary considerably. This result implies that the seismic force profile changes significantly over time during earthquakes and does not follow first-mode force distribution exactly. Consequently, the SDOF model that considers the fundamental mode cannot predict the maximum inter-story drift ratio accurately.

At the DBE level (S_a = 0.87g), inelastic behavior induces a noticeable difference in the seismic force distributions of SMADBF-I and BRBF. The floor inertia forces acting on the roof are 622 and 652 kN in BRBF and SMADBF-I, respectively, at the moment with the peak sixth-story drift ratio. The difference is 30 kN. These forces can be used to estimate the inter-story drift ratio if the slight damping forces are ignored. The beam-to-column connections are hinge connections in this model; thus, the lateral story shear forces are resisted by the two braces and cause the yielding of these braces. The post-yield stiffness of the braces is only 1% of the initial elastic stiffness. Hence, the difference of 30 kN in the story shear forces results in an increased inter-story drift ratio of 0.63% in SMADBF-I at the DBE level (as shown in Figure 5.13). A slight deviation in the seismic force profile may significantly alter the deformation demand in the inelastic range given a small post-yield stiffness ratio α. This fact may enhance the coupling of difference vibration modes in the inelastic range.

The base shear forces are 2368 and 2300 kN in BRBF and SMADBF-I, respectively, at the moment with the peak first-story drift ratio. The difference is approximately 68 kN at the DBE level. In the first story, the beam-to-column connections are hinge connections, but the column bases are fixed. The fixed column bases also contribute to resist the lateral seismic forces. The first-story braces do not yield and behave elastically at these base shear levels. Consequently, the discrepancy of 68 kN in the base shear forces results in a minor difference in the first-story drift ratios of SMADBF-I and BRBF. Thus, a slight change in seismic force distribution may not modify the deformation demand significantly in the elastic range.

Figure 5.15 presents the time histories of the inter-story drift ratios in all six stories under the ground motion LA20×1.2. The peak value of each inter-story drift ratio is indicated in the figure as well. The inter-story drift ratios in the different stories are not synchronized during the vibration, and the peak inter-story drift ratios in the upper stories occur later in the responses of BRBF and SMADBF-I. For example, the values of θ_6 peak at 0.5 and 2.0 s later than those of θ_1 in BRBF and SMADBF-I, respectively. Thus, the assumption that the frames vibrate in the first mode shape is inaccurate in the situation of inelastic behavior.

5.8 Effect of Improving *α* and *β*

The comparison results between SMADBF-I and BRBF with the same post-yield stiffness ratio in the previous section indicate that SMADBF-I is always associated with larger deformation demand in both SDOF and MDOF systems. The increased demand in the SDOF system is caused by the limited energy dissipation of SMADBF-I, whereas that in the multi-story frame is induced by the combination of reduced energy dissipation and more significant high-mode contribution to the seismic response of SMADBF-I. The analysis results of the SDOF systems demonstrate the benefit of an increased α or β in terms of controlling the fundamental-mode seismic response of SMADBF. The effect of enhancing either α or β is evaluated further in the six-story braced frames. The improvement scheme shown in

Table 5.1 is adopted, that is, increasing α from 0.01 to 0.20 or increasing β from 0.5 to 1.0. Figure 5.16 illustrates the cyclic pushover curves of three SMADBFs, namely, SMADBF-I, SMADBF-II, and SMADBF-III.

Figure 5.17 presents the geometric mean of the IDA curves for the peak roof drift ratio $\theta_{\text{peak}}^{\text{roof}}$ and the maximum inter-story drift ratio $\theta_{\max}$ of various six-story frames. Specifically, Figure 5.17(a) suggests that increases in α and β control $\theta_{\text{peak}}^{\text{roof}}$ almost equally effectively, whereas Figure 5.17(b) indicates that an increased post-yield stiffness α can reduce $\theta_{\max}$ more effectively than an increased energy dissipation factor β can. When α increases to 0.20, SMADBF-II can achieve a seismic performance that is comparable to that of BRBF in terms of $\theta_{\text{peak}}^{\text{roof}}$ and $\theta_{\max}$. Although increasing β improves seismic performance as well, the seismic performance of SMADBF-III remains slightly inferior to that of BRBF, because the energy dissipation of SMADBF-III is significantly lower.

Figure 5.18 plots the distribution of the peak inter-story drift ratios θ_{peak} along the building height at the DBE and MCE levels. All of the curves are the geometric means of the 20 earthquake records. The peak inter-story drift ratios are effectively reduced by increasing either α or β, particularly in the upper stories. Compared with the SMADBF-I, the θ_{peak} in the top-story is reduced by 23% and 31% in SMADBF-II and SMADBF-III, respectively, at the DBE level. This finding confirms the effects of mitigating the higher mode behavior. The maximum value of θ_{peak} is 1.22% at the top story of SMADBF-II and is 1.14% at the third story of SMADBF-III. An increased α in SMADBF-II limits deformation at the lower stories better, whereas an increased β in SMADBF-III controls the upper-story deformation more effectively. In general, increasing either α or β leads to more uniform distribution of peak inter-story drift ratios along the building height in SMADBF-II and SMADBF-III. This result implies that they can help mitigate the high-mode effect in the inelastic seismic response. A similar observation can be made regarding the results at the MCE level.

Figure 5.19 shows the geometric means of the IDA curves for the maximum residual inter-story drift ratios θ_{residual} in different six-story frames. θ_{residual} is ignorable in all three SMADBFs even if seismic intensity exceeds the MCE level, and it is not affected by the increase in either α or β. A minimal residual deformation corresponds to a significantly reduced repair cost after earthquakes. Nonetheless, a nontrivial θ_{residual} is obtained for BRBF as long as the frame behaves inelastically at the DBE level. The geometric mean of θ_{residual} reaches 0.5% at the DBE level. This value was regarded as the threshold for demolishing a building (McCormick et al. 2008). Therefore, the large θ_{residual} value of BRBF will be associated with substantial economic loss after an earthquake, whereas SMADBFs can remain safe for immediate occupancy.

To examine the height-wise distribution of peak inter-story drift ratios further, the story-to-story variability of these ratios is evaluated through

$$\sigma_{\text{story}} = \exp[\text{std}(\log(\theta_{i,\text{peak}}))], \quad i=1,2,\ldots 6 \tag{5.2}$$

under each individual ground motion. Figure 5.20 compares the geometric means of σ_{story} in the BRBFs and SMADBFs in IDA. In general, a high σ_{story} is observed in the inelastic range, thus implying less uniformity in the distribution of inter-story drift ratios under strong earthquakes. Increasing either α or β can reduce the concentration of inter-story drift ratios. In particular, increasing α to 0.20 in SMADBF-II can considerably reduce σ_{story}. As a result, the distribution of θ_{peak} in SMADBF-II is more uniform than that in BRBF. The observation is consistent with the illustration in Figure 5.18.

The record-to-record variability in the maximum inter-story drift ratios is evaluated by

$$\sigma_{\text{record}} = \exp[std(\log(\theta_{\text{max,j}}))]\,, \quad j = 1,2,\ldots 20 \tag{5.3}$$

where $\theta_{\text{max,j}}$ is the maximum inter-story drift ratio under an individual ground motion. Similarly, an increased α or β effectively reduces record-to-record variability σ_{record} in SMADBFs, as shown in Figure 5.21. SMADBF-I, SMADBF-II, and SMADBF-III exhibit larger, smaller, and comparable σ_{record} values, respectively, than BRBF does. Thus, increasing α alleviates story-to-story and record-to-record variability more effectively than increasing β does.

5.9 Summary

The seismic performance of SMADBF is numerically studied and compared with that of BRBF in the current study. Special attention is paid to the contribution of high-mode to the inelastic behavior of SMADBF. Three parameterized SMADBFs and one BRBF are compared systematically through SDOF analysis, pushover analysis, and IDA. A suite of 20 ground motions is scaled to varying seismic intensity levels in IDA such that the variation of seismic performance from elastic to inelastic behavior can be observed clearly. All of the frames share similar elastic characteristics and yielding strength but differ in terms of hysteretic properties, such as energy dissipation and post-yield stiffness. One SMADBF with a post-yield stiffness ratio α = 0.01 and energy dissipation capacity β = 0.5 is regarded as a baseline case that has the same elastic and post-yield stiffness as BRBF. The other two improved SMADBFs either have an increased α(=0.20) or β(=1.0). These variables are used to study the effects of different improvement schemes on the control of high-modes effect.

If SMADBF and BRBF share the same elastic properties, yield strength, and post-yield stiffness, then the former always exhibits a heavier deformation demand than the latter does in the inelastic response. The difference in the SDOF analysis is mainly ascribed to the significantly reduced energy dissipation of SMADBF. This difference is amplified further in the IDA of six-story braced frames because of the increasingly evident high-mode contribution in the seismic response of SMADBF. The high-mode contribution is coupled with the fundamental mode in the inelastic seismic response and induces the concentration of inter-story drift ratios in the top stories. As a result, SMADBF is subject to 60% higher maximum inter-story drift ratio than BRBF is at the DBE level.

Nonetheless, this SMADBF deficiency can be effectively overcome by increasing either the energy dissipation factor or the post-yield stiffness ratio. The results of the parametric study indicate that both improvement schemes can successfully mitigate the high-mode effect in the inelastic response of SMADBFs, and result in a relatively uniform distribution of the inter-story drift ratios of SMADBFs without the significant inelastic deformation concentration in the top stories. In particular, when the post-yield stiffness ratio increases to 0.20 in SMADBF, the maximum inter-story drift ratio of SMADBF can be effectively reduced to a level that is comparable to that of BRBF. Furthermore, the IDA analysis results suggest that increasing the post-yield stiffness can reduce the record-to-record variability of the maximum inter-story drift ratio under the 20 ground motions. Increasing the energy dissipation factor can control the roof drift ratio just as well, but it controls the maximum inter-story drift ratio slightly less effectively than increasing post-yield stiffness does. Meanwhile, all SMADBFs exhibit minimal post-earthquake permanent deformation. This SC capability is a main advantage of SMADBFs over BRBFs and conventional steel braced frames.

Table 5.1 Parameters of BRB and SMADBs

Brace Type	Frame Name	Parameters of Braces	
		α	β
BRB	BRBF	0.01	-
SMADB	SMADBF-I	0.01	0.5
	SMADBF-II	0.20	0.5
	SMADBF-III	0.01	1.0

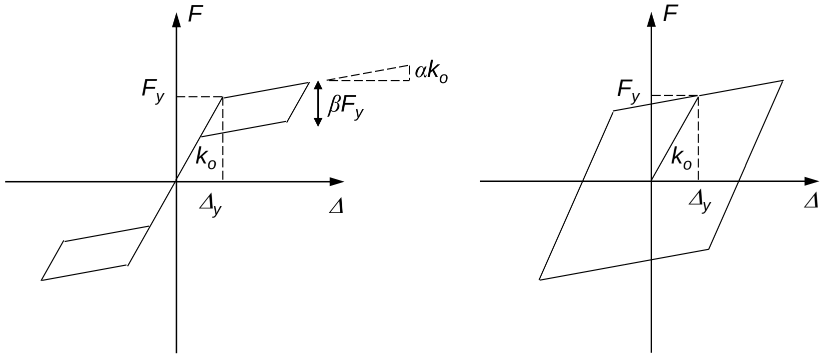

(a) SMADB (b) BRB

Figure 5.1 Simplified constitutive model of SMADBs and BRB

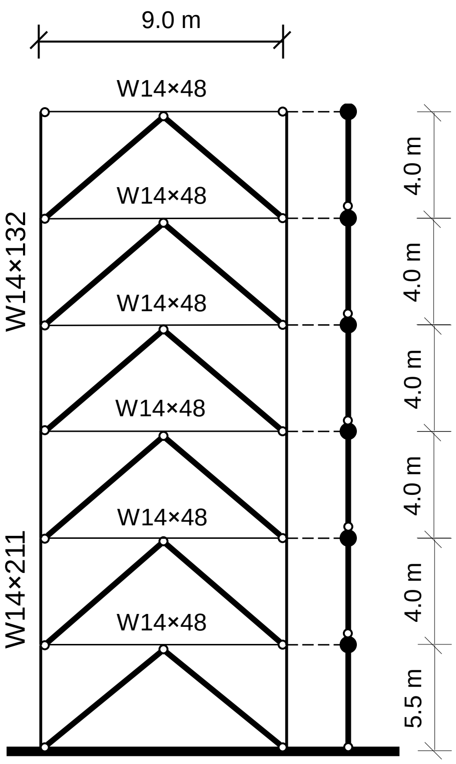

Properties of braces:

Story	Yield Strength (kN)	Initial Stiffness (kN/m)
6	394	0.734E+05
5	711	1.326E+05
4	961	1.793E+05
3	1161	2.165E+05
2	1306	2.435E+05
1	1704	2.878E+05

Figure 5.2 Modeling of the prototype frame in OpenSees

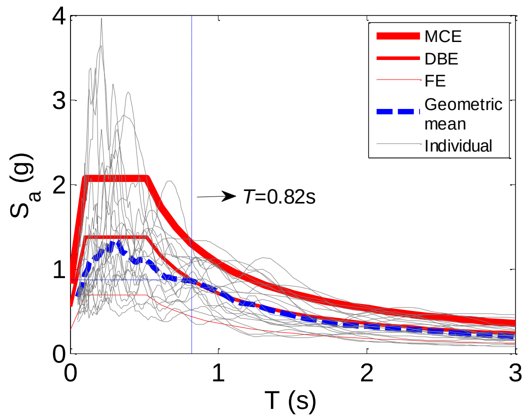

Figure 5.3 Elastic response spectra of the selected ground motion records

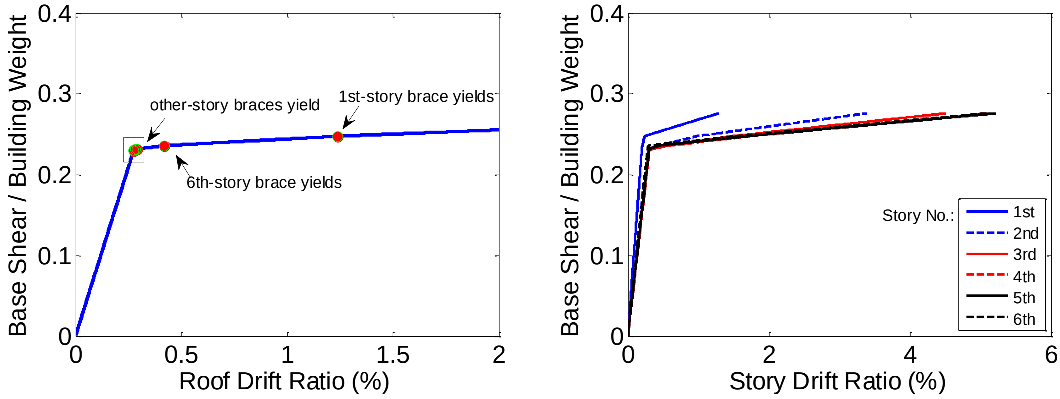

(a) Base shear vs. roof drift ratio (b) Base shear vs. inter-story drift ratio

Figure 5.4 Nonlinear pushover analysis of the frames (SMADBF-I and BRBF) subjected to the first-mode lateral force pattern

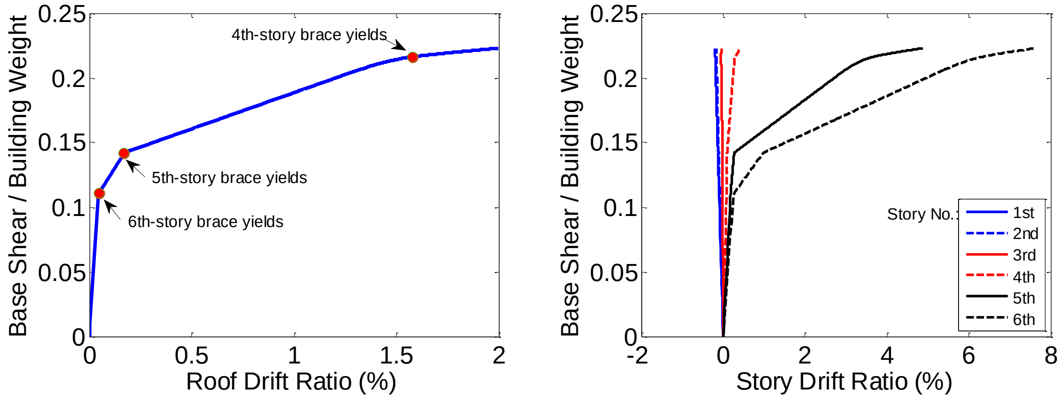

(a) Base shear vs. roof drift ratio (b) Base shear vs. inter-story drift ratio

Figure 5.5 Nonlinear pushover analysis of the frames (SMADBF-I and BRBF) subjected to the second-mode lateral force pattern

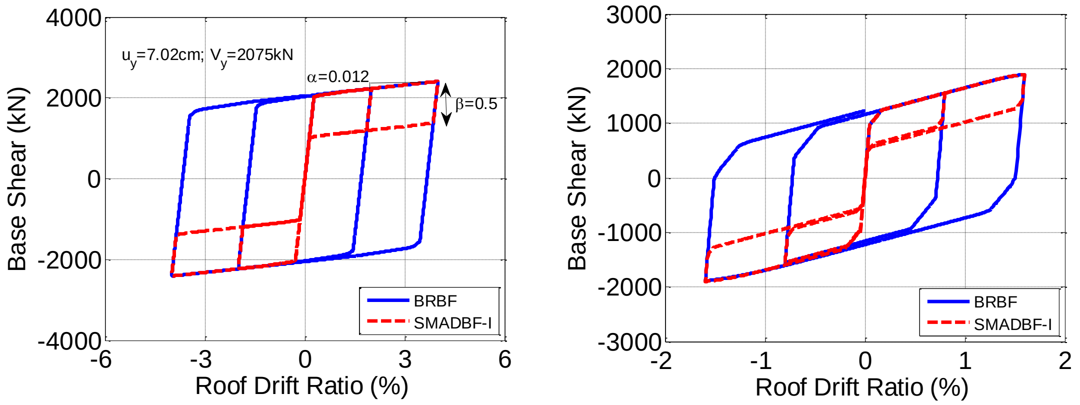

(a) First-mode force pattern (b) Second-mode force pattern

Figure 5.6 Cyclic pushover curves of the SMADBF-I and BRBF

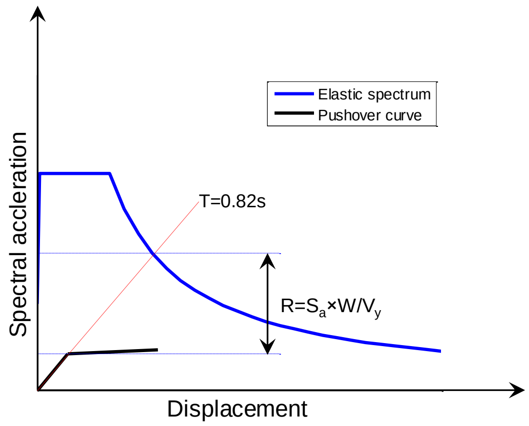

Figure 5.7 Definition of strength reduction factor, *R*

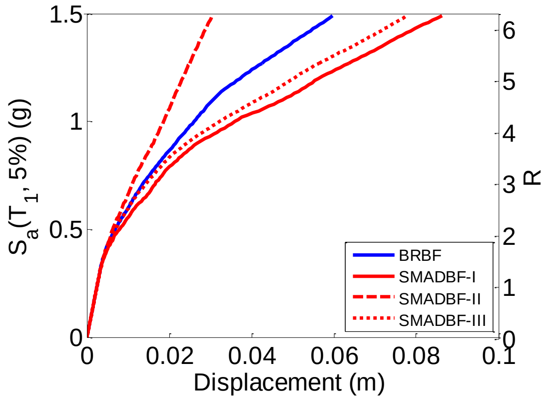

(a) T = 0.2 s

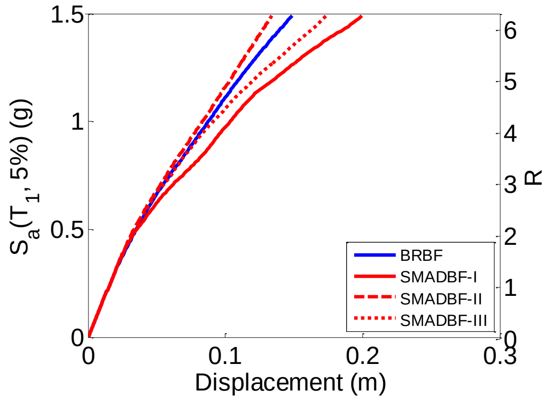

(b) T = 0.5 s

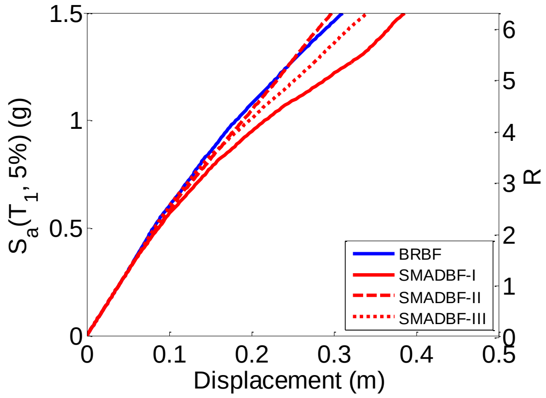

(c) T = 0.8 s

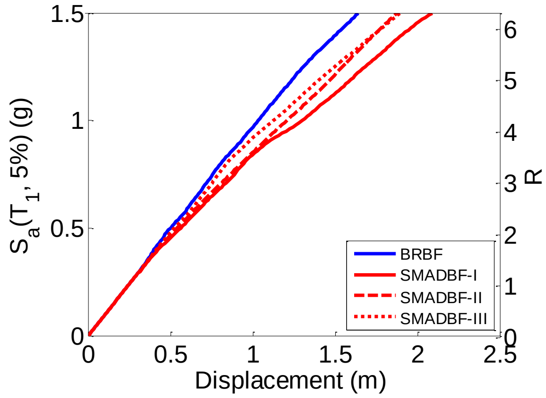

(d) T = 2.0 s

Figure 5.8 Effect of α and β on seismic deformation demand of SDOF systems with various natural periods

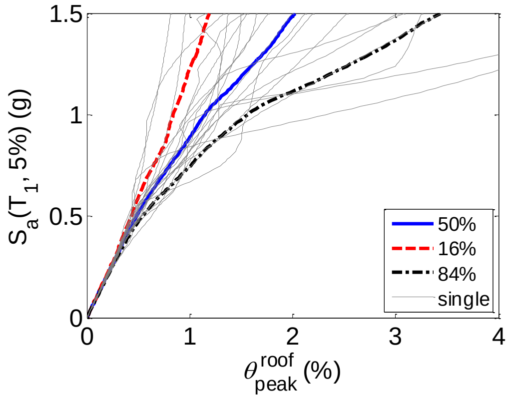

(a) Peak roof drift ratio

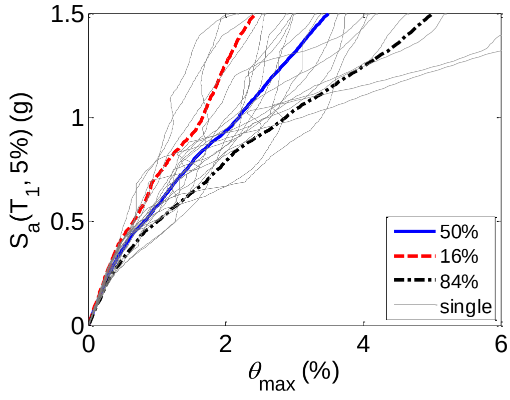

(b) Maximum inter-story drift ratio

Figure 5.9 IDA curves of SMADBF-I under varying seismic intensity levels

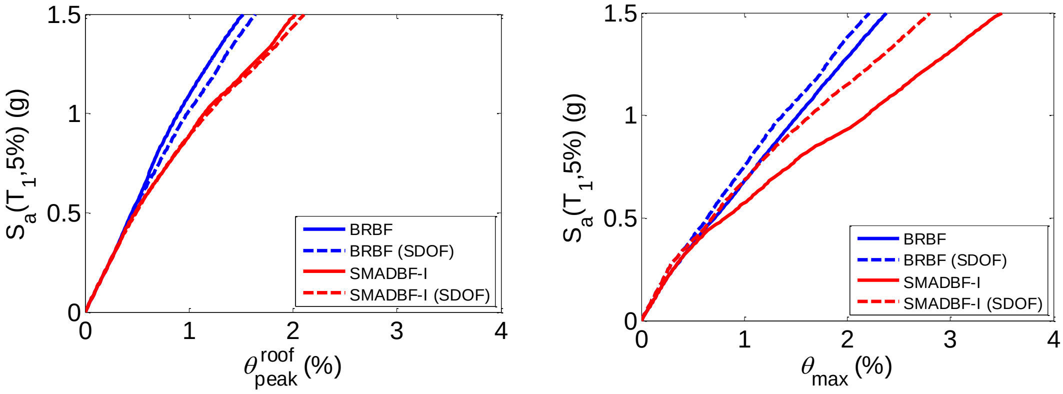

(a) Peak roof drift ratio (b) Maximum inter-story drift ratio

Figure 5.10 IDA curves of SMADBFs and BRBF in comparison with the corresponding SDOF predictions

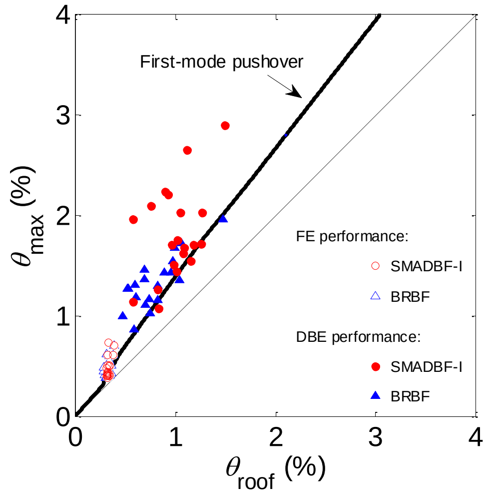

Figure 5.11 Relationship between θ_{max} and θ_{roof}

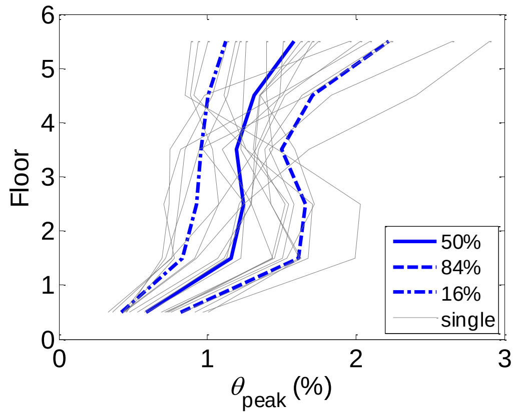

Figure 5.12 Height-wise distribution of peak inter-story drift ratio in SMADBF-I at the DBE level

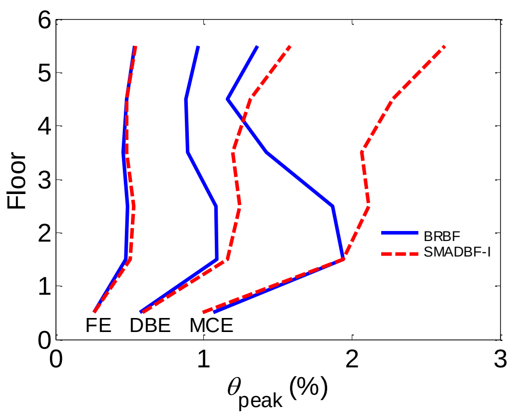

Figure 5.13 Geometric mean of peak inter-story drift ratio at FOE, DBE and MCE levels

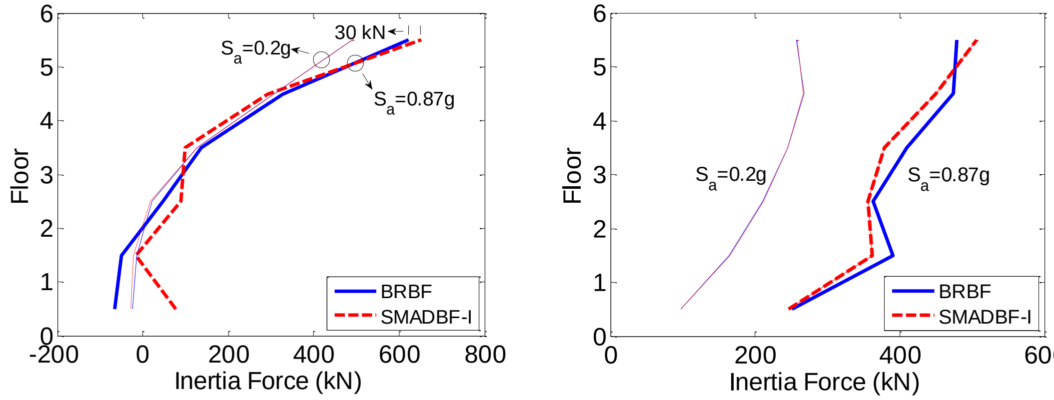

(a) At the moment of $\theta_{6,peak}$ (b) At the moment of $\theta_{1,peak}$

Figure 5.14 Geometric mean of transient inertia forces over the building height at the moments when θ_6 and θ_1 reach their peak values

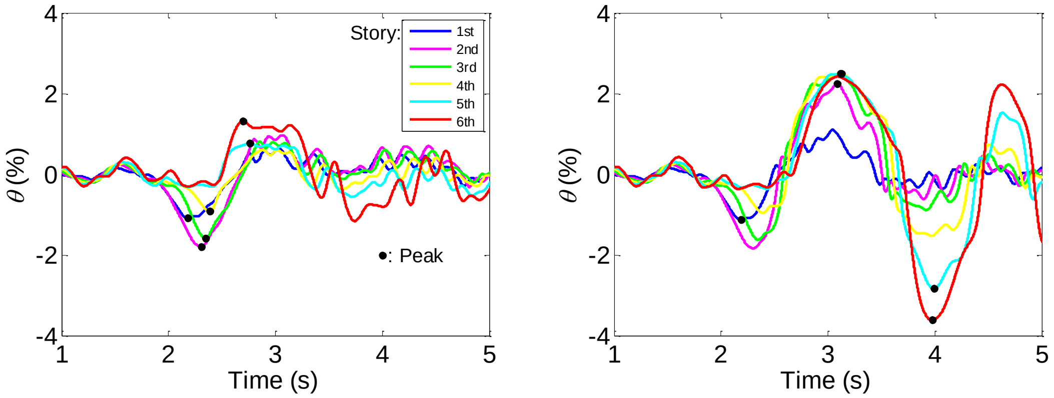

(a) BRBF (b) SMADBF-I

Figure 5.15 Time history response of interstory drift ratio, subjected to ground motion record LA20×1.2

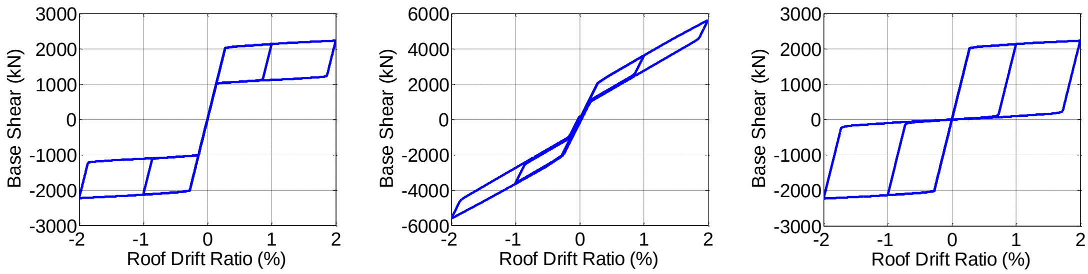

(a) SMADBF-I (b) SMADBF-II (c) SMADBF-III

Figure 5.16 Results of the first-mode pushover analysis of all structural systems

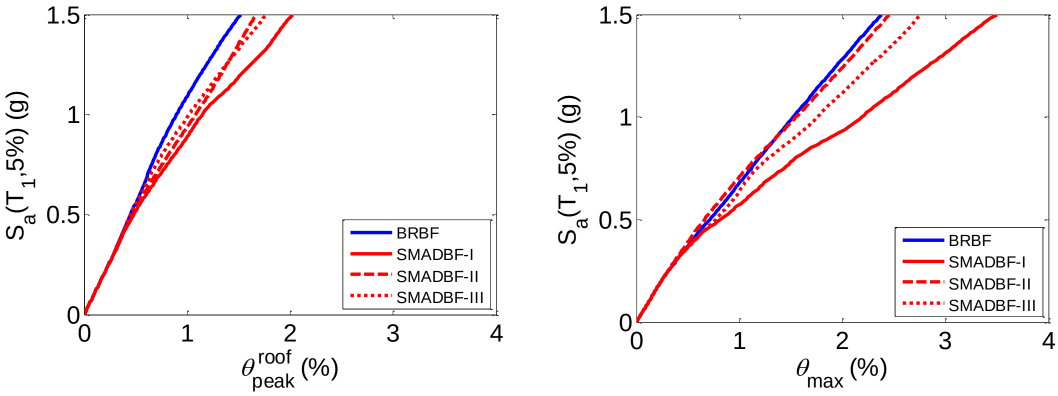

(a) Peak roof drift ratio (b) Maximum inter-story drift ratio

Figure 5.17 IDA curves of various structural systems that indicate the effect of increasing α and β in SMADBFs

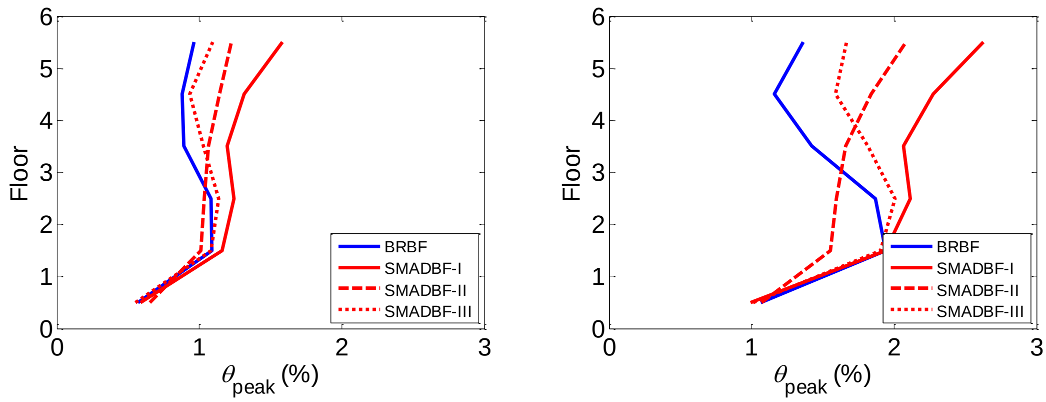

(a) DBE (b) MCE

Figure 5.18 Geometric-mean θ_{peak} over building height at the DBE and MCE levels, exhibiting effect of increasing α or β on mitigating higher modes effect

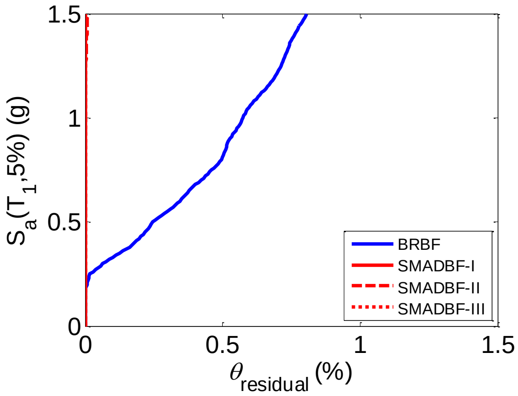

Figure 5.19 Geometric mean of maximum residual inter-story drift ratio in IDA

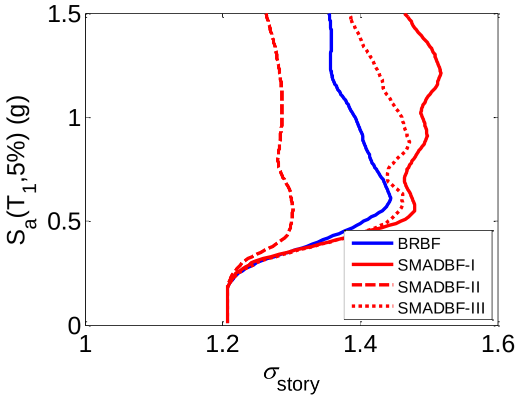

Figure 5.20 Geometric mean of σ_{story} in IDA

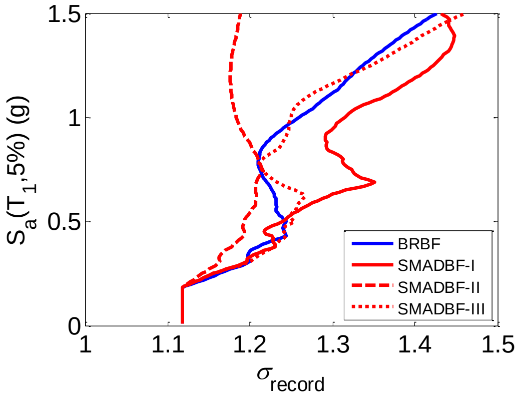

Figure 5.21 Standard deviation of θ_{max} under different seismic records in IDA

Chapter 6 Shaking Table Test and Numerical Study of SMADBF

6.1 Introduction

This chapter presents shaking table test and numerical study of a reduced-scale SMADBF. According to Chapter 1 that reviews the state-of-the-art of SMADBF, the superior seismic performance of this emerging framing system could be summarized as: (a) The good ductility of SMA enables the frames to be deformed to a larger interstory drift ratio than conventional braced frames. (b) The SC characteristics of SMADB minimize the residual deformation of the frames even if the frames experience large peak deformation under severe earthquakes. (c) The repeatable superelastic behavior makes SMADB reusable after severe earthquakes without the need for replacement. Consequently, the frame can sustain a series of mainshock and aftershocks without significant performance deterioration. (d) A properly designed SMADBF can remain nearly damage-free under small and moderate earthquakes and sustain very limited damage under severe earthquakes. Although these advantages have been illustrated through past numerical simulations to a certain degree of success, supportive experimental studies for such high performance can be rarely found. To address this knowledge gap, the current chapter presents the shaking table tests of a 1/4-scaled two-story one-bay steel frame with diagonal SMADBs. The design and fabrication of the tested SMADBF is introduced. The seismic performance of the SMADBF is assessed through two series of incremental dynamic tests, in which the frame is subjected to ground motions with incremental intensity levels, including typical near-fault ground motion records. The seismic demand and damage of the frame are experimentally evaluated with respect to various response indices and are further compared with numerical simulation results. In particular, no repair or replacement is conducted during the intervals between the tests to examine the ability of SMADBF to resist several strong earthquakes. The presented experimental and numerical study not only validates the aforementioned advantages of SMADBF, but also provides a more in-depth understanding of the seismic performance of SMADBF under multiple seismic hazard levels.

6.2 Design of the Tested Frame

6.2.1 Prototype Frame

As an emerging type of seismic-resisting structure, SMADBF lacks of a well-developed design methodology. A prototype SMADBF is designed in this study by following the traditional design method for BRBF (ASCE 2010). Figure 6.1 shows the perspective and plan views of the prototype frame, which is a two-story steel frame with five bays in each direction. The story height and bay width are 4.0 and 6.0 m, respectively. In each direction, there are a total of six braced bays to resist seismic lateral force, whereas the other bays undertake vertical gravity load only. The seismic mass is taken as 91 kg/m^2, which is selected in consideration of the testing capacity of the shaking table. Consequently, the floor mass of the frame is 82 tons, and the tributary floor mass for a one-bay braced frame is equal to 13.6 tons. The frame is assumed to be located on a Class D site according to ASCE (2010).

A force-based design method specified in the ASCE 7-10 (2010) is adopted for the prototype SMADBF. Table 6.1 summarizes the main design parameters used. The fundamental period of the two-story SMADBF is estimated to be 0.35 s. The design base shear and equivalent lateral force are determined according to the provisions in ASCE (2010). The yield strength of the designed braces is equal to 160.3 and 106.9 kN in the first and second floors, respectively. In particular, all the beam-to-column connections and column bases are designed to be non-moment-resisting connections. It is noteworthy that the design of the SC structures is not specified in existing seismic provisions; the design parameters for BRBF is approximately taken in this study, such as the period parameters C_t and x, response modification coefficient R, deflection amplification factor C_d, and overstrength factor Ω_0. However, by no means does this imply that the SMADBF exhibits seismic behavior similar to BRBF. Apparent differences in hysteresis loops and post-yield stiffness ratios, both of which may affect seismic performance, have been noticed between BRBF and SMADBF in past studies (e.g. Zhu and Zhang 2007b; Moradi et al. 2014). In recognition of the lack of a rational design methodology for SC structures, this thesis will develop a simple yet effective PBSD approach in next chapter on the basis of the numerical and experimental results in Chapters 5 and 6.

6.2.2 Scaled Tested Frame

A 1/4-scale SMADBF is designed for the shaking table test. The full-scale prototype frame is scaled down according to the similitude law presented in Table 6.2. According to the scaling factors, the story height and bay width of the tested model are equal to 1.0 and 1.5 m, respectively. The floor mass is equal to 850 kg, and the yield strength of SMADBs is equal to 10.02 and 6.68 kN for the first and second floors, respectively.

6.3 Preparation of the Tested Frame

This section introduces the structural system which is a braced frame with SMADBs. SMADBs serve as the kernel component of the tested frame. The two SMADBs described in Chapter 3 are utilized in the tested frame. Figure 6.2(a) shows the elevation view of the scaled structural model tested on the shaking table. The structural model consists of two connected parts: a braced frame and a mass simulation frame. The braced frame provides lateral seismic resistance to the entire structural model, and the mass frame simulates the tributary floor mass under earthquakes. The two-story SMADBF is mounted on the shaking table through pin connections at the column bases, which are different from typically fixed column bases in common braced frames. Figure 6.2(b) shows a close-up view of the brace-to-frame and beam-to-column connections. The brace-to-gusset connection is a true pin connection, which guarantees that the brace undertakes axial force only. A bolted splice plate is utilized to connect beam webs and simulate a beam-to-column connection that mainly transfers axial force with limited flexural constraint. The centerlines of the braces, beams, and columns intersect at the same point to eliminate eccentric loads in these members. The pin-connection design in

SMADBF minimizes the shear force and bending moment in all the frame members and leads to the following characteristics: (1) Axial force becomes the dominant action in the frame members. (2) Lateral seismic force is completely resisted by the SMADB elements without any moment-resisting frame effect. (3) Rotation release allows large lateral deformation of the frame without significant plastic damage.

In the braced bay, the beams and columns have a built-up wide flange section of H100 × 50 × 5 × 7 (i.e., depth, width, web thickness, and flange thickness, respectively). Such a section represents nearly the smallest wide flange section commercially available in the local market. The selected section is moderately stronger than that compliant with the similitude law. Since the frame members do not contribute to the lateral force resistance and they remain elastic under the major action of the axial force, the overstrength of the beam and column members imposes very limited influence on the seismic performance of the entire structural system.

In the mass simulation frame, the seismic floor mass (i.e., 850 kg according to the similitude law) is simulated by seven steel plates on each floor level. Figure 6.3(a) shows a photo of a frame model being tested on the shaking table. The floor mass is supported by H-section columns, whose lower and upper ends are both frictionless hinge connections (as shown in Figure 6.2(a)). Consequently, the mass simulator is essentially a leaning frame that carries gravity in the vertical direction but does not contribute any lateral resistance in the entire system. The mass simulation frame is connected to the braced frame through a specially designed joint that allows free rotation [Figure 6.2(b)]. The steel joint consists of Parts A and B, where Part A is welded to the column flange and aligned to the centerline of the beam, and Part B is fabricated by welding a steel cylinder to a steel plate and connected to the mass simulation frame. Such a design allows the relative rotation between two parts with minimal friction. As a result, these connectors constrain the lateral displacements of the two frames at the floor levels and transmit horizontal inertial force to the braced bay without any transmission of vertical load or bending moment. The adoption of the mass simulation frame has the following advantages: (1) It can accommodate a relatively large mass with sufficient space. (2) It avoids applying unreasonably large axial forces to the columns in the braced bay. (3) It avoids strengthening the beams in the braced bay by the steel plates. (4) It offers an appropriate way of simulating the P-Delta effect of seismic inertial forces. Figure 6.3(b) shows a photo of the connector between the braced frame and mass simulator frame. Figure 6.3(c) and (e) show the connections in the beams and at the column bases.

In addition to the braced frame and mass simulator frame, another supporting frame is built to prevent the out-of-plane displacement (or even instability) of the braced frame being tested. The ball bearings between the supporting and tested frames provide sufficient out-of-plane constraints but negligible in-plane force to the tested frame. A close-up view of a typical ball bearing is shown in Figure 6.3(d). As a result, the in-plane seismic behavior of the tested SMADBF in the ground motion direction can be regarded as unaffected by the supporting frame.

6.4 Experimental Setup and Program

6.4.1 Testing Apparatus and Sensor System

The test was conducted on a 3 m × 3 m unidirectional shaking table housed in the Structural Dynamics Laboratory of The Hong Kong Polytechnic University. The maximum ground acceleration of the shaking table could reach ±1 g. The MTS feedback control system was calibrated before the formal tests. The calibration could effectively reduce the error of the feedback control system, although discernable errors still existed when input ground motions contained relatively high peak ground acceleration (PGA). Thus, the actual ground motions of the shake table were recorded at each test via an accelerometer mounted on the shaking table.

A total of 28 strain gauges, 4 linear variable displacement transducers (LVDTs), and 5 accelerometers were used in this experimental study. Figure 6.4 shows close-up views of some of the installed sensors. The strain gauges were glued on the beams, columns, braces, and force-transmitting connectors to measure their deformation. Two LVDTs were installed between the supporting and tested frames to measure the relative displacement of the tested frame in the direction of ground motion, and the other two were installed on the braces to measure the axial displacement of the braces. The peak and residual deformation and displacement from the strain gauges and LVDTs were closely monitored after running each test, because these indices are related to the structural damage extent. Two accelerometers were installed on each floor level. One was mounted on the right column flange [Figure 6.4(b)], and the other on the addition mass at the same level. An additional accelerometer was placed on the surface of the shaking table to record the actual ground motions to which the tested structural model was subjected. The recorded ground motions were used as the input in the numerical simulations described in the next section. A data acquisition system with a sampling frequency of 2000 Hz was used to record the signals produced by the strain gauges, LVDTs, and accelerometers.

6.4.2 Ground Motions and Testing Program

Before the formal tests, random and harmonic ground motions of low intensity levels were input to examine the dynamic characteristics (such as the fundamental frequency and damping ratio) of the tested SMADBF. Such dynamic characterizations were also performed after the seismic ground motion tests to examine the likely changes of the dynamic characteristics.

In the formal tests, the SMADBF was subjected to two series of ground motions. The two ground motions, denoted as LA17 and NF09, were previously developed by Somerville et al. (1997) to represent far- and near-fault ground motions, respectively. The record LA17 corresponds to a DBE in Los Angeles. The information of these two input ground motions is presented in

Table 6.3. Figure 6.5 shows the acceleration and velocity time histories of the two selected ground motion records. The record NF09 has a relatively shorter duration than LA17, but contains a long-period pulse evident in the velocity time history. Figure 6.6 shows the 5%-damping response spectra of the two ground motions, including the spectral acceleration and displacement demands.

The two ground motions were both scaled to various intensity levels, and the same SMADBF was subjected to a series of "incremental dynamic tests." Table 6.4 presents the series of input ground motions in the real testing orders. Such incremental dynamic tests enable the examination of the seismic performance of the SMADBF under a wide range of seismic intensities, which cover mild, moderate, and high seismic hazard levels. Among all the tests, Test No. 7 represents the strongest ground motion in which the structural damage under a significant earthquake can be assessed. In the following two tests, two scaled-down ground motions were input to examine the seismic performance of the tested frame when subjected to some large aftershock events.

6.5 Numerical Simulation Model

Numerical simulations of the tested SMADBF were conducted for comparison with the experimental results. The numerical model was built in the computer program OpenSees (2013). Figure 6.7 shows the modeling details of the tested SMADBF. The numerical modeling technique is essentially similar to that in Chapter 5, so attentions are only given to how to model some actual details in this experiment. The beam-column connections were shifted away from the column centerlines and were modeled as semi-rigid connections whose rotational stiffness was determined based on the actual testing configuration. Only the in-plane seismic responses of the frame were analyzed. The torsional response of the frame about the vertical axis was not considered, because the supporting frame constrains the out-of-plane displacement during the tests. The mass simulation frame was idealized as a leaning column. The stiffness and strength of the leaning columns were modeled according to the practical constructions. The leaning column was connected to the floor mass through pin connections.

Considering no damage or buckling was observed in the bracing elements during the tests, the SMADBs were modeled as axially loaded members with the actual length. The required material properties were calculated based on the actual stiffness and strength of the tested braces because the brace length differed from the length of the SMA wires. To accurately capture the cyclic behavior of the SMADBs shown in Figure 3.5, including SC behavior and initial slackness, a hybrid material model was introduced, as shown in Figure 6.8. The new model is essentially a combination of two types of material models: (1) *SelfCentering* material, which properly simulates the FS hysteresis of SMA materials, and (2) *ElasticMultiLinear* material, which accounts for the initial slackness in the braces. The bilinear force-displacement relationship of the latter material facilitates capturing the initial low stiffness of SMADBs shown in Figure 3.5 and more accurately simulating the seismic behavior of the tested frame model. The initial stiffness and slackness of the bilinear model were calibrated based on the measurement data from the LVDTs in the experiments. These two material models were connected in series to achieve the target cyclic behavior. The *Series* command was used to construct the final constitutive model of the SMADBs. A similar treatment was also adopted by Erochko et al. (2014) in their modeling of the SC energy-dissipative braces to consider some factors, such as pretension of tendons, slip of friction surface, and contact of end plates.

Rayleigh damping was adopted to account for the inherent damping of the frame structure. The final damping ratio used in the numerical model was given as 4%. Similar to the shaking table tests, the IDA of the numerical model was performed under varying seismic intensity levels. The actual ground accelerations recorded in the shaking table test were used as the input ground motions.

6.6 Experimental and Numerical Results

The results of the shaking table tests of SMADBF, together with those of the numerical simulations, are presented and discussed in this section. In particular, the seismic performance of SMADBF under different seismic intensities is systematically evaluated, which to the best of our knowledge is yet to be reported in the literature. The seismic demands of interest include global responses (such as peak and residual roof displacements, interstory drift, base shear, etc.) and internal loadings of the SMADBF model.

6.6.1 Dynamic Characteristics

The dynamic characteristics of the tested SMADBF were evaluated when the frame was subjected to random and sine wave excitations. The PGA of the ground motions ranged from 0.01 g to 0.05 g, which induced the elastic behavior of the tested frame. The dynamic characterization indicated that the SMADBF model had a fundamental frequency of 2.3 Hz, which was close to the initial estimation in the design stage. The equivalent damping ratio was approximately 4%. A consistent damping ratio was also used in the numerical modeling and simulation.

6.6.2 Displacement Response

Figure 6.9 shows the time histories of the roof displacement and the corresponding roof drift ratio in all the test cases, where the roof drift ratio refers to the ratio of roof displacement to building height. The figures are presented in the order of ground motion intensities. Satisfactory agreement between the experimental tests and numerical simulations can be observed in Figure 6.9. Generally, numerical simulations can accurately predict the peak displacement responses in the shaking table tests, although noticeable discrepancy is observed in the entire time histories. The vibration duration under seismic record LA17 was typically longer. Thanks to the excellent SC capacity provided by the SMADBs, the residual displacement was negligible after all the shaking table tests, including the cases with highly significant ground motions LA17×1.5 and NF09×1.0. This result implied that the designed SMADBF could sustain a MCE with significantly limited damage and permanent deformation, which could considerably reduce post-earthquake repair cost and downtime.

In real scenarios, a structure may be subjected to a large number of major aftershocks following the mainshock event. For example, 286 major aftershocks (> 4.0 Ms) were reported after the Wenchuan Earthquake in China in 2008 (SCEA 2008). Structural safety under major aftershocks has recently drawn increasing attention from the earthquake engineering community. To investigate this effect, two test cases of LA17 × 0.75 and NF09 × 0.75 were conducted after the test with the most significant ground motion LA17 × 1.5. No repair or modification of the frame was conducted before the two aftershock tests. No residual deformation and performance deterioration were observed in the displacement time histories under LA17 × 0.75 and NF09 × 0.75, demonstrating the potential capability of SMADBF to withstand the mainshock and several major aftershocks without the need for major repair.

Figure 6.10 shows the maximum interstory drift ratios along the frame height for each test case. The relative displacement of the two adjacent floors was calculated from the difference of two LVDT readings installed on the floor levels. In Figure 6.10(a), the maximum interstory drift ratios are approximately 1.7% and 2.1% at the DBE and MCE seismic hazard levels, respectively. In general, the tested SMADBF exhibits a fairly uniform distribution of interstory drift ratios under both ground motions of different intensities. The seismic behavior of the two-story SMADBF is dominated by the fundamental vibration mode, and the high-mode effect that may lead to non-uniform interstory drift distribution is not significant in this model. The results of the numerical simulations show a satisfactory agreement with the experimental results in both Figure 6.9 and Figure 6.10, which justify the efficacy of the numerical model established in the program OpenSees.

6.6.3 Base Shear

Figure 6.11 shows the time histories of the base shear from the experimental results and numerical simulations for all seismic loading cases. The base shear is calculated as the summation of seismic inertial forces on different floors:

$$V_{base} = \sum_{i=1}^{2} m_i \cdot a_i \tag{6.1}$$

where m_i is the floor mass on the ith floor and a_i is the absolute acceleration measured by the accelerometer on the ith floor. Good agreement is again observed between the experimental and numerical results. Generally, the numerical simulations tend to slightly underestimate the base shear in comparison with the shaking table test results, which may be attributed to the discrepancy between the experimental hysteresis and numerical constitutive model of SMADB or measurement errors of accelerations. The maximum base shear of 18.0 kN occurs in the strongest loading case of LA17×1.5, which is consistent with the cyclic behavior of the SMADB in the first story shown in Figure 3.5.

6.6.4 IDA Curves

Figure 6.12 further compares the IDA curves of the peak roof drift ratios, brace displacement, roof accelerations, and base shear from the experimental data and numerical simulations. In the figure, PGA is adopted as the intensity measurement (*IM*) of the scaled ground motions, and the peak roof drift ratio, roof accelerations, and base shear are regarded as a damage measure (*DM*). As shown in Figure 6.12(a), the peak roof drift ratio is less than 1.0% under a moderate earthquake (i.e., LA17×0.5), and increases to approximately 1.5% and 2.0% in the cases of DBE (i.e., LA17 × 1.0) and MCE (i.e., LA17 × 1.5) earthquakes, respectively. Figure 6.12(b) shows the deformation of the 1st-story brace, which exhibits a similar trend with the roof drift ratio. The 2nd-story brace exhibits a slightly smaller deformation demand than the 1st-story brace; but the brace deformation between two stories is generally uniform. The peak roof acceleration shown in Figure 6.12(c) is approximately 0.5 g under a moderate earthquake and reaches approximately 1.0 and 1.2 g at DBE and MCE levels, respectively. The base shear in Figure 6.12(d) shows a nearly identical trend with the acceleration, as the base shear can be calculated from the floor accelerations and masses. Furthermore, Figure 6.12 shows very similar trends under LA17 and NF09. This similarity reveals that the remarkable velocity pulse in the near-fault record NF09 does not exert a negative impact on the studied SMADBF in terms of the *DM* shown in Figure 6.12.

6.6.5 Truss Mechanism

The internal loadings in the frame members are examined in this section. Figure 6.13 shows the seismic inertial force on the frame and the internal loadings at four joints at the instant that the base shear reaches its peak value in the case of LA17 × 1.0. According to Figure 6.11, the peak base shear occurs at t = 3.3 s in the experiment and at a slightly different instant in the simulations. To maintain consistency, the internal loadings at t = 3.3 s are presented for both the experimental and numerical results in Figure 6.13. In the numerical simulations, the internal loading of different elements can be directly extracted from the OpenSees model; whereas in the experimental results, the bending moments and axial forces are indirectly calculated from the readings of the strain gauges mounted on two flanges of the H-shaped section. The strain measurement indicates that the deformation is in the elastic range; thus, Hook's law is applied to calculate the stress from the strain gauge measurement. Figure 6.13 presents the internal loadings from both the experimental and numerical results. In the experimental results, shear forces are not available, and axial forces and bending moments are calculated at the locations with strain gauges. The inertia of the braced frame is omitted in the calculation, given that it is considerably smaller than that produced by the mass simulation frame. Again, satisfactory agreement is found between the experimental data and numerical simulations.

As shown in Figure 6.13, the braces are subjected only to axial forces. Although shear forces and bending moments are detectable in the steel beam and column members, axial force is still the dominant action. Thus, these structural members are mainly subjected to axial forces, and the entire braced bay behaves in a manner similar to a truss, mainly because of the pin connection design in the tested frame. The truss mechanism is beneficial because it allows large deformation without causing plastic damage in the members. As a result, yielding or local buckling does not occur in the beams and columns even in the most serious cases, such as LA17 × 1.5 and NF09 × 1.0. The inelastic deformation is mainly concentrated in the SMADBs and can recover upon unloading because of the superelasticity of the Ni-Ti wires. In the entire test series, no repair of the frame members is conducted, although some sensors are damaged because of inappropriate installation. It clearly demonstrates that a properly designed SMADBF can sustain several significant earthquakes and major aftershocks without the need for repair or replacement of any structural members. It is possible to design a SC SMADBF that is free of structural damage and residual deformation after strong earthquakes.

6.6.6 Behavior of SMADB

Figure 6.12(b) shows the IDA curves of SMADB displacement. A comparison with Figure 3.5 reveals the deformation levels of SMADB at different seismic intensity levels. Under a moderate earthquake, the SMADB is in its elastic behavior; as the earthquake intensity increases to DBE and MCE hazard levels, the SMADB undergoes inelastic deformation. Under the most intense earthquake (i.e., LA17 × 1.5), the peak deformation of SMADB is up to 18 mm. The SMADB is subjected to significantly inelastic deformation, but it can still recover from deformation according to Figure 3.5.

After the completion of all the nine testing cases listed in Table 6.4, the SMADBs were removed from the frame and cyclically tested again on the MTS machine. Figure 6.14 compares the hysteresis behavior of the 1st-story SMADB before and after the series of shaking table tests. The two hysteretic loops are quite consistent with minimal discrepancy in the initial slackness. The stable SC cyclic behavior indicates that the SMADB is associated with negligible strength or stiffness degradation after many loading cycles in a series of shaking table tests. Thus, well-designed SMADBs in a real frame building are reusable without any performance degradation after several earthquakes. This salient feature will make SMADBs very appealing in highly seismic regions.

6.7 Summary

The SC steel frame with novel SMADBs is investigated experimentally and numerically in this study. In particular, the seismic performance of SMADBF is validated through a series of shaking table tests of a 1/4-scaled two-story one-bay frame model. Good agreement is observed in the comparisons between the experimental and numerical results. The SMADBs enable the frame to successfully return to the zero position with limited structural damage from a peak interstory drift ratio up to over 2.0%. Such a peak magnitude is considerably larger than those reported in previous experimental studies, and offers important evidence that SMADBF, as an emerging type of seismic-resisting structure, can withstand highly intensified seismic hazards.

In the shaking table tests, the tested frame model was consecutively subjected to a total of nine ground motion records with incremental intensity levels. The displacement time history showed that nearly zero residual deformation accumulated after the entire run of earthquakes. The near-fault earthquakes did not induce an intensified seismic response. The examination of the internal loads in the frame revealed that the axial forces are the dominant actions in the frame and that the existence of SMADB, together with the pin-connection design, forms a desirable truss mechanism that protects the beams and columns against severe damage under severe earthquakes. The numerical simulations showed that the proposed model could properly simulate the cyclic behavior of SMADB and the seismic response of the SC braced frame. The time histories of the obtained roof displacement and base shear were compared, and good agreement was achieved between the numerical simulation and experimental data.

The SC steel frame with SMADB could sustain several strong earthquakes without severe damage, performance deterioration, or permanent deformation of the frame. The SMADBs were also reusable without the need for replacement or repair. These merits of SMADBF will considerably reduce the post-earthquake repair cost in comparison with conventional structures. Therefore, the investigated SMADBF will be a promising high-performance seismic-resisting structural system when a seismic performance level of immediate occupancy or operation is desired under strong earthquakes.

Table 6.1 Seismic design parameters of SMADBF prototype

Seismic design category	D
Redundancy factor, ρ	1.3
Occupancy category	II (Office)
Importance factor	$I_e = 1$
Damping ratio	5%
Mapped spectral acceleration at short-periods, S_S	2.0 g
Mapped spectral acceleration at 1-sec period, S_1	0.707 g
Damping coefficients	B_S = 1.0, B_1 = 1.0
Site coefficients	F_a = 1.0, F_v = 1.5
Response modification coefficient, R	7
Overstrength factor, Ω_o	2
Deflection amplification factor, C_d	5½

Table 6.2 Similitude laws used for the reduced model

Quantities	Scaling factor, *S* = Model / Prototype
Length	$S_L = 1/4$
Modulus of elasticity	$S_E = 1$ (same material)
Acceleration/gravity	$S_a = 1$
Force	$S_F = S_E \times S_L^2 = 1/16$
Inertia mass	$S_M = S_F / S_a = 1/16$
Time	$S_T = \sqrt{S_L / S_a} = 1/2$

Table 6.3 Ground motions in the shake table tests

Record	Name	Station	Year	M	PGA (g)	Distance (km)
LA17	Northridge	Sylmar	1994	6.7	0.57	6.4
NF09	Erzincan	95 Erzincan	1992	6.7	0.43	2.0

Table 6.4 Shake table test sequence

Test No.	Record	Scalar	PGA (g)
1	LA17	0.25	0.14
2	LA17	0.50	0.29
3	NF09	0.25	0.11
4	NF09	0.50	0.22
5	LA17	1.00	0.57
6	NF09	1.00	0.43
7	LA17	1.50	0.89
8	LA17	0.75	0.43
9	NF09	0.75	0.32

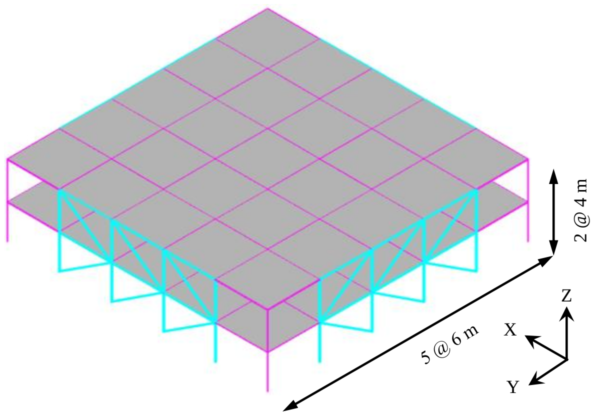

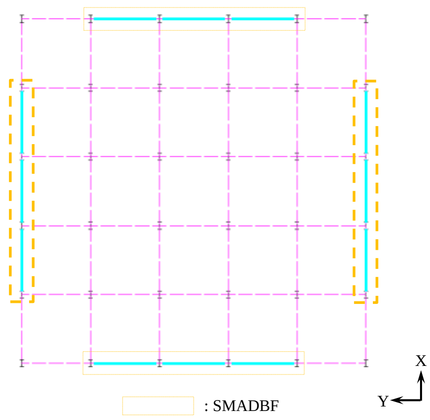

Figure 6.1 Perspective and plan views of the prototype frame

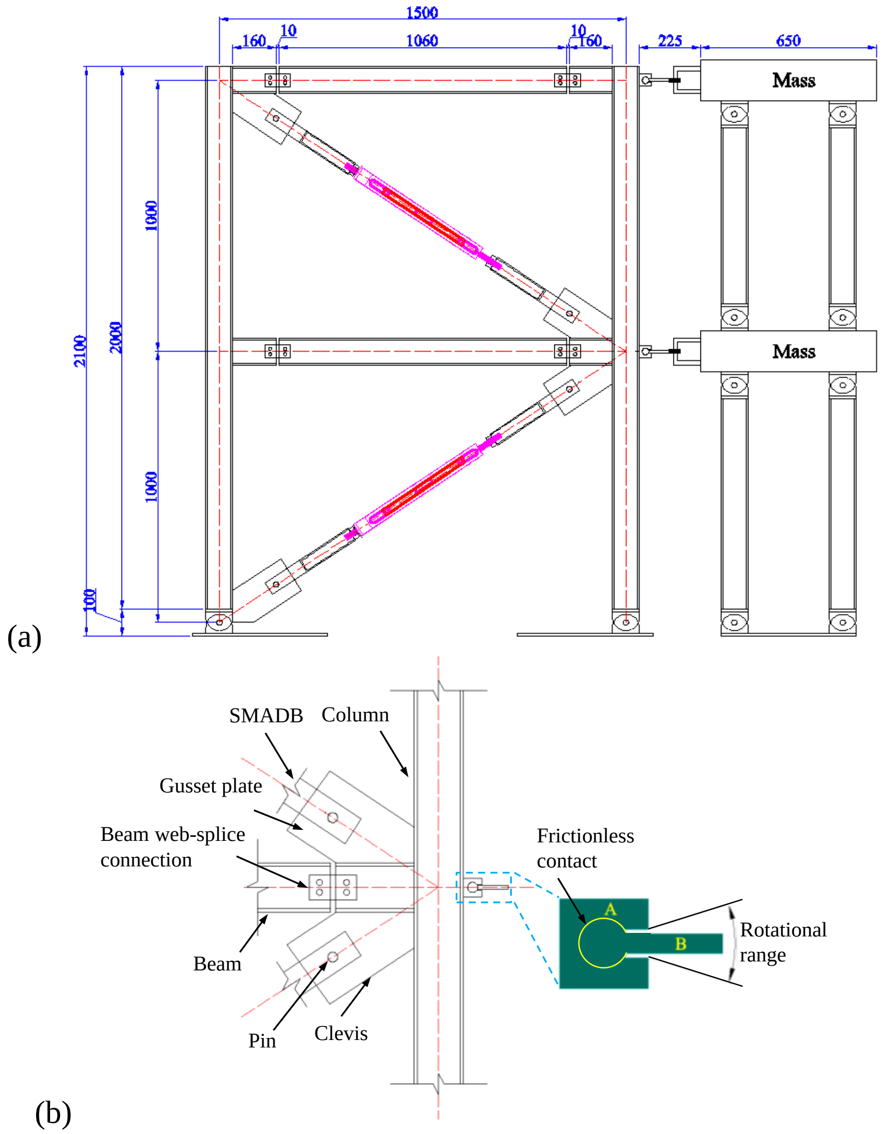

Figure 6.2 The schematic of the tested SMADBF model: (a) elevation view (dimension unit: mm) and (b) close-up view of brace-frame and frame-mass connections

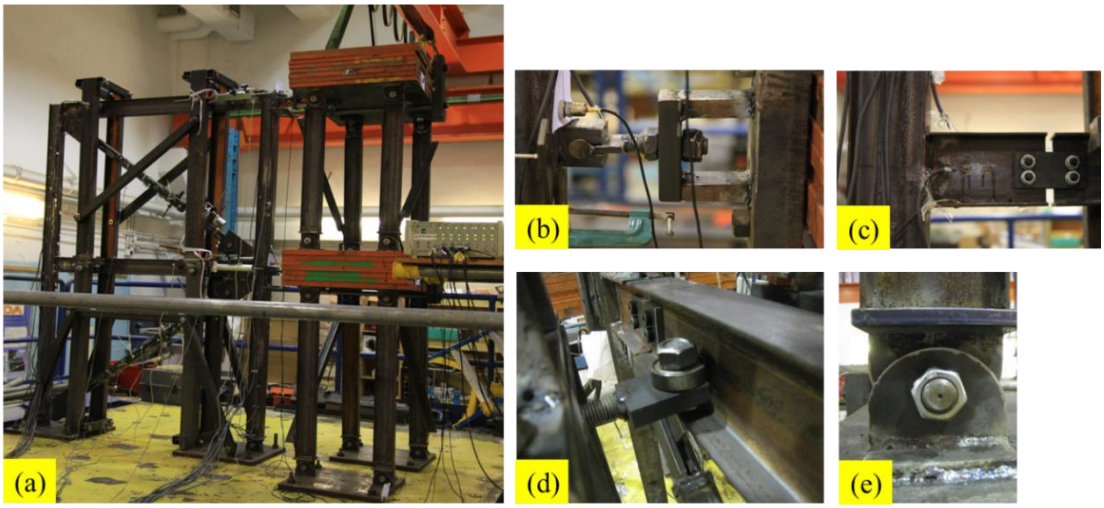

Figure 6.3 The tested frame on the shaking table: (a) global view of the model, (b) pinned connection between the frame and mass system, (c) beam-to-column connection, (d) ball-bearing of the out-of-plane constraint frame, and (e) pinned joint at the column base

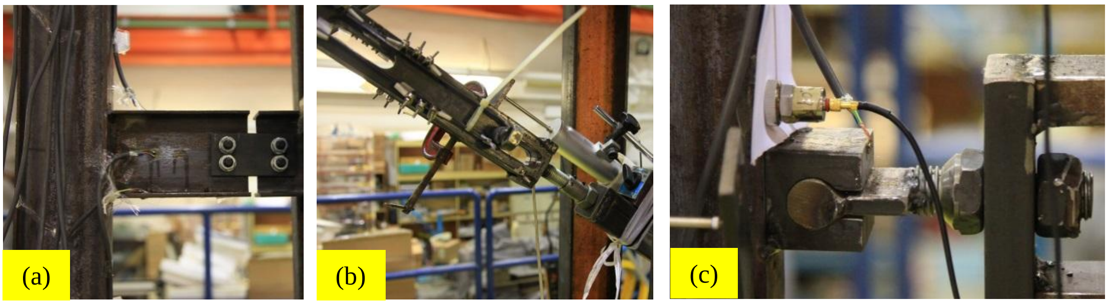

Figure 6.4 Sensor setup in the shake table test: (a) strain gauge, (b) LVDT, and (c) accelerometer

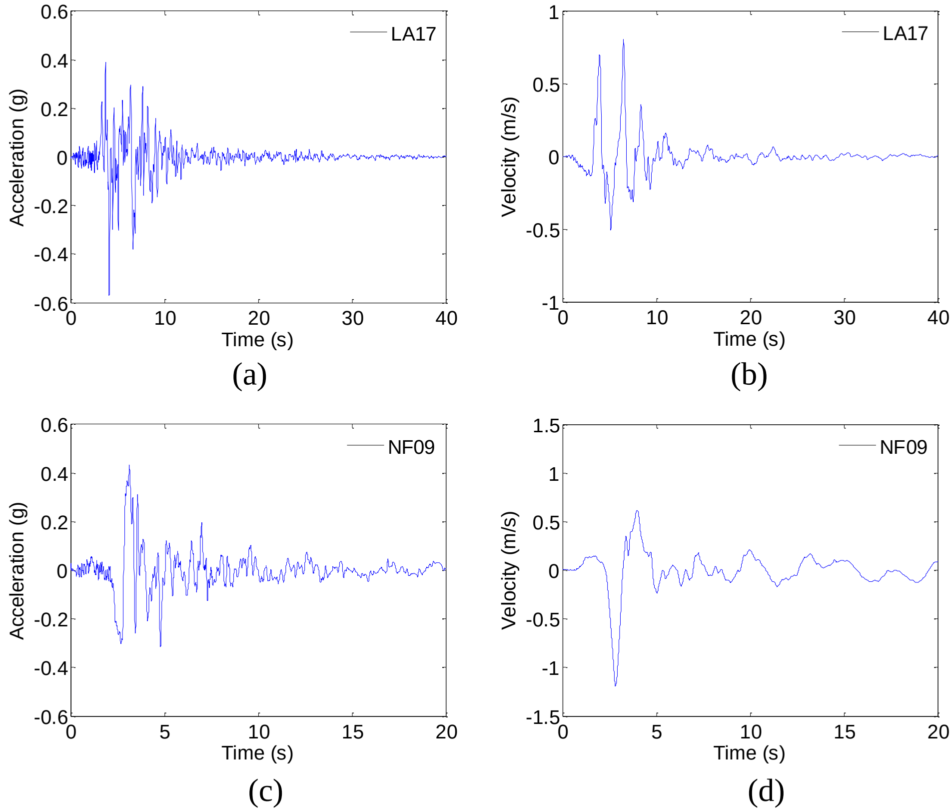

Figure 6.5 Time histories of selected input ground motion records: (a) acceleration of LA17, (b) velocity of LA17, (c) acceleration of NF09, and (d) velocity of NF09

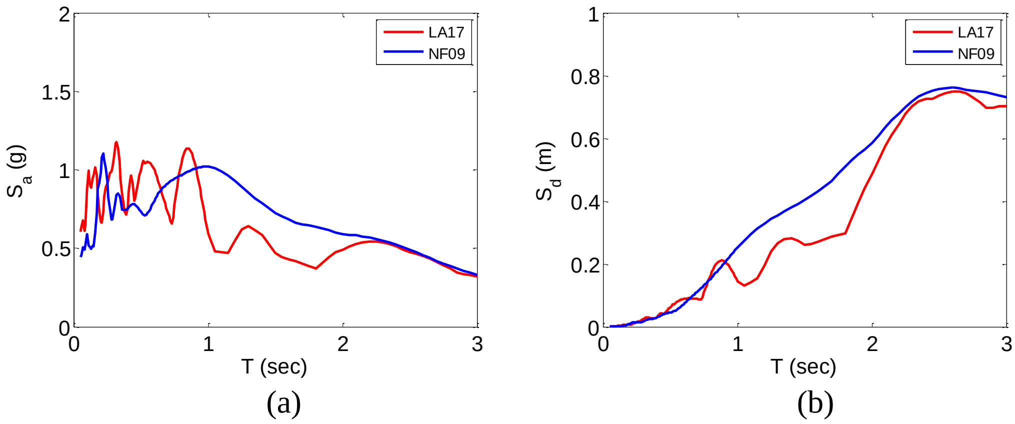

Figure 6.6 Elastic response spectrum of the selected ground motion records (5% damping ratio): (a) spectral acceleration and (b) spectral displacement

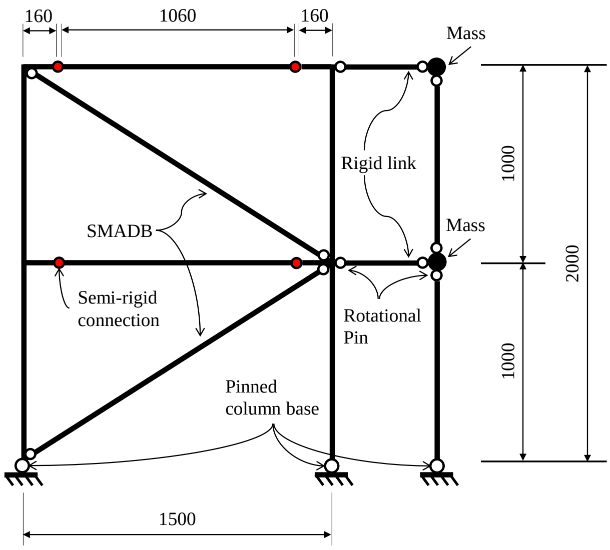

Figure 6.7 Numerical model of the SMADBF in OpenSees (unit: mm)

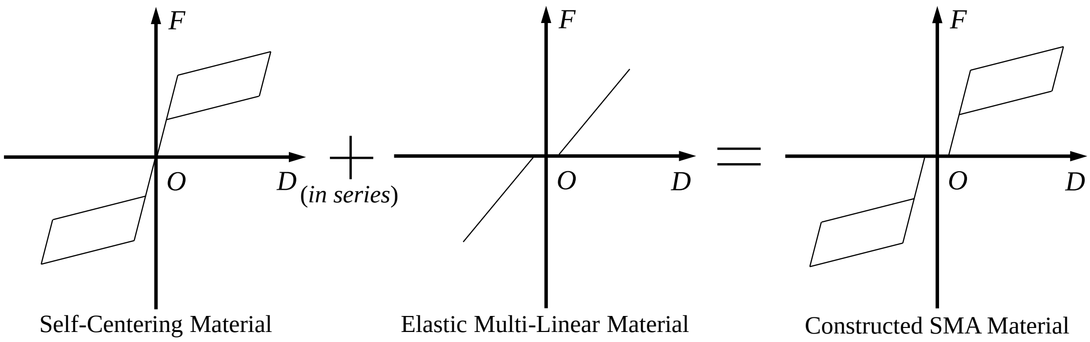

Figure 6.8 Modeling of the cyclic behavior of SMADB

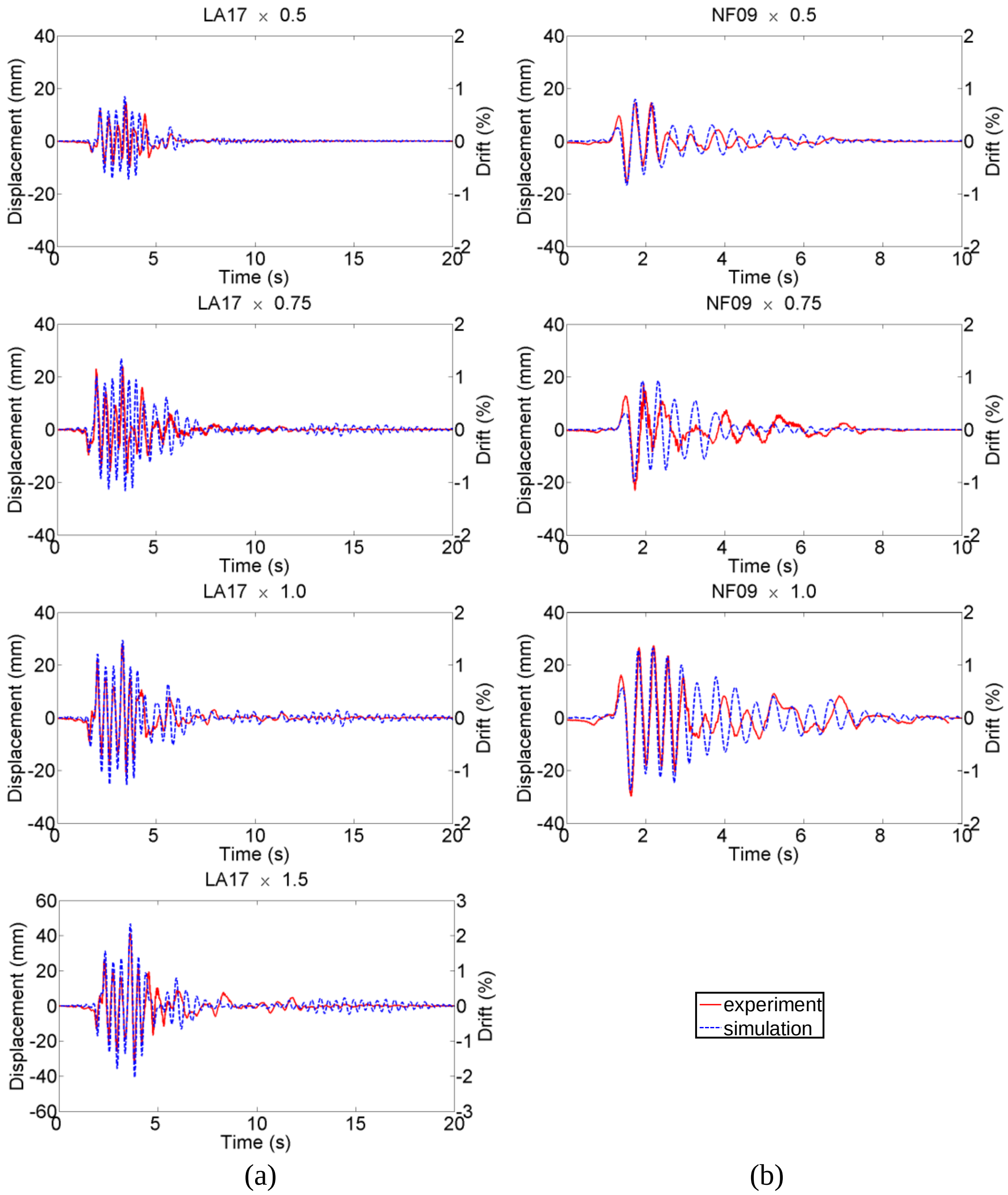

Figure 6.9 Time histories of the roof displacement, subjected to ground motion records (a) LA17 and (b) NF09 at different seismic intensities

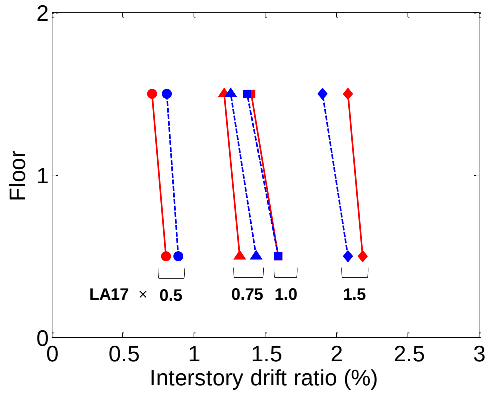

(a)

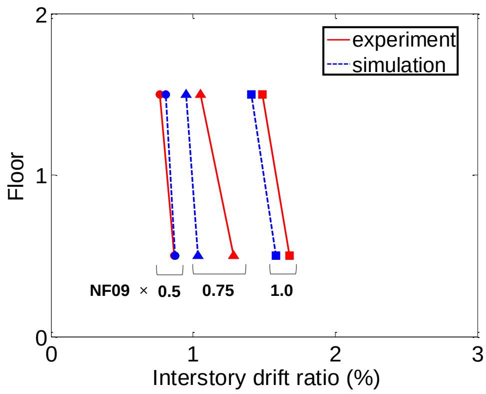

(b)

Figure 6.10 Maximum interstory drift ratio along the building height at different ground motion intensities: (a) LA17 and (b) NF09

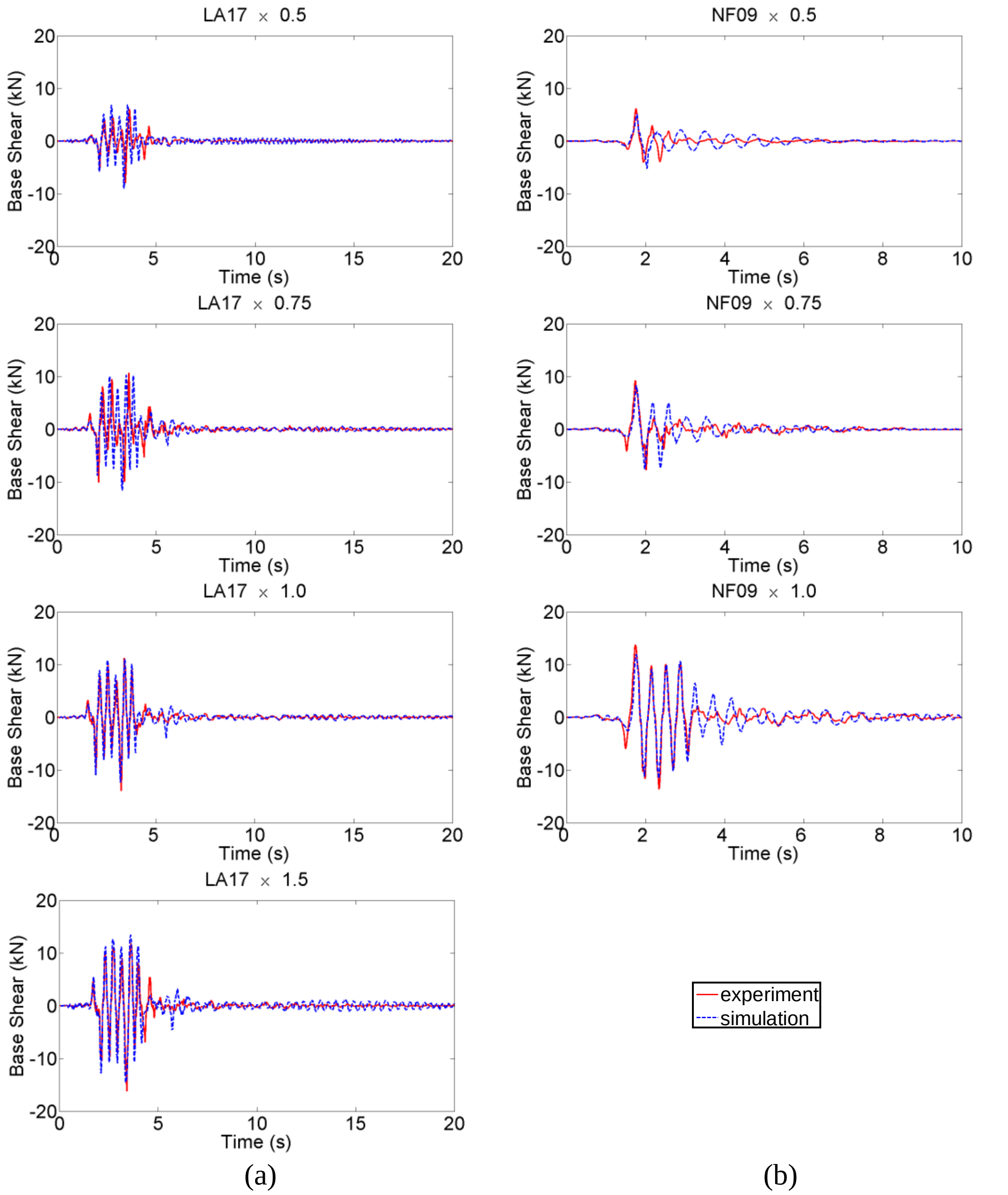

Figure 6.11 Time histories of the base shear, subjected to ground motion records (a) LA17 and (b) NF09 at different seismic intensities

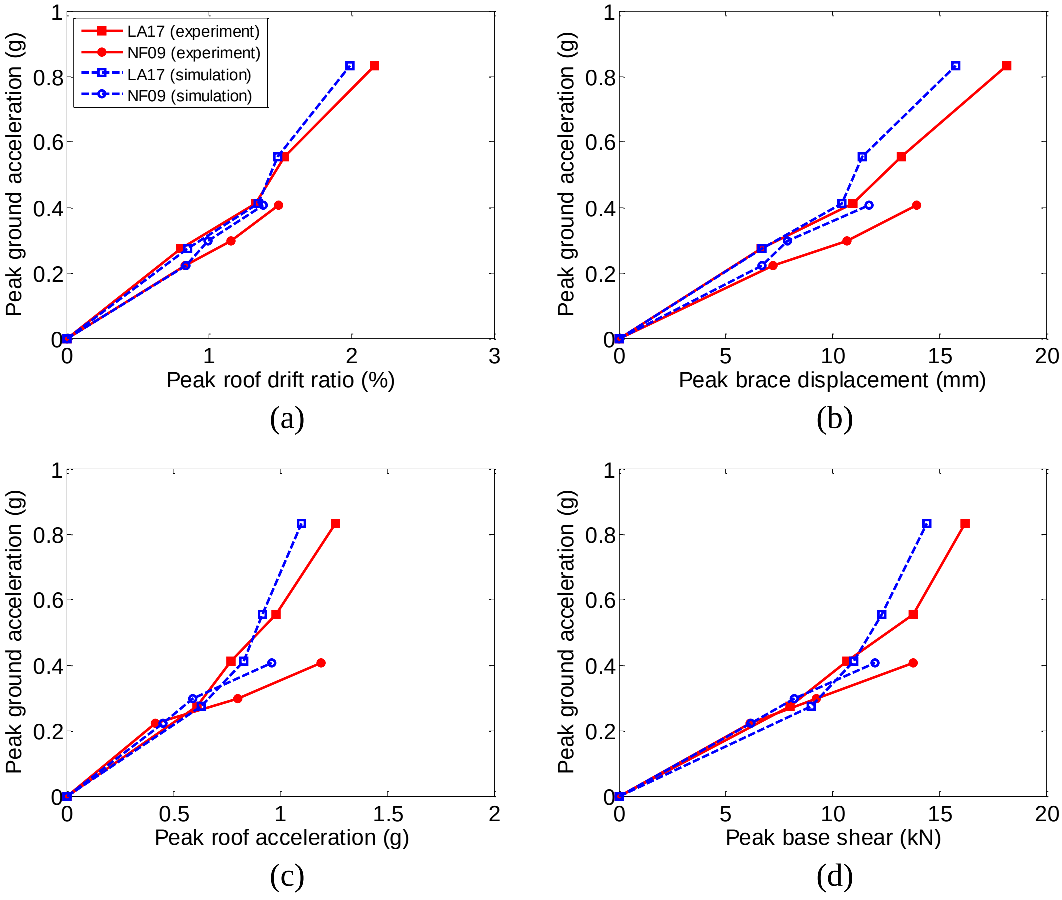

Figure 6.12 IDA curves: (a) roof drift ratio, (b) 1st-story brace displacement, (c) roof acceleration, and (d) base shear

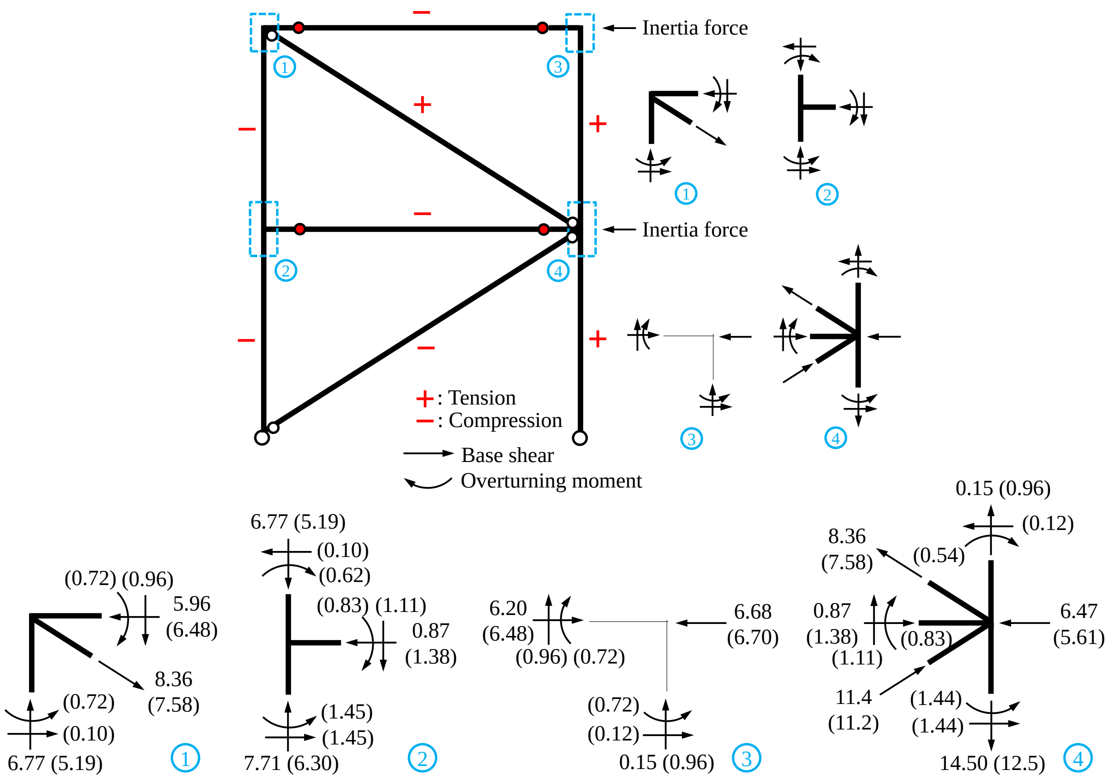

Figure 6.13 Force diagram of the framing system at the moment when the base shear reaches its maximum, taking the case of LA17 × 1.0 as an example. (Numerical results are enclosed in brackets; unit: kN for force and kN·m for moment.)

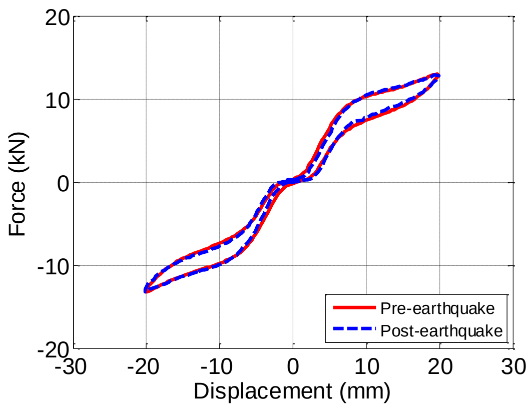

Figure 6.14 Pre- and post-earthquake performance of the 2nd story SMA-based damper

Chapter 7 Performance-based Seismic Design Method

7.1 Introduction

In the experimental study presented in Chapter 6, the reduced-scale SMADBF is designed as per the provision for BRBF. However, the apparently different seismic behavior of SMADBF and BRBF described in Chapter 5 revealed the deficiency of this expedient. Thus, there is an urgent need to develop a simple yet effective seismic design approach for SMADBF. In contrast to extensive investigations on SC building structures, the corresponding seismic design methods of SC structures have been rarely studied (Priestley and Kowalsky 2000; Kim and Christopoulos 2009; Dowden et al. 2011; O'Reilly et al. 2012; Eatherton et al. 2014). Recently, Kim and Christopoulos (2009) proposed and validated a design procedure for PT SC MRFs, in which the prescribed performance targets were set similarly to those of welded steel MRFs. Eatherton et al. (2014) developed a design method for an SC rocking frame by focusing on controlling several performance limit states; single and dual frames were designed using their method, but seismic performance was not examined.

A rational design methodology for steel braced frames with SC SMADBs has never been reported in literature. This chapter proposes an *ad hoc* PBSD method for SC steel braced frames with SMADBs. The performance-based plastic design method (Leelataviwat et al. 1999), which was previously developed for traditional steel moment and braced frames, is extended to the design of SMADBFs. A multistory SC steel frame with novel SMADBs is designed as an example in consideration of the prescribed seismic performance targets. Different SMA cables may exhibit various "post-yield" stiffness ratios and energy dissipation capacities depending on material properties. The variability in these two factors is particularly considered in the proposed PBSD method. Moreover, the effect of potential high modes in seismic response of SMADBFs is also considered during the design process. A systematic numerical assessment validates that steel SMADBFs designed via the proposed method can achieve the prescribed seismic performance satisfactorily. Although this method is intended for multistory frames with SMADBs, the proposed design framework can be conveniently extended to other SC structures with FS hysteresis.

7.2 SMADB

As shown in Chapter 3, the experimental results of the fabricated SMADB made of Ni-Ti cables are associated with the parameters are $\alpha = 0.16$, $\beta = 0.5$, $\sigma_y = 465$ MPa, and $E_{SMA} = 46.5$ GPa, where σ_y and E_{SMA} are calculated based on the cross-sectional area and length of the Ni-Ti cables, respectively. It is noteworthy that the Ni-Ti cables used in the tested brace may be replaced by a variety of other SMA cables with significantly different cyclic properties. The variability in FS hysteresis, particularly in two essential parameters (post-yield stiffness ratio α and energy dissipation factor β) should be explicitly considered in a design method if it is intended for different types of SMADBs. Different combinations of parameters α and β are also considered in the case studies.

Moreover, the deformation capacity of SMA cables also differs significantly. As can be seen in Chapter 2, the superelastic strain of Ni-Ti cables reaches up to 8%, whereas monocrystalline Cu-Al-Be cables may exhibit superelastic strain of over 19%. Therefore, the current chapter assumes that SMA deformation does not exceed superelastic strain. Thus, the hardening behavior that may occur after the completion of superelastic phase transformation strain is not considered in this chapter. The adopted generalized FS hysteresis enables the extension of the proposed method to the design of other types of SC braced frames. It is noteworthy that the occurrence of hardening behavior and residual deformation at extremely large strain values may affect the seismic behavior of structures with SMA devices. Hardening behavior is generally beneficial to limiting structural displacement but tends to transfer a significant amount of force to adjacent structural members connected to braces. This phenomenon should be considered in design cases where SMA would likely deform to extremely large strain values.

7.3 SC SDOF System

The seismic behavior of structures is often dominated by structural fundamental modes. Nonlinear SDOF systems with FS hysteresis are systematically investigated under a suite of ground motions in this section. The used ground motions are the same as those discussed in Chapter 4.

7.3.1 μ-R-T Relationship

The seismic analyses of SC SDOF systems with varying FS hysteresis (as illustrated in Figure 7.1) are presented in this section under the selected 20 DBE-level ground motions. The SDOF systems with varying elastic periods T and ductility ratios μ are analyzed, where the elastic periods T range from 0.1 sec to 3.0 sec at an interval of 0.1 sec, and the ductility ratios μ are equal to 2, 3, 4, 5, and 6. In particular, the hysteresis parameters α ranging from 0.0 to 0.20 and β ranging from 0.1 to 0.9 are considered in the analyses. Nonlinear constant-μ analyses of SC SDOF systems are performed, in which a constant ductility demand is initially prescribed and the corresponding strength reduction factors R, which is the ratio of the base shear of elastic SDOF to the yield force of the SC SDOF system, are subsequently searched by iteratively changing the yield point of SC SDOF systems. Consequently, the μ-R-T relationship of SDOF systems with FS hysteresis is constructed. Figure 7.2 shows the μ-R-T relationships of four FS models with different α and β combinations, namely, (α = 0.04, β = 0.5), (α = 0.04, β = 0.9), (α = 0.16, β = 0.5), and (α = 0.16, β = 0.9). In comparison with the first baseline case, the second and third combinations represent cases with enhanced β and α levels, and the fourth combination represents the simultaneous increase of α and β. Large α and β values are generally beneficial to SC SDOF systems because they allow using large strength-reduction factors R. Therefore, the variability in hysteretic parameters α and β should be appropriately considered in designing SC structures. The following formula proposed by Seo (2005) is adopted in this chapter to simulate the μ-R-T relationships shown in Figure 7.2:

$$R = \mu^{\exp\left(a/T^b\right)} \tag{7.1}$$

where a and b are the coefficients that depend on the aforementioned hysteretic parameters. Parameter a is usually negative. This empirical relationship is selected among various options because of the following reasons. (1) The formula has a clear physical implication: when $T \rightarrow 0$, $R \rightarrow 1$, and when $T \rightarrow \infty$, $R \rightarrow \mu$. (2) The influence of hysteretic parameters α and β can be conveniently incorporated into this formula. (3) The relationship is expressed using a relatively simple single formula. Through regression analyses based on Figure 7.2, the following two coefficients are suggested:

$$a = -0.38 + 0.51\alpha + 0.16\beta \tag{7.2a}$$

$$b = 0.31 - 0.05\alpha + 0.18\beta \tag{7.2b}$$

Figure 7.2 compares the results of the numerical simulations and regression functions. Each curve in the figure represents a constant-μ curve. The adopted empirical formula agrees with the numerical simulation results well in all the cases shown in Figure 7.2.

Given the estimated initial period T and the ductility target μ of the SDOF system, the required strength reduction factor R can be determined according to Equation (7.1), and the design base shear v_y of the SDOF system is calculated as follows:

$$v_y = \frac{w \cdot S_a}{R \cdot g} \tag{7.3}$$

where w is the weight of the SDOF system, g is the gravity acceleration, and S_a is the spectral acceleration that corresponds to the natural period of the SDOF system. It is noted that a similar empirical relationship for SC SDOF system was introduced by Liu et al. (2011). However, a more precise μ-R-T relationship is derived in this chapter. Although Equation (7.3) can be directly employed in the design of SDOF systems, it requires further modification with consideration of high-mode effect in order to design multi-story braced SC frames.

7.3.2 Modified Energy Equivalent Condition

Based on the energy balance concept (Housner 1956; Leelataviwat et al. 1999), Lee et al.

(2004) proposed a modified energy equivalent equation as follows:

$$e_e + e_p = \gamma e_i \tag{7.4}$$

where e_i is the peak strain energy of an elastic SDOF system; e_e and e_p represent the peak elastic and plastic strain energy, respectively, of a corresponding inelastic SDOF system with the same initial period T; and γ is a modification factor that depends on inelastic behavior. Lee et al. (2004) proposed a simple estimation of γ based on the ductility demand for EP behavior. However, the seismic analyses of the SC SDOF systems reveal that the modification factor is not only dependent on ductility demand μ and natural period T, but is also affected by hysteretic parameters α and β. Thus, a new estimation of factor γ is derived for the SC SDOF system in this chapter.

For two SDOF systems (elastic and inelastic, respectively) with the same initial stiffness k_e, Figure 7.3 illustrates the energy equivalence concept in the form of peak base shear vs. peak displacement curves, in which v_y and δ_y refer to the yield force and the corresponding yield displacement, respectively, of the inelastic SDOF system. v_e and δ_e are the peak resisting force and displacement, respectively, of the corresponding elastic SDOF system. $\delta_u = \mu \cdot \delta_y$ represents the peak displacement of the inelastic SDOF system. Finally, α denotes the post-yield stiffness ratio. In the two SDOF systems, the three energy terms in Equation (7.4) can be computed as follows:

$$e_e = \frac{1}{2} v_y \delta_y \tag{7.5}$$

$$e_p = \frac{1}{2} v_y \delta_y (\mu - 1)\left[2 + \alpha(\mu - 1)\right] \tag{7.6}$$

$$e_i = \frac{1}{2} v_e \delta_e = \frac{1}{2} v_y \delta_y R^2 \tag{7.7}$$

Substituting Equations (7.5) to (7.7) into Equation (7.4) provides the estimation of the energy modification factor γ as follows:

$$\gamma = \frac{\alpha(\mu - 1)^2 + 2(\mu - 1) + 1}{R^2} \tag{7.8}$$

If the μ-R-T relationship developed in the last subsection for the SC SDOF system is substituted, then the energy modification factor can be expressed as a function $\gamma(\mu, T, \alpha, \beta)$ that considers the effects of the ductility demand μ, natural period T, and hysteretic parameters α and β of SC SDOF systems.

7.4 PBSD Approach for SMADBF

The emerging PBSD method is a probabilistic design framework that aims to realize the prescribed seismic performance of structures. Performance assessment elements are treated as a discrete Markov process that is described in a probabilistic form as follows (Deierlein et al. 2003):

$$\lambda(DV) = \iiint G\langle DV \mid DM \rangle dG\langle DM \mid EDP \rangle dG\langle EDP \mid IM \rangle d\lambda(IM) \tag{7.9}$$

where the intensity measure *IM* is commonly represented by the 5%-damped spectral acceleration at the fundamental period, i.e. $S_a(T_1, 5\%)$; *EDP* denotes engineering demand parameters such as peak inter-story drift ratios and floor accelerations; *DM* is a damage measure that refers to the damage extent of both structural and non-structural components; and *DV* is the decision variable that includes building cost, dollar losses, downtime, and casualty risks, among others. Given that *DM* is closely related to *EDP*, *DM* may be directly represented by *EDP*.

In this chapter, the performance-based plastic design method (Leelataviwat et al. 1999), one of the well-known PBSD methods, is modified for SMA-based SC structural systems. This PBSD method has been successfully applied in the design of various structural systems. However, this study is the first attempt to extend this method to the design of seismic-resisting SC frames with SMADBs.

7.4.1 Performance-based Plastic Design Method

The performance-based plastic design procedure was firstly proposed by Leelataviwat et al. (1999). It was originated from the energy equivalence concept through an investigation of an elastic and perfectly plastic structural system (Housner 1956). Since then, the performance-based plastic design method has been successfully applied to the seismic designs of steel moment frames (Lee et al. 2004), concentrically braced frames (Chao and Goel 2006a), eccentrically braced frames (Chao and Goel 2006b), truss moment frames (Goel and Chao 2008), buckling-restrained braced frames (Sahoo and Chao 2010), and buckling-restrained knee-braced truss moment frames (Yang et al. 2014). The key concept in the performance-based plastic design remains to be the modified energy equivalent condition (Lee et al. 2004). When applied to multi-story frames, the modified energy equivalent condition is expressed as follows:

$$E_e + E_p = \gamma E_i \tag{7.10}$$

where E_e and E_p denote the peak elastic and plastic strain energy, respectively, of an inelastic MDOF structure; E_i is the peak elastic strain energy of a corresponding elastic MDOF structure with the same elastic periods; and γ indicates the energy modification factor.

When a structure behaves elastically, the peak strain energy can be approximated by the seismic input energy as follows (Housner 1956):

$$E_i = \frac{1}{2}\frac{W}{g}S_v^2 = \frac{1}{2}\frac{W}{g}\left(\frac{S_a T}{2\pi}\right)^2 \tag{7.11}$$

where W is the total building weight; T is the fundamental period of the structural system; and S_v and S_a are the pseudo-velocity and pseudo-acceleration spectra, respectively. The total building weight W, instead of the first modal weight, is used in Equation (7.11) to account for multiple vibration modes. The estimation shown in Equation (7.11) is based on the assumption that the pseudo-velocity spectra for different vibration modes are nearly constant and can be represented by the spectral value corresponding to the fundamental period $S_v(T)$.

In an inelastic structure, Akiyama (1985) approximated elastic vibrational energy by reducing the MDOF structure into an SDOF system with a weight W:

$$E_e = \frac{1}{2}\frac{W}{g}\left(\frac{V_y g}{W}\frac{T}{2\pi}\right)^2 = \frac{WT^2 g}{2\pi^2}\left(\frac{V_y}{W}\right)^2 \tag{7.12}$$

which implies that the relationship between the yielding base shear V_y and the corresponding pseudo-acceleration A_y is

$$V_y = \frac{W}{g} A_y \tag{7.13}$$

The preceding equation is accurate for an SDOF system; however, it only functions as an approximation that may slightly underestimate pseudo-acceleration for an MDOF structure (Chopra 2001). The plastic energy E_p of an inelastic multistory frame can be computed based on the lateral seismic force and plastic floor displacement of each floor. Compared with Lee et al. (2004), the computation of E_p in this study particularly considers the favorable effect of the "post-yield" stiffness ratio α in a form similar to that of Equation (7.6), as follows:

$$E_p = \frac{1}{2}\left(\sum_{i=1}^{n} F_i h_i \theta_p\right)\left[2 + \alpha\left(\mu - 1\right)\right] \tag{7.14}$$

where F_i is the lateral seismic force on the ith floor, and θ_p is the plastic roof drift ratio. The variables can be expressed respectively as

$$F_i = C_i \cdot V_y \tag{7.15}$$

$$\theta_p = (\mu - 1)\theta_y \tag{7.16}$$

where n is the number of floors, C_i is the lateral force coefficient on the ith floor, h_i is the height of the ith floor from the base, and θ_y is the roof drift ratio that corresponds to the yield base shear force.

If the energy modification factor γ derived for the SC SDOF system is used for MDOF structures, the design base shear can be determined by solving Equation (7.10) after substituting Equations (7.8), (7.11), (7.12), and (7.14), as follows:

$$V_y / W = \left(-\lambda + \sqrt{\lambda^2 + 4\gamma S_a^2}\right) / 2 \tag{7.17}$$

$$\lambda = \left[1 + \frac{\alpha(\mu - 1)}{2}\right]\left(\frac{8\pi^2}{T^2 g}\right)\left(\sum_{i=1}^{n} C_i h_i\right)\theta_p \tag{7.18}$$

Equation (7.17) determines the design base shear of a multistory steel frame. If a single-story steel frame is of interest, the design base shear can be determined by a simpler formula, that is, Equation (7.3). Notably, knowledge on the structural fundamental period T, which is often unknown at the beginning of a design, is required in determining design base shear. In practice, the structural fundamental period T can be initially evaluated according to empirical relations in ASCE 7-10 (2010) or according to elastic or inelastic displacement spectrum using direct displacement-based method (Priestley and Kowalsky 2000). Iteratively adjusting T may be necessary after the initial design. Moreover, some parts of the derivation are based on the simplified SDOF assumption. Thus, Equation (7.17) only offers a reasonable approximation of the design base shear of an inelastic structure.

Equation (7.17) also enables the consideration of different lateral force distributions, which is discussed in the following subsection. Given that Equations (7.8) and (7.14) are used, determining design base shear appropriately accounts for the effects of hysteretic parameters α and β, which is essential in designing SMADBFs. Figure 7.4 plots the minimum normalized design base shear V_y/W as a function of α and β by assuming T = 1.2 s and μ = 5. The selected T and μ are consistent with the design example of the six-story braced frame presented in Section 7.5. A large α or β corresponds to small design base shear forces. When β = 0.5, increasing α from 0 to 0.2 reduces the normalized design base shear from 0.216 to 0.174, which corresponds to a decrease of approximately 20%. When α = 0, increasing β from 0.1 to 0.9 reduces the normalized design base shear from 0.246 to 0.188, which corresponds to a decrease of approximately 24%. Thus, increasing α or β has comparable benefits in reducing design base shear. Reduction reaches up to 39% when α and β are simultaneously increased from 0 to 0.2 and from 0.1 to 0.9, respectively.

7.4.2 Lateral Force Pattern

The nonlinear dynamic analyses in Chapter 5 show that the seismic behavior of SC steel braced frames may exhibit a noticeable high-mode effect. Consequently, the high-mode effect tends to result in the concentration of the maximum inter-story drift ratio in the upper stories. To mitigate the high-mode effect in seismic response of SMADBFs, a modified lateral force pattern proposed by Chao et al. (2007) is used in this chapter instead of the conventional pattern defined in ASCE 7-10 (2010). The modified lateral force pattern is defined as

$$C_i = \left(p_i - p_{i+1}\right)\left(\frac{w_n h_n}{\sum_{j=1}^{n} w_j h_j}\right)^{qT^{-0.2}} \tag{7.19}$$

$$p_i = \left(\frac{\sum_{j=i}^{n} w_j h_j}{w_n h_n}\right)^{qT^{-0.2}} \tag{7.20}$$

where w_j and h_j is the floor weight and floor height of the jth floor, respectively; and q affects the lateral force distribution along the building height and may vary with different structural systems. The lateral force distribution factors are normalized to obtain $\sum_{i=1}^{n} C_i = 1$.

Figure 7.5 shows a direct comparison between the ASCE-compliant force pattern and the modified lateral force patterns with q equal to 0.50 and 0.75, respectively, for the six-story frame described in the next section. Compared with ASCE 7-10 (2010), the force patterns adopted in this chapter allocate greater forces on top of a building. The seismic force acting on the roof is increased by approximately 67% and 23% when q is equal to 0.50 and 0.75, respectively. Such a large force on the top strengthens brace design in the upper stories. As suggested in previous studies (Chao et al. 2007), a q value equal to 0.75 is adopted to consider the high mode-induced concentration of the maximum inter-story drift in the top stories.

7.4.3 Design of SMADBs

The design shear force in each story can be determined with the lateral force distribution along the building height, and thus, the bracing elements that resist the lateral forces can be designed accordingly. The design of SMADBs depends on bracing configurations. If an inverted V-bracing configuration is utilized, then the cross-section area A_i and length l_i of the SMA cables in one brace in the ith story are given respectively by

$$A_i = \frac{\sum_{j=i}^{n} C_j V_y}{2\cos\theta_i \cdot \sigma_y} \tag{7.21}$$

$$l_i = \frac{E_{SMA}\theta_y\left(h_i - h_{i-1}\right)\cos\theta_i}{\sigma_y},\ \ h_0 = 0 \tag{7.22}$$

where E_{SMA} and σ_y are the elastic modulus and "yield" stress of the SMA cables, respectively; and θ_i is the inclination angle of the brace in the ith story.

7.4.4 Design of Frame Members

The beam and column members of SMADBFs can be designed in a manner similar to that of BRBFs according to the AISC provisions (2010). To avoid potential overloading, the adjusted brace strength should be used in the frame member design as follows:

$$P = \phi\omega R_y F_y \tag{7.23}$$

where F_y is the yield strength of braces; the overstrength factor R_y, resistant factor ϕ, and strain hardening adjustment factor ω are set as 1.1, 0.9, and 1.5, respectively. The strain hardening adjustment factor ω accounts for the increased brace force induced by the nontrivial post-yield stiffness ratio α. However, some superelastic SMAs (e.g., Ni-Ti) may experience highly apparent strain hardening after the completion of stress-induced phase transformation; a higher ω factor should be set if such strain hardening behavior is expected to occur. The SMA cables in the current configuration are stretched when the brace is subjected to either tension or compression. Consequently, the compressive and tensile strengths of the brace remain nearly the same, and thus, compression strength adjustment is unnecessary. If the beam-to-column connections are designed as hinge connections, then bending moments in the frame members are minimized, and frame columns and beams can be designed to mainly carry axial loads.

7.4.5 Step-by-step Design Procedure

The flowchart of the proposed design method for a multistory SMADBF is provided in Figure 7.6. The design procedure is outlined as follows.

1. Specify the design parameters of the SMADBF, such as the total number of stories n, story height h_i, number of braced bays, and tributary weight w_i in each floor level.
2. Characterize the "post-yield" stiffness ratio α and energy dissipation factor β of the selected SMA materials.
3. Specify the performance objectives, and determine the corresponding controlled *EDP*, such as the peak inter-story drift ratio θ_u and ductility demand μ.
4. Estimate the fundamental period T of the brace frame according to some empirical formula (e.g., ASCE 7-10 (2010)) or according to elastic or inelastic displacement spectrum using direct displacement-based method (Priestley MJN and Kowalsky 2000). The iterative adjustment of T may be necessary until the selected T converges to the final design value.
5. Calculate the yield inter-story drift ratio by $\theta_y=\theta_u/\mu$, and the inelastic inter-story drift ratio by $\theta_p=\theta_u-\theta_y$.
6. Determine the lateral force pattern C_i according to Equation (7.19), which considers a high-mode effect.
7. Determine the strength reduction factor R of the SDOF system by substituting T, μ, α, and β into Equation (7.1).
8. Determine λ by substituting θ_p, μ, α, and C_i into Equation (7.18), and determine γ subsequently according to Equation (7.8).
9. Determine the design base shear V_y by substituting λ, γ, S_a, and W into Equation (7.17).
10. Determine the lateral force F_i on each floor according to Equation (7.15).
11. Design the SMADBs, including the determination of cross-section area and length of the SMA cables according to Equations (7.21) and (7.22), respectively.
12. Design column and beam members based on the adjusted brace strength.

13. Check the fundamental period T of the frame, and adjust the design if the actual T is far from the initial assumption in Step 4.
14. Evaluate structural seismic performance, and adjust the design if the seismic performance fails to satisfy the performance objectives. For example, the design base shear V_y and the lateral force pattern C_i can be modified.

7.5 Design Example of SMADBF

7.5.1 Building Model

A six-story braced frame is adopted in this section. It has identical configuration, mass, and dimension as that in Chapter 5. Figure 7.7 repeats the plan and elevation layouts of the prototype structure. Different from Figure 5.2, the size of columns and beams is still unknown until the design is completely conducted. The original design employed a response modification factor of 8 and an occupancy importance factor of 1, while the proposed method will not use these two design parameters.

This six-story frame, including the braces, beams, and columns, is redesigned as several SMADBFs using the PBSD method presented in the last section. Moreover, all beam-to-column connections in the original design are modified as hinge connections in this chapter because the latter can eliminate connection moment and accommodate large rotation without damage (Fahnestock et al. 2007). Figure 7.7(b) shows a close-up view of the beam-to-column connection suggested by Fahnestock et al. (2007).

7.5.2 Seismic Performance Targets

The modern PBSD should properly consider structural and non-structural damages. The designed SMADBFs can bear a large lateral deformation without significant damage because of the excellent superelasticity of SMAs and the hinge design of beam-to-column connections. Among many damage measure indices, the peak inter-story drift ratio is often regarded as the most straightforward option. However, the limits of inter-story drift ratio that correspond to damage levels vary among different design specifications. For example, ASCE (41-06) (2007) presents a wide range of inter-story drift ratios from 1% to 2% for various non-structural components at the DBE hazard level. The Vision 2000 report (1995) defines three performance targets that correspond to three seismic hazard levels in consideration of structural and non-structural damages (i.e., 0.5%, 1.5%, and 2.5% at the FOE, DBE, and MCE hazard levels, respectively). The report (SEAOC 1995) also recommends the post-earthquake residual inter-story drift ratios to be negligible, 0.5%, and 2.5% at the FOE, DBE, and MCE levels, respectively. For simple illustration, these performance targets suggested by the Vision 2000 report are adopted in this chapter.

The target ductility demands require considering the typical deformation capacity of SMA materials. For example, the superelastic strain of Ni-Ti is up to 8%, which corresponds to a ductility of 8, whereas monocrystalline Cu-Al-Be exhibits a considerably greater deformation capacity. In the present chapter, the ductility demands of a story drift are set as 1.7, 5.0, and 8.0 at the FOE, DBE, and MCE seismic hazard levels, respectively. These ductility demands correspond to a yield inter-story drift ratio of θ_y = 0.3%. The SMADBs undertake the same ductility demand.

Seismic damage in different types of non-structural components can be deformation- or acceleration-sensitive. In addition to the peak and residual inter-story drift ratios, floor accelerations should also be assessed. However, the acceleration limits for different non-structural components vary significantly (ASCE 2007). In this chapter, the limits for peak floor accelerations are assumed as 0.5, 1.0, and 1.5 g at the FOE, DBE, and MCE levels, respectively.

Figure 7.8 summarizes the performance targets at three seismic hazard levels. It should be noted that the current performance targets are set as sample illustrations. Designers or stakeholders can decide different performance targets if desired.

7.5.3 Building Design

The presented PBSD method does not obtain the design base shear by directly using the response modification factor but implicitly considers the μ-R-T relationship when computing the energy modification factor of input energy. Moreover, the ASCE 7-10 (2010) code uses the equivalent lateral force design method; whereas the PBSD method is based on a prescribed displacement or deformation targets, which will reduce iteration loops. In this chapter, different SC structures designed with various design base shears are expected to achieve the same performance objectives as long as the design base shears are determined from the V_y/W-α-β surface.

The aforementioned six-story frame is redesigned as six-story SMADBFs using the design procedure presented in Section 7.4.3 and outlined in Figure 7.6. Performance targets are specified at three hazard levels. The braced frames can be designed according to the performance targets at any level or even three levels simultaneously as long as the corresponding seismic spectrum is used. In this case study, the SMADBFs are initially designed according to the performance targets (including peak inter-story drift ratio and ductility demand) at the DBE level. The seismic performance of the designed frames is then assessed at the FOE and MCE levels.

Given that the developed PBSD approach enables the consideration of the variability in hysteretic parameters α and β of SMADBs, four frames with different combinations of α and β parameters are designed to examine the efficacy of the developed PBSD approach. The four frames are denoted as S1 to S4 (Table 7.1) and designed to satisfy the same performance targets. Structure S3 employs SMADBs with smaller values for hysteretic parameters α and β. Compared with S3, Structures S1 and S4 correspond to enhanced α and β parameters, respectively. Structure S2 employs braces with simultaneously enhanced α and β parameters. Among them, the parameters in Structure S1 are consistent with the brace testing results in Chapter 3.

Table 7.1 summarizes the building information of the four designed frames, including the initial design information, the design base shear, the fundamental period, and the information of SMADBs and frame members. Table 7.1 enables direct examination of the influences of the hysteretic parameters on the final design of steel braced frames. As shown in Figure 7.4, the variation in hysteretic parameters α and β leads to the distinct change in design base shear. Among the four cases, S3 and S2 are associated with the highest and lowest design base shears, respectively, whereas S1 and S4 exhibit an intermediate design base shear. Consequently, the final designs of S3 and S2 consume the most and least amount of steel, respectively. S1 and S4 use similar amounts of steel. Moreover, design base shear determines the lateral force distribution along the building height, and the lateral forces subsequently determine the cross-section areas of the SMA cables in the braces. However, the length of the SMA cables in the braces is determined by the yielding inter-story drift ratio θ_y. Thus, all four frames use the same cable lengths: 1.05 m in the first story and 0.90 m in the other stories. Compared with S3, Structures S1 and S4 reduce the material consumption of steel and SMA by approximately 4% and 13%, respectively. Structure S2 reduces steel and SMA consumption by 15% and 25%, respectively. These results indicate that using SMADBs with greater α and β values in the design is favorable and cost-effective.

The fundamental period of the six-story frames is initially estimated according to the displacement target. According to the displacement-based design method (Priestley and Kowalsky 2000), the target roof displacement of the frame is transformed to the target displacement of an equivalent SDOF, and then structural fundamental period can be estimated from elastic or inelastic displacement spectrum. The initial estimation of the fundamental period is approximately 1.20s, which is only slightly shorter than those of the final designs of the frames ranging 1.22 s to 1.39 s. Therefore, no iterative adjustment of the fundamental period is performed in the design.

7.5.3 Seismic Performance Assessment

The numerical models are also built in OpenSees (2013), using identical modeling technology as that described in Chapter 5 except for the structural member information. Nonlinear time-history analyses are conducted to assess the seismic performance of the four designed SMADBFs at three seismic intensity levels. The 20 ground motions described in previous chapter are also employed in the dynamic simulations. This suite of ground motions originally corresponds to the DBE hazard level, but is also scaled down and up to represent the FOE and MCE levels, respectively. The durations of dynamic simulations are sufficiently long, and thus, free vibration decays and structural residual deformation can be accurately measured. The evaluated performance indices include the peak inter-story drift ratio, residual inter-story drift ratio, peak floor acceleration, and peak ductility demand of the SMADBs, where the inter-story drift ratio is defined as the ratio of the relative displacement between two adjacent floors to the corresponding story height. The ductility demand is defined as the ratio of peak displacement to "yield" displacement.

Figure 7.9 presents the results of the peak inter-story drift ratios and brace ductility demands of Frame S1 under FOE, DBE, and MCE seismic ground motions. Apparent record-to-record deviations can be observed among the results. Thus, the geometric mean of the 20 values is also plotted. Since the frame is directly designed according to the DBE spectrum and the corresponding performance targets, the seismic performance at the DBE level is first examined. Figure 7.9(c–d) show that the designed frame can satisfy the performance targets in terms of peak inter-story drift ratios and peak ductility at the DBE hazard level. The maximum inter-story drift demand at the DBE level occurs in the top story and is equal to 1.48%. The minimum response occurs in the first story, mainly because of the contribution of the fixed column bases. In general, the geometric mean inter-story drift ratios are distributed uniformly along the building height. Similar observations can be made for the brace ductility demand. Since the SMADBs are major seismic-resisting components, the brace ductility demands are essentially the same as the ductility demand of inter-story drift. Compared with the performance targets, the brace design is slightly conservative in terms of ductility demand, because the designed structure yields a bit later than expected due to the influence of fixed column bases. Another similar SMADBF is also designed using the ASCE code-compliant lateral force pattern shown in Figure 7.9. The geometric mean responses of this code-compliant frame are also shown in Figure 7.9. The deformation concentration in the upper two stories demonstrates a noticeable high-mode effect. As a result, the seismic performance of the counterpart frame considerably exceeds the design targets. This comparison clearly illustrates the benefit of the modified lateral force pattern presented in Section 7.4.2 in the PBSD procedure.

Figure 7.9(a–b) and (e–f) show the peak inter-story drift ratios and brace ductility demands of Structure S1 under the FOE- and MCE-level ground motions, respectively. At the MCE level, observations similar to those at the DBE levels may be made. The designed Frame S1 well satisfies the MCE performance targets of the peak inter-story drift, but it demonstrates a slightly smaller brace ductility demand than the performance targets. The first story still presents the minimum geometric mean response, whereas the other stories exhibit quite uniform response. At the FOE level, the designed Structure S1 slightly exceeds the performance targets in terms of inter-story drift ratios, because it is directly designed at the DBE level, that is, the design base shear is determined based on the DBE spectrum. In this example, the performance targets at the FOE level are more critical than those at the other levels. Thus, this result clearly indicates that the design of seismic-resisting structures may not always be governed by the performance targets under significant earthquakes. If a significant exceedance of the performance targets is observed, then the structural design should be adjusted or the structure should be redesigned according to the most stringent performance targets (i.e., the FOE-level performance targets in this case). However, no further adjustment to the design is made in this case given that the inter-story drift ratios exceed the targets by less than 0.1% and brace ductility demand still satisfies the performance targets. The ductility demands in some FOE-level cases are less than a unit, which implies that those braces are fully elastic. Figure 7.10 compares the seismic performance of the four designed frames (S1–S4) in terms of peak inter-story drift ratios and peak ductility demands. The performance targets at the three seismic hazard levels are also illustrated in the figure. All four frames are designed to satisfy the same performance targets despite the different design base shears used in each frame. In general, all the structures perform similarly and satisfy design targets, except for slight exceedances of the inter-story drift targets at the FOE level. This result validates the efficacy of the proposed PBSD method, which can design the SMADBFs by considering different hysteretic parameters to achieve the same seismic performance.

Figure 7.11 examines peak floor acceleration demand at the FOE, DBE, and MCE levels. Floor acceleration demands are satisfactorily controlled and are less than the performance targets in all four structures at the three seismic hazard levels. The distribution of peak floor accelerations is fairly uniform along the building height. In general, the four design frames exhibit similar seismic performances with regard to peak acceleration demands. Structure S2 gives the best control performance at the three seismic levels because its braces are designed with enhanced α and β values.

Figure 7.12 shows the residual inter-story drift ratios of the four designed frames after FOE, DBE, and MCE earthquakes. The residual inter-story drift ratios are nearly zero at the FOE and DBE levels, and remain very small even at the MCE level. The residual inter-story drift ratio tends to concentrate in the first story because of the yielding of the fixed column bases. No plastic hinges are formed in the beam and column sections except for the fixed column bases. The residual deformation in the upper stories is attributed to the unrecovered plastic rotation at the column bases. The geometric mean residual inter-story drift ratio is less than 0.01% at the MCE level, which is considerably less than the peak inter-story drift ratios. The inelastic deformation is nearly completely recovered because of the excellent SC capacity of SMADBs.

Figure 7.13 plots the most critical points of P-M interactions at the column bases, where the horizontal and vertical axes represent the normalized bending moment and axial load, respectively. Since the bending moment dominates the deformation, these critical points occur when the bending moments reach their peak values. All points are assembled in the first quadrant for easy comparison. The four frames (S1–S4) have no plastic hinge under all ground motions at the FOE level and most ground motions at the DBE levels. As ground motion intensity increases, plastic hinges form in several cases at the DBE level and more so at the MCE level. A similar trend is observed in all four structures. Although the formed plastic hinges produce large inelastic deformation demand, residual deformation remains minimal because of the SC capability of SMADBs. This can be illustrated by the stress-strain curve of the outermost fiber at the column base section shown in Figure 7.14, which corresponds to the seismic response of Structure S1 under the ground motion record LA 18 is selected as the representative case.

7.6 Summary

This chapter investigates the seismic design of SC steel frames with SMADBs. The novel seismic-resisting bracing elements using superelastic SMAs exhibit favorable SC and energy-dissipation capabilities. Based on the performance-based plastic design, this chapter develops a PBSD approach for SMADBFs with the following particular modifications: (1) the μ-R-T relationship of SDOF systems with FS models is determined through regression analysis and used in PBSD; (2) two important hysteretic parameters, namely, the "post-yield" stiffness ratio and the energy dissipation factor, are explicitly considered in PBSD to account for the great variability in these two hysteretic parameters; and (3) a modified lateral force pattern is used in PBSD to mitigate the noticeable high-mode effect that was highlighted in previous seismic analyses of SMADBFs. To validate the developed PBSD approach, four examples of six-story seismic-resisting SMADBFs are designed with different combinations of "post-yield" stiffness ratio (α) and hysteresis width (β). The four frames are initially designed according to the prescribed performance targets at the DBE level, whereas the seismic performances of the designed frames at three seismic hazard levels (i.e., FOE, DBE, and MCE) are assessed through nonlinear time-history analyses after the design process.

The results of the nonlinear time-history analyses successfully validate the developed PBSD approach for SMADBFs. Some notable observations are as follows:

1. Despite their different designs, the four SMADBFs associated with different hysteretic parameters can satisfactorily achieve the same performance targets prescribed in advance;
2. The final designs of the four SMADBFs reveal that greater α and/or β parameters of braces are favorable in terms of cost-effectiveness;
3. The modified lateral force pattern adopted in PBSD can successfully mitigate the high-mode effect in seismic responses; as a result, the designed SMADBFs exhibit uniform height-wise distribution of peak inter-story drift ratios, even if the frames exhibit inelastic behavior during severe earthquakes; and
4. The properly designed SMADBFs exhibit limited structural damage and permanent deformation even after very strong earthquakes, which clearly demonstrates the superior seismic performance of this emerging type of SC seismic-resisting structural systems.

Table 7.1 Building design information

Structures		S1	S2	S3	S4
α		0.16	0.16	0.04	0.04
β		0.5	0.9	0.5	0.9
V_y/W		0.140	0.120	0.161	0.139
T (s)		1.29	1.39	1.22	1.29
Sectional area of SMA cable in a brace (mm^2)	6th story	743.7	637.1	848.6	734.7
	5th story	1166.4	999.3	1330.9	1152.2
	4th story	1472.4	1261.5	1680.2	1454.6
	3rd story	1693.6	1451.0	1932.6	1673.1
	2nd story	1843.4	1579.3	2103.5	1821.1
	1st story	2276.3	1950.2	2597.5	2248.7
Length of SMA cable (m)	Other stories	0.90	0.90	0.90	0.90
	1st story	1.05	1.05	1.05	1.05
Volume of SMA (cm^3)		17229	14760	19660	17020
Column sections	4th–6th story	W14×53	W14×48	W14×53	W14×53
	1st–3rd story	W14×132	W14×120	W14×132	W14×132
Beam sections	4th–6th story	W14×30	W14×26	W14×34	W14×30
	1st–3rd story	W14×38	W14×30	W14×43	W14×38
Steel weight (ton)		9.9	8.8	10.3	9.9

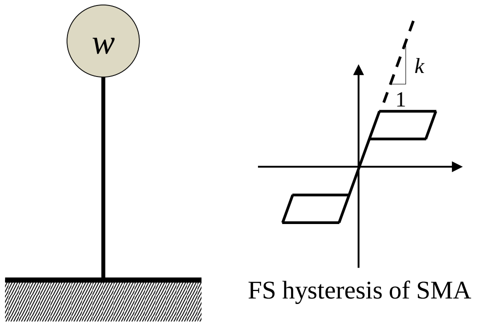

$$T = 2\pi\sqrt{\frac{w}{k \cdot g}}$$

Figure 7.1 Inelastic SC SDOF systems with FS hysteresis

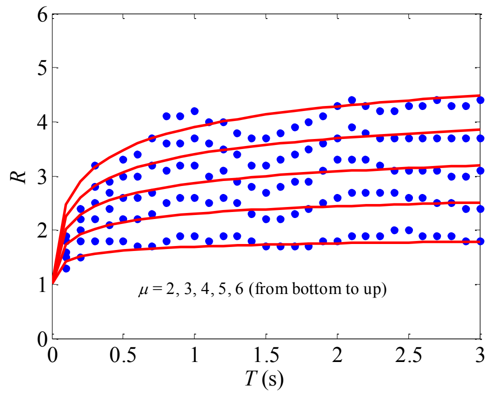

(a) α = 0.04, β = 0.5

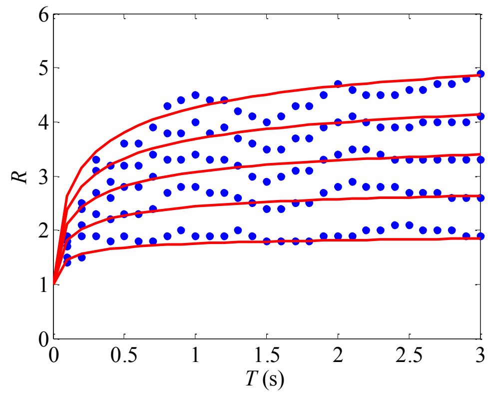

(b) α = 0.04, β = 0.9

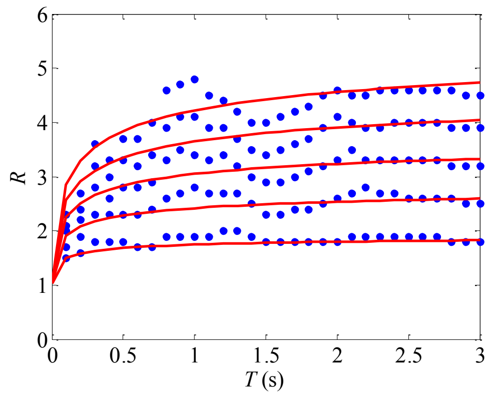

(c) α = 0.16, β = 0.5

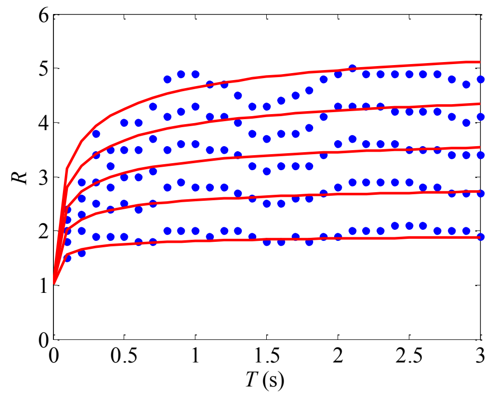

(d) α = 0.16, β = 0.9

Figure 7.2 μ-R-T relationships of SC SDOF (Dots: numerical simulation; Lines: fitting curves)

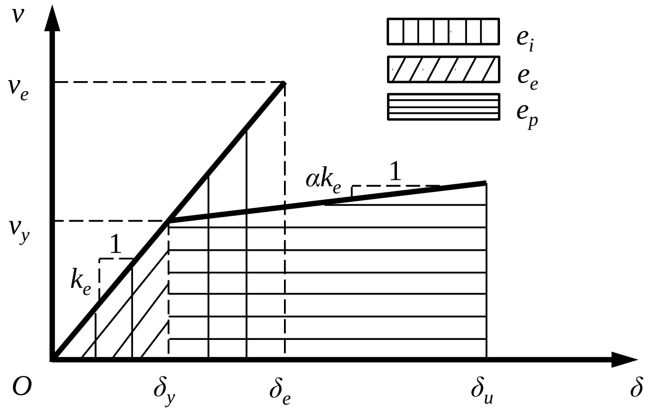

Figure 7.3 Energy equivalence concept in PBSD method

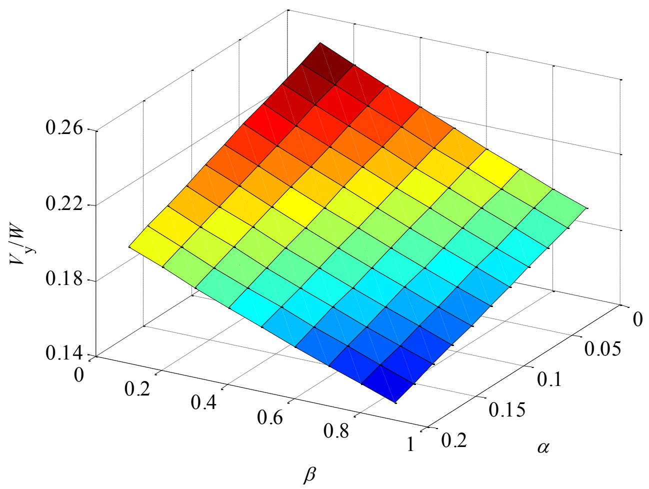

Figure 7.4 Relationship between design base shear and properties of SMADBF (T = 1.2 s and μ = 5)

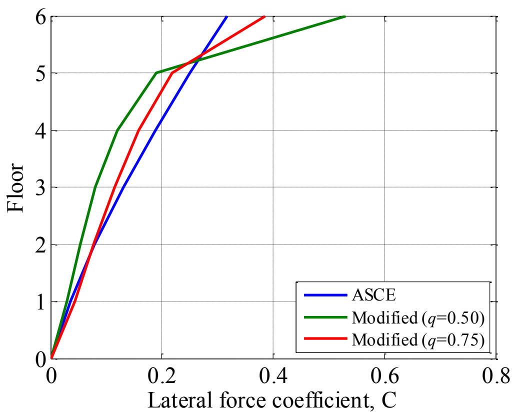

Figure 7.5 Different lateral force patterns (T = 1.2 s)

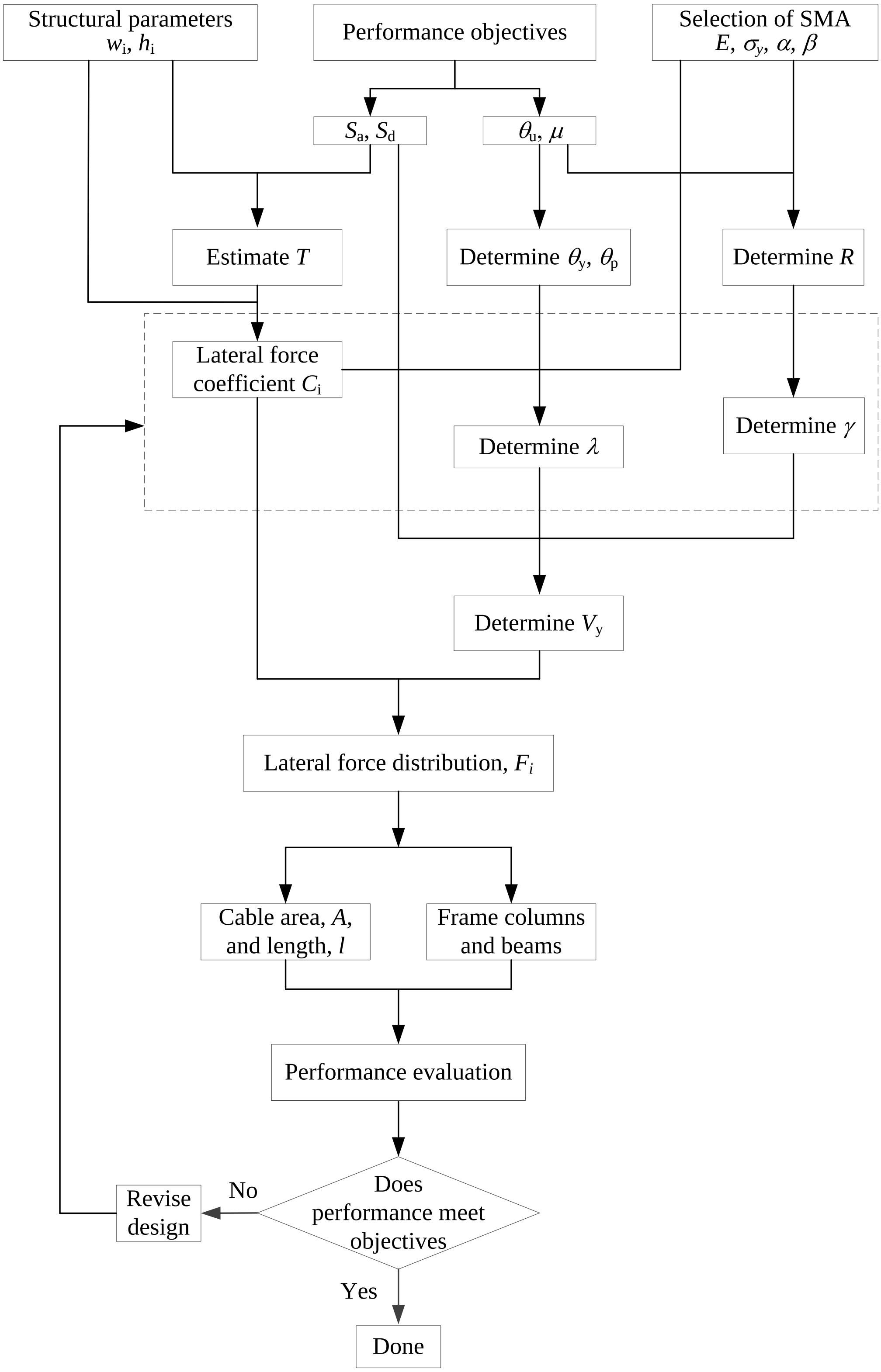

Figure 7.6 Design flow chart of SMADBF

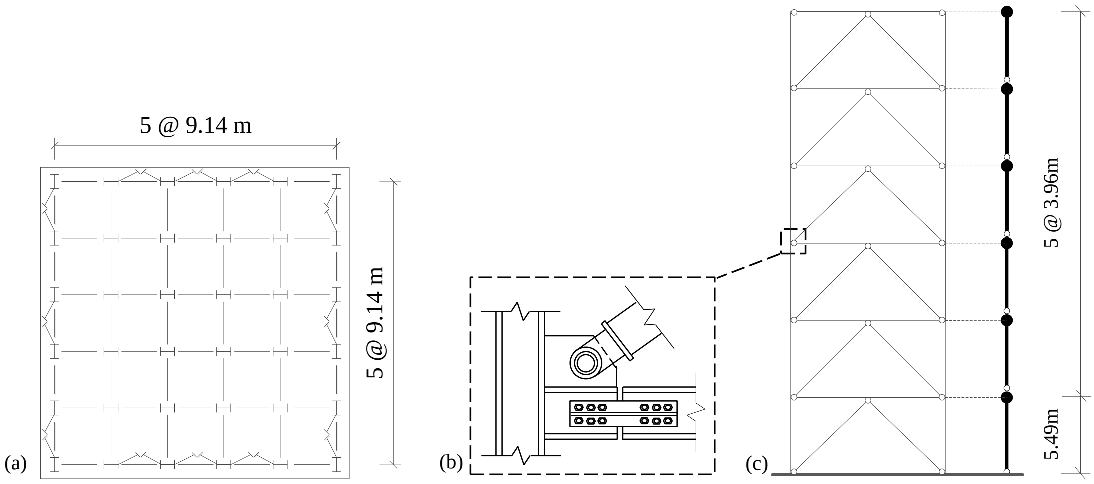

Figure 7.7 Prototype 6-story frame building with SMADB: (a) plan layout; (b) brace-to-frame and beam-to-column connections; (c) elevation view

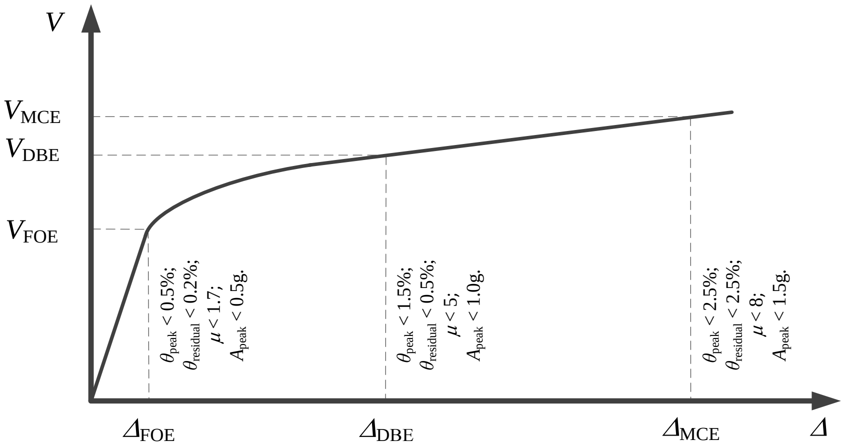

Figure 7.8 Performance targets at three discrete seismic hazard levels

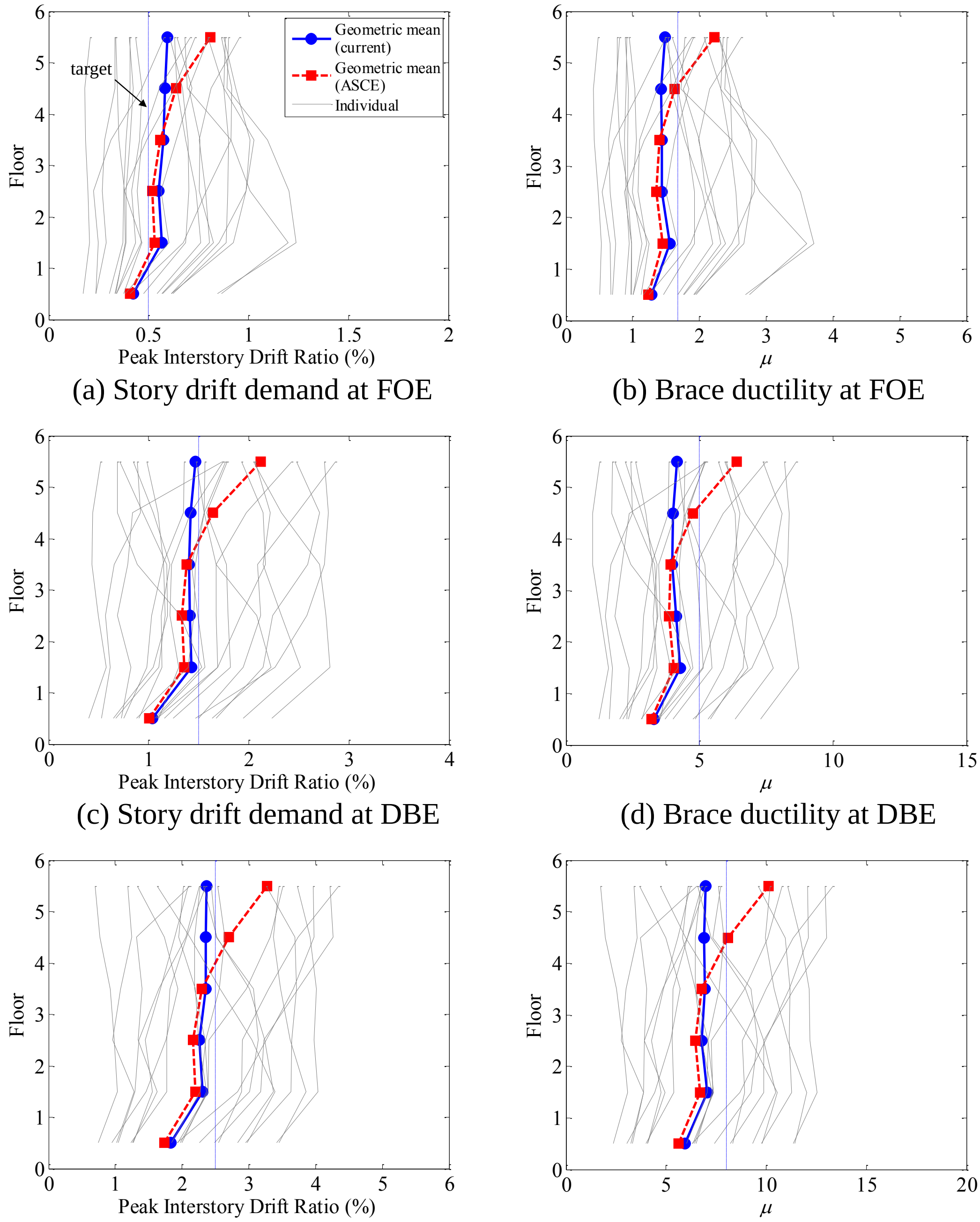

(a) Story drift demand at FOE (b) Brace ductility at FOE

(c) Story drift demand at DBE (d) Brace ductility at DBE

(e) Story drift demand at MCE (f) Brace ductility at MCE

Figure 7.9 Seismic performance of Structure S1 at three hazard levels

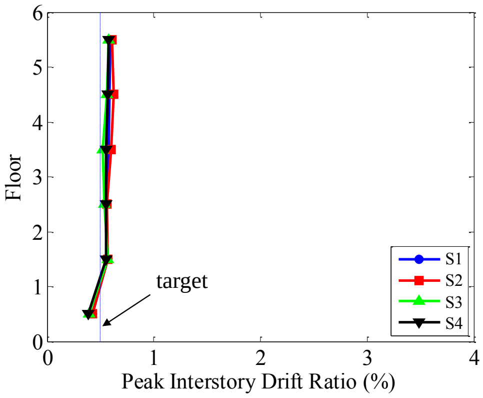

(a) Story drift demand at FOE

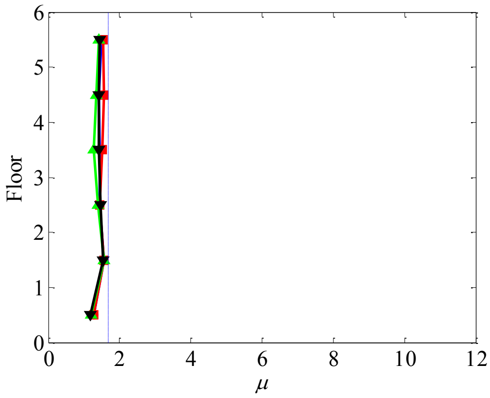

(b) Brace ductility at FOE

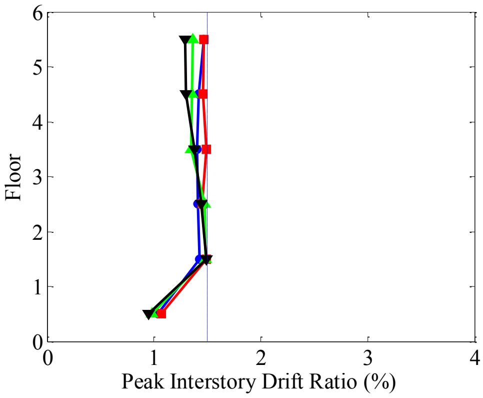

(c) Story drift demand at DBE

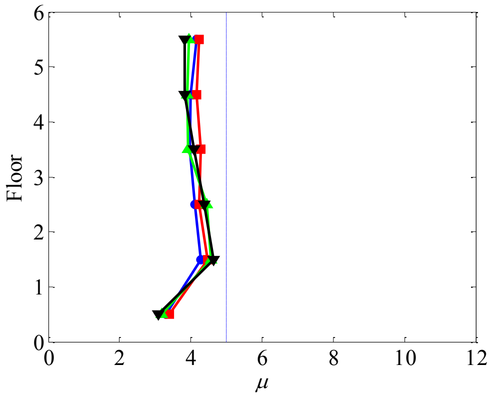

(d) Brace ductility at DBE

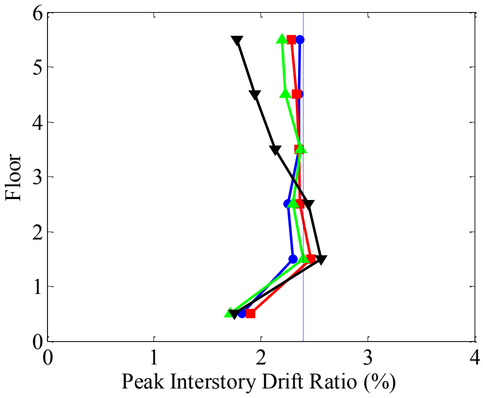

(e) Story drift demand at MCE

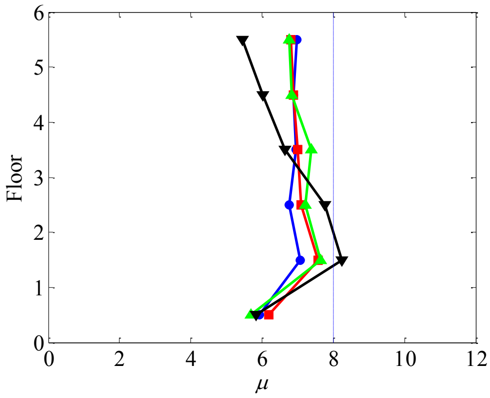

(f) Brace ductility at MCE

Figure 7.10 Seismic performances of the four designed frames with various hysteretic parameters of SMADBs

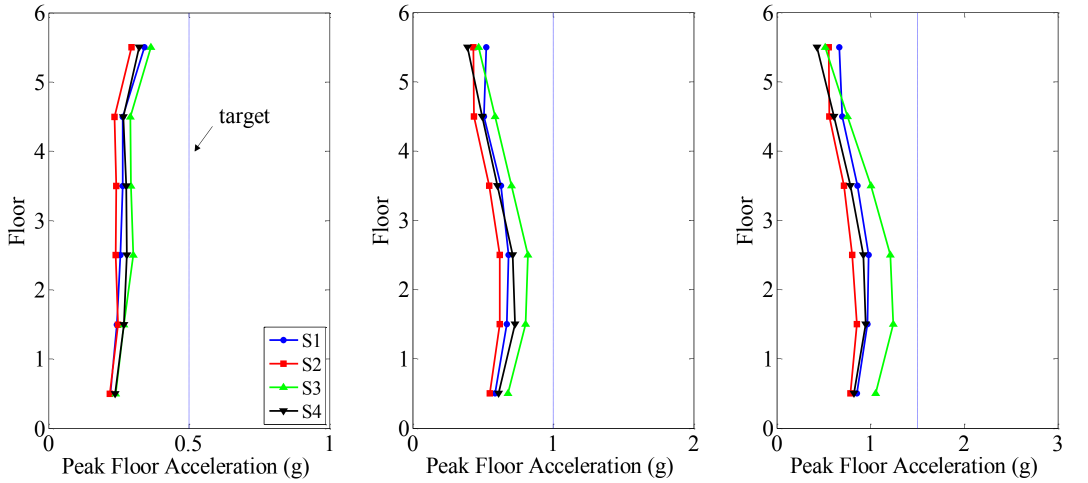

(a) FOE (b) DBE (c) MCE

Figure 7.11 Peak floor acceleration along the building height at three seismic hazard levels

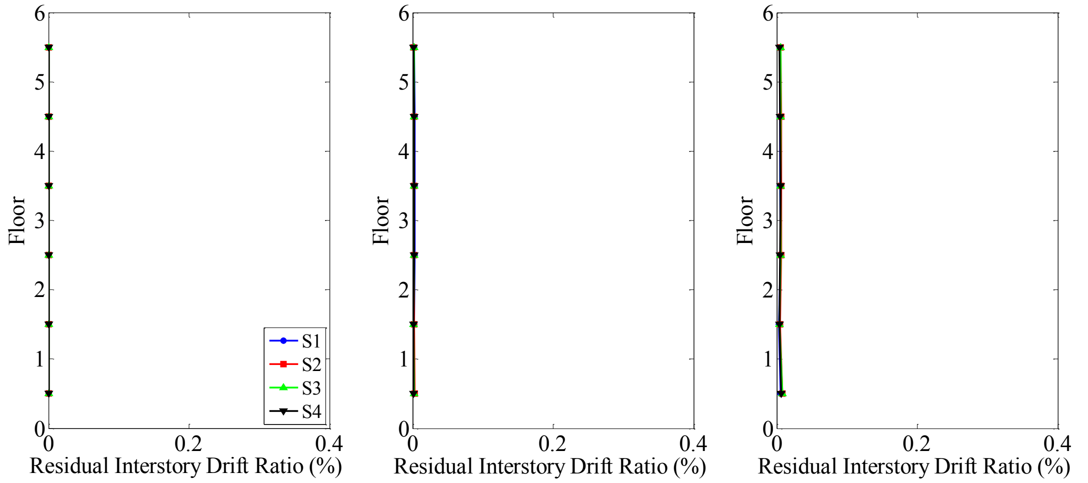

(a) FOE (b) DBE (c) MCE

Figure 7.12 Residual inter-story drift ratio along the building height at three seismic hazard levels

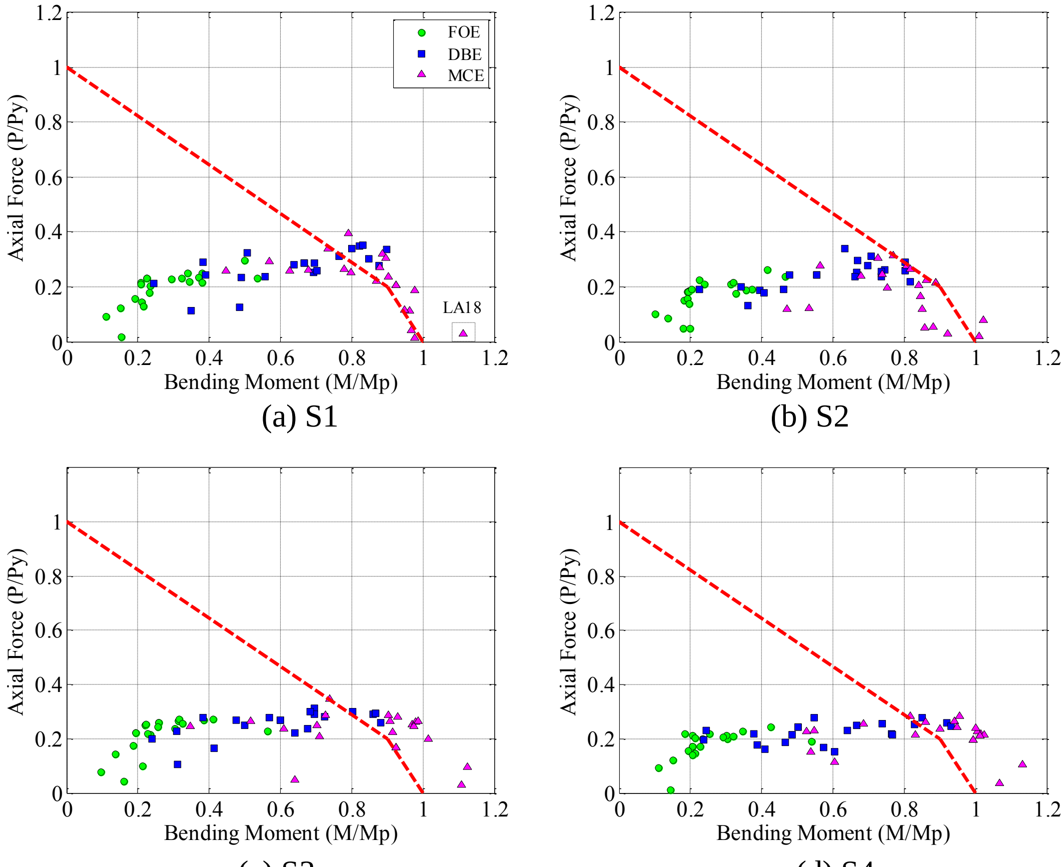

(a) S1

(b) S2

(c) S3

(d) S4

Figure 7.13 The most critical P-M interactions at the column bases at three seismic hazard levels

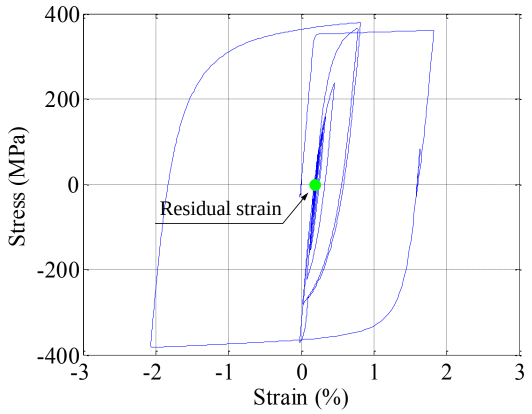

Figure 7.14 Stress-strain of the outermost fiber at column base section of Structural S1 under ground motion LA18

Chapter 8 Conclusions

8.1 Summary

Recent post-earthquake surveys and associated studies indicated that reducing residual deformation represents an inevitable need for next-generation high-performance SC structures. This need has motivated scholars to investigate and develop a variety of advanced seismic-resisting structural systems, such as SC structures with an FS hysteretic behavior. Given their inherent FS hysteresis, good fatigue life, excellent corrosion resistance, and relatively stable mechanical performance, SMAs are recognized as a promising material for an easy realization of seismic-resisting SC structures. This study numerically and experimentally investigates the seismic performance of SMA-based isolated bridges and braced frames. These two types of SMA-based SC structures are analyzed at various seismicity levels. This study is completed by conducting the following tasks:

- Different types of superelastic SMAs are compared based on material testing results. The considered properties include hysteresis characteristics, training effect, strain amplitude effect, loading frequency effect, temperature effect, and fatigue life.
- Two kinds of SMA-based energy dissipating devices are manufactured. One is wire-based, and the other is in a spring form. The mechanical behavior of these devices are discussed. The wire-based damper is the key component of the SMA-based brace installed in the braced frame.
- IDA of SMA-based isolated bridges is performed to evaluate the capability of SMA-based isolators in protecting bridges against small to large earthquakes.
- SMA-based braced frame is analyzed from a novel perspective focusing on the high-mode effect in seismic response. Direct comparisons with a similar BRBF provide valuable insights into this topic. Potential solutions to reduce the high-mode effect are also proposed.

- A series of shaking table tests and numerical simulations are conducted on a 1/4-scale model of SMA-based braced frame. This testing program is administered for the proof-of-concept and to validate a few numerical results through experimental tests.
- A PBSD method for SMA-based braced frames is developed to facilitate the seismic design of such emerging structures with a simple and effective design procedure.

8.2 Conclusions

- Ni-Ti and monocrystalline Cu-Al-Be wires both show excellent superelasticity. In particular, the monocrystalline Cu-Al-Be wires show two distinct phase transformation plateaus in stress–strain cycles and exhibit a substantial superelastic strain up to 19% at −40 °C. The Ni-Ti wires show an 8% superelastic strain above 0 °C. Both of these wires are considered suitable in seismic applications. Ni-Ti wires are used in the experimental study mainly because of their relatively low cost.
- The hysteretic shapes and equivalent damping ratios of superelastic SMA wires evidently depend on strain amplitude. The comparison between the quasi-static and dynamic testing results indicates that monocrystalline Cu-Al-Be wires are generally less sensitive to loading frequency. Contrarily, Ni-Ti wires are relatively more sensitive to loading frequency than the Cu-Al-Be wires, but they can still maintain a stable behavior within the seismic loading frequency range.
- Both types of SMA wires show a good fatigue performance and can sustain several thousands of loading cycles. This capability assures that these wires can withstand several severe earthquakes and aftershocks without the need for replacement.
- The spring tests show that air and water quench both produce excellent superelastic behavior of SMA springs. Changes in loading frequencies affect SMA springs at a significantly lower extent than SMA wires and bars.

- Spring index significantly affects the behavior of superelastic SMA springs. A small spring index generates large damping, but it reduces ductility capacity. Using less number of active coils generates a similar effect, that is, damping is improved when the ductility capacity is reduced. Hollow wires produce lower strength but larger damping than solid wires. The equivalent damping ratio of superelastic SMA springs can be enhanced through pre-stressing.
- The numerical analysis shows that the SMADBF exhibits a more significant high-mode contribution than its BRBF counterpart. Such a contribution is coupled with the fundamental mode in inelastic seismic response and causes the interstory drift ratios to concentrate in the top stories.
- The high-mode-induced deficiency of SMADBFs can be effectively mitigated by increasing either the energy dissipation factor or the post-yield stiffness ratio. The relevant findings may be applicable to other multi-story SC frames.
- Protected by SMA-based isolators, the highway bridge can fully achieve the target displacement under the prescribed seismic hazard levels. SMA-based SC isolators can effectively protect the superstructure of the highway bridge by reducing the damage in the piers and by limiting the total residual displacement of the highway bridge, especially at FE and DBE levels.
- The shaking table test results indicate that the SMADBs enable the tested frame to successfully return to the zero position with limited structural damage from a peak interstory drift ratio of more than 2.0%. This peak magnitude is considerably larger than those reported in previous experimental studies and proves that as an emerging type of seismic-resisting structures, SMADBF can withstand highly intensified seismic hazards.
- In the shaking table tests, the tested frame model was consecutively subjected to nine ground motion records with incremental intensity levels. The displacement time histories showed that nearly zero residual deformation accumulated after the whole run of earthquakes. The near-fault earthquakes did not induce an intensified seismic response.

- The numerical simulations demonstrate that the proposed model satisfactorily simulates the cyclic behavior of the SMA-based damping brace and the seismic response of the SC steel braced frame. Good agreement is achieved in the comparison of the time history response of roof displacement and base shear between the numerical simulation and experimental data.
- The SC steel frame with SMADBs can sustain several strong earthquakes without severe damage, performance deterioration, or permanent deformation of the frame. SMADBs can also be reused without the need for replacement or repair.
- In spite of their different designs, the four SMADBFs with different hysteretic parameters that are designed according to the proposed design method can satisfactorily achieve the same performance targets prescribed in advance. This observation clearly justifies the effectiveness of the proposed PBSD for SMADBFs.
- The final designs of the SMADBF reveal that large post-yield stiffness and energy dissipation parameters of SMADBs are favorable in terms of cost-effectiveness.
- The modified lateral force pattern adopted in PBSD can successfully mitigate the high-mode effect in seismic responses. As a result, the designed SMADBFs exhibit quite a uniform heightwise distribution of peak interstory drift ratios even if the frames behave inelastically under severe earthquakes.
- The properly designed SMADBFs experience an extremely limited structural damage and permanent deformation even after the occurrence of severe earthquakes. This finding clearly demonstrates the excellent seismic performance of this emerging type of seismic-resisting SC structural system.

8.3 Future work

The following future works are recommended along the lines of the current research.

- A sophisticated constitutive model for monocrystalline Cu-Al-Be SMA should be developed to accurately capture its complex hysteresis.

- If such a constitutive model is developed, then the potential use of monocrystalline Cu-Al-Be SMA wires as damping devices in seismic-resisting systems can be evaluated by subjecting them to real seismic ground motion records.
- Although the excellent low-temperature performance of monocrystalline Cu-Al-Be wires implies their potential outdoor applications, the corrosion resistance of monocrystalline Cu-Al-Be SMAs needs to be carefully assessed because they may be exposed to a corrosive outdoor environment.
- Compared with the commonly used axial behavior, the flexural and torsional behavior has not been paid enough attention gained in the past decades from the viewpoint of earthquake engineering. Making use of these two capacities of superelastic SMAs for seismic protection imposes new challenges. Therefore, further studies on bending- and torsion-based SMA dampers should be conducted in the future.
- The parametric analysis on SMA springs should be given further attention, and finite element analyses may help understand the cyclic behavior of SMA springs.
- High-performance SMA spring-based dampers in seismic applications may require a large force capacity, which warrants some future exploration.
- SMA-based isolated bridges have received considerable research attention, whereas building structures protected by SMA-based isolators are yet to be widely looked into. Further research should be conducted to understand the seismic behavior of SMA-based isolated buildings.
- The current findings with regard to high-mode effect in SC structures are drawn from multi-story braced frames. General studies on SC MDOF systems should be performed to generalize the conclusions obtained in this thesis.
- The proposed PBSD method can be extended to other SC structures of different structural forms.
- Although many studies have emphasized that the use of SMAs can significantly reduce the repair cost and downtime of buildings, a quantitatively cost analysis

is still missing. As such, a probabilistic framework for loss estimation should be developed for SMA-based SC structures. Obtaining quantitative evidence from cost analysis can help SMAs receive due attention from the earthquake engineering community.

Although the past studies have demonstrated the promising performance of SMAs in the seismic protection of civil structures, the applications of these alloys in real structures are still limited. The reason behind this case is the insufficient experimental validation and the high material cost at present. Future research should systematically address the lack of experimental validation. The higher initial cost of SMA material than that of conventional civil engineering materials may be compensated by the remarkably reduced post-earthquake repair cost and downtime owing to SC capability. The cost-effectiveness of SMA-based dampers or isolators needs cautious investigations in the future as well.

References

Abbott, A., (2001), “Rescuers of Europe's cultural heritage struggle for funding”, *Nature*, 414(6864): 572–572.

AISC, (2010), *Seismic provisions for structural steel buildings*. ANSI/AISC 341-10. Chicago.

Akiyama, H., (1985), *Earthquake-resistant limit-state design of buildings*, University of Tokyo Press, Japan.

Alam, M.S., Youssef, M.A., and Nehdi, M., (2008), “Analytical prediction of the seismic behavior of superelastic shape memory alloy reinforced concrete elements”, *Engineering Structures*, 30:3399–3411.

Alam, M.S., Youssef, M.A., and Nehdi, M., (2009), “Seismic performance of concrete frame structures reinforced with superelastic shape memory alloys”, *Smart Structures and Systems*, 5(5): 565–585.

American Society of Civil Engineers (ASCE), (2010), *Minimum design loads for buildings and other structures*, Reston, VA.

American Society of Civil Engineers (ASCE), (2007), *Seismic Rehabilitation of Existing Buildings (41-06)*, Reston, VA.

Andrawes, B., and DesRoches, R., (2005), “Unseating prevention for multiple frame bridges using superelastic devices”, *Smart Materials and Structures*, 14(3): 60–67.

Andrawes, B., and DesRoches, R., (2007a), “Comparison between shape memory alloy seismic restrainers and other bridge retrofit devices”, *Journal of Bridge Engineering, ASCE*, 12(6): 700–709.

Andrawes, B., and DesRoches, R., (2007b), “Effect of ambient temperature on the hinge opening in bridges with shape memory alloy seismic restrainers”, *Engineering structures*, 29(9): 2294–2301.

Applied Technology Council (ATC), (1996), *Seismic Evaluation and Retrofit of Concrete Buildings*, Report No. ATC-40, Redwood City, CA.

Araki, Y., Endo, T., Omori, T., Sutou, Y., Koetaka, Y., and Kainuma, R., et al, (2011), "Potential of superelastic Cu-Al-Mn alloy bars for seismic applications", *Earthquake Engineering and Structural Dynamics*, 40(1):107–115.

Araki, Y., Maekawa, N., Shrestha, K. C., Yamakawa, M., Koetaka, Y., Omori, T., and Kainuma, R., (2014), "Feasibility of tension braces using Cu-Al-Mn superelastic alloy bars", *Structural Control and Health Monitoring*, 21(10): 1304–1315.

Asgarian, B., and Moradi, S., (2011), "Seismic response of steel braced frames with shape memory alloy braces", *Journal of Constructional Steel Research*, 67(1): 65–74.

Auricchio, F., and Sacco, E., (2001), "Thermo-mechanical modelling of a superelastic shape-memory wire under cyclic stretching-bending loadings", *International Journal of Solids and Structures*, 38(34): 6123–6145.

Attanasi, G., and Auricchio, F., (2011), "Innovative superelastic isolation device", *Journal of Earthquake Engineering*, 15(S1): 72–89.

Auricchio, F., Fugazza, D., and Desroches, R., (2006), "Earthquake performance of steel frames with nitinol braces", *Journal of Earthquake Engineering*, 10(S1): 45–66.

Birman, V., (1997), "Review of mechanics of shape memory alloy structures", *Applied Mechanics Reviews*, 50(11): 629–645.

Bo, Z., and Lagoudas, D., (1999), "Thermomechanical modeling of polycrystalline SMAs under cyclic loading, part IV: modeling of minor hysteresis loops", *International Journal of Engineering Science*, 37(9):1205–1249.

Branco, M., Gonçalves, A., Guerreiro, L., and Ferreira, J., (2014), "Cyclic behavior of composite timber-masonry wall in quasi-dynamic conditions reinforced with superelastic damper", *Construction and Building Materials*, 52: 166–176.

Brinson, L.C., (1993), "One-dimensional constitutive behavior of shape memory alloys: thermomechanical derivation with non-constant material functions and redefined martensite internal variable", *Journal of Intelligent Material Systems and Structures*, 4(2), 229–242.

Brocca, M., Brinson, L.C., and Bažant, Z.P., (2002), "Three-dimensional constitutive model for shape memory alloys based on microplane model", *Journal of the*

Mechanics and Physics of Solids, 50(5): 1051–1077.

Cardone, D., Dolce, M., and Ponzo, F.C., (2006), "The behaviour of SMA isolation systems based on a full-scale release test", *Journal of Earthquake Engineering*, 10(06): 815–842.

Casarotti, C., and Pinho, R., (2007), "An adaptive capacity spectrum method for assessment of bridges subjected to earthquake action", *Bulletin of Earthquake Engineering*, 5(3): 377–390.

Casciati, F., and Faravelli, L., (2009), "A passive control device with SMA components: from the prototype to the model", *Structural Control and Health Monitoring*, 16(7-8): 751–765.

Casciati, F., Faravelli, L., and Al Saleh, R., (2009), "An SMA passive device proposed within the highway bridge benchmark", *Structural Control and Health Monitoring*, 16(6):657–667.

Casciati, F., Faravelli, L., and Fuggini, C., (2008), "Cable vibration mitigation by added SMA wires", *Acta Mechanica*, 195(1–4): 141–155.

Casciati, F., Faravelli, L., and Hamdaoui, K., (2007), "Performance of a base isolator with shape memory alloy bars", *Earthquake Engineering and Engineering Vibration*, 6(4): 401–408.

Cecconi, M., Pane, V., and Vecchietti, A., (2014), "Seismic displacement-based design of embedded retaining structures", *Bulletin of Earthquake Engineering*, 1–23.

Chao, S.H., and Goel, S.C., (2006a), "A seismic design method for steel concentric braced frames (CBF) for enhanced performance", *Proceedings of the 4th International Conference on Earthquake Engineering*, Taipei, Taiwan.

Chao, S.H., and Goel, S.C., (2006b), "Performance-based seismic design of eccentrically braced frames using target drift and yield mechanism as performance criteria", *Engineering Journal, AISC*, 43(3): 173–200.

Chao, S.H., Goel, S.C., and Lee, S.S., (2007), "A seismic design lateral force distribution based on inelastic state of structures", *Earthquake Spectra*, 23(3): 547–569.

Chopra, A.K., and Goel, R.K., (1999), "Capacity-demand-diagram methods based on inelastic design spectrum”, *Earthquake Spectra*, 15(4): 637–656.

Chopra, A.K., and Goel, R.K., (2000), “Evaluation of NSP to estimate seismic deformation: SDF systems”, *Journal of Structural Engineering, ASCE*, 126(4): 482–490.

Christopoulos, C., Filiatrault, A., and Folz, B., (2002a), “Seismic response of self-centring hysteretic SDOF systems”, *Earthquake Engineering and Structural Dynamics*, 31(5):1131–1150.

Christopoulos, C., Filiatrault, A., Uang, C.M. and Folz, B., (2002b), “Post-tensioned energy dissipating connections for moment resisting steel frames”, *Journal of Structural Engineering, ASCE*, 128(9): 1111–1120.

Christopoulos, C., Tremblay, R., Kim, H.J., and Lacerte, M., (2008), “Self-centering energy dissipative bracing system for the seismic resistance of structures: development and validation”, *Journal of Structural Engineering, ASCE*, 134(1): 96–107.

Chung, J.H., Heo, J.S., and Lee, J.J., (2006), “Modeling and numerical simulation of the pseudoelastic behavior of shape memory alloy circular rods under tension/torsion combined loading”, *Smart Materials and Structures*, 15: 1651–1660.

Clayton, P.M., Berman, J.W., and Lowes, L.N., (2011), “Seismic design and performance of self-centering steel plate shear walls”, *Journal of Structural Engineering, ASCE*, 138(1):22–30.

Constantinou, M.C., and Symans, M.D., (1993), “Experimental study of seismic response of buildings with supplemental fluid dampers”, *The Structural Design of Tall Buildings*, 2(2): 93–132.

Deierlein, G.G., Krawinkler, H., and Cornell, C.A., (2003), “A framework for performance-based earthquake engineering”, *Proceedings of the Pacific Conference on Earthquake Engineering*, 1–8.

DesRoches, R., and Delemont M., (2002), “Seismic retrofit of simply supported bridges using shape memory alloys”, *Engineering Structures*, 24: 325–332.

DesRoches, R., McCormick, J., and Delemont, M., (2004), “Cyclic properties of superelastic shape memory alloy wires and bars”, *Journal of Structural Engineering,* *ASCE*, 130(1):38–46.

DesRoches, R., and Smith, B., (2004), "Shape memory alloys in seismic resistant design and retrofit: a critical review of their potential and limitations", *Journal of Earthquake Engineering*, 8(03): 415–429.

DesRoches, R., Taftali, B., and Ellingwood, B.R., (2010), "Seismic performance assessment of steel frames with shape memory alloy connections. Part I—analysis and seismic demands", *Journal of Earthquake Engineering*, 14(4): 471–486.

Dezfuli, F.H., and Alam, M.S., (2013), "Shape memory alloy wire-based smart natural rubber bearing", *Smart Materials and Structures*, 22(4): 045013.

Dezfuli, F.H., and Alam, M.S., (2014), "Performance-based assessment and design of FRP-based high damping rubber bearing incorporated with shape memory alloy wires", *Engineering Structures*, 61(1):166–183.

Dolce, M., Cardone, D., and Marnetto, R., (2000), "Implementation and testing of passive control devices based on shape memory alloys", *Earthquake Engineering and Structural Dynamics*, 29(7): 945–968.

Dolce, M., and Cardone, D., (2001a), "Mechanical behaviour of shape memory alloys for seismic applications 1. Martensite and austenite NiTi bars subjected to torsion", *International Journal of Mechanical Sciences*, 43(11): 2631–2656.

Dolce M., and Cardone D., (2001b), "Mechanical behavior of shape memory alloys for seismic applications 2. Austenite NiTi wires subjected to tension", *International Journal of Mechanical Sciences*, 43(11):2657–2677.

Dolce, M., Cardone, D., and Ponzo, F., (2001), "Comparison of different passive control systems for r/c frames through shaking table tests", *Proceedings of the 5th World Congress on Joints, Bearings and Seismic Systems for Concrete Structures*, Rome, Italy.

Dolce, M., Cardone, D., and Ponzo, F.C., (2007b), "Shaking-table tests on reinforced concrete frames with different isolation systems", *Earthquake Engineering and Structural Dynamics*, 36(5):573–596.

Dolce, M., Cardone, D., Ponzo, F.C., and Valente, C., (2005), "Shaking table tests on reinforced concrete frames without and with passive control systems", *Earthquake*

Engineering and Structural Dynamics, 34(14):1687–1717.

Dong, J., Cai, C.S., and Okeil, A.M., (2010), "Overview of potential and existing applications of shape memory alloys in bridges", *Journal of Bridge Engineering, ASCE*, 16(2): 305–315.

Dowden, D.M., Purba, R., and Bruneau, M., (2011), "Behavior of self-centering steel plate shear walls and design considerations", *Journal of Structural Engineering, ASCE*, 138(1): 11–21.

Duerig, T.W., Melton, K.N., Stockel, D., and Wayman, C.M., (1990), *Engineering Aspects of Shape Memory Alloys*, Butter worth-Heinemam, London.

Dwairi, H., and Kowalsky, M., (2006), "Implementation of inelastic displacement patterns in direct displacement-based design of continuous bridge structures", *Earthquake Spectra*, 22(3): 631–662.

Eatherton, M.R., Ma, X., Krawinkler, H., Deierlein, G.G., and Hajjar, J.F., (2014), "Quasi-static cyclic behavior of controlled rocking steel frames", *Journal of Structural Engineering, ASCE*, 140(11), 04014083.

Eatherton, M.R., Ma, X., Krawinkler, H., Mar, D., Billington, S., Hajjar, J.F., and Deierlein, G.G., (2014), "Design concepts for controlled rocking of self-centering steel-braced frames", *Journal of Structural Engineering, ASCE*, 140(11), 04014082.

Ellingwood, B.R., Taftali, B., and DesRoches, R., (2010), "Seismic performance assessment of steel frames with shape memory alloy connections, Part II–Probabilistic seismic demand assessment", *Journal of Earthquake Engineering*, 14(5): 631–645.

Erochko, J., Christopoulos, C., and Tremblay, R., (2012), "Design and testing of an enhanced elongation telescoping self-centering energy-dissipative (T-SCED) brace", *Proceedings of the 15th World Conference on Earthquake Engineering*, Lisbon, Portugal.

Erochko, J., Christopoulos, C., and Tremblay, R., (2014), "Design, testing, and detailed component modeling of a high-capacity self-centering energy-dissipative brace", *Journal of Structural Engineering, ASCE*, 141(8), 04014193.

Erochko, J., Christopoulos, C., Tremblay, R. and Kim, HJ. (2013), "Shake table testing and numerical simulation of a self-centering energy dissipative braced frame". *Earthquake Engineering and Structural Dynamics*, 42(11): 1617–1635.

Fahnestock, L.A., Ricles, J.M., and Sause, R., (2007), "Experimental evaluation of a large-scale buckling-restrained braced frame", *Journal of Structural Engineering, ASCE*, 133(9): 1205–1214.

Fang, C., Yam, M.C., Lam, A.C., and Xie, L., (2014), "Cyclic performance of extended end-plate connections equipped with shape memory alloy bolts", *Journal of Constructional Steel Research*, 94: 122–136.

Faravelli, L., and Casciati, S., (2003), "Dynamic behavior of shape memory alloy structural devices: numerical and experimental investigation", *Solid Mechanics and its Applications*, 106: 63–72.

FEMA, (1997), *NEHRP Commentary on the guidelines for the seismic rehabilitation of buildings*, FEMA 274, Federal Emergency Management Agency, Washington, DC.

FEMA, (1997), *NEHRP Recommended provisions for seismic regulations for new buildings and other structures*, Federal Emergency Management Agency, Washington, DC.

Filiatrault, A., and Cherry, S., (1987), "Performance evaluation of friction damped braced steel frames under simulated earthquake loads", *Earthquake Spectra*, 3(1): 57–78.

Freeman, S.A., Nicoletti, J.P., and Tyrell, J.V., (1975). "Evaluations of existing buildings for seismic risk – A case study of Puget Sound Naval Shipyard, Bremerton, Washington", *Proceedings of 1st U.S. National Conference on Earthquake Engineering*, EERI, Berkeley, 113–122.

Freeman, S.A., (1978), "Prediction of response of concrete buildings to severe earthquake motion", *American Concrete Institute*, Detroit, MI, 589–605.

Garlock, M.M., Ricles, J.M., and Sause, R., (2003). "Cyclic load tests and analysis of bolted top-and-seat angle connections", *Journal of Structural Engineering, ASCE*, 129(12), 1615–1625.

Garlock, M.M., Ricles, J.M., and Sause, R., (2005), "Experimental studies of full-scale posttensioned steel connections", *Journal of Structural Engineering, ASCE*, 131(3):

438–448.

Garlock, M.M., Sause, R., and Ricles, J.M., (2007), “Behavior and design of posttensioned steel frame systems”, *Journal of Structural Engineering, ASCE*, 133(3): 389–399.

Ghassemieh, M., and Kargarmoakhar, R., (2013), “Response modification factor of steel frames utilizing shape memory alloys”, *Journal of Intelligent Material Systems and Structures*, 24(10): 1213–1225.

Gillet, Y., Patoor, E., and Berveiller, M., (1998), “Calculation of pseudoelastic elements using a non-symmetrical thermomechanical transformation criterion and associated rule”, *Journal of Intelligent Material Systems and Structures*, 9(5): 366–378.

Goel, S.C., and Chao, S.H., (2008), “Performance-based plastic design of special truss moment frames”, *Engineering Journal, AISC*, 45(2): 127–150.

Graesser, B.E.J. and Cozzarelli, F.A., (1992), “Shape-memory alloys as new materials for aseismic isolation”, *Journal of Engineering Mechanics, ASCE*, 117(11): 2590–2608.

Gur, S., and Mishra, S.K., (2013), “Multi-objective stochastic-structural-optimization of shape-memory-alloy assisted pure-friction bearing for isolating building against random earthquakes”, *Soil Dynamics and Earthquake Engineering*, 54: 1–16.

Gur, S., Mishra, S.K., and Chakraborty, S., (2014), “Performance assessment of buildings isolated by shape-memory-alloy rubber bearing: Comparison with elastomeric bearing under near-fault earthquakes”, *Structural Control and Health Monitoring*, 21(4):449–465.

Hashemi, SMT., and Khadem, SE., (2006), “Modeling and analysis of the vibration behavior of a shape memory alloy beam”, *International Journal of Mechanical Sciences*, 48(1): 44–52.

Hautcoeur, A., Eberhardt, A., Patoor, E., and Berveiller, M., (1995), “Thermomechanical behavior of monocrystalline Cu-Al-Be shape memory alloys and determination of the metastable phase diagram”, *Journal de Physique IV*, 5:459–64.

Hedba, D.A., and White, S.R., (1994), “Hysteresis training of nitinol wires”, In: Garcia, Cudney, Dasgupta, editors. Adaptive structures and composite materials: analysis and applications. New York: ASME. 1–8.

Housner, G.W., (1956), “Limit design of structures to resist earthquakes”, *Proceedings of the World Conference on Earthquake Engineering*, 5:1–11.

Housner, G.W. (1963), “The behavior of inverted pendulum structures during earthquakes”, *Bulletin of the Seismological Society of America*, 53(2): 403–417.

Huang, B., Zhang, H., Wang, H., and Song, G., (2014), “Passive base isolation with superelastic nitinol SMA helical springs”, *Smart Materials and Structures*, 23(6), 065009.

Indirli, M., Castellano, M.G., Clemente, P., and Martelli, A., (2001). Demo-application of shape memory alloy devices: the rehabilitation of the S. Giorgio Church bell tower. *Proceedings of SPIE's 8th Annual International Symposium on Smart Structures and Materials*. International Society for Optics and Photonics.

Jee, K.K., Han, J.H., Kim, Y.B., Lee, D.H., and Jang, W.Y., (2008), “New method for improving properties of SMA coil springs”, *The European Physical Journal Special Topics*, 158(1): 261–266.

Johnson, R., Padgett, J.E., and Maragakis, M.E., et al., (2008), “Large scale testing of nitinol shape memory alloy devices for retrofitting of bridges”, *Smart Materials and Structures*, 17(3): 1–10.

Kappos, A.J., Gidaris, I.G., and Gkatzogias, K.I., (2012), “Problems associated with direct displacement-based design of concrete bridges with single-column piers, and some suggested improvements”, *Bulletin of Earthquake Engineering*, 10(4): 1237–1266.

Kawashima, K., MacRae, G. A., Hoshikuma, J. I., and Nagaya, K., (1998), “Residual displacement response spectrum”, *Journal of Structural Engineering, ASCE*, 124(5): 523–530.

Kelly, J.M., Skinner, R.I., and Heine, A.J., (1972), “Mechanisms of energy absorption in special devices for use in earthquake resistant structures”, *Bulletin of NZ Society for Earthquake Engineering*, 5(3): 63–88.

Kim, H.J., and Christopoulos, C., (2009), “Seismic design procedure and seismic response of post-tensioned self-centering steel frames”, *Earthquake Engineering and Structural Dynamics*, 38(3): 355–376.

Kowalsky, M.J., (2002), “A displacement-based approach for the seismic design of continuous concrete bridges”, *Earthquake Engineering and Structural Dynamics*, 31(3): 719–747.

Lafortune, P., McCormick, J., DesRoches, R., and Terriault, P., (2007), “Testing of superelastic recentering pre-strained braces for seismic resistant design”, *Journal of Earthquake Engineering*, 11(3): 383–399.

Leelataviwat, S., Goel, S.C., and Stojadinovic, B., (1999), “Toward performance-based seismic design of structures”, *Earthquake Spectra*, 15(3): 435–461.

Lee, S.S., Goel, S.C., and Chao, S.H., (2004), “Performance-based seismic design of steel moment frames using target drift and yield mechanism”, *Proceedings of the 13th World Conference on Earthquake Engineering*, Vancouver, BC Canada, 1–6.

Li H., Mao C.X., and Ou, J.P., (2008), “Experimental and theoretical study on two types of shape memory alloy devices”, *Earthquake Engineering and Structural Dynamics*, 37: 407–426.

Liang, C., and Rogers, C.A., (1990), “One-dimensional thermomechanical constitutive relations for shape memory materials”, *Journal of Intelligent Material Systems and Structures*, 1(2): 207–234.

Liang, C., and Rogers, C.A., (1997), “Design of shape memory alloy springs with applications in vibration control”, *Journal of Intelligent Material Systems and Structures*, 8(4): 314–322.

Liew, K.M., Kitipornchai, S., Ng, T.Y., and Zou, G.P., (2002), “Multi-dimensional superelastic behavior of shape memory alloys via nonlinear finite element method”, *Engineering Structures*, 24(1): 51–57.

Lin, Y.Y., and Chang, K.C., (2003), “Study on damping reduction factor for buildings under earthquake ground motions”, *Journal of Structural Engineering, ASCE*, 129(2): 206–214.

Lin, Y.C., Sause, R., and Ricles, J.M., (2013), “Seismic performance of steel self-centering, moment-resisting frame: Hybrid simulations under design basis earthquake", *Journal of Structural Engineering, ASCE*, 139(11): 1823–1832.

Liu, M., Li, H., Song, G., and Ou, J., (2007), "Investigation of vibration mitigation of stay cables incorporated with superelastic shape memory alloy dampers", *Smart Materials and Structures*, 16(6), 2202.

Liu, J.L., Zhu, S., Xu, Y.L., and Zhang, Y., (2011), "Displacement-based design approach for highway bridges with SMA isolators", *Smart Structures and Systems*, 8(2):173–190.

Malekpour, S., Ghaffarzadeh, H., and Dashti, F., (2013), "Direct displacement-based design of steel-braced reinforced concrete frames", *The Structural Design of Tall and Special Buildings*, 22(18): 1422–1438.

Marriott, D., Pampanin, S., and Palermo, A., (2009), "Quasi-static and pseudo-dynamic testing of unbonded post-tensioned rocking bridge piers with external replaceable dissipaters", *Earthquake Engineering and Structural Dynamics*, 38(3): 331–354.

McCormick, J., Aburano, H., Ikenaga, M., and Nakashima, M., (2008). "Permissible residual deformation levels for building structures considering both safety and human elements", *Proceedings of the 14th World Conference on Earthquake Engineering*, Beijing, China.

McCormick, J., DesRoches, R., Fugazza, D., and Auricchio, F., (2007), "Seismic assessment of concentrically braced steel frames with shape memory alloy braces", *Journal of Structural Engineering, ASCE*, 133(6), 862–870.

Mirzaeifar, R., DesRoches, R., and Yavari, A., (2010), "Exact solutions for pure torsion of shape memory alloy circular bars", *Mechanics of Materials*, 42(8): 797–806.

Mirzaeifar, R., DesRoches, R., and Yavari, A., (2011), "A combined analytical, numerical, and experimental study of shape-memory-alloy helical springs", *International Journal of Solids and Structures*, 48(3): 611–624.

Mirzaeifar, R., DesRoches, R., Yavari, A., and Gall, K. (2013), "On superelastic bending of shape memory alloy beams", *International Journal of Solids and Structures*, 50(10): 1664–1680.

Miyazaki, S., Imai, T., Igo, Y., and Otsuka, K., (1986), "Effect of cyclic deformation on the pseudoelasticity characteristics of Ti-Ni alloys", *Metallurgical Transactions A*, 17A, 115–120.

Moradi, S., Alam, MS., and Asgarian, B., (2014), “Incremental dynamic analysis of steel frames equipped with NiTi shape memory alloy braces”, *The Structural Design of Tall and Special Buildings*, 23(18), 1406–1425.

Morgan, N.B., and Broadley, M., (2004), “Taking the art out of smart!-Forming processes and durability issues for the application of NiTi shape memory alloys in medical devices”, *Proceedings for the Materials and Processes for Medical Devices Coference*, Anaheim, CA, 247–252.

Muntasir Billah, A.H.M., and Shahria Alam, M., (2012), “Seismic performance of concrete columns reinforced with hybrid shape memory alloy (SMA) and fiber reinforced polymer (FRP) bars”, *Construction and Building Materials*, 28(1): 730–742.

Neuenhofer, A., and Filippou, F.C., (1997), “Evaluation of nonlinear frame finite-element models”, *Journal of Structural Engineering, ASCE*, 123(7):958–966.

Nicoletti, M., Braga, F., and Dolce, M., (1997), “Memory Alloys for New Seismic Isolation and Energy Dissipation Devices: First Achievements of the MANSIDE Project”, *Proceedings of International Post-SMiRT Conference Seminar on Seismic Isolation, Passive Energy Dissipation, and Active Control of Vibrations of Structures*, Taorrnina, Italy.

OpenSees. “Open system for earthquake engineering simulation (OpenSees), v 2.4.1 [Computer software]”, Pacific Earthquake Engineering Research Center, Berkeley, CA. 2013.

O’Reilly, G.J., Goggins, J., and Mahin, S.A., (2012), “Performance-based design of a self-centering concentrically braced frame using the direct displacement-based design procedure”, *15 WCEE*, Lisboa.

Otani, S., (1997), “Lessons learned from past earthquakes”, *Proceedings of Fourth Turkish National Conference on Earthquake Engineering*.

Otsuka, K., Sakamoto, H., and Shimizu, K., (1979), “Successive stress-induced martensitic transformations and associated transformation pseudoelasticity in Cu-Al-Ni alloys”, *Acta Metallurgica*, 27(4):585–601.

Otsuka, K., and Wayman, C.M., (1998), “Mechanism of shape memory effect and superelasticity”, *Shape Memory Materials*, 27–49.

Otsuka, K., and Wayman, C.M., (1999), *Shape memory materials*. Cambridge University Press.

Ozbulut, O.E., and Hurlebaus, S., (2011), “Optimal design of superelastic-friction base isolators for seismic protection of highway bridges against near-field earthquakes”, *Earthquake Engineering and Structural Dynamics*, 40(3): 273–291.

Ozbulut, O.E., and Hurlebaus, S., (2012), “A comparative study on the seismic performance of superelastic-friction base isolators against near-field earthquakes”, *Earthquake Spectra*, 28(3): 1147–1163.

Ozbulut, O.E., Hurlebaus, S., and DesRoches, R., (2011), “Seismic response control using shape memory alloys, a review”, *Journal of Intelligent Material Systems and Structures*, 22(14):1531–1549.

Ozbulut, O.E., Mir, C., Moroni, M.O., Sarrazin, M., and Roschke, P.N., (2007), “A fuzzy model of superelastic shape memory alloys for vibration control in civil engineering applications”, *Smart Materials and Structures*, 16(3), 818.

Ozbulut, O., and Silwal, B., (2014), “Performance of isolated buildings with superelastic-friction base isolators under high seismic hazards”, *Structures Congress, ASCE*.

Özdemir, H., (1976), “Nonlinear transient dynamic analysis of yielding structures”, Doctoral dissertation, University of California, Berkeley.

Padgett, J.E., DesRoches, R., and Ehlinger R., (2010), “Experimental response modification of a four-span bridge retrofit with shape memory alloys”, *Structural Control and Health Monitoring*, 32(3):165–173.

Pall, A.S., and Marsh, C., (1982), “Response of friction damped braced frames”, *Journal of Structural Engineering, ASCE*, 108(9): 1313–1323.

Parulekar, Y.M., Kiran, A.R., Reddy, G.R., Singh, R.K., and Vaze, K.K., (2014), “Shake table tests and analytical simulations of a steel structure with shape memory alloy dampers”, *Smart Materials and Structures*, 23(12), 125002.

Patoor, E., Lagoudas, D.C., Entchev, P.B., Brinson, L.C., and Gao, X., (2006), “Shape memory alloys, Part I: General properties and modeling of single crystals", *Mechanics of materials,* 38(5): 391–429.

Pennucci D., Calvi G.M, and Sullivan T.J., (2009), "Displacement-based design of precast walls with additional dampers", *Journal of Earthquake Engineering*, 13:S1, 40–65.

Poland, C.D., and Hom, D.B., (1997), "Opportunities and pitfalls of performance based seismic engineering", *Proceedings of Seismic Design Methodologies for the Next Generation Codes*, Slovenia, 69–78.

Prahlad, H., and Chopra, I., (2003), "Development of a strain-rate dependent model for uniaxial loading of SMA wires", *Journal of Intelligent Material Systems and Structures*, 14: 429–442.

Prakash, V., Powell, G.H. and Campbell, S., (1993), "DRAIN-2DX: Base program and user guide", Rep. No. UCB/SES-93/17, Univ. of California, Berkeley, Calif.

Predki, W., Klönne, M., and Knopik, A., (2006), "Cyclic torsional loading of pseudoelastic NiTi shape memory alloys: Damping and fatigue failure", *Materials Science and Engineering: A*, 417(1): 182–189.

Priestley, M.J.N., (1993), "Myths and fallacies in earthquake engineering-conflicts between design and reality", *Bulletin of the New Zealand National Society for Earthquake Engineering*, 26(3): 329–341.

Priestley, M.J.N., (1997), "Displacement based seismic assessment of reinforced concrete buildings", *Journal of Earthquake Engineering*, 1(1): 157–192.

Priestley, M.J.N., (2000), "Performance-based seismic design". Keynote Address, *Proceedings of 12th World Conference on Earthquake Engineering*. Auckland.

Priestley, M.J.N., (2003), "Myths and fallacies in earthquake engineering, Revisited", The Mallet Milne Lecture, IUSS Press, Pavia, Italy.

Priestley, M.J.N., Calvi, G.M., and Kowalsky M.J., (2007), *Displacement based seismic design of structures*, IUSS Press, Pavia, Italy.

Priestley, M.J.N., and Grant, D.N., (2005), "Viscous damping in seismic design and analysis", *Journal of Earthquake Engineering*, 9(sup2): 229–255.

Priestley, M.J.N., and Kowalsky, M.J., (2000), "Direct displacement-based seismic design of concrete buildings", *Bulletin of the New Zealand Society for Earthquake Engineering*, 33(4): 421–444.

Priestley, M.J.N., and MACRASE, G., (1996), "Seismic tests of precast beam-to-column joint subassemblages with unbonded tendons", *PCI journal*, 41(1): 64–81.

Priestley, M.J.N., Sritharan, S., Conley, J.R., and Pampanin, S., (1999), "Preliminary results and conclusions from the PRESSS five-story precast concrete test building", *PCI Journal*, 44(6): 42–67.

Rafiqul Haque, A.B.M., and Alam, M.S., (2013), "Direct Displacement-Based Design of Industrial Rack Clad Buildings", *Earthquake Spectra*, 29(4): 1311–1334.

Rao, A., and Srinivasa, A.R., (2013), "A two species thermodynamic preisach model for the torsional response of shape memory alloy wires and springs under superelastic conditions", *International Journal of Solids and Structures*, 50(6): 887–898.

Reedlunn, B., Churchill, C.B., Nelson, E.E., Shaw, J.A., and Daly, S.H., (2014), "Tension, compression, and bending of superelastic shape memory alloy tubes", *Journal of the Mechanics and Physics of Solids*, 63: 506–537.

Reinhorn, A., (1997), "Inelastic analysis techniques in seismic evaluation", *In: Seismic design methodologies for the next generation of codes: proceedings of the international workshop*, Bled, Slovenia.

Ricles, J.M., Sause, R., Garlock, M.M., and Zhao, C., (2001), "Post-tensioned seismic resistant connections for steel frames", *Journal of Structural Engineering, ASCE*, 127(2): 113–121.

Rojas, P., Ricles, J.M., and Sause, R., (2005), "Seismic performance of post-tensioned steel moment resisting frames with friction devices", *Journal of Structural Engineering*, 131(4): 529–540.

Saadat, S., Noori, M., Davoodi, H., Hou, Z., Suzuki, Y., and Masuda, A., (2001), "Using NiTi SMA tendons for vibration control of coastal structures", *Smart Materials and Structures*, 10(4), 695.

Sabelli, R., Mahin, S.A., and Chang C., (2003), "Seismic demands on steel-braced buildings with buckling-restrained braces", *Engineering Structures*, 25: 655–666.

Sahoo, D.R., and Chao, S.H., (2010), “Performance-based plastic design method for buckling-restrained frames”, *Engineering structures*, 32: 2950–2958.

Sakamoto, H., Shimizu, K., and Otsuka, K., (1985), “A detailed observation on successive stress-induced martensitic transformations in Cu-Al-Ni alloy single crystals above A_f”, *Transactions of the Japan Institute of Metals*, 26(9):638–645.

Savi, M.A., Pacheco, P.M.C., Garcia, M.S., Aguiar, R.A., de Souza, L.F.G., and da Hora, R.B., (2015), “Nonlinear geometric influence on the mechanical behavior of shape memory alloy helical springs”, *Smart Materials and Structures*, 24(3), 035012.

Schmidt, I., and Lammering, R., (2004), “The damping behaviour of superelastic NiTi components”, *Materials Science and Engineering: A*, 378(1): 70–75.

Scott, M.H., Franchin, P., Fenves, G.L., and Filippou, F.C., (2004), “Response sensitivity for nonlinear beam-column elements”, *Journal of Structural Engineering, ASCE*, 130(9):1281–1288.

SEAOC, (1995), “Performance based seismic engineering of buildings”, Vision 2000 report. Structural Engineers Association of California, Volumes I and II, Sacramento, California.

Seo, C.Y., (2005), “Influence of ground motion characteristics and structural parameters on seismic responses of SDOF systems”, Ph.D. dissertation, Department of Civil and Environmental Engineering, Lehigh University, Bethlehem, PA.

Sepulveda, J., Boroschek, R., Herrera, R., Moroni, O., and Sarrazin, M., (2008), “Steel beam-column connection using copper-based shape memory alloy dampers”, *Journal of Constructional Steel Research*, 64(4):429–435.

Sharabash, A.M. and Andrawes, B.O., (2009), “Application of shape memory alloy dampers in the seismic control of cable-stayed bridges”, *Engineering Structures*, 31: 607–616.

Shen, K.L., and Soong, T.T., (1995), “Modeling of viscoelastic dampers for structural applications”, *Journal of Engineering Mechanics*, 121(6): 694–701.

Shigley, J.E., Mischke, C.R., Budynas, R.G., Liu, X., and Gao, Z., (1989), *Mechanical engineering design (Vol. 89)*, New York: McGraw-Hill.

Shinozuka, M., Chaudhuri, S.R., and Mishra, S.K., (2015), “Shape-memory-alloy supplemented lead rubber bearing (SMA-LRB) for seismic isolation", *Probabilistic Engineering Mechanics*, 41: 34–45.

Shrestha, K.C., Araki, Y., and Nagae, T., et al. (2013), "Effectiveness of superelastic bars for seismic rehabilitation of clay-unit masonry walls", *Earthquake Engineering and Structural Dynamics*, 42: 725–741.

Somerville, P., Smith, N., Punyamurthula, S., and Sun J., (1997), "Development of ground motion time histories for Phase 2 of the FEAM/SAC steel project", *SAC Background document SAC/BD-91/04*, SAC joint venture, Sacramento, California.

Song, G., Ma, N., and Li, H.N., (2006), "Applications of shape memory alloys in civil structures", *Engineering Structures*, 28(9):1266–1274.

Speicher, M., Hodgson, D.E., DesRoches, R., and Leon, R.T., (2009), "Shape memory alloy tension/compression device for seismic retrofit of buildings", *Journal of Materials Engineering and Performance*, 18(5–6): 746–753.

Speicher, M.S., DesRoches, R., and Leon, R.T., (2011), "Experimental results of a NiTi shape memory alloy (SMA)-based recentering beam-column connection", *Engineering Structures*, 33(9): 2448–2457.

Tanaka, K., Kobayashi, S., and Sato, Y., (1986), "Thermomechanics of transformation pseudoelasticity and shape memory effect in alloys", *International Journal of Plasticity*, 2(1): 59–72.

Tobushi, H., and Tanaka, K., (1991), "Deformation of a shape memory alloy helical spring (analysis based on stress-strain-temperature relation)", *JSME International Journal*. Series 1, solid mechanics, strength of materials, 34(1): 83–89.

Tobushi, H., Iwanaga, H., and Tanaka, K., (1998), "Influence of strain rate on superelastic properties of NiTi shape memory alloys", *Mechanics of Materials*, 30:141–150.

Toi, Y., Lee, J.B., and Taya, M., (2004), "Finite element analysis of superelastic, large deformation behavior of shape memory alloy helical springs", *Computers and Structures*, 82(20): 1685–1693.

Tremblay R., Lacerte M. and Christopoulos C., (2008), "Seismic response of multistory buildings with self-centering energy dissipative steel braces", *Journal of Structural*

Engineering, ASCE, 134(1): 108–120.

Tsai, C.S., and Tsai, K.C., (1995), "TPEA device as seismic damper for high-rise buildings", *Journal of Engineering Mechanics, ASCE,* 121(10):1075–1081.

Uang, C.M., (1991), "Establishing R (or R_w) and C_d factors for building seismic provisions", *Journal of Structural Engineering, ASCE,* 117(1): 19–28.

Van de Lindt, J.W., and Potts, A., (2008), "Shake table testing of a superelastic shape memory alloy response modification device in a wood shearwall", *Journal of Structural Engineering,* 134(8): 1343–1352.

Wada, A., and Nakashima, M., (2004), "From infancy to maturity of buckling restrained braces research", *Proceedings of the 13th World Conference on Earthquake Engineering,* Vancouver, British Columbia, Canada.

Walter Yang, C.S., DesRoches, R., and Leon, R.T., (2010), "Design and analysis of braced frames with shape memory alloy and energy-absorbing hybrid devices", *Engineering Structures,* 32(2): 498–507.

Whittaker, A.S., Bertero, V.V., Thompson, C.L., and Alonso, L.J., (1991), "Seismic testing of steel plate energy dissipation devices", *Earthquake Spectra,*7(4): 563–604.

Wilde, K., Gardoni, P., and Fujino, Y., (2000), "Base isolation system with shape memory alloy device for elevated highway bridges", *Engineering Structures,* 22(3):222–229.

Wilson, J.C., and Wesolowsky, M.J., (2005), "Shape memory alloys for seismic response modification: a state-of-the-art review", *Earthquake Spectra,* 21(2): 569–601.

Wolons, D., Gandhi, F., and Malovrh, B., (1998), "Experimental investigation of the pseudoelastic hysteresis damping characteristics of shape memory alloy wires", *Journal of Intelligent Material Systems and Structures,* 9(2):116–126.

Wolski, M., Ricles, J.M., and Sause, R., (2009), "Experimental study of a self-centering beam-column connection with bottom flange friction device", *Journal of Structural Engineering, ASCE,* 135(5): 479–488.

Wu, H., (1990), "Cu-based shape memory alloys. In: Engineering aspects of shape memory alloys", Butterworth-Heinemann Ltd, 69–88.

Wu, M.H., (2001), “Fabrication of nitinol materials and components”, *Proceedings of the International Conference on Shape Memory and Superelastic Technologies*, Kunming, China.

Xie, Z., Liu, Y., and Van Humbeeck, J., (1998), “Microstructure of NiTi shape memory alloy due to tension-compression cyclic deformation”, Acta Materialia, 46(6): 1989–2000.

Yam, M.C., Fang, C., Lam, A.C., and Zhang, Y., (2015), “Numerical study and practical design of beam-to-column connections with shape memory alloys”, *Journal of Constructional Steel Research*, 104: 177–192.

Yang, T.Y., Li, Y.J., and Leelataviwat, S., (2014), “Performance-based design and optimization of buckling restrained knee braced truss moment frame”, *Journal of Performance of Constructed Facilities, ASCE*, 28, SPECIAL ISSUE: Performance of Timber and Hybrid Structures, A4014007.

Youssef, M.A., Alam, M.S., and Nehdi, M., (2008), “Experimental investigation on the seismic behavior of beam-column joints reinforced with superelastic shape memory alloys”, *Journal of Earthquake Engineering*, 12(7): 1205–1222.

Zhang, Y., Camilleri, J.A., and Zhu, S., (2008), “Mechanical properties of superelastic Cu-AlBe wires at cold temperatures for the seismic protection of bridges”, *Smart Materials and Structures*,17(2):1–9.

Zhang, Y., Hu, X., and Zhu, S., (2009), “Seismic performance of benchmark base-isolated bridges with superelastic Cu-Al-Be restraining damping device”, *Structural Control and Health Monitoring*, 16(6):668–685.

Zhang, Y., and Zhu, S., (2007), “A shape memory alloy-based reusable hysteretic damper for seismic hazard mitigation”, *Smart Material and Structures*, 16(5): 1603–1613.

Zhu, S., and Zhang, Y., (2007a), “A thermomechanical constitutive model for superelastic SMA wire with strain-rate dependence”, *Smart Materials and Structures*, 16(5):1696–1707.

Zhu, S., and Zhang, Y., (2007b), “Seismic behavior of self-centering braced frame buildings with reusable hysteretic damping brace”, *Earthquake Engineering and*

Structural Dynamics, 36(10): 1329–46.

Zhu, S., and Zhang, Y., (2008), “Seismic analysis of concentrically braced frame systems with self-centering friction damping braces”, *Journal of Structural Engineering*, *ASCE*, 134(1): 121–131.

Zhu, S., and Zhang, Y., (2013), “Loading rate effect on superelastic SMA-based seismic response modification devices”, *Earthquakes and Structures*, 4(6): 607–627.

“List of aftershocks of the Wenchuan earthquake exceeding M4” (in Chinese). Sichuan Quake Prevention and Disaster Reduction Information Network, by SCEA. 2008-07-18. Archived from the original on 2008-07-30. Retrieved 2008-10-25. From http://www.scdzj.gov.cn/zt/kzjzzzcc/wcdz4jml/